Department of Chemistry

An Infrared Spectroelectrochemical Approach for Understanding Electrocatalysis at Supported Metal Nanoparticles

---

Ian McPherson

St Anne's College

Supervisor:

Prof. Kylie Vincent

A thesis submitted in partial fulfilment of the requirements

for the degree of Doctor of Philosophy

Trinity Term 2015

An Infrared Spectroelectrochemical Approach for Understanding Electrocatalysis at Supported Metal Nanoparticles

A thesis submitted for the degree of Doctor of Philosophy

Ian McPherson, St Anne's College, Michaelmas 2015

This thesis describes the development and application of a new in situ infrared (IR) approach to studying electrocatalysis at supported nanoparticle catalysts that are used in proton exchange membrane (PEM) fuel cells. Such fuel cells running on small organic molecules are an attractive technology for use in transport applications and portable electronic devices, however one major challenge facing this technology is the slow oxidation of the organic molecules at the electrode surface. Furthermore, the mechanisms by which these organic molecules are oxidised are still not clear, hampering the design of new electrode materials. In situ IR spectroscopy has been used extensively to investigate the mechanism of reactions on model catalysts, however extension of these techniques to real fuel cell catalysts is challenging and much less advanced.

A new approach to in situ IR spectroscopy of supported electrocatalysts is therefore developed, inspired by the geometry of PEM fuel cell electrodes. The approach overcomes many of the limitations of previous approaches, allowing solution flow over the catalyst layer, cyclic voltammetry up to scan rates of $1\,\mathrm{V\ s^{-1}}$ and spectroscopic detection of surface adsorbed species with time resolution of 0.5 s. The utility of this approach is demonstrated through a study of the mechanism of two model reactions, carbon monoxide (CO) and formic acid (FA) oxidation, on a commercial fuel cell catalyst.

In situ IR measurements made during CO stripping experiments on a commercial carbon-supported Pt catalyst reveal two strongly bipolar IR peaks in the CO stretching region. An empirical model for the bipolar peak shape is developed and used to extract peak parameters. Electrochemical measurement of the CO coverage then enables calibration of the IR peak intensity with coverage. This quantitative relationship enables features such as dipole-dipole coupling in the CO adlayer to be discussed. In situ IR spectra recorded during the stripping voltammogram reveal the presence of two linear CO peaks, assigned to different sites on the catalyst. The potential dependence of the two peak intensities is used to discuss the mechanism of CO oxidation on the catalyst.

The in situ approach is extended to the study of FA oxidation on the commercial Pt catalyst. As well as adsorbed CO, two potential-dependent peaks are assigned to adsorbed formate - the first time formate has been observed on a nanoparticle catalyst during electrooxidation. Furthermore, one of the peaks is assigned to an IR surface selection rule-prohibited mode, providing evidence for the previously proposed size-dependence of the selection rule. The effects of concentration, pH, isotope and supporting electrolyte on the adsorbed species are examined and related to the current in order to understand different aspects of the mechanism on nanoparticle catalysts. The results are discussed in the context of previous work on macroscopic electrodes.

Overall an approach to in situ IR spectroscopy of nanoparticle electrocatalysts is presented and is used to probe the mechanisms of CO and FA oxidation under conditions relevant to fuel cells.

Acknowledgements

First of all I would like to sincerely thank Prof. Kylie Vincent for giving me the opportunity to work in her group over the past 5 years, and for the encouragement, fun and freedom that has come with this. I would also like to thank Dr Philip Ash for his enthusiasm, guidance and patience in all things spectroscopy and Dr Holly Reeve for making the group such a friendly and enjoyable one to work in. Jonathan Quinson is gratefully acknowledged for his time and skill obtaining SEM images, as well as for hosting numerous barbecues. Gary Chang is also thanked for his superior tuckshop and useful discussions. I also owe much to Dr Adam Healy and Dr Juan Liu for their prior work in this area, Dr Robert Jacobs for extensive use of his lab, instruments and time, and latterly to Dr Matteo Duca and Dr Simantini Nayak for their help and advice. The rest of the Vincent group (Zul, Pong, Ricardo, Tom, Min-Wen, Tianze and Ellie) are thanked for their friendship and sense of humour over the last 5 years.

Dr Lewys Jones and Aakash Varambhia are thanked for the STEM images, particle size analysis and useful discussions. Mr Charles Jones is warmly thanked for sharing his time, expertise and enthusiasm for engineering in the Student Workshop, along with all of the staff in the PTCL Mechanical workshop. Dr Bob Watkins in the Department of Physics Metallography workshop is also gratefully acknowledged for his time and useful discussions.

Outside of the lab, I would first like to thank my family for their unwavering support over the last 26 years. The various inhabitants of 84 Percy Street, John, Jonny, Jonny, Conor, Tom and Row, are also gratefully acknowledged for a fun, if not bizarre, 2 years of puns, angling shows, brewing and Viking parties.

Finally I extend my deepest thanks to Amy for her love, encouragement and patience; I couldn't have done this without you.

Nomenclature

δ(CH)	In plane bending vibration of C−H
$\Delta_r G^\circ$	Standard Gibbs energy of reaction
ϵ	Dielectric constant
γ	Fitted peak width
ν_s	Singleton wavenumber, wavenumber of adsorbed species in the absence of lateral interactions
ν_s(OCO)	Symmetric stretching vibration of OCO
ϕ	Inner potential, the work done on bringing a test charge from infinity into an electrode
θ_i	Angle of incidence
$\tilde{\nu}$(CO)	The wavenumber of the C−O stretching vibration
$\tilde{\nu}_0$	Fitted peak wavenumber
A	Absorbance
E	Electrode potential, a measured difference in inner potentials
E°	Standard electrode potential, reactants at unit activity
F	Faraday Constant, $F = N_A \times q = 96\,485\,\mathrm{Cmol}^{-1}$
f	Fitted oscillator strength
f/f_0	Relative oscillator strength
i	Current
iR_u	Voltage drop due to uncompensated resistance, R_u
$k(\tilde{\nu})$	Extinction coefficient
$n(\tilde{\nu})$	Refractive Index
n_∞	Baseline refractive index
Q_CO	Charge measured for CO oxidation

$Q_{\mathrm{H}}^{\mathrm{CO}}$ Charge measured for H desorption in the presence of CO

$Q_{\mathrm{H}}^{\mathrm{max}}$ Maximum charge measured for H desorption

R Reflectance

$r_{s,p}$ Fresnel coefficients for s, p-polarised light

(hkl) Surface with Miller indices h, k, l

(ads) adsorbed

A Absorbance

ATR Attenuated Total Reflection

CE Counter Electrode

DEMS Differential Electrochemical Mass Spectrometry

DFT Density Functional Theory

FTIR Fourier Transform Infrared

GDL Gas Diffusion Layer

HAADF-STEM High Angle Annular Dark Field Scanning Transmission Electron Microscopy

HCOO(ad) Adsorbed bridging formate

IFF Interdigitated Flow Field

IRE Internal Reflection Element

IRRAS Infrared Reflection-Absorption Spectroscopy

KIE Kinetic Isotope Effect

PEEK polyether ether ketone

PEMFC Proton Exchange Membrane Fuel Cell

Pt/C Pt catalyst supported on carbon black

rds Rate Determining Step

RE Reference Electrode

SE Sense Electrode

SEIRA Surface Enhanced Infrared Absorption

SEM Scanning Electron Microscope

SHE Standard Hydrogen Electrode

SXS Surface X-ray Scattering

TOF Turnover frequency, molecules produced per site per second

UHV Ultra High Vacuum

WE Working Electrode

Contents

List of Figures

List of Tables

Chapter 1

Introduction

There is an increasingly urgent need to find viable renewable alternatives to fossil fuel-based power generation. This need is driven by the requirement to reduce carbon emissions, due to their contribution to climate change, [1] the increasing volatility in the price of imported fossil fuel, [2] and the detrimental impact emissions from combustion processes have on public health. [3]

One such alternative for electricity generation is the fuel cell. [4,5] These devices couple an oxidation reaction occurring at one electrode with a reduction reaction occurring at a second electrode, with the resulting flow of electrons between the two electrodes providing an electrical current. One type of fuel cell which has received much interest for use in portable electronic and vehicular applications is the proton exchange membrane fuel cell (PEMFC). [4–9]

1.1 Proton Exchange Membrane Fuel Cells

The PEMFC operates by coupling the electrochemical oxidation of a hydrogen-containing fuel at one electrode, with the reduction of atmospheric oxygen at a second electrode. The archetypal PEMFC reaction is the oxidation of pure H_2 to H_2O. The fuel, H_2, is oxidised

at the anode to release 2 electrons, with a standard potential, E° of 0.0 V.

$$H_2 \longrightarrow 2\,H^+ + 2\,e^- \qquad E^\circ = 0.00\,V$$

The electrons released are used to reduce O_2 from the air.

$$\tfrac{1}{2}\,O_2 + 2\,H^+ + 2\,e^- \longrightarrow H_2O \qquad E^\circ = 1.23\,V$$

Overall the reaction is the oxidation of H_2 to form H_2O and the theoretical open circuit voltage is 1.23 V.

$$H_2 + \tfrac{1}{2}O_2 \longrightarrow H_2O \qquad E^\circ(O_2/H_2O) - E^\circ(H^+/H_2)$$
$$= 1.23\,V$$

These oxidation and reduction reactions occur at the surface of an electrode. It is found that the rate of these reactions depend strongly on the composition and structure of the electrode surface, an effect known as electrocatalysis, since the electrode enhances the reaction rate without being consumed. The best electrocatalysts are often found to be precious metals such as Pt and Pd. [10, 11] To maximise utilisation of these precious electrode materials, the electrode is made from small particles of the metal which are formed into high surface area, porous electrodes. To ensure these particles remain dispersed and in good electrical contact they are supported on a high surface area conducting material such as carbon black. [4, 5, 10] Such supported catalysts are often denoted Pt/C, where Pt represents the metal catalyst and C the carbon support. Figure 1.1A shows a schematic illustration of these porous electrodes. [6, 10]

The electrodes in a PEMFC are separated by a membrane. This prevents the fuel and oxidant from mixing (known as crossover), which would decrease the polarisation

of the cell. The membrane does allow movement of H^+ ions between the compartments, however, which is essential to balance the charge of the electrons flowing from one electrode to the other. The membrane is made from a sulfonated fluoropolymer, such as Nafion, in which the proton conducting ability arises from the $-SO_3^-$ groups present throughout the structure. [12] Electrical connection to the electrodes is made first via contact with a porous conductive layer known as the gas diffusion layer, and then by contact with a conductive plate known as a flow field. The flow field has a series of flow channels to ensure fuel and oxidant reach all parts of the respective electrodes.

A scanning electron microscope (SEM) image of a supported catalyst layer is shown in fig. 1.1B. The large amount of dark space reveals the material's porous nature, while the bright spots indicate clusters of metal particles. A metal particle is shown in more detail through the use of dark field scanning transmission electron microscopy (fig. 1.1C), where the lattice fringes and sharp edges reveal the crystalline nature of the metal particle.

A major challenge facing the widespread adoption of PEMFCs running on H_2 is the lack of technologies available for the safe and economical production, [13] storage [14] and distribution of H_2 gas. [15] For example, the primary method of H_2 production, methane steam reforming (eq. (1.1)) followed by the water gas shift reaction (eq. (1.2)), produces gas containing significant amounts of CO. This is problematic for fuel cells as CO strongly adsorbs to many of the electrocatalysts, decreasing their activity and therefore the performance of the cell, in a process known as poisoning. [16]

$$CH_4 + H_2O \rightleftharpoons CO + 3\,H_2 \tag{1.1}$$

$$H_2O + CO \rightleftharpoons H_2 + CO_2 \tag{1.2}$$

As an alternative to H_2 gas, a range of small organic molecule fuels have been proposed (table 1.1). [17, 18] The use of organic liquids, such as formic acid (HCOOH) and

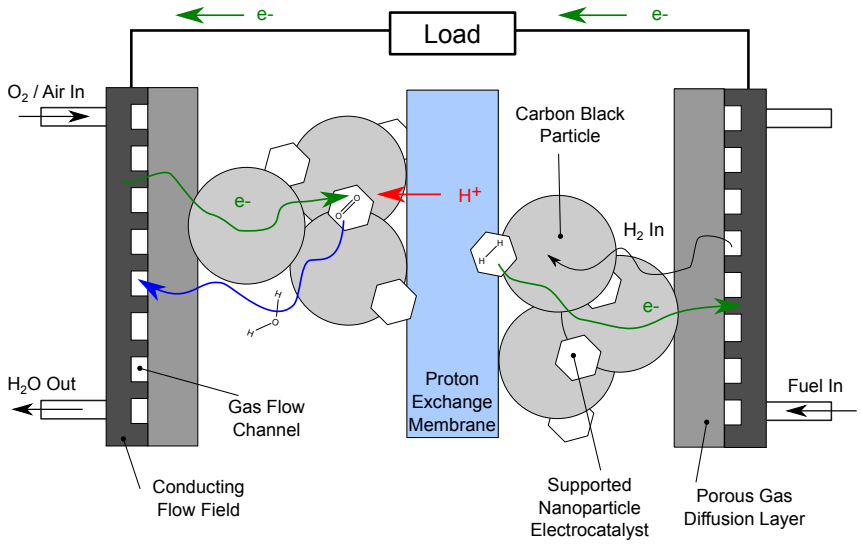

(A)

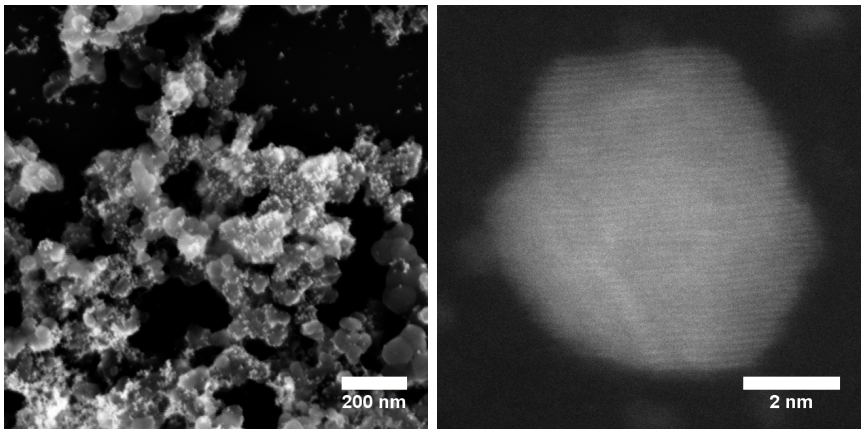

(B) (C)

Figure 1.1: A: Schematic illustration of a proton exchange membrane fuel cell (PEMFC). B: Scanning electron micrograph of a supported catalyst layer. Image courtesy of Jonathan Quinson. C: Dark field scanning transmission electron micrograph of an individual catalyst nanoparticle. Image courtesy of Lewys Jones.

Table 1.1: Comparison of fuels considered for use in PEMFCs.

Fuel	Reaction	Energy Density[a] /kWh kg^{-1}	$\Delta_r G^{\circ}$[b] /kJ mol^{-1}	E° /V
Hydrogen	$H_2 + \frac{1}{2}O_2 \longrightarrow H_2O$	5.0	-237	1.23
Methanol	$CH_3OH + \frac{3}{2}O_2 \longrightarrow CO_2 + 2\,H_2O$	6.1	-697	1.21
Formic acid	$HCOOH + \frac{1}{2}O_2 \longrightarrow CO_2 + H_2O$	1.7	-285	1.48
Petrol		10.2		

[a] From references [19, 20].
[b] From reference [21].

methanol (CH_3OH), as fuels has several advantages over H_2 gas; as well as posing fewer safety concerns, there already exists the technology and infrastructure for the storage and transportation of these liquid fuels. In addition, such fuels can provide comparable energy densities to that of compressed liquid H_2. [19, 20]

Methanol is the most investigated alternative fuel for PEMFCs and has a very similar energy density to liquid H_2. [22] Methanol fuel cells suffer from fuel crossover however, limiting practical methanol concentrations in the fuel stream to around 2 M and consequently limiting methanol's practical energy density. An alternative to methanol is formic acid; formic acid fuel cells exhibit much lower crossover rates than those running on methanol, which is thought to be due to repulsion between the formate anion and the anionic SO_3 groups in Nafion. [8] Thus, while formic acid has a lower formal energy density than methanol, because it can be used at concentrations up to 20 M, [18] it is a viable alternative.

A major disadvantage of using any small organic molecule as a fuel, however, is the low oxidation current obtained due to their much slower electrode kinetics. [23, 24] The significantly more complex nature of organic molecules compared to H_2 is likely to lead to multiple reaction pathways, the nature and identity of which are still not fully understood. The production of PEMFCs capable of operating on small organic molecule fuels therefore

requires developments in the mechanistic understanding of the oxidation reactions, as well the development of improved electrocatalysts. Ideally these two tasks are related, with developments in mechanistic understanding being used to inform catalyst design, and the discovery of improved catalysts providing mechanistic insight.

1.2 Mechanistic Studies of Electrocatalysis in PEMFCs

The fundamental parameters used to describe an electrode are its potential relative to a reference electrode and the current it is passing. While these parameters have long been used to investigate electrochemical reaction mechanisms, they offer limited information on the individual species present at the electrode. As a result a variety of spectroscopic techniques have been combined with electrochemical measurements in order to characterise the surface of the electrode and the species in its vicinity (table 1.2).

1.2.1 IR Reflection Spectroscopy of Electrodes

Of the *in situ* techniques, it is Fourier Transform Infrared (FTIR) spectroscopy that is the most widely used. *In situ* FTIR spectroscopy probes the vibrational frequencies of species at the electrode surface; as well as providing a unique signature with which to identity species at the surface, the values of individual vibrational frequencies provide information on the local environment of the species through their dependence on the bond force constants, and thus indirectly the electronic structure, of the molecule.

Measuring IR spectra from the surface of an electrode presents several challenges. The spectrum is usually obtained by recording the light reflected from the surface of the electrode (fig. 1.2). In the case of IR reflection-absorption spectroscopy (IRRAS, fig. 1.2A) where an electrode is immersed in solution, the IR beam is required to pass through the electrolyte twice, once to reach the electrode and then again after it is reflected. This is problematic as water is a very strong absorber of IR radiation. To ensure that a sufficient

Table 1.2: Techniques for *in situ* characterisation of species at the electrode/electrolyte interface.

Technique	Advantages	Disadvantages	Refs.
FTIR[a]	Able to detect desorbed and adsorbed intermediates. Reveals information on intramolecular bonding of adsorbates. Basic measurements can be made with routine instrumentation. In theory timescale limited by instrument electronics (ns). Readily combined with other *in situ* techniques, *e.g.* (DEMS, STM).	Interference from IR absorption by water. Resulting small pathlength cells lead to poor electrochemical control and large electrochemical time constants.	[25]
Raman	Aqueous electrolytes and common cell materials both transparent at excitation wavelengths, allowing broad scope for experimental geometry. Broad wavenumber range ($1\,\mathrm{cm}^{-1}$ to $4000\,\mathrm{cm}^{-1}$) reveals surface - intermediate bonding as well as intramolecular bonding. Rough (metal) surfaces can give enhanced absorption.	Small scattering cross section means spectra only observed in case of resonant enhancement from either source (resonance Raman, RR) or surface plasmon (surface enhanced Raman spectroscopy, SERS). RR requires laser wavelength matches adsorbate absorption band. SERS is only operational for Au, Ag or Cu electrodes. Strategies to introduce these metals onto other surfaces exist, such as shell-isolated nanoparticle-enhanced Raman spectroscopy, SHINERS, or tip enhanced Raman spectroscopy, TERS. Instrumentation less widely available than FTIR.	[26–29]
SFG[b]	Inherently surface sensitive due to requirement for an interface to break material symmetry. Suitable for rough and smooth surfaces, rough surfaces even providing up to factor 10^4 enhancement.	Specialist equipment required. If IR frequencies are generated the problem remains of strong attenuation by water.	[30]

[a] Fourier Transform Infrared Spectroscopy
[b] Sum Frequency Generation

Techniques for *in situ* characterisation of species at the electrode/electrolyte interface (cont.)

Technique	Advantages	Disadvantages	Refs.
SECM[c]	Permits analysis of reactions with µm lateral spatial resolution and even higher height resolution. Permits high throughput screening of arrays of catalysts.	Slow time resolution for full scans (minutes to hours). Problems arise deconvoluting the current response from the change in electrode-tip distance and the change with catalytic activity.	[31, 32]
DEMS[d]	Detect volatile adsorbates synchronously with voltammetry. Intrinsically quantitative.	Adsorbed species not detected directly. Calibration essential for quantitative measurement, can lead to misinterpretation.	[32, 33]
SXS[e]	X-rays interact weakly with matter, allowing 'buried' interfaces to be examined. X-ray wavelengths are on the order of atomic spacing, allowing techniques to probe changes in atomic position. Enables periodic structures such as adlayers to be examined.	Synchrotron source required.	[34, 35]
NMR[f]	Reveals electronic properties of metal and adsorbates, such as local density of states. Dynamics, of *e.g.* surface diffusion, can be studied via analysis of spin relaxation times.	Expensive instrumentation. Highly specialised experimental design. Long acquisition times (hours).	[36, 37]

[c] Scanning Electrochemical Microscopy
[d] Differential Electrochemical Mass Spectrometry
[e] Surface X-ray Scattering
[f] Nuclear Magnetic Resonance

amount of light reaches the electrode and then emerges from the cell the electrolyte layer is made very thin, between 1 µm to 10 µm. [38] Even at these thicknesses, the adsorbate layer is around 10^3 times thinner than the electrolyte and so sensitivity can be an issue. [39]

The thin layer of electrolyte also causes many problems for electrochemistry. Diffusion of reactants into the layer and products out of the layer is extremely limited, leading to depletion of reactant and accumulation of products at the electrode surface. For gaseous products this can lead to bubble formation which disrupts both the electrochemical control and the spectroscopic measurement. The thin layer also creates a very high solution resistance which will affect the potential control, slowing down the response of the electrode to changes in applied potential and, depending on the counter electrode position, cause inhomogeneity in the potential across the electrode. [25]

An alternative geometry for recording the IR reflection spectrum is to use an attenuated total reflection (ATR) geometry. In this geometry an IR beam is incident from within an optic known as the internal reflection element (IRE) of higher refractive index than the electrolyte, such that at the IRE/electrolyte interface the beam is totally internally reflected. During total internal reflection an exponentially decaying field, or evanescent wave, is established which decays into the electrolyte, sampling any species at the interface (section 2.3.3.6). Since the evanescent wave does not propagate through the electrolyte the intensity lost to the electrolyte is significantly decreased. The ATR geometry can be applied to spectroelectrochemistry in two ways: one approach is known as the 'Otto' configuration and is very similar to the IRRAS geometry in that the electrode is pressed against the IRE (fig. 1.2B). [40] This approach still suffers from all of the electrochemical problems associated with the thin layer however.

A more useful geometry is that of Kretschmann, in which a thin (ca 100 nm) metal layer is deposited directly onto the IRE (fig. 1.2C). [41] The evanescent wave penetrates through the metal layer, allowing the metal/solution interface to be sampled. In this

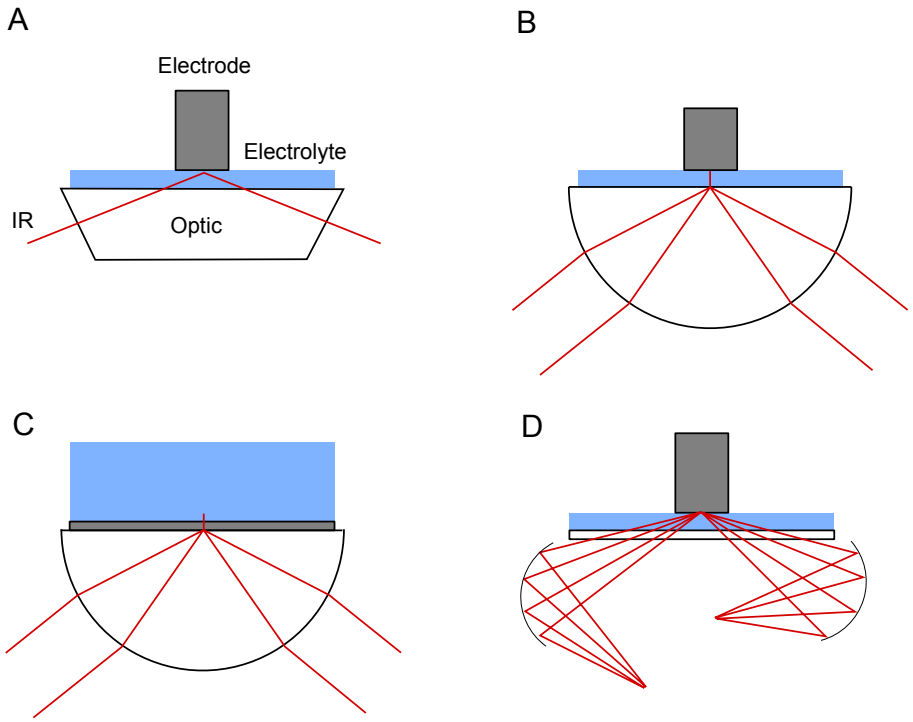

Figure 1.2: The various geometries used to measure IR spectra of electrode surfaces. A: Reflection-absorption geometry used in IRRAS. B: Attenuated total reflection (ATR) in an Otto geometry. C: ATR in the Kretschman geometry. D: Diffuse reflection geometry. In all cases the white areas represent the IR transparent optic through which the IR beam enters, blue areas the electrolyte, grey areas the electrode and the red line the path of the IR beam.

geometry there is no restriction on the thickness of the electrolyte layer, removing many of the limitations seen in the other geometries. Furthermore, the rough nature of the deposited thin films leads to enhanced IR absorption of any species at the surface, an effect known as surface enhanced infrared absorption (SEIRA, section 2.3.4.2). This approach, referred to as ATR-SEIRA, has increased the scope of *in situ* IR spectroscopy by making weak peaks visible and by significantly increasing the time resolution possible in spectroelectrochemical measurements. [39, 42]

Figure 1.2D shows a fourth geometry for measuring the spectrum of an electrode surface. This geometry collects the diffuse reflection from an electrode and is therefore suitable for measuring spectra from rough surfaces. However, the weak signal provided by the diffuse reflection generally precludes the use of this technique in solution, limiting reports of this technique to electrocatalysis in solid electrolytes with gaseous reactants. Such an approach was used to measure spectra from the catalyst layer in an operational fuel cell. [43]

1.2.2 IR Reflection Spectroscopy of Nanoparticle Electrodes

Practical considerations have meant that the three reflection geometries suitable for studying electrodes in solution are generally applied to macroscopic metal electrodes, the larger size of these electrodes being more conducive to spectroscopic measurement and detailed characterisation. The use of such electrodes to represent the nanoparticle catalysts found in fuel cells is not perfect, however, as there often exists large differences between them and real nanoparticle catalysts. [44–47] As a result there has also been much interest in the development of in situ methods which can be applied to the nanoparticle catalysts themselves. [48–51] While much progress has been made in this area, there still remain several challenges to overcome before the level of detail obtained on real catalysts matches that obtained from model systems.

Table 1.3: Different configurations of *in situ* infrared spectroscopy applied to nanoparticle electrocatalysts.

Geometry	IRRAS		ATR
Electrode	Au	GC	Au
Supported	Pt/C/Au [49–51]	Pt/C/GC [52], PtSn/C/GC [53]	Pt/C/Au [54]
Unsupported	Pt/Au [48]	Pt/GC [55, 56], Pt/HOPG [55]	Pt/Au [57], Pd/Au [58]

In general the techniques used to study macroscopic electrodes can be readily extended to the study of nanoparticles by simply depositing the nanoparticles onto a macroscopic electrode. To avoid contributions to the spectra from species at the surface of the supporting electrode, rather than at the deposited nanoparticle, the electrode is usually chosen to be inert under the reaction conditions. For example, much of the early interest in nanoparticle catalysis focused on CO oxidation. Since Au does not strongly absorb CO, it has been used extensively as the bulk electrode material in a range of studies (table 1.3). This strategy is limited, however, as CO adsorption is not always completely absent on Au, [51] and many other species, such as $HCOO^-$, an intermediate in formic acid oxidation, do adsorb on Au. [59] To completely remove any interference from the supporting electrode carbon can be used, although to date this has only been demonstrated in IRRAS rather than ATR configurations (see table 1.3), which again suffer from problems with diffusion. Furthermore, while materials such as glassy carbon are relatively inert to the reaction conditions, and will not lead to chemisorption of CO, their lower reflectivity can lead to unwanted distortion in the measured reflection spectra. [60]

To incorporate carbon as the supporting electrode in an ATR configuration, thus avoiding the reflectivity problems while maintaining effective mass transport, a porous carbon electrode layer can be used. This approach has been shown to allow the measurement of dissolved species within a porous fuel cell electrode, [61] and has been optimised to measure species adsorbed directly on a carbon black electrode. [62] To date, however,

there are no reports of species adsorbed on metal catalysts being detected using a carbon support electrode in an ATR configuration.

1.3 Summary

Proton exchange membrane fuel cells operating on small organic molecule fuels are an attractive technology for sustainable power generation. The adoption of PEMFCs is limited in part by the inadequate performance and high price of suitable electrocatalysts. The rational design of new catalysts however requires an appreciation of the mechanism of fuel oxidation, which in the case of small organic molecules is still the subject of debate. *In situ* spectroscopic characterisation of the species present at the surface of the electrode during catalysis can provide evidence for particular mechanisms and much work has been carried out on the *in situ* characterisation of macroscopic electrodes. However, the complex nature of real PEMFC catalysts makes their *in situ* characterisation difficult to perform and analyse.

1.4 Aims

This thesis has two main aims. The first aim is to develop an approach to *in situ* IR spectroscopy of real PEMFC catalysts which overcomes the limitations inherent in the techniques used to study macroscopic electrodes. The second aim is to use this approach to study some of the reactions relevant to PEMFCs. In particular, the oxidation of the common poisoning species carbon monoxide will be examined on a Pt/C catalyst. This study will then form the background to a more detailed investigation into the mechanism of formic acid oxidation at the same Pt/C catalyst.

1.5 Outline

The theory of electrocatalysis and infrared spectroscopy, used in the development of the spectroscopic approach and in the interpretation of the subsequent data, is introduced in Chapter 2. A brief survey of existing *in situ* IR cell designs is then given in Chapter 3, followed by a description of a new cell design and its subsequent refinement to a working setup. The *in situ* cell is then applied to a study of carbon monoxide oxidation at a commercial carbon-supported Pt catalyst in Chapter 4. Simulation and fitting of the observed spectra is carried out and the mechanism of oxidation on supported nanoparticle catalysts is discussed based on the results. Chapter 5 presents a comprehensive review of the *in situ* IR characterisation of formic acid oxidation on Pt, and the mechanisms proposed as a result. This is followed by an investigation of the mechanism on the same Pt/C catalyst used in Chapter 4 with the *in situ* approach developed herein. The results of both mechanistic investigations are summarised and future directions discussed in Chapter 6.

References

[1] C. B. Field, V. R. Barros, M. D. Mastrandrea, K. J. Mach, M.-K. Abdrabo, N. Adger, Y. A. Anokhin, O. A. Anisimov, D. J. Arent, J. Barnett, and others, "Summary for policymakers," *Climate change 2014: impacts, adaptation, and vulnerability. Part a: global and sectoral aspects. Contribution of working group II to the fifth assessment report of the intergovernmental panel on climate change*, pp. 1–32, 2014.

[2] National Grid, "UK Future Energy Scenarios," tech. rep., 2014.

[3] Department for Environment, Food and Rural Affairs, "Air Pollution in the UK 2013," tech. rep., 2014.

[4] J. Larminie and A. Dicks, *Fuel cell systems explained*. Chichester, West Sussex: J. Wiley, 2003.

[5] L. Carrette, K. A. Friedrich, and U. Stimming, "Fuel Cells: Principles, Types, Fuels, and Applications," *ChemPhysChem*, vol. 1, pp. 162–193, Dec. 2000.

[6] V. Mehta and J. S. Cooper, "Review and analysis of PEM fuel cell design and manufacturing," *Journal of Power Sources*, vol. 114, no. 1, pp. 32–53, 2003.

[7] A. Brouzgou, A. Podias, and P. Tsiakaras, "PEMFCs and AEMFCs directly fed with ethanol: a current status comparative review," *Journal of Applied Electrochemistry*, vol. 43, pp. 119–136, Dec. 2012.

[8] N. V. Rees and R. G. Compton, "Sustainable energy: a review of formic acid electrochemical fuel cells," *Journal of Solid State Electrochemistry*, vol. 15, pp. 2095–2100, Oct. 2011.

[9] S. Song, V. Maragou, and P. Tsiakaras, "How Far Are Direct Alcohol Fuel Cells From Our Energy Future?," *Journal of Fuel Cell Science and Technology*, vol. 4, pp. 203–209, June 2006.

[10] S. Litster and G. McLean, "PEM fuel cell electrodes," *Journal of Power Sources*, vol. 130, pp. 61–76, May 2004.

[11] H. A. Gasteiger, S. S. Kocha, B. Sompalli, and F. T. Wagner, "Activity benchmarks and requirements for Pt, Pt-alloy, and non-Pt oxygen reduction catalysts for PEMFCs," *Applied Catalysis B: Environmental*, vol. 56, pp. 9–35, Mar. 2005.

[12] K. A. Mauritz and R. B. Moore, "State of Understanding of Nafion," *Chemical Reviews*, vol. 104, pp. 4535–4586, Oct. 2004.

[13] C. E. Thomas, I. F. Kuhn Jr, B. D. James, F. D. Lomax Jr, and G. N. Baum, "Affordable hydrogen supply pathways for fuel cell vehicles," *International Journal of Hydrogen Energy*, vol. 23, pp. 507–516, June 1998.

[14] D. K. Ross, "Hydrogen storage: The major technological barrier to the development of hydrogen fuel cell cars," *Vacuum*, vol. 80, pp. 1084–1089, Aug. 2006.

[15] R. B. Moore and V. Raman, "Hydrogen infrastructure for fuel cell transportation," *International Journal of Hydrogen Energy*, vol. 23, pp. 617–620, July 1998.

[16] P. Trens, R. Durand, B. Coq, C. Coutanceau, S. Rousseau, and C. Lamy, "Poisoning of Pt/C catalysts by CO and its consequences over the kinetics of hydrogen chemisorption," *Applied Catalysis B: Environmental*, vol. 92, pp. 280–284, Nov. 2009.

[17] C. Lamy, E. M. Belgsir, and J. M. Leger, "Electrocatalytic oxidation of aliphatic alcohols: application to the direct alcohol fuel cell (DAFC)," *Journal of Applied Electrochemistry*, vol. 31, no. 7, pp. 799–809, 2001.

[18] X. Yu and P. G. Pickup, "Recent advances in direct formic acid fuel cells (DFAFC)," *Journal of Power Sources*, vol. 182, pp. 124–132, July 2008.

[19] C. E. Borroni-Bird, "Fuel cell commercialization issues for light-duty vehicle applications," *Journal of Power Sources*, vol. 61, pp. 33–48, July 1996.

[20] J. Yeom, R. Jayashree, C. Rastogi, M. Shannon, and P. Kenis, "Passive direct formic acid microfabricated fuel cells," *Journal of Power Sources*, vol. 160, pp. 1058–1064, Oct. 2006.

[21] S. Uhm, H. J. Lee, and J. Lee, "Understanding underlying processes in formic acid fuel cells," *Physical Chemistry Chemical Physics*, vol. 11, pp. 9326–9336, Oct. 2009.

[22] A. S. Arico, S. Srinivasan, and V. Antonucci, "DMFCs: from fundamental aspects to technology development," *Fuel cells*, vol. 1, no. 2, pp. 133–161, 2001.

[23] S. B. Brummer and A. C. Makrides, "Adsorption and Oxidation of Formic Acid on Smooth Platinum Electrodes in Perchloric Acid Solutions," *The Journal of Physical Chemistry*, vol. 68, pp. 1448–1459, June 1964.

[24] A. Capon and R. Parsons, "The oxidation of formic acid on noble metal electrodes: II. A comparison of the behaviour of pure electrodes," *Journal of Electroanalytical Chemistry and Interfacial Electrochemistry*, vol. 44, pp. 239–254, June 1973.

[25] P. A. Christensen, "In situ Infrared Spectroelectrochemistry," in *Encyclopedia of Electrochemistry*, Wiley-VCH Verlag GmbH & Co. KGaA, 2007.

[26] P. Cao, Y. Sun, and R. Gu, "Surface-Enhanced Raman Spectroscopy Studies on the Adsorption and Electrooxidation of Carbon Monoxide at the Platinum-Formic Acid Interface," *The Journal of Physical Chemistry B*, vol. 108, pp. 4716–4722, Apr. 2004.

[27] Z.-Q. Tian and B. Ren, "Raman Spectroscopy of Electrode Surfaces," in *Encyclopedia of Electrochemistry*, Wiley-VCH Verlag GmbH & Co. KGaA, 2007.

[28] D.-Y. Wu, J.-F. Li, B. Ren, and Z.-Q. Tian, "Electrochemical surface-enhanced Raman spectroscopy of nanostructures," *Chemical Society Reviews*, vol. 37, pp. 1025–1041, Apr. 2008.

[29] A. V. Rudnev, A. Kuzume, Y. Fu, and T. Wandlowski, "CO Oxidation on Pt(100): New Insights based on Combined Voltammetric, Microscopic and Spectroscopic Experiments," *Electrochimica Acta*, vol. 133, pp. 132–145, July 2014.

[30] Héctor D. Abruña, *Electrochemical interfaces : modern techniques for in-situ interface characterization*. New York ; Cambridge: VCH, 1991.

[31] B. R. Horrocks, "Scanning Electrochemical Microscopy," in *Encyclopedia of Electrochemistry*, Wiley-VCH Verlag GmbH & Co. KGaA, 2007.

[32] A. S. Bandarenka, E. Ventosa, A. Maljusch, J. Masa, and W. Schuhmann, "Techniques and methodologies in modern electrocatalysis: evaluation of activity, selectivity and stability of catalytic materials," *Analyst*, vol. 139, pp. 1274–1291, Feb. 2014.

[33] H. Baltruschat, "Differential electrochemical mass spectrometry," *Journal of the American Society for Mass Spectrometry*, vol. 15, pp. 1693–1706, Dec. 2004.

[34] N. M. Marković, B. N. Grgur, C. A. Lucas, and P. N. Ross, "Electrooxidation of CO and H2/CO Mixtures on Pt(111) in Acid Solutions," *The Journal of Physical Chemistry B*, vol. 103, pp. 487–495, Jan. 1999.

[35] S. Ye, T. Kondo, N. Hoshi, J. Inukai, S. Yoshimoto, M. Osawa, and K. Itaya, "Recent Progress in Electrochemical Surface Science with Atomic and Molecular Levels," *Electrochemistry*, vol. 77, no. 1, pp. 2–20, 2009.

[36] Y. Y. Tong, A. Wieckowski, and E. Oldfield, "NMR of Electrocatalysts," *The Journal of Physical Chemistry B*, vol. 106, pp. 2434–2446, Mar. 2002.

[37] F. Blanc, M. Leskes, and C. P. Grey, "In Situ Solid-State NMR Spectroscopy of Electrochemical Cells: Batteries, Supercapacitors, and Fuel Cells," *Accounts of Chemical Research*, vol. 46, pp. 1952–1963, Sept. 2013.

[38] T. Iwasita and F. C. Nart, "In situ infrared spectroscopy at electrochemical interfaces," *Progress in surface science*, vol. 55, no. 4, pp. 271–340, 1997.

[39] M. Osawa, "In-situ Surface-Enhanced Infrared Spectroscopy of the Electrode/Solution Interface," in *Advances in Electrochemical Sciences and Engineering*, vol. 9, pp. 269–314, Weinheim, Germany: Wiley-VCH Verlag GmbH, July 2006.

[40] A. Otto, "Excitation of nonradiative surface plasma waves in silver by the method of frustrated total reflection," *Zeitschrift für Physik*, vol. 216, pp. 398–410, Aug. 1968.

[41] E. Kretschmann, "Die bestimmung optischer konstanten von metallen durch anregung von oberflächenplasmaschwingungen," *Zeitschrift für Physik*, vol. 241, pp. 313–324, Aug. 1971.

[42] M. Osawa, "Electrocatalytic Reactions on Platinum Electrodes Studied by Dynamic Surface-Enhanced Infrared Absorption Spectroscopy (SEIRAS)," in *In-situ Spectroscopic Studies of Adsorption at the Electrode and Electrocatalysis*, pp. 209–246, Amsterdam: Elsevier Science B.V., 2007.

[43] I. Tkach, A. Panchenko, T. Kaz, V. Gogel, K. A. Friedrich, and E. Roduner, "In situ study of methanol oxidation on Pt and Pt/Ru-mixed with Nafion anodes in a direct methanol fuel cell by means of FTIR spectroscopy," *Physical Chemistry Chemical Physics*, vol. 6, no. 23, p. 5419, 2004.

[44] M. L. Sattler and P. N. Ross, "The surface structure of Pt crystallites supported on carbon black," *Ultramicroscopy*, vol. 20, no. 1–2, pp. 21–28, 1986.

[45] F. Maillard, E. R. Savinova, P. A. Simonov, V. I. Zaikovskii, and U. Stimming, "Infrared Spectroscopic Study of CO Adsorption and Electro-oxidation on Carbon-Supported Pt Nanoparticles: Interparticle versus Intraparticle Heterogeneity," *The Journal of Physical Chemistry B*, vol. 108, pp. 17893–17904, Nov. 2004.

[46] M. Arenz, K. J. J. Mayrhofer, V. Stamenkovic, B. B. Blizanac, T. Tomoyuki, P. N. Ross, and N. M. Markovic, "The Effect of the Particle Size on the Kinetics of CO Electrooxidation on High Surface Area Pt Catalysts," *Journal of the American Chemical Society*, vol. 127, pp. 6819–6829, May 2005.

[47] K. Mayrhofer, M. Arenz, B. Blizanac, V. Stamenkovic, P. Ross, and N. Markovic, "CO surface electrochemistry on Pt-nanoparticles: A selective review," *Electrochimica Acta*, vol. 50, pp. 5144–5154, Sept. 2005.

[48] K. A. Friedrich, F. Henglein, U. Stimming, and W. Unkauf, "Investigation of Pt particles on gold substrates by IR spectroscopy particle structure and catalytic activity," *Colloids and Surfaces A: Physicochemical and Engineering Aspects*, vol. 134, pp. 193–206, Mar. 1998.

[49] K. A. Friedrich, F. Henglein, U. Stimming, and W. Unkauf, "In-situ vibrational spectroscopy on Pt electrocatalysts," *Electrochimica Acta*, vol. 47, pp. 689–694, Dec. 2001.

[50] S. Park, Y. Tong, A. Wieckowski, and M. J. Weaver, "Infrared reflection-absorption properties of platinum nanoparticle films on metal electrode substrates: control of anomalous optical effects," *Electrochemistry Communications*, vol. 3, pp. 509–513, Sept. 2001.

[51] V. Stamenković, M. Arenz, P. N. Ross, and N. M. Marković, "Temperature-Induced Deposition Method for Anchoring Metallic Nanoparticles onto Reflective Substrates for in Situ Electrochemical Infrared Spectroscopy," *The Journal of Physical Chemistry B*, vol. 108, pp. 17915–17920, Nov. 2004.

[52] C. Rice, Tong, E. Oldfield, A. Wieckowski, F. Hahn, F. Gloaguen, J.-M. Léger, and C. Lamy, "In Situ Infrared Study of Carbon Monoxide Adsorbed onto Commercial Fuel-Cell-Grade Carbon-Supported Platinum Nanoparticles: Correlation with ^{13} C NMR Results," *The Journal of Physical Chemistry B*, vol. 104, pp. 5803–5807, June 2000.

[53] S. Beyhan, J.-M. Léger, and F. Kadırgan, "In situ FTIR investigation of acetic acid electrooxidation on carbon supported Pt–Sn based trimetallic catalysts: Influence of the nature of the third metal," *Applied Surface Science*, vol. 321, pp. 426–431, Dec. 2014.

[54] A. M. Hofstead-Duffy, D.-J. Chen, and Y. J. Tong, "An in situ attenuated total reflection-surface enhanced infrared absorption spectroscopic study of enhanced methanol electro-oxidation activity on carbon-supported Pt nanoparticles by poly(vinylpyrrolidone) of different molecular weights," *Electrochimica Acta*, vol. 82, pp. 543–549, Nov. 2012.

[55] O. Cherstiouk, P. Simonov, and E. Savinova, "Model approach to evaluate particle size effects in electrocatalysis: preparation and properties of Pt nanoparticles supported on GC and HOPG," *Electrochimica Acta*, vol. 48, pp. 3851–3860, Nov. 2003.

[56] G.-Q. Lu, S.-G. Sun, S.-P. Chen, and L.-R. Cai, "Novel properties of dispersed Pt and Pd thin layers supported on GC for CO adsorption studied using in situ MS-FTIR reflection spectroscopy," *Journal of Electroanalytical Chemistry*, vol. 421, pp. 19–23, Jan. 1997.

[57] A. M. Levendorf, D.-J. Chen, C. L. Rom, Y. Liu, and Y. J. Tong, "Electrochemical and in situ ATR-SEIRAS investigations of methanol and CO electro-oxidation on PVP-free cubic and octahedral/tetrahedral Pt nanoparticles," *RSC Advances*, vol. 4, pp. 21284–21293, May 2014.

[58] H.-X. Zhang, S.-H. Wang, K. Jiang, T. André, and W.-B. Cai, "In situ spectroscopic investigation of CO accumulation and poisoning on Pd black surfaces in concentrated HCOOH," *Journal of Power Sources*, vol. 199, pp. 165–169, Feb. 2012.

[59] A. Bewick and S. Pons, "Advances in infrared and raman spectroscopy.," vol. 12 of *Advances in infrared and Raman spectroscopy.*, pp. 1–63, London: Wiley and Heyden, 1985.

[60] C. Pecharromán, A. Cuesta, and C. Gutiérrez, "Comments on the paper by M.-S. Zheng and S.-G. Sun entitled 'In situ FTIR spectroscopic studies of CO adsorption on electrodes with nanometer-scale thin films of ruthenium in sulfuric acid solutions' [J. Electroanal. Chem. 500 (2001) 223]," *Journal of Electroanalytical Chemistry*, vol. 529, pp. 145–154, July 2002.

[61] R. F. B. De Souza, J. C. M. Silva, F. C. Simões, M. L. Calegaro, A. O. Neto, and M. C. Santos, "New Approaches for the Ethanol Oxidation Reaction of Pt/C on Carbon Cloth Using ATR-FTIR.," *International Journal of Electrochemical Science*, vol. 7, no. 6, 2012.

[62] A. J. Healy, P. A. Ash, O. Lenz, and K. A. Vincent, "Attenuated total reflectance infrared spectroelectrochemistry at a carbon particle electrode; unmediated redox control of a [NiFe]-hydrogenase solution," *Physical Chemistry Chemical Physics*, vol. 15, pp. 7055–7059, Apr. 2013.

Chapter 2

Theory

In this chapter consideration is given to the theory behind electrocatalyis by metal nanoparticles, and to the theory and practice of making the relevant electrochemical and infrared spectroscopic measurements. For the most part only theories and mathematical expressions which are subsequently used are presented, the exceptions being the discussions of effective medium theories and surface enhancement, which serve as mini-reviews of the current literature and justification for the theoretical approaches taken later on. Finally, while almost all data shown is taken directly from the literature, the numerical calculations of the surface ratio in the section on the surface selection rule was carried out for this work.

2.1 Electrocatalysis

An electrocatalytic reaction occurs in a number of different steps, each of which can affect the rate (fig. 2.1). The first step is transport of the reactant to the electrode. Once at the interface, the reactant must adsorb, possibly dissociating as a result. Once adsorbed the reactant can undergo charge transfer and further chemical reactions. For the reaction to be catalytic the resulting species must then desorb and be transported away from the surface. Transport to and from the electrode is independent of the crystallographic

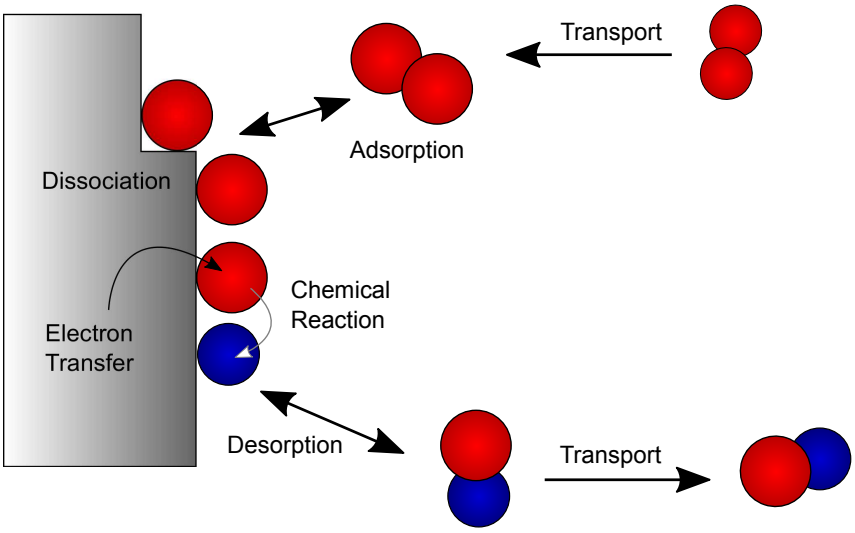

Figure 2.1: The processes involved in electrocatalysis.

orientation of the surface whereas the remaining steps: adsorption, chemical reaction and electron transfer, can all be heavily influenced by it.

2.1.1 Transport

Transport to the electrode can occur by diffusion, the statistical movement of species from regions of high concentration to lower concentration, by convection, the bulk movement of solution, or, for charged species, by migration, the movement of species under the influence of an electric field. [1] In general the rate of transport of species in electrocatalysis is controlled so that it does not limit the rate of reaction. This is accomplished in the PEMFC by the flow of gas over the electrodes. In the case of solution experiments mass transport is controlled by forced convection, either pumping solution through a thin layer cell, or by rotating a cylindrical electrode (fig. 2.2).

In the case of the rotating disc electrode the mass transported-limited current is given by the Levich equation (eq. (2.1)), where n is the number of electrons transferred, F is the Faraday constant, A is the area of the electrode, D is the diffusion coefficient of the reacting species, ν is the kinematic viscosity of the solvent, c_∞ is the bulk concentration of reacting species and ω is the angular frequency of the electrode. For the wall jet electrode

(fig. 2.2), in which the nozzle of the jet d is much smaller than the electrode diameter $2r$, and in the limiting case that the electrode-cell wall separation is much greater than the electrode-nozzle separation, the limiting current is given by eq. (2.2). It can be seen that V_f, the volumetric flow rate, plays a similar role to ω in relating flow rate to limiting current. [2]

$$i_{\mathrm{L,RDE}} = 1.554nFAD^{2/3}\nu^{-1/6}c_\infty\omega^{1/2} \tag{2.1}$$

$$i_{\mathrm{L,WJE}} = 1.38nFd^{-1/2}r^{3/4}D^{2/3}\nu^{-5/12}c_\infty V_\mathrm{f}^{3/4} \tag{2.2}$$

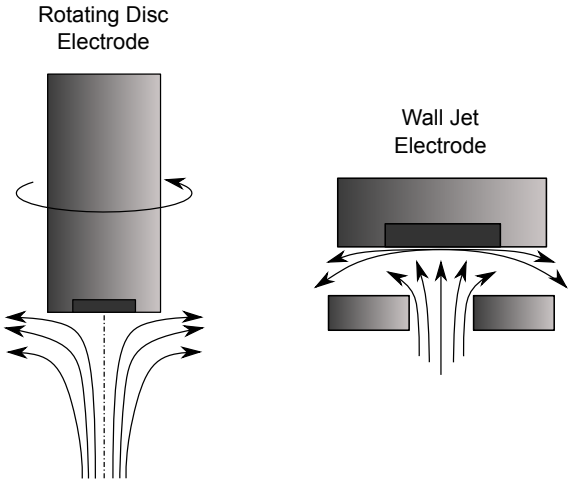

Figure 2.2: Methods for forced convection.

2.1.2 Adsorption and Surface Chemical Reaction

Adsorption, here used to mean chemisorption, the formation of a covalent bond to the surface, is central to the idea of electrocatalysis and is the origin of the surface sensitivity of many electrocatalytic reactions. This sensitivity is rationalised in terms of the electrode material's ability to adsorb and dissociate reactants and then form and desorb products. The striking dependence of the rate of some reactions on the electrode material is shown in fig. 2.3, in which the rate of the hydrogen evolution reaction (HER) for a range of metal electrodes is plotted as a function of the respective M−H bond strengths. [3] It can be seen

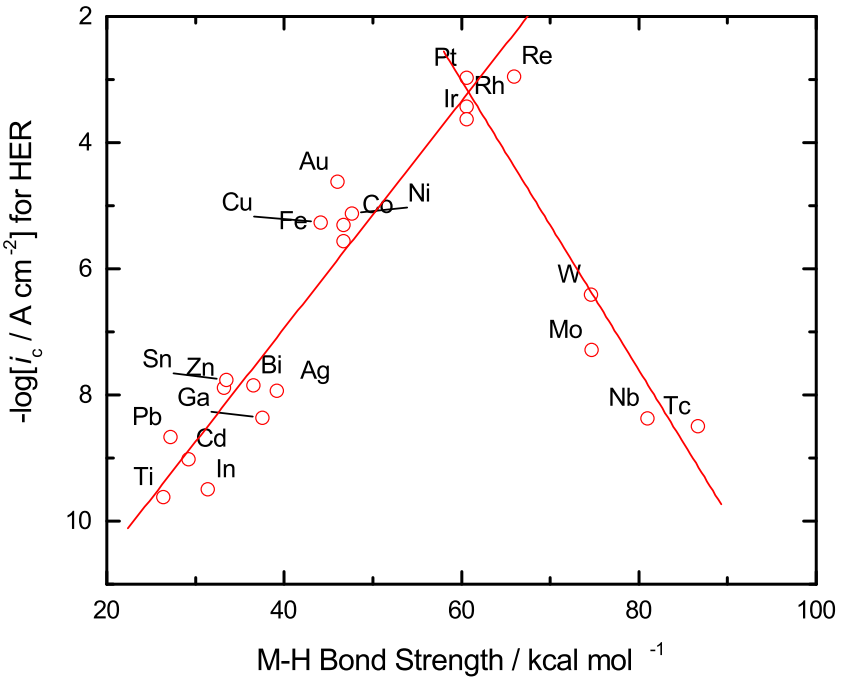

Figure 2.3: Volcano plot formed by plotting the observed hydrogen evolution reaction (HER) current as a function of M−H bond strength for a range of metals. Adapted from reference 3.

that the current increases with bond strength up to a certain point, and then decreases. This peak-shaped plot, known as a Volcano plot, is found for many different reactions. [4–7] The plot illustrates the Sabatier principle: that good catalysts adsorb reactants strongly enough to provide reactive species, but not so strongly that these species do not desorb, blocking further adsorption. This can also be expressed conceptually by a rate equation $\nu \propto \theta(1-\theta)$, where the rate, ν, depends on both the fractional coverage of reactant, θ, and the coverage of free sites, $(1-\theta)$. The maximum rate occurs at $d\nu/d\theta = 0$, that is when $\theta = \frac{1}{2}$.

The strength of adsorption can be understood with reference to the structure of the catalyst surface. However, the porous, inhomogeneous nature of real electrocatalysts, evident in fig. 1.1B, means their surfaces are very complex and hard to define. To understand the general effect of surface composition and structure on electrocatalysis, therefore, model systems have been developed which mimic aspects of the real catalysts while remaining well

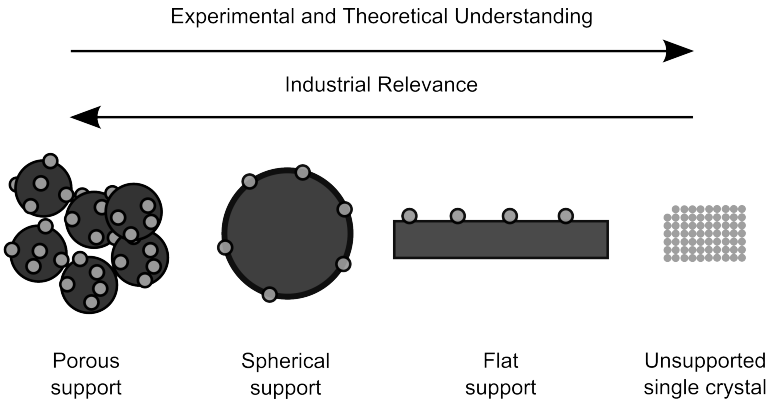

Figure 2.4: The relationship between model and applied catalysts. Adapted from reference [8].

defined. [8–10] The relationship between real and model catalysts is shown in fig. 2.4. [8] As the understanding of reactions at single crystal surfaces increases, and as experimental techniques are refined, increasingly realistic surfaces are being examined. However, by far the best characterised model electrocatalysts are unsupported single crystals. Various ultra high vacuum (UHV) techniques allow the atomic and electronic structure of these single crystals to be studied down to the level of single atoms. [8, 9, 11] This has led to a wealth of information on the surface chemistry of various catalysts and how it relates to their atomic and electronic structure.

2.1.2.1 Single Crystals as Model Catalysts

The structure of most transition metals can be described by the close packing of their constituent atoms in either cubic or hexagonal symmetries. At the surface of a metal this symmetry is maintained, although the under-coordination of the surface atoms can lead to reconstruction of the surface - changes in lattice spacing, or loss of periodic arrays of atoms - to minimise the surface energy. [10] The symmetry at the surface is determined by the relative orientation of the surface to the unit cell, described in terms of the Miller indices (hkl). The surfaces produced by cutting along the three low-index, or basal, planes

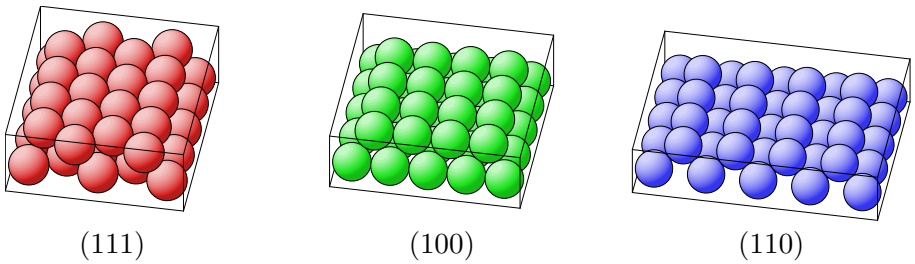

(111) (100) (110)

Figure 2.5: The three basal planes of an fcc metal. The top two layers of atoms are shown in each case.

of a face centred cubic (fcc) metal are shown in fig. 2.5.

It can be seen that of the three basal planes, only the (111) plane is close packed, with the (100) and (110) planes exhibiting progressively lower coordination and more open structures. This has implications for both the steric and electronic properties of the adsorption sites available. Adsorption can occur on top of a single atom (atop of linear coordination) or between two (bridging), three (threefold) or even four atoms (fourfold coordination). On the (111) surface atop, bridging and threefold sites are present, while on the (100) fourfold sites become available. Planes with higher Miller indices can be considered as consisting of terraces of one basal plane, joined by steps whose sites resemble those of a different basal plane (table 2.1). [12] For example, the (332) plane (fig. 2.6A) is comprised of (111) planes, separated by steps of (110) geometry. Even higher index planes, in which all Miller indices are different, contain kinks, atoms of lower coordination number again (fig. 2.6B).

2.1.2.2 Supported Metal Nanoparticles as Catalysts

The surface of a metal nanoparticle is subject to the same constraints as a bulk surface in terms of minimising its surface energy. As a result the same structures that are found at the surface of bulk single crystals are found at the surface of nanoparticles. In fact, the principle of minimum surface energy can be used to predict the shape of a nanoparticle. The Gibbs-Wulff theorem states that the ratio of the distance of a facet from the particle

Table 2.1: Miller indices and Lang, Joyner, Samorjai (LJS) notation of some stepped surfaces[a]

LJS Notation[b]	Miller Index
Pt(S)$[(n-1)(111)\times(110)]$	Pt$(n,n,n-2)$
Pt(S)$[n(110)\times(111)]$	Pt$(2n-1,2n-1,1)$
Pt(S)$[n(111)\times(100)]$	Pt$(n+1,n-1,n-1)$
Pt(S)$[n(100)\times(111)]$	Pt$(2n-1,1,1)$

[a] Adapted from reference [13].
[b] Lang, Joyner and Samorjai (LJS) notation is described in reference [12].

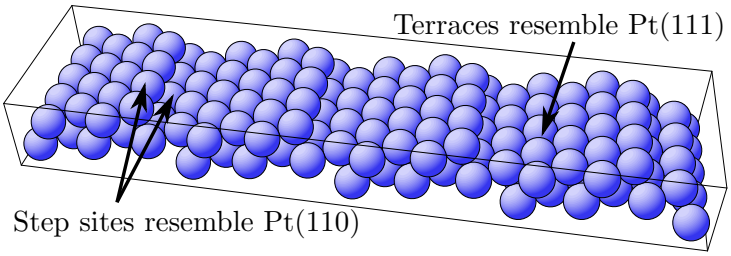

(A)

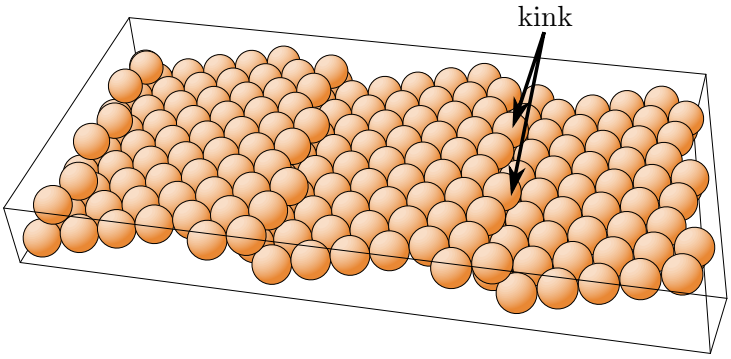

(B)

Figure 2.6: High Miller index surfaces (a) The (332) Surface. The surface can also be described as Pt$[(n-1)(111)\times(110)]$, where $n=6$ indicating that it consists of (111) terraces n atoms wide, separated by (110) steps. [14] (b) The (10 8 7) surface.

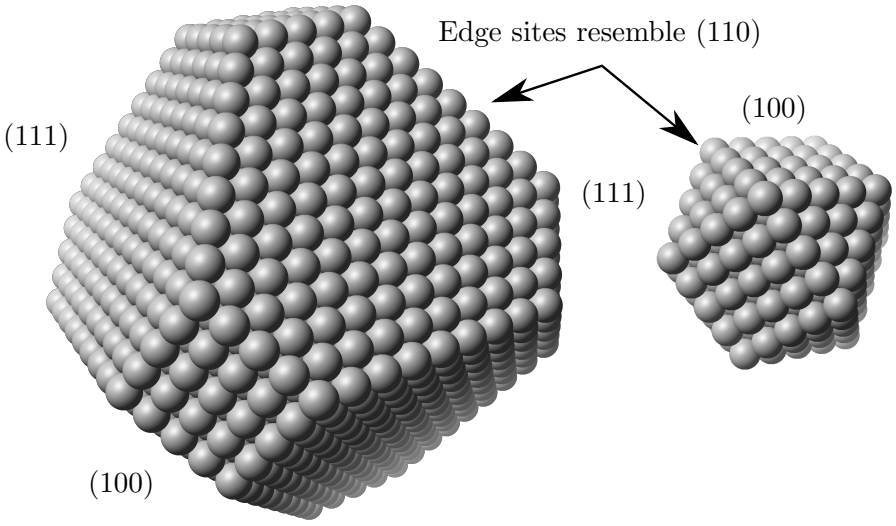

Figure 2.7: Idealised nanoparticle structures. Left: A 4.45 nm particle with a truncated octahedron shape. The particle contains 3101 atoms, of which 930 are at the surface. Right: A 1.86 nm particle based on a cuboctahedron. The particle contains 490 atoms of which 230 are at the surface.

centre to its surface energy always remains constant. [15] Using this relationship, minimum energy structures, known as Wulff Polyhedra, can be computed for a given number of atoms. For example, the minimum energy structure of many Pt nanoparticles is a truncated octahedron (fig. 2.7). [16] This shape is dominated by (111) facets meeting at (100) faces and connected via edges of (110) symmetry. The apparent utility of model electrodes is evident, as extended regions of (111) and (110) symmetry can be prepared on model electrodes, and their catalytic behaviour characterised.

2.1.2.3 The Correlation Between Single Crystals and Nanoparticle Surfaces

The weaknesses of the single crystal model for understanding nanoparticle surfaces is that there remain some sites without a suitable model, for example corner sites. Furthermore, real particles are unlikely to consist of exactly the right number of atoms to form perfect regular shapes, and the additional atoms will lead to many more low coordinate or 'defect' sites on the surface. [17, 18] Thus nanoparticle reactivity cannot simply be described as a

weighted average of the different activities of each facet, as determined from model experiments. This is found experimentally, where the specific activity of many reactions show significant dependence on the size of the nanoparticle, with both increase and decrease in activity with size observed. [19–21] While the exact relationship between activity and size can be overstated, due to the inherent size distribution of any real catalyst sample, the differences can be significant.

The origin of any difference between the activity on single crystals and nanoparticles, including any observed size effects, must be considered separately for each reaction, however in general such differences arise from a combination of:

1. Changes in the *d*-band centre (*vide infra*) for sites of the same coordination [9]
2. Changes in the overall number of low coordinate ('defect') sites [17, 22, 23]
3. Changes in the ratio of more:less active facets [24, 25]
4. Metal-support interactions [26, 27]
5. Changes in the size of atomic ensembles (contiguous atoms) on the surface [20]
6. Diffusional coupling of dissolved intermediates between particles of different sizes [28, 29]

To a certain extent these effects can be separated in electronic (1-4) and geometric (5,6) contributions, although the distinction is slightly arbitrary. These effects can also often be considered in different contexts, for example the number of low coordinate sites can be considered based on the roughening of the surface, or the presence of grain boundaries, [23] or the formation of larger particles. [17] In addition, the same effect can both increase and decrease the rate of reaction, for example adsorption energy: while the enhanced adsorption of CO may lead to greater poisoning and a decrease in rate, the enhanced adsorption of OH may facilitate CO oxidation and increase the rate. [19]

2.1.2.4 The *d*-band Centre Model

The empirical relationship between the nature of the metal, the surface structure and the observed trends in activity can be related to the strength of adsorption by considering the electronic structure of the metal surface. At the surface of a metal the effects of screening mean that the electronic structure of individual sites can be considered separately. [30] Thus properties such as adsorption energy can depend not only on the identity of the metal but also on the symmetry and local coordination number. Hammer and Nørskov proposed that the reactivity of the surface can be explained based solely on consideration of the energy of the d electrons, represented by the first moment of the local density of d states, otherwise known as the centre of the local d-band. [31] The adsorption energy at different metals and metal sites is then rationalised based on the coupling of the metal d-band to the adsorbate molecular orbitals (MOs).

Figure 2.8 shows the effect on a typical adsorbate MO of coupling first with the broad metal s-band, which lowers the adsorbate energy and broadens the level into a band, and secondly with the metal d-band, which splits the adsorbate band into two bands, with bonding and antibonding character, respectively. The coupling between the adsorbate and the s-band is largely independent of the nature of the metal, leaving the interaction with the d-band as the dominant parameter. [32]

The adsorption energy of the adsorbate MO can be determined from perturbation theory and is dependent on the coupling between the adsorbate/metal s-band and the metal d-band, described by the coupling constant V, and the energy difference between the two states ΔE. [33] In the limit $\Delta E \gg V$ then the coupling is given by eq. (2.3).

$$\Delta = \frac{V^2}{\Delta E} \tag{2.3}$$

If the adsorbate-metal bonding is considered to be dominated by interactions with an

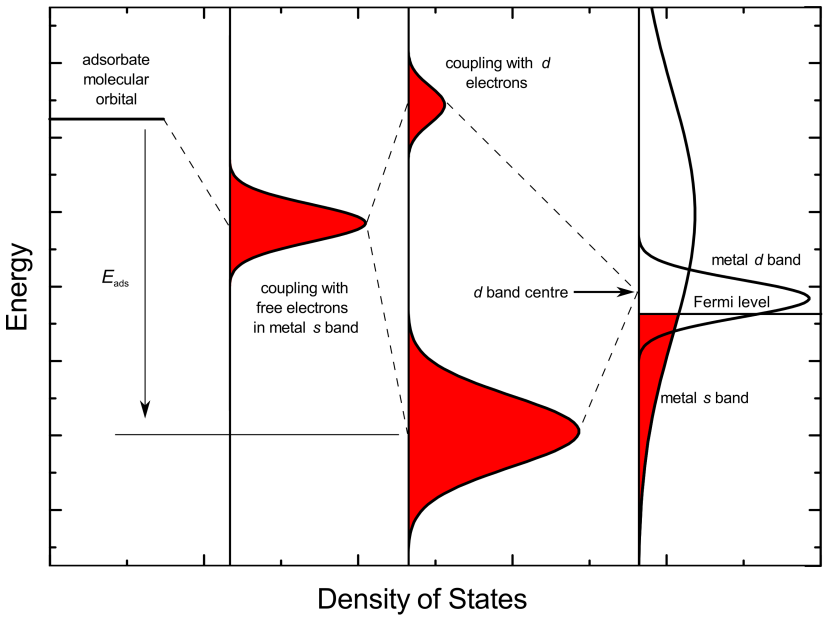

Figure 2.8: The relationship between the metal d-band and adsorption energy. Adapted from reference [32].

adsorbate MO of higher energy than the metal d band, such as the $\pi*$ MO found in adsorbates like carbon monoxide, [33] then it can be seen that increasing the d-band centre will increase the coupling between the two states and therefore increase the bond strength. Evidence for this correlation has been found both theoretically and experimentally. [34,35] Figure 2.9A shows the relationship between the d-band centre for various sites and the calculated adsorption energy of CO.

It can also be seen from fig. 2.9 that the d-band centre in the region of a particular metal site is very sensitive to the local coordination number. The reason for this sensitivity is the decrease in d-bandwidth with decreasing coordination. Figure 2.10A shows the effect of decreasing the width of a band near the Fermi level. As the band narrows the number of electrons above the Fermi level decreases, causing the band centre to move upwards by a value δ to maintain the Fermi level. This effect was calculated for different surface sites on Pt and is shown in fig. 2.10B. It can be seen that the d-band centre moves upwards on going from a reconstructed 'over-coordinated' (100)-hex surface, to the close packed (111)

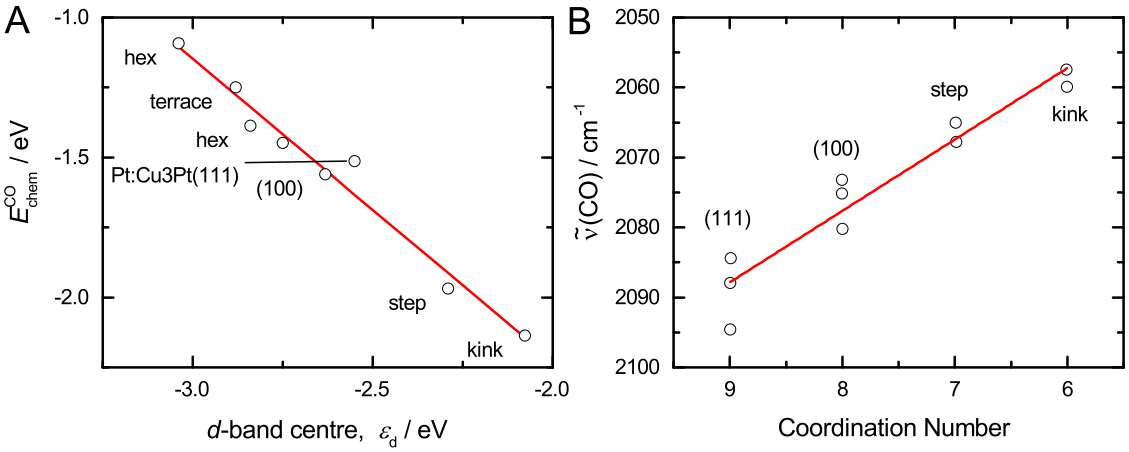

Figure 2.9: A: The correlation between the calculated metal d-band centre, ϵ_d and the CO chemisorption energy $E^{\mathrm{CO}}_{\mathrm{chem}}$. Adapted from reference [32]. B: The correlation between the local coordination number and $\tilde{\nu}$(CO), the CO stretching wavenumber. Adapted from reference [36].

surface, to a step site and then to a kink site.

The CO stretching frequency is observed to vary greatly with surface structure (fig. 2.9B). The figure shows the correlation between $\tilde{\nu}$(CO), the energy of the C−O stretching vibration, and the coordination number. This relationship is significant as $\tilde{\nu}$(CO) is readily obtained from spectroscopy and therefore provides a handle on the adsorption sites present on the catalyst. It can be seen that in contrast to the CO adsorption energy, whose magnitude increases as the coordination number decreases, the C−O strength decreases. To explain this relationship using the d-band centre theory it is necessary to understand the bonding of CO to metal surfaces.

2.1.2.5 The Electronic Structure of Adsorbed Carbon Monoxide

The molecular orbital diagram for CO can be constructed using the linear combination of atomic orbitals approach (fig. 2.11). [37] This analysis leaves the largely non-bonding lone pair-like 5σ orbital on C as the highest occupied molecular orbital (HOMO) and two unfilled π^* orbitals as the lowest unoccupied molecular orbital (LUMO).

In the Blyholder model for CO chemisorption the 5σ HOMO interacts with an empty

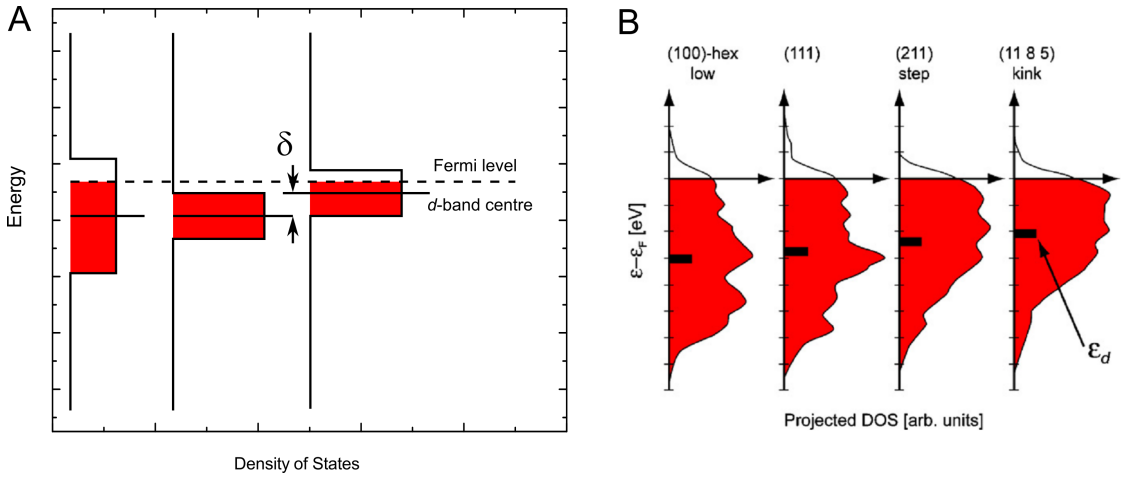

Figure 2.10: The relationship between the metal d-band and adsorption energy. Panel B reprinted from reference [32], Copyright 2007, with permission from Elsevier.

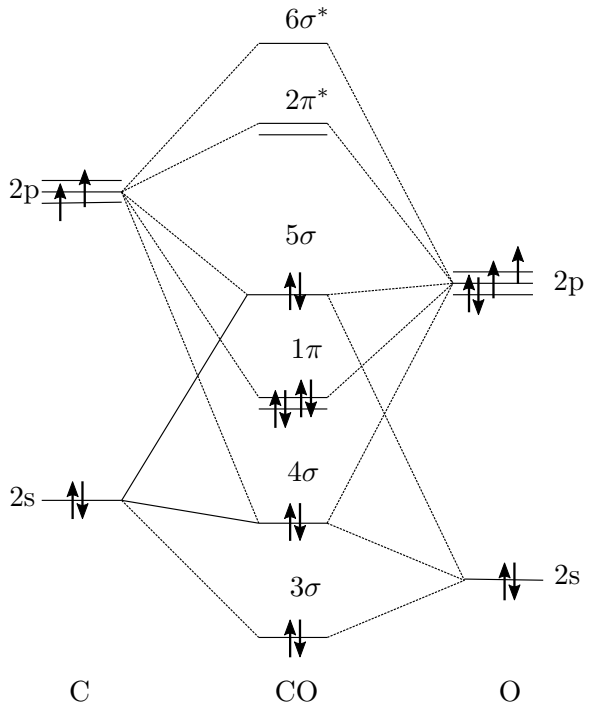

Figure 2.11: Molecular orbital diagram for CO.

$5\sigma \rightarrow d\sigma$ $2\pi^* \leftarrow d\pi$

Figure 2.12: Blyholder model for CO adsorption on metal surfaces. The model involves σ-donation from the ligand to the metal and π-backdonation from the metal to the ligand.

$d\sigma$ orbital to form a M−C bond. [38] The metal is then able to dissipate some of this charge by overlap of its partially-filled $d\pi$ orbitals with the π^* LUMO of CO. While this weakens the C−O bond it strengthens the M−C bond. This model was proposed to rationalise the effect of metal coordination number on the observed CO stretching frequency; adsorption sites with high coordination numbers share their electron density with the surrounding atoms which would decrease the extent of donation possible into each CO LUMO and therefore lead to stronger C−O bonds. Conversely, sites with low coordination numbers, such as step or kink sites, have fewer neighbours with which to share their electron density, resulting in more back donation, weaker C−O bonds but stronger M−C bonds. This explanation rationalises the trends in $\tilde{\nu}$(CO) seen in fig. 2.9B.

More recent measurements of chemisorbed CO on Ni using X-ray emission spectroscopy (XES), which can measure the site- and atom-specific local density of states, have questioned the Blyholder picture of molecular orbitals, however. [39] The results of XES reveal that the majority of the C 2p and O 2p (σ bond) electron density in CO adsorbed on Ni is concentrated on the O atom, with electron density on the metal site actually repelled by the presence of CO (fig. 2.13A). Similarly, the π electron density, coming only from the $2\pi^*$ orbital in the Blyholder model, is observed to come from both 1π and $2\pi^*$, forming a bonding orbital with the metal $d\pi$ orbitals and leaving a lone pair-like orbital on O (fig. 2.13B). This data suggests that the σ interaction is predominantly repulsive and all of the M−C−O bonding arises from π interactions. The model therefore suggests that observations in spectra of adsorbed CO previously rationalised using the σ-bonding/π-

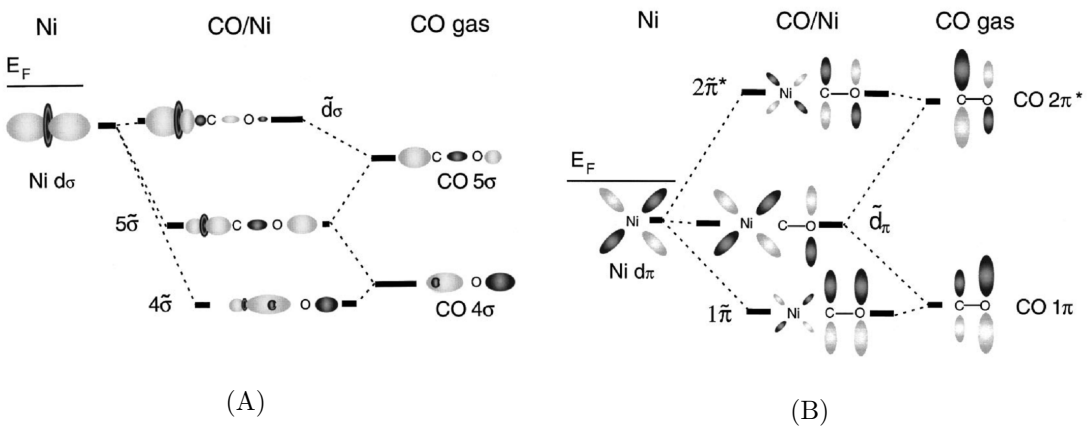

(A) (B)

Figure 2.13: The molecular orbital diagram for CO adsorbed on Ni suggested by Fölisch et al. (a) The σ framework. (b) The π framework. Reprinted with permission from reference [39]. Copyright 2000, AIP Publishing LLC.

antibonding model are better rationalised on the basis of a balance between π-bonding and σ repulsion. [35]

2.1.2.6 Kinetic Isotope Effects

When an atom in a reacting molecule is substituted for a heavier isotope it is often observed that the rate of the reaction decreases. This phenomenon is known as the kinetic isotope effect (KIE) and can be explained qualitatively with reference to the potential energy diagram for a reaction involving C−H bond breaking (fig. 2.14). On isotopic substitution the dominant change in the potential energy curve of a molecule is a decrease in the zero point energy. [37] To a first approximation the lower curve in fig. 2.14 can therefore represent both C−H species and C−D species. To react the C−H species must gain enough energy to reach the transition state, taken to be the lowest vibrational energy level of the activated complex. The activation energy is then given by the difference between the ground state and transition state zero point energies. The same is true for the C−D species, except the ground state zero point energy is now lower than that of C−H due to the increased mass of the species. In a late transition state, where the C−H bond is mostly broken, the bonding is weak and the potential energy curve for the transition state is very

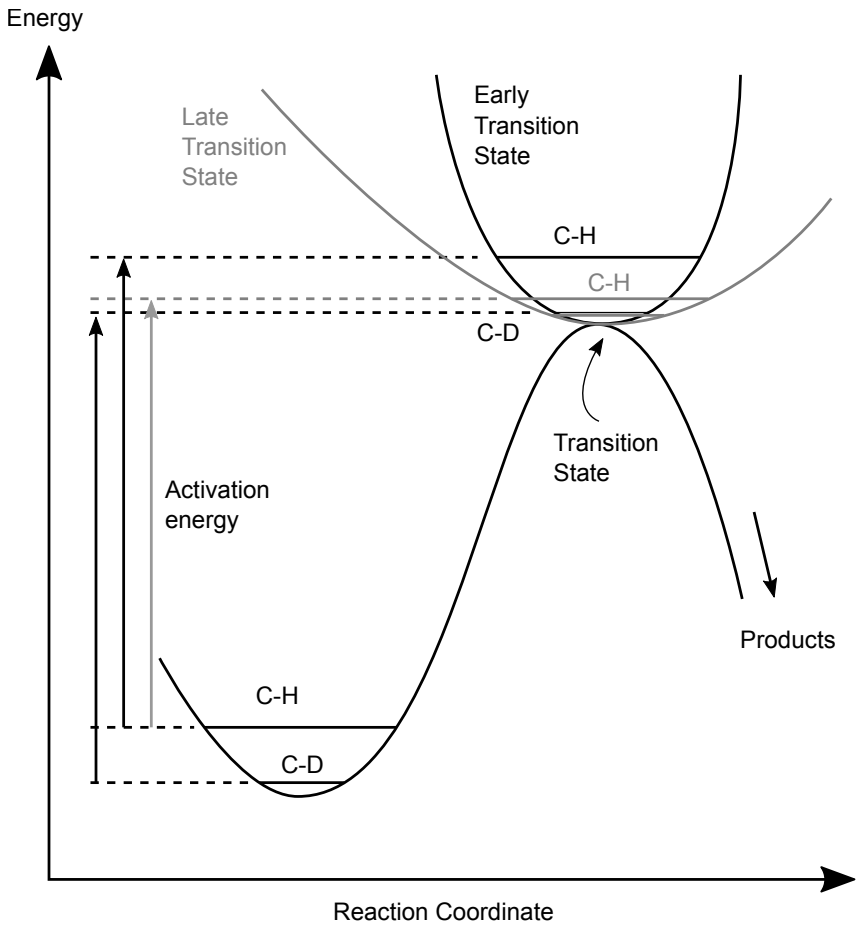

Figure 2.14: The origin of the kinetic isotope effect. Two case are shown: where significant C−H bonding remains in the transition state the potential energy curve remains narrow (black curve); where the C−H bond is partially broken in the transition state the potential energy curve becomes much wider (grey line) and the difference between the C−H and C−D zero point energies decreases. Adapted from reference [40].

broad. This has the effect of decreasing the spacing between vibrational energy levels, making the zero point energy of the two isomers very close. As a result the activation energy, the difference between the lowest vibrational energy levels of the ground and transition states, is larger for the heavier isotope and the reaction is therefore slower than with the lighter isotope. Conversely, with an early transition state the potential energy curve of the activated complex is much narrower leaving a larger difference between the zero point energies of the two isomers and therefore a smaller difference in activation energies, and rates, of the two isotopomers.

2.1.3 Charge Transfer

Charge transfer between the electrocatalyst and the adsorbate makes electrochemical energy conversion possible and separates electrocatalysis from heterogeneous catalysis. The driving force for the charge transfer is quantified by the electrochemical potential.

2.1.3.1 The Electrochemical Potential

The electrochemical potential, $\tilde{\mu}_{\mathrm{B}}^{\alpha}$, is defined as the change in Gibbs energy of a phase α with respect to the change in amount of a species B in the phase, at otherwise constant composition, temperature, T, and pressure, p. [41]

$$\tilde{\mu}_{\mathrm{B}}^{\alpha} = \left(\frac{\partial G}{\partial n_{\mathrm{B}}^{\alpha}} \right)_{T,p,n_{\mathrm{j}\neq\mathrm{B}}} \tag{2.4}$$

The electrochemical potential can be calculated from the chemical potential of the phase by addition of a term $z_{\mathrm{B}} F \phi^{\alpha}$ to account for interactions with the electric field at the electrode, where z_{B} is the charge on species B, F is the charge of 1 mol of unit charges, known as the Faraday constant, and ϕ^{α} is the work done on bringing a test charge from

infinity into the phase α, also known as the inner potential.

$$\tilde{\mu}_{\mathrm{B}}^{\alpha} = \mu_{\mathrm{B}}^{\alpha\circ} + RT \ln a_{\mathrm{B}} + z_{\mathrm{B}} F \phi^{\alpha} \tag{2.5}$$

The electrochemical potential can be used to calculate the position of chemical equilibrium between species, and therefore the direction of spontaneous reaction. It also represents the maximum electrical work available from a system. For two phases α and β in equilibrium, the electrochemical potential can be used to calculate the difference in their inner potentials ($\phi^{\alpha} - \phi^{\beta}$), given the symbol E.

$$\tilde{\mu}_{\mathrm{B}}^{\alpha} - \tilde{\mu}_{\mathrm{B}}^{\beta} = \mu_{\mathrm{B}}^{\alpha\circ} - \mu_{\mathrm{B}}^{\beta\circ} + RT \ln(a_{\mathrm{B}}^{\alpha}/a_{\mathrm{B}}^{\beta}) + z_{\mathrm{B}} F(\phi^{\alpha} - \phi^{\beta}) \overset{eqm.}{=} 0 \tag{2.6}$$

$$(\phi^{\alpha} - \phi^{\beta}) = (\mu_{\mathrm{B}}^{\beta\circ} - \mu_{\mathrm{B}}^{\alpha\circ}) + \frac{RT}{z_{\mathrm{B}} F} \ln\left(\frac{a_{\mathrm{B}}^{\beta}}{a_{\mathrm{B}}^{\alpha}}\right) \tag{2.7}$$

$$E = E^{\circ} + \frac{RT}{z_{\mathrm{B}} F} \ln\left(\frac{a_{\mathrm{B}}^{\beta}}{a_{\mathrm{B}}^{\alpha}}\right) \tag{2.8}$$

Equation (2.8) is known as the Nernst equation and relates the electrical potential difference between two phases to the activities of their components. This equation can be made more practical by generalising for a system with multiple components, with stoichiometric numbers ν, and substituting the activities for concentrations.

$$E = E^{\circ\prime} - \frac{RT}{zF} \sum_{i} \nu_i \ln\left(\frac{c_i}{c^{\circ}}\right) \tag{2.9}$$

The standard potential E° from equation 2.8 has been replace by the formal potential, $E^{\circ\prime}$, that is defined in terms of the concentrations rather than the activities. This means $E^{\circ\prime}$ includes the ionic strength of the solution, via the activity coefficients, and is therefore a slight function of the remaining components of the electrolyte solution. [41]

For any significant transfer to occur net charge cannot accumulate in the phase and

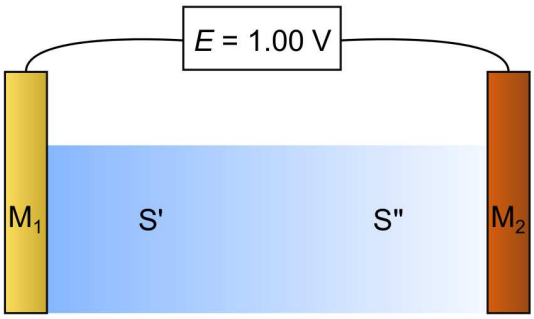

Figure 2.15: Schematic illustration of an electrochemical cell. Electrodes made of metals M_1 and M_2 are immersed in an ionic solution, with composition S' in the vicinity of M_1 and composition S" in the vicinity of M_2. A voltmeter connected between the two electrodes reports the cell voltage, E.

must be removed. This is accomplished by coupling an opposing charge transfer reaction that can remove the charge. In general it is useful if the two reactions can be spatially separated so that they occur at different electrodes. This can be accomplished as long as both electronic and ionic connectivity between the electrodes is maintained, usually by connecting the electrodes at one point with an electronic conductor, such as a metal wire, and at another with an ionic conductor, such as an ionic solution. This arrangement is known as an electrochemical cell and is shown in fig. 2.15.

The electrical connection between the electrodes provides a means of measuring the difference in their potential, by inserting an electrometer at the point shown in fig. 2.15. In this case the measured potential difference E is given by the sum of the potential differences across each interface (eq. (2.10)). [42]

$$E = \Delta\phi_{\mathrm{M}_1/\mathrm{S}'} + \Delta\phi_{\mathrm{S}'/\mathrm{S}''} + \Delta\phi_{\mathrm{M}_2/\mathrm{S}"} + \Delta\phi_{\mathrm{M}_1/\mathrm{M}_2} \tag{2.10}$$

In electrocatalyst research it is common to study the anode and cathode materials separately, thus limiting the number of factors controlling the current. [1, 42] In this case it is desirable to know the potential difference across just the electrode of interest. To

be able to interpret the measured cell voltage in terms of the potential difference at just one electrode the potential difference across the other electrode and across the solution must remain constant and well defined during experiments. This can be accomplished by choosing a second electrode with a well-defined, kinetically facile, electrode reaction. If high concentrations of both oxidised and reduced components are present at this electrode, small changes in their concentration will have a negligible effect on their ratio and therefore on the potential. Such electrode systems are known reference electrodes (RE). Some half reactions which have been used to make reference electrodes are: [1, 43]

$$2\,H^+ + 2\,e^- \rightleftharpoons H_2 \tag{2.11}$$

$$AgCl + e^- \rightleftharpoons Ag + Cl^- \tag{2.12}$$

$$Hg_2Cl_2 + 2\,e^- \rightleftharpoons 2\,Hg + 2\,Cl^- \tag{2.13}$$

Under standard conditions ($pH_2/p^\circ = 1$, $a_{H^+} = 1$) the reaction in eq. (2.11) is known as the standard hydrogen electrode (SHE) and its electrode potential is defined as 0 V at all temperatures. The reversible hydrogen electrode (RHE) uses the same reaction with $pH_2 = 1$ bar but with the H^+ activity of the electrolyte of interest.

To ensure fast electrode kinetics at the SHE, high surface area Pt black is used as the electrode material. This surface is highly susceptible to the adsorption of organic impurities, even at trace levels. As a result the reactions in eq. (2.12) and eq. (2.13) are often used instead. Although nominally the reduction of a metal cation (eq. (2.14), the low solubility of the cation in chloride solutions means that the Ag^+ concentration can be written in terms of the Cl^- concentration and the solubility product K_{sp} (eq. (2.16)). [43] This means that the potential of the Ag/AgCl RE is actually determined by the Cl^- concentration (eq. (2.17)). To maintain a stable potential, reference electrodes using these systems either use a saturated or near-saturated Cl^- solution (3 M to 3.5 M), which

is separated from the working electrode solution using a porous frit.

$$E = E^{\circ\prime} - \frac{RT}{F} \ln \frac{1}{[\mathrm{Ag}^+]} \tag{2.14}$$

$$\mathrm{AgCl} \overset{K_{sp}}{\rightleftharpoons} \mathrm{Ag}^+ + \mathrm{Cl}^- \tag{2.15}$$

$$[\mathrm{Ag}^+] = \frac{K_{\mathrm{sp}}}{[\mathrm{Cl}^-]} \tag{2.16}$$

$$E = E^{\circ\prime} - \frac{RT}{F} \ln[\mathrm{Cl}^-] \tag{2.17}$$

Even with large concentrations of reactants in the reference electrode, significant passage of current through the cell will inevitably lead to depletion of Cl^- and therefore a change in potential. To avoid this problem the potentiostat circuit was developed. In this circuit two electrode couples exist - the original working electrode/reference electrode couple and a new couple between the working electrode and a third electrode known as the counter electrode (CE). In the circuit the potential is measured across the WE/RE couple, while current flows between the WE/CE couple, with the potentiostat controlling the WE/CE voltage to maintain a constant WE/RE voltage. The potentiostat is discussed further in section 2.2.2.

2.1.3.2 Capacitance and the Electrical Double Layer

In general the discontinuity in atomic environments at the surface leads to some degree of charge separation, giving surfaces a net charge. The electric field established by this charge separation serves to orient ionic species at the surface. This storage of electrical potential energy at the surface by accumulation of charge is known as capacitance. There have been several theories proposed to describe the electric field at the surface. [42]

Figure 2.16 illustrates some features of the double layer and shows the potential energy as a function of distance from the electrode described by the Stern model. [42] A positively charged electrode will tend to attract anions (blue) and polar solvents such as water (grey)

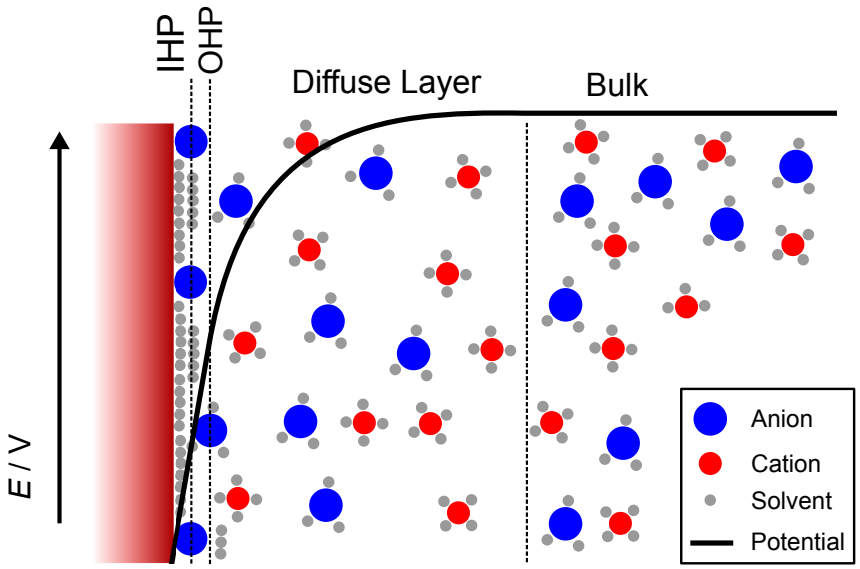

Figure 2.16: The electrical double layer illustrating the position of anions (blue), cations (red) and solvent (grey). Specific adsorption of dehydrated anions defines the Inner Helmholtz Plane (IHP), while adsorption of solvated anions establishes the Outer Helmholtz Plane (OHP). The concentration of anions near the electrode drops of exponentially, giving rise to the diffuse layer. In the Stern model specific adsorption is neglected and the potential distribution is linear between the electrode and the OHP (black line).

while repelling cations (red). This leads to a layer of water adsorbing at the interface, along with solvated anions. The plane through the mid-point of the adsorbed solvated anions is known as the Outer Helmholtz Plane (OHP), this layer in combination with the metal surface charge giving rise to the term double layer. The change in potential from the electrode surface to the OHP is considered linear in the Stern model. [42] Thermal energy ensures not all of the anions in the vicinty of the electrode are adsorbed; although their accumulation does affect the potential the change in anion concentration with distance from the electrode is much slower creating the so-called 'diffuse layer'. The Stern model fails for anions other than F^-, however, due to specific adsorption (adsorption of the naked anion), which greatly perturbs the potential distribution, making it highly non-linear. [42] Specific adsorption is also highly significant in electrocatalysis, as it affects the number of metal sites available for catalysis. Note that specific adsorption is generally limited to

anions, due to their larger size and corresponding weaker solvation.

If the charge of the electrode is increased, by increasing the electrode potential, further movement of ions up to the electrode is observed to balance the increased charge. This movement of charge through the circuit, without charge transfer between phases, is known as capacitive, or non-Faradaic, current. [1] Since the 'electrode potential' is the difference between the potentials of the electrode and solution, the equilibrium electrode potential is only obtained once this movement of charge has stopped. The finite rate at which this charge can accumulate therefore limits the rate at which the electrode potential can be changed. The characteristic time taken for the capacitive current to become insignificant is known as the time constant, $\tau = RC_{\mathrm{dl}}$ and is a function of the total resistance R and the double layer capacitance C_{dl}. [1]

2.1.3.3 Electrode Kinetics

The origin of the potential dependence of the current can be seen by considering the effect of potential on the activation energy of the species undergoing electron transfer. In purely chemical reactions the rate constant is exponentially dependent on the activation energy, the energy required to reach the transition state. [37]

$$k \propto e^{-\Delta^{\ddagger}G/RT} \tag{2.18}$$

In an electrochemical reaction the effect of potential is to increase or decrease the energy required to reach the transition state. Hence, for each elementary reaction the current can be written:

$$j \propto e^{\alpha\Delta\phi/RT} \tag{2.19}$$

$$\alpha_{a/c} = (+/-)(RT/F)(d\ln|j_{a/c}|/dE) \tag{2.20}$$

where j is the current density, $\Delta\phi$ is the potential drop at the electrode-solution interface and $\alpha_{a/c}$ is the anodic/cathodic 'transfer coefficient', determined experimentally via eq. (2.20) and often found to be close to 0.5. [44, 45] For elementary oxidation and reduction reactions, of species R and O, respectively, in which the rate of reaction is much slower than the rate of mass transport,

$$\mathrm{O} + \mathrm{ne}^- \longrightarrow \mathrm{R} \tag{2.21}$$

$$\mathrm{R} \longrightarrow \mathrm{O} + \mathrm{ne}^- \tag{2.22}$$

the anodic and cathodic current current density j_a and j_c, respectively, can be written as:

$$j_a = nFk_a[\mathrm{R}]\exp(\alpha_a FE/RT) \tag{2.23}$$

$$j_c = -nFk_c[\mathrm{O}]\exp(-\alpha_c FE/RT) \tag{2.24}$$

where n is the number of electrons transferred, F is the Faraday constant, k_a and k_c are the anodic and cathodic rate constants, [R] and [O] represent the surface concentrations, E is the electrode potential, R is the gas constant and T is the temperature. [45] At equilibrium the potential is E_{eq} and the values of the anodic and cathodic currents are equal and opposite, with magnitude j^0, known as the exchange current density (eq. (2.26)). [45] The current away from equilibrium can then be described in terms of the deviation of the potential from equilibrium, the overpotential $\eta = E - E_{\mathrm{eq}}$, the transfer coefficient, α, and the exchange current density, j^0 (eq. (2.27)). This equation is known as the Butler-Volmer

equation. [45]

$$j = j_a = j_c = 0 \tag{2.25}$$

$$j^0 = nFk_a[R]\exp(\alpha_a FE_{\text{eq}}/RT) = nFk_c[O]\exp(-\alpha_a FE_{\text{eq}}/RT) \tag{2.26}$$

$$j = j^0[\exp(\{1-\alpha_a\}F\eta/RT) - \exp(-\alpha_c F\eta/RT)] \tag{2.27}$$

For a system containing multiple oxidised species $A, B, ...$ along with their reduced counterparts A', B', with stoichoimetric coefficients a, b, and a', b', the total current can be written: [42]

$$j = j_a + j_c = nF(kc_A^a c_B^b ... e^{\alpha_a FE/RT} - kc_{A'}^{a'} c_{B'}^{b'} ... e^{\alpha_c FE/RT}) \tag{2.28}$$

To understand the mechanism of the reaction giving rise to the current it is useful to know the order of reaction with respect to the various reactants. This can be found using a plot of $\ln(j)$ versus $\ln(c_A)$, where the slope of the line will provide the order of reaction with respect to species A.

$$\left(\frac{\partial \log j}{\partial \log c_A}\right)_{c_B,E} = a \tag{2.29}$$

For reactions involving adsorbed species, rate equations are often formulated in terms of the coverage θ_A as opposed to the concentration c_A. This is useful where the coverage can be measured directly, for example through in situ characterisation of the electrode. Coverage and concentration are related by an adsorption isotherm. For the reductive adsorption of cation A^+ at a vacant site:

$$A^+ + e^- \rightleftharpoons A(\text{ads}) \tag{2.30}$$

At equilibrum the forward and backward rates are equal and can be written:

$$k_1(1-\theta_A)c_A e^{-\alpha EF/RT} = k_{-1}\theta_A c_A e^{(1-\alpha)EF/RT} \tag{2.31}$$

This can be rearranged into an electrochemical version of the Langmuir isotherm. [46]

$$K = \frac{k_1}{k_{-1}} \tag{2.32}$$

$$\frac{\theta_A}{1-\theta_A} = Ke^{-EF/RT} \tag{2.33}$$

$$\theta = \frac{Ke^{-EF/RT}}{1+Ke^{-EF/RT}} \tag{2.34}$$

For strong adsorption $Kc_A e^{-EF/RT} \gg 1$, θ tends to 1 and the current becomes zero order in component A. For weak adsorption $Kc_A e^{-EF/RT} \ll 1$, θ tends towards $Kc_A e^{-EF/RT}$ and the order tends towards 1. For reactions involving intermediate coverages of adsorbed species the reaction order can therefore be expected to vary between 0 and 1.

2.2 Electrochemical Techniques

To examine the potential dependence of a reaction the current is generally measured over a range of applied potentials. For real world applications it is the steady state current generated by the device over periods of hours which is of interest. However, when the aim is to study the mechanism of reaction it can be advantageous to measure the current over much shorter periods of time, enabling the lifetime of chemical species to be examined as well as minimising the effects of slow accumulation of impurities at the electrode. [42]

A common electrochemical technique is to sweep the potential applied to the electrode in a linear ramp. [1,42] The current is therefore recorded over a wide range of potentials in a relatively short amount of time. This technique is known as linear sweep voltammetry and the resulting current response provides characteristic peaks at the potentials where

electrochemical processes are occurring. Sometimes a subsequent sweep is carried out in the opposite direction in an attempt to reverse the electrochemical processes which have just occurred, revealing information on the reversibility and kinetics of the process. In this case the technique is known as cyclic voltammetry.

The Faradaic (*i.e.* non-capacitive) current, i observed during the oxidation of an adsorbed species in linear sweep voltammetry has been derived theoretically. [46] The rate of oxidation of an adsorbed species, that is, the current, is proportional to the rate of change of coverage of the species with time:

$$i \propto -\frac{d\theta}{dt} \tag{2.35}$$

Assuming the adsorption is governed by the Langmuir isotherm, the potential dependent forward and backward rates of adsorption/desorption enable the coverage to be described in terms of potential (eq. (2.34)). The dependence of potential on time is given by the scan rate, ν:

$$\nu = \frac{dE}{dt} \tag{2.36}$$

When combined with the charge for oxidation of the entire monolayer, q, the Faradaic current i can be found (eq. (2.37)). The shape of the current-potential curve is observed to be a peak, with the peak potential dependent on the equilibrium constant of adsorption and the peak current a linear function of scan rate.

$$i = \frac{qF}{RT}\frac{Ke^{-EF/RT}}{(e^{-EF/RT}+K)^2}\cdot\nu \tag{2.37}$$

The peak potential E_p being given by eq. (2.38) and the peak current i_p by eq. (2.39).

$$E_p = -RT/F \ln K \tag{2.38}$$

$$i_p = (qF/4RT) \cdot \nu \tag{2.39}$$

2.2.1 Adsorption of H

Metals such as Pt are efficient catalysts for the reduction of protons to hydrogen, and for the oxidation of hydrogen to protons. [3] At potentials just above that at which hydrogen evolution occurs, H^+ is observed to adsorb on the Pt to form H(ads). [42]

$$H^+ + e^- \xrightarrow{Pt} H(ads) \tag{2.40}$$

The different basal planes of Pt adsorb H with different strengths, for the reasons discussed in section 2.1.2.4. This variation in adsorption energy gives rise to different equilibrium constants for the adsorption and therefore current peaks at different potentials during a linear potential sweep. In general peaks below 0.25 V correspond to H adsorbed on low coordinate sites: (110) domains, steps of (110) orientation and kinks. [47] The peak around 0.27 V arises from H adsorbed on short (100) terraces, the peak at 0.256 V from (111) terraces and steps of (100) orientation, and peaks above 0.3 V from wide (100) terraces. [47]

Similarly, just below the potential of oxygen evolution water is adsorbed and deprotonated (eq. (2.41)), this also giving rise to current peaks. The current measured in a full potential cycle from just above hydrogen evolution to just below oxygen evolution is shown in fig. 2.17. [48]

$$H_2O + \rightleftharpoons OH(ads) + H^+ + e^- \tag{2.41}$$

The formation of H(ads) and OH(ads) species on Pt is partially responsible for its well

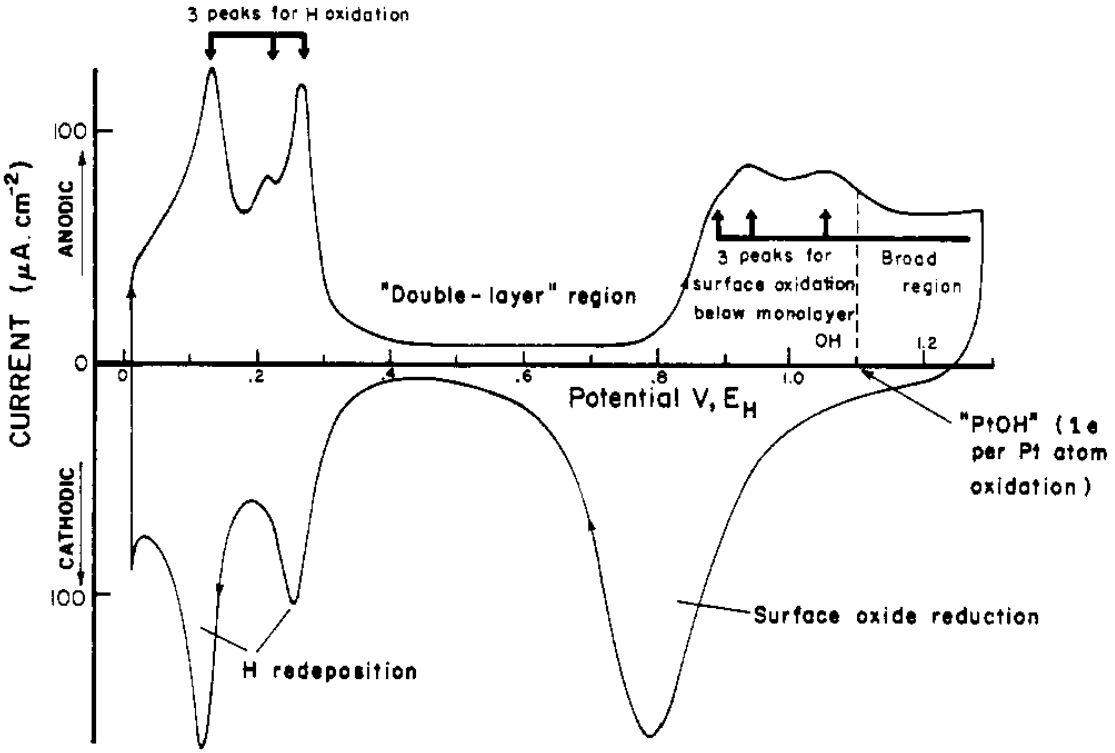

Figure 2.17: Cyclic voltammogram of polycrystalline Pt in 1 M H_2SO_4 solution. Adapted with permission from reference [48]. Copyright 1973 American Chemical Society.

known catalytic activity; almost all organic species can be oxidised on the surface of Pt by OH(ads) at high enough potentials. [42] By cycling between the two extreme potentials any adsorbed impurities will therefore be oxidised and desorb, producing a clean Pt surface. Once clean, the charge due to adsorption of H can be used to estimate the electrochemically active surface area of Pt, assuming one H adsorbs on each Pt site. [49, 50] A reproducible value of the surface area is often taken to imply a reproducibly clean Pt surface. The areas used to calculate the H desorption charge are shown in fig. 2.17.

2.2.2 The Potentiostat

The potentiostat circuit uses negative feedback to keep the potential of the working electrode constant. A schematic of a basic potentiostat circuit is shown in fig. 2.18. During operation the user sets the desired voltage to be applied, V_{app}. The voltage difference between the reference electrode (RE) and the working electrode (WE) is then measured via

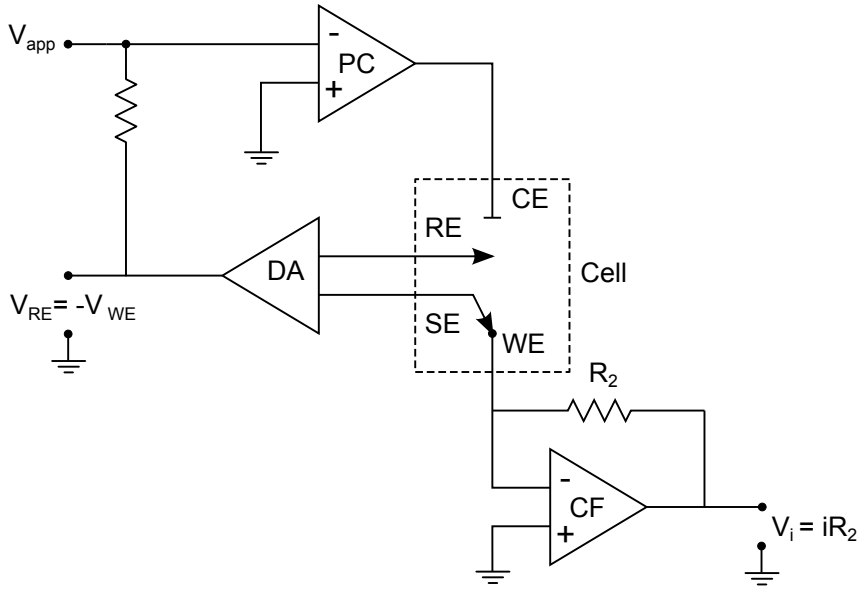

Figure 2.18: Schematic illustration of a potentiostat. Triangles represent the operational amplifiers making up the potential control (PC), differential amplifier (DA) and current follower (CF) circuits. V_{app} is the applied potential. The working, reference, counter and sense electrodes are denoted WE, RE, CE and SE, respectively. [1, 51]

a differential amplifier (DA), using a separate physical connection to the working electrode known as the sense electrode (SE). If the measured voltage is greater than the applied voltage set by the user, then the output of the potential control operational amplifier (PC) becomes negative, decreasing the WE/CE voltage, and therefore the WE potential. Similarly, if the measured voltage is less than the applied voltage, the WE/CE voltage will become positive and the WE potential will be increased. This continual adjustment ensures that the WE potential remains at the applied potential.

To ensure that the measurement of the current and potential do not draw significant current which might affect the potential, it is carried out using very high input impedance amplifiers, such that negligible current is needed to produce an output voltage. The voltage is either equal to the input voltage (voltage follower) or proportional to the input current (current follower, CF). To further minimise the affect of potential drops in the measurement circuit, the SE completely separates the measurement and control circuits.

The applied potential does not have to be constant and often linear and cyclic voltage

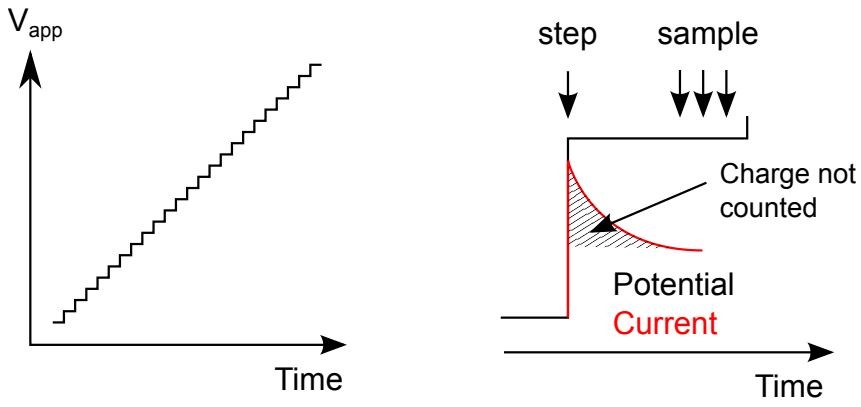

Figure 2.19: The effects of measuring H adsorption with a staircase waveform.

ramps are used (section 2.2). Most modern potentiostats generate these waveforms digitally, approximating linear sweeps with a 'staircase' pattern of potential steps (fig. 2.19). In such cases the current is sampled shortly after stepping the potential. This has the effect of decreasing the amount of capacitive current measured and enables multiple samples of the current at each potential, increasing the signal/noise ratio. However, when very fast processes which occur on timescales comparable to the the capacitive current are examined, H adsorption for example, a lot of the current from this process is lost by sampling at times after the potential step. This loss is most significant for slow scan rates where the H adsorption currents are smaller. This effect can be important if the H adsorption charge is used to calculate electroactive surface areas. Underestimating the surface area when characterising electrocatalysts will lead to the specific activity being overstated and incorrect conclusions being drawn.

To minimise the effect of staircase waveforms an integrator can be used. An integrator circuit uses a capacitor to accumulate the charge passed and an amplifier to provide an output proportional to the voltage across the capacitor. The charge passed is calculated as $Q = C \cdot V$, where C is the capacitance and V the measured voltage, which enables the current to be estimated as $i \approx \Delta Q/\Delta t$. As well as providing a continuous measurement of current, the integrator also provides some degree of smoothing, removing noise from the data.

2.2.3 Sources of Error in Potential Control

It should be remembered that the potentiostat is actually measuring the whole cell voltage, as given by eq. (2.10), and not just $\Delta\phi_{\mathrm{M}_1-\mathrm{S}'}$. As such, if any of the other potential differences in eq. (2.10) become significant compared to the working electrode potential difference, they will share part of the applied voltage and cause the working electrode potential to deviate from the applied potential. One way to minimise the effect of this it to work with small currents: Ohms law $V = iR$ shows that large values of R cannot give large values of V if i is small. For example a resistance of 1 kΩ in a circuit passing 1 µA will only contribute 1 mV to the cell voltage, while the same resistance would give rise to a drop of 1 V with a current of 1 mA. This is also the reason that separate working and sense connections are made to the working electrode: the minimal current flowing the measurement circuit leads to minimal voltage errors.

Another way to minimise the error in potential measurement is to decrease the solution resistance term ($\Delta\phi_{\mathrm{S}'-\mathrm{S}''}$). This is accomplished by the addition of an inert salt, known as the supporting electrolyte. However, even with a supporting electrolyte added, the resistance is often significant, meaning the potential of the solution changes significantly between the working and counter electrodes (fig. 2.20). [52] To further minimise the effect this has on the measured potential, the reference electrode should sample the solution as close to the working electrode as possible. Placing the reference electrode itself directly in front of the working electrode would create its own resistance by screening the electrode, and so a fine capillary, known as a Luggin capillary, is often used to access solution near the working electrode. As minimal current passes through the measurement circuit, minimal voltage is dropped through the capillary and so it can be used to locate the reference electrode relatively far from the working electrode. In addition, the relatively narrow diameter of the capillary hinders diffusion between the cell solution and the solution inside it, providing some separation of the analyte solution and possible disruptive ions

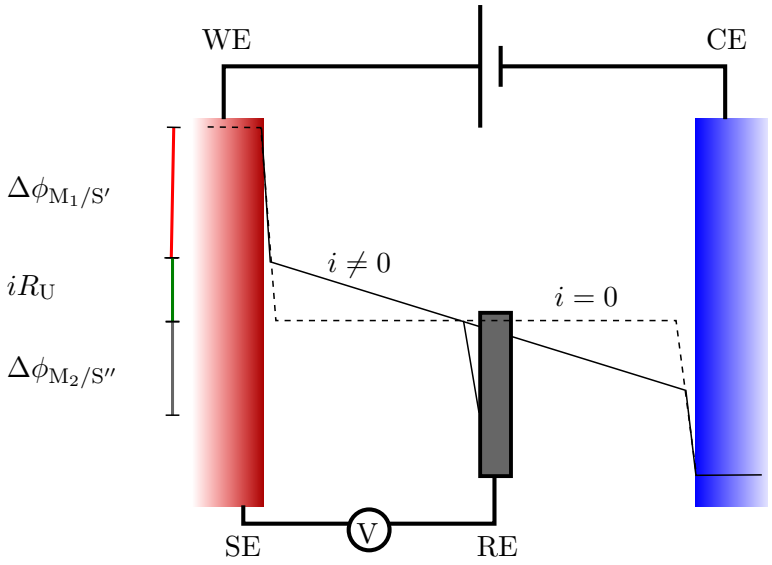

Figure 2.20: The potential difference across an electrochemical cell. The potential at equilibrium is shown schematically by the dashed black line, whereas the potential during current flow is shown by the solid black line. For the case of current flow the potential drops across the two interfaces and the bulk solution are shown on the left hand side. Adapted from reference [52].

like Cl^- that are found in reference electrode systems.

2.3 Vibrational Spectroscopy

Vibrational spectroscopy is a powerful technique in chemistry that allows the identification and quantification of unknown chemical species based on their interaction with infrared light. The primary information available from IR spectroscopy is the energy at which IR light is absorbed, which, being related to the spacing of vibrational energy levels in the molecule provides a good handle on the molecule's identity. Furthemore, since the intensity of light absorbed is measured the technique also provides a way of quantifying the amount of species present.

To obtain this information the intensity of IR light absorbed by a sample is calculated from the observed loss of intensity of an IR source after it has interacted with the sample.

In many cases the IR light can be transmitted through the sample, however in some cases this is not possible and the light must be reflected from the sample instead. Under certain conditions the two methods provide very similar results and as such can be analysed purely in terms of the absorption of light by the sample. In other cases, as in this thesis, consideration must also be given to the reflectivity of the sample.

Initially the molecular basis for IR absorption by molecules is introduced, along with the origin of the basic spectroscopic parameters, intensity and linewidth. This discussion is then extended to consider the effects of transmission and reflection from dielectric media on the measured spectra, resulting in the derivation of a Lorentzian peak function. The effect of conducting media on the transmission and reflection of IR light is then discussed, with reference to various models proposed in the literature. The section concludes with a brief discussion of the behaviour of species adsorbed on conducting media in IR light and a description of the Fourier Transform IR technique used to record the spectra in this thesis.

2.3.1 Molecular Vibrations

The vibrational potential energy of a molecule is a function of the position of its constituent nuclei, or more specifically, a function of their displacement from their equilibrium positions. The dependence of this potential on displacement is represented by the Morse potential, shown in fig. 2.21 for the diatomic molecule AB. [37] At small negative displacements from the equilibrium bond length increasing overlap of the core electrons leads to repulsion, while at small positive displacements the overlap of the bonding electrons is decreased, also resulting in an increase in energy. At much larger positive displacements the decrease in overlap is so great the molecule dissociates.

A more general expression for the vibrational potential energy is found by expressing the energy as a power series using the Taylor expansion. [53] The fundamental vibrations

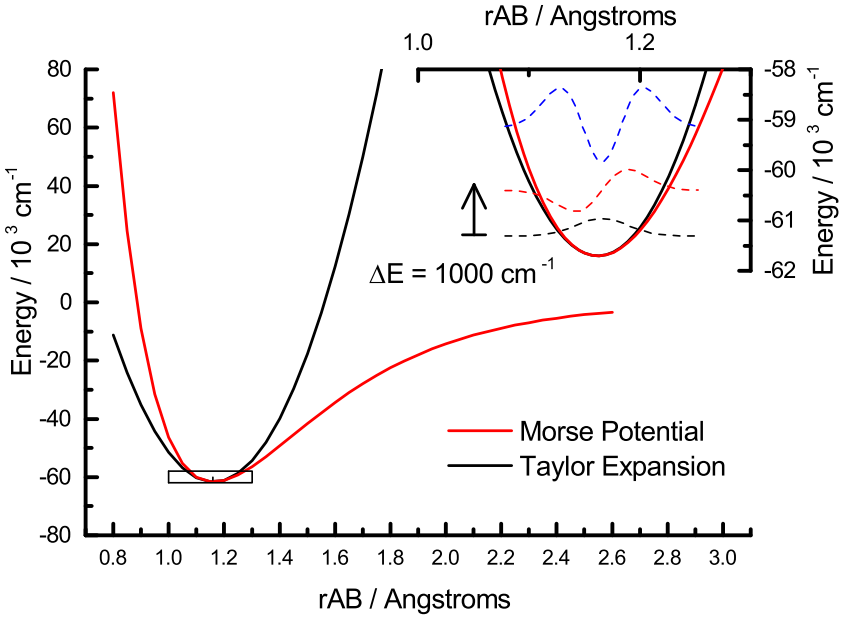

Figure 2.21: The potential energy of a diatomic molecule. The Morse potential (red line) describes the potential energy of diatomic molecule AB as a function of the A−B bond distance, rAB. For small displacements it can be approximated by a second order Taylor expansion (black line). Inset: the small displacement region approximated by the Taylor expansion. The first three vibrational wavefunctions for a harmonic oscillator are shown (dashed lines, not to scale).

of molecules involve displacements much smaller than that leading to dissociation, and as a result the expansion only needs to go up to second order, as shown by fig. 2.21, inset. To generalise for poly atomic molecules the expansion is written as a sum over all of the mixed partial derivatives of potential with respect to the i^{th} and j^{th} atoms. As we are interested in the changes in energy, the constant $V(0)$ term can be set to 0. The term $\partial V/dx_i$ evaluated at $x = 0$ is also zero, leaving an approximate expression for the potential energy in terms of the individual atomic displacements x_i and the force constants k_{ij}: [53]

$$V = V(0) + \sum_i \left(\frac{\partial V}{\partial x_i}\right)_0 x_i + \frac{1}{2}\sum_{i,j}\left(\frac{\partial^2 V}{\partial x_i \partial x_j}\right)_0 x_i x_j + \cdots \tag{2.42}$$

$$\approx \frac{1}{2}\sum_{i,j} k_{ij} x_i x_j \qquad k_{ij} = \left(\frac{\partial^2 V}{\partial x_i \partial x_j}\right)_0 \tag{2.43}$$

Combining the potential energy with the kinetic energy, T:

$$T = \sum_i \frac{1}{2} m_i \left(\frac{dx_i}{dt}\right)^2 = \frac{1}{2} m \dot{x_i}^2 \tag{2.44}$$

the total classical energy E can be written as:

$$E = T + V = \frac{1}{2}\sum_i m\dot{x_i}^2 + \frac{1}{2}\sum_{i,j} k_{ij} x_i x_j \tag{2.45}$$

The interaction between one nucleus with the remaining nuclei are accounted for via the mixed partial derivative and the mixed $x_i x_j$ terms. It would, however, be much simpler if the potential energy could be written purely in terms of the motions of individual atoms, rather than as the product of two atomic displacements. This can be accomplished by first rewriting the energy in terms of mass-weighted coordinates $q_i = m_i^{1/2} x_i$ then looking for combinations Q_i of individual motions q_i that occur in phase. The collective motions would not affect the motion of any other combination, and could therefore be written without any cross terms. In this way the motion of the molecule, and its energy levels,

can be considered as the sum of groups of distinct motions, rather than as the simultaneous motion of all of the atoms. These combinations are known as normal modes and have effective force constants λ.

$$E = \frac{1}{2}\sum_i \dot{q}_i^2 + \frac{1}{2}\sum_{ij} K_{ij} q_i q_j; \qquad K_{ij} = \left(\frac{\partial^2 V}{\partial q_i \partial q_j}\right)_0 = \left(\frac{1}{m_i m_j}\right)^{1/2} k_{ij} \tag{2.46}$$

$$E = \frac{1}{2}\sum_i \dot{Q_i}^2 + \frac{1}{2}\sum_i \lambda_i Q_i^2 \tag{2.47}$$

The l new force constants λ_l of the normal modes are found by finding the determinant of the secular equation (eq. (2.48)) which can then be used to make combinations of the j individual atomic motions by solving eq. (2.49). [53]

$$|\mathbf{K} - \lambda \mathbf{1}| = 0 \tag{2.48}$$

$$\sum_j (K_{ij} - \lambda_l \delta_{jl}) c_{jl} = 0 \tag{2.49}$$

The wavenumbers of these normal modes, $\tilde{\nu}$, is given by

$$\tilde{\nu} = \frac{\lambda_l^{\frac{1}{2}}}{2\pi c} \tag{2.50}$$

As the total classical energy of the molecule is a sum of the energy of each mode, the Hamiltonian operator, H, that provides the allowed energies for the quantised system is also a sum of Hamiltonians for each mode, and the vibrational wavefunction ψ of the molecule is therefore a product of wavefunctions for each mode. [53] Operating on ψ with

H provides the energy E_{v_l} for the energy levels v_l in each vibrational mode l. [53]

$$H = \sum_l H_l \tag{2.51}$$

$$\psi = \psi_{\nu_1}(Q_1)\psi_{\nu_2}(Q_2)\dots \tag{2.52}$$

$$E_{v_l} = (v_l + \tfrac{1}{2})hc\tilde{\nu} \qquad v_l = 0, 1, 2, \dots \tag{2.53}$$

2.3.2 Infrared Spectroscopy

The vibrational energy levels of a molecule are revealed by the absorption and emission of light, with only photons of an energy equal to the difference between two vibrational energy levels being able to stimulate absorption or emission (eq. (2.54)). Furthermore, the selection rule in IR spectroscopy $\Delta v = \pm 1$, [37] means that the allowed energies of vibrational transitions ΔE for a molecule undergoing simple harmonic oscillator are: [41]

$$\Delta E = hc\tilde{\nu} \tag{2.54}$$

This fundamental equation links the energy of light absorbed by a molecule with its structure and is the basis for molecular spectroscopy. Further information is available from a spectrum in terms of the relative intensity of the the light absorbed. The rate at which absorption and emission occur is given by the Einstein coefficient B (eq. (2.55)) which is related to the transition dipole moment μ_{fi} between the final, f and initial, i, vibrational states (eq. (2.56)). [37] The transition dipole is the dipole formed during the redistribution of charge that accompanies a vibrational transition.

$$B = \frac{|\mu_{fi}|^2}{6\epsilon_0\hbar^2} \tag{2.55}$$

$$\mu_{fi} = \int \psi_f^* \hat{\mu} \psi_i d\tau \tag{2.56}$$

The requirement that $B \neq 0$ gives rise to the gross selection rule for IR spectroscopy, $d\mu/dQ \neq 0$, that is the transition dipole moment of the molecule must change with the displacement of the normal mode. [37] The symmetry of the normal mode can be used to judge whether the fundamental transition ($\Delta v_{1\leftarrow 0}$) causes a change in dipole moment: since in the harmonic approximation the ground-state vibrational wavefunction is totally symmetric, the normal mode must span the same irreducible representation as a component of the electric dipole moment. The components of the dipole moment transforms as translations, and so the rule simplifies further to state that the normal mode must belong to the same symmetry group as either x, y or z. [37] An additional 'selection rule' known as the surface selection rule is often invoked when discussing spectra of surfaces, however its origin is not quantum mechanical and so it is discussed later.

2.3.2.1 Bandwidths in IR Spectra of Adsorbed Species

Homogeneous Broadening Infrared absorption always occurs over a finite range of energies due to the quantum mechanical uncertainty relation between the energy and time operators. [37] The relationship is such that the more precisely the lifetime of a state is known, the greater the uncertainty in its energy and the broader the range of energies that are absorbed. Spontaneous emission of light limits the lifetime of an excited state and gives rise to a natural linewidth. The rate of spontaneous emission is proportional to the cube of frequency of light being emitted and is therefore negligible at IR frequencies, not leading to significant broadening. [37]

Spontaneous emission aside, the vibrational excited state of an ensemble of oscillators is characterised by two lifetimes, T_1 and T_2. [54] The first lifetime, T_1, is the time before which the excited state dissipates its energy to its surroundings, which in the case of adsorbed species is likely to be via collisions with the surface or solvent molecules. The second lifetime, T_2 is the time over which the excited oscillations remain in phase. Elastic

Table 2.2: Vibrational lifetimes and resulting natural linewidths of HCOOH and CO under different conditions.

System	Lifetime, τ / ps	Lifetime Broadening / cm^{-1}	Ref.
HCOOH dimers in Ar matrix	500	0.01	[55]
HCOOH dimers in gas phase	20	0.27	[56]
HCOOH CCl_4 solution (0.05 M)	4	1.33	[56]
Linear CO/Pt (UHV)	1	5.3	[57]
Bridging CO/Pt (UHV)	0.2	26.5	[57]

collisions, in which the oscillator does not dissipate energy, will result in a random change in phase of the oscillator. Over time the accumulated random phase differences in the ensemble will lead to interference, known as dephasing, and the coherent state will cease to exist. The effect of the two processes is to shorten the lifetime of the excited state, increasing the uncertainty in its energy, and therefore the width of the absorption band. The magnitude of this broadening can be calculated in wavenumbers using the relation $5.3\,cm^{-1}/\tau$, where τ is the total lifetime given in picoseconds. [37] The importance of the environment in determining the natural linewidth of an oscillator can be seen in table 2.2, where adsorbed species show large natural linewidths due to collisions with the surface which give rise to very fast relaxation. The uncertainty in energy means that broadening occurs equally on the high and low energy sides of the peak energy, and as such gives rise to homogeneously broadened bands which can be described by a Lorentzian profile.

Inhomogeneous Broadening In addition to homogeneous broadening, inhomogeneous broadening is also observed, where the absorption band width changes by different amounts on either side of the peak maximum. In general inhomogeneous broadening arises from a distribution in the properties of the oscillators themselves and is particularly relevant to the changes in bandwidth that occur with changes in surface coverage.

The simplest example is chemically induced broadening, where at high coverage, the number of adsorbed species becomes greater than the number of single adsorption sites,

and a second type of adsorption site starts to be filled. Since this second site is likely to give rise to an adsorbed species with a different frequency, and possibly lifetime, the overlap of the absorption bands for the two species is likely to result in a combined band with a different, broader shape.

More complex explanations for inhomogeneous broadening can be found in terms of the changes associated with dipole-dipole coupling (*vide infra*). Such coupling in disordered adlayers can give rise to multiple normal modes which will vary in frequency and energy, their sum giving rise to complex broad band shapes. Similar effects can be observed when island formation occurs, especially when the coverage decreases, as the ratio of oscillators on the edge to those in the centre of the island increases and the chemically distinct edge oscillators begin to contribute to the normal modes of the island, broadening the band.

2.3.3 The Transmission and Reflection of Infrared Light

The absorption of IR light by *molecules* has been discussed above. It was noted how absorption only occurred at certain frequencies, that absorbed IR energy excited vibrations in the molecule and that these vibrations could be approximated as simple harmonic oscillation. It was also mentioned that for the absorption to be allowed quantum mechanically, the transition between vibrational energies had to induce a dipole moment in the molecule. These concepts can be extended to consider how IR light interacts with bulk matter, and therefore how this light can be absorbed, transmitted and reflected.

2.3.3.1 The Maxwell Equations

The material equations (eqs. (2.57) to (2.59)) are used in conjunction with the Maxwell equations (not shown) to define how electromagnetic radiation interacts with matter. [58] They define the conductivity, σ to relate the electric field to the current density, the dielectric constant, ϵ to relate the electric displacement with the electric field and the

magnetic permeability, μ to relate the magnetic induction to the magnetic field.

$$\mathbf{j} = \sigma\mathbf{E} \tag{2.57}$$

$$\mathbf{D} = \epsilon\mathbf{E} \tag{2.58}$$

$$\mathbf{B} = \mu\mathbf{H} \tag{2.59}$$

For non-conducting (dielectric), non-magnetic media, *i.e.* where $\sigma \approx 0$ and $\mu \approx 1$, the properties of the media are completely determined by ϵ. Thus to describe the propagation of light through such media expressions for ϵ must be developed. When conducting media, such as metals, are considered, the same expressions involving ϵ can often be used, but with a modified version of ϵ to include the conductivity. The molecular basis for ϵ will first be introduced, before the difference in conducting media are introduced.

2.3.3.2 The Dielectric Constant ϵ

Consider a bulk phase in which all of the charge displaced during vibration of the constituent molecules was replaced with an effective point charge e, at an effective displacement x_p from its equilibrium position. An incident oscillating electromagnetic field of the appropriate frequency $E_0 e^{-i\omega t}$ will drive this point charge into oscillation. As it oscillates, the charge will interact with its environment such that the oscillating charge loses some of its energy. In this scenario of driven, damped harmonic oscillation the motion of the point charge is given by eq. (2.60). [59] The solution to this equation gives the displacement of the charge, x_p (eq. (2.61)) and the resulting dipole moment (eq. (2.62)). The polarisability of the material, the ease with which an external E field, E_0, can induce a change in charge distribution, is therefore given by eq. (2.63) and from this the dielectric function $\epsilon(\tilde{\nu})$ of the material can be derived (eq. (2.64)). To link the strength of the induced oscillation with the strength of coupling given by quantum mechanics, the $Ne^2/\epsilon_0 m$ term is replaced

by $(2N\omega_0/\epsilon_0\hbar)|\mu_{fi}|^2$. [59]

$$m\ddot{x} + \gamma m\dot{x} + \beta x = eE_0 e^{-i\omega t} \tag{2.60}$$

$$x_p = \frac{eE_0}{m}(\omega_0^2 - \omega^2 - i\tilde{\nu}\gamma)^{-1} \tag{2.61}$$

$$p_x = ex_p \tag{2.62}$$

$$\alpha(\tilde{\nu}) = \frac{p_x}{E_0} = \frac{e^2}{m}(\tilde{\nu}_0^2 - \tilde{\nu}^2 - i\tilde{\nu}\gamma)^{-1} \tag{2.63}$$

$$\epsilon(\tilde{\nu}) = 1 + \frac{Ne^2}{\epsilon_0 m}(\tilde{\nu}_0^2 - \tilde{\nu}^2 - i\tilde{\nu}\gamma)^{-1} \tag{2.64}$$

To account for absorption by different vibrations, the function is taken as the sum over all modes j. If the frequencies of the different absorptions are well separated then the contribution of an individual resonance $\tilde{\nu}_j$ to the overall dielectric function $\epsilon(\tilde{\nu})$ becomes

$$\begin{aligned} &\epsilon(\tilde{\nu}_j) \to f_j/\tilde{\nu}_{0j}^2 = \epsilon_b \quad \tilde{\nu} \ll \tilde{\nu}_{0j} \\ &\epsilon(\tilde{\nu}_j) \to 0 \qquad\qquad\quad \tilde{\nu} \gg \tilde{\nu}_0 \end{aligned} \tag{2.65}$$

To obtain the dielectric function just around a single resonance we can therefore combine the contributions to $\epsilon(\tilde{\nu})$ from other resonances in a single constant baseline ϵ_b. This gives a general expression for the dielectric function around a single resonance (eq. (2.66)). [59] This equation has the form of a Lorentzian function.

$$\epsilon_j(\tilde{\nu}) = \epsilon_b + \frac{f_j}{\tilde{\nu}_{0j}^2 - \tilde{\nu}^2 - i\tilde{\nu}\gamma_j} \qquad f = \frac{2N\omega_0}{\epsilon_0\hbar}|H_{ij}|^2 \tag{2.66}$$

The importance of the dielectric function is that it describes how incident electromagnetic radiation propagates through a medium. As the frequency of the radiation approaches the resonant frequency of a vibrational mode, the radiation can couple to it and excite

a transition to a different vibrational energy level. This excited state then relaxes, re-emitting the radiation, but with a slight time delay corresponding to a shift in phase of the wave. The incident and re-emitted radiation are superposed into one electromagnetic wave travelling through the material.

The phase of the superposed wave therefore depends on the contribution of the re-emitted wave; at frequencies far below the resonant frequency the contribution is small and the phase is largely unaffected, as the frequency approaches the resonant frequency however the re-emitted phase lags more and more until it becomes 180° out of phase and the wave is totally cancelled: the light has been absorbed. Approaching the resonant frequency from the higher frequency side the same situation occurs, except the the phase of the emitted wave leads the phase of the incident wave, this inverse frequency dependence being known as anomalous dispersion. The phase of a propagating wave and its attenuation, described by the index of refraction, $n(\tilde{\nu})$, and the extinction coefficient $k(\tilde{\nu})$, are related to the dielectric function through eq. (2.69), where the complex refractive index $\hat{n}(\tilde{\nu})$, from now on referred to just as the refractive index, is a complex number composed of the index of refraction as the real part and the index of absorption as the imaginary part. [58]

$$\hat{n}(\tilde{\nu})^2 = \mu\hat{\epsilon} \tag{2.67}$$

$$\hat{n}(\tilde{\nu}) \approx \sqrt{\epsilon(\tilde{\nu})} \tag{2.68}$$

$$\approx n(\tilde{\nu}) + i\kappa(\tilde{\nu}) \tag{2.69}$$

2.3.3.3 The Dielectric Constant for Conducting Media

When the dielectic constant of conducting materials such as metal are considered the effect of conductivity in the Maxwell equations must be accounted for. This can be readily

accomplished using a complex dielectric constant $\hat{\epsilon}$ (eq. (2.70)). [60] A consequence of this conductivity is much larger values of κ for metals than for dielectric media, for example at $2000\,\mathrm{cm}^{-1}$ $\hat{n}(\mathrm{Pt}) = 4.1064 + 19.838\mathrm{i}, |\hat{n}| = 20.2$ compared to $\hat{n}(\mathrm{Si}) = 3.4261 + 0\mathrm{i}, |\hat{n}| = 3.43$. [61, 62]

$$\hat{\epsilon} = \epsilon + \frac{\sigma}{i\omega\epsilon_0} \tag{2.70}$$

2.3.3.4 Kramers-Kronig Relation

The physical origin of the relationship between the attenuation of light propagating through a medium and its change in phase were introduced above. A mathematical description of the relationship between $n(\tilde{\nu})$ and $k(\tilde{\nu})$ is given by the Kramers-Kronig transformations (eq. (2.72)), where $\mathcal{P}$ indicates the principle value of the integral should be taken. To maintain this relationship in simulated spectra, it is usual to simulate the expected absorption index spectrum and from this compute the refractive index.

In general the Kramers-Kronig integral is not analytic and must be evaluated numerically. [63, 64] One method for doing this is to use the causal relationship between the absorption and change in phase. [63] To quote Peterson *et al.*:

> 'The full procedure is easily stated. To calculate the imaginary part of the frequency response from the real part, first, Fourier transform the real part to the time domain, second, invert algebraic signature for all negative times, and third, Fourier transform back to the frequency domain. The result will be the imaginary part of the frequency response.'

This approach enables the use of fast Fourier transform (FFT) routines, readily available in software such as Matlab, for computing the integral. The result of carrying out the subsequent FFTs on model data is shown in fig. 2.22. The calculations were carried out in Matlab based on code by Miloš Popović. [65]

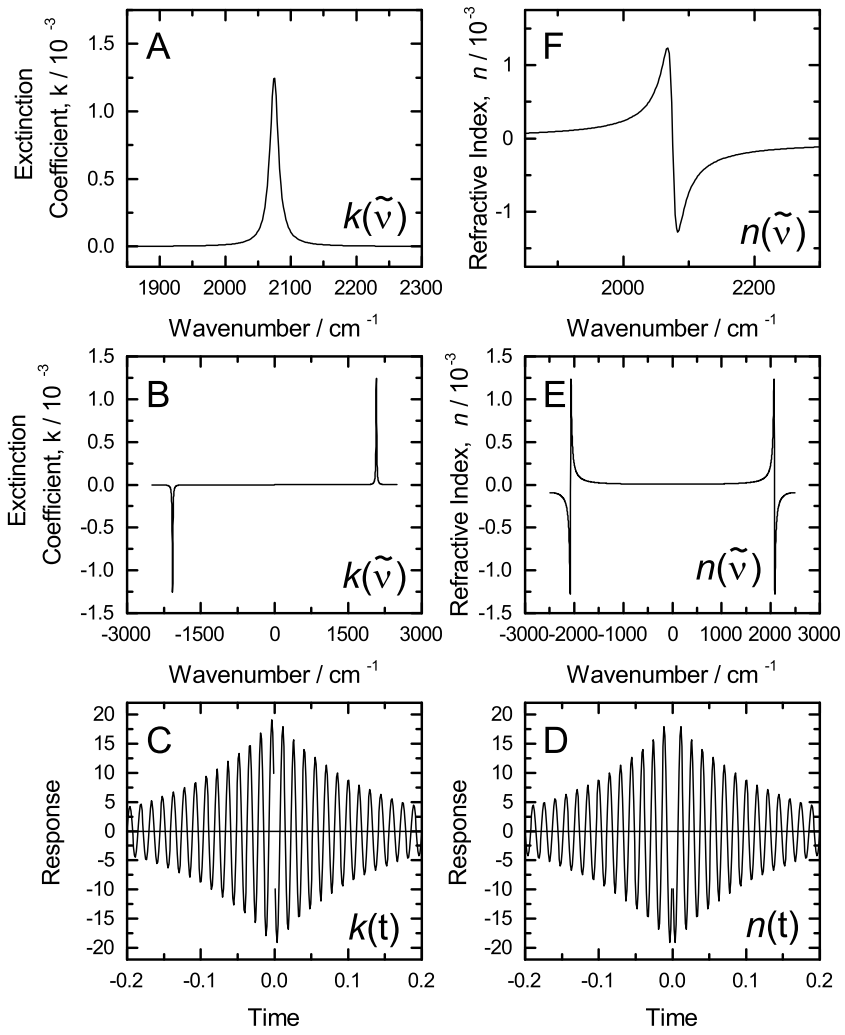

Figure 2.22: The double fast Fourier transform (FFT) method for computing the Kramers-Kronig transform. The extinction coefficient is fitted or modelled as a Lorentzian peak (A). The model is extrapolated to negative wavenumbers (B) and transformed using a FFT into the time domain (C, note only times close to 0 are shown). The function of time is made symmetric via multiplication by -1 for negative times (D). The second FFT then transforms the symmetric function back to the wavenumber domain (E) revealing the real part of the refractive index (F).

$$k(\tilde{\nu}) = \frac{f_j}{\tilde{\nu}_{0j}^2 - \tilde{\nu}^2 - i\tilde{\nu}\gamma_j} \tag{2.71}$$

$$n(\tilde{\nu}) = n_\infty + \frac{1}{\pi}\mathcal{P}\int_{-\infty}^{\infty} \frac{k(\tilde{\nu})d\,\tilde{\nu}}{(\tilde{\nu}_0 - \tilde{\nu})} \tag{2.72}$$

2.3.3.5 Transmission

With a function for the optical constants the effect of the material on incident light can be understood. A collimated beam of IR light propagating through a material can be modelled as plane wave, with oscillating orthogonal electric and magnetic components. [66] Considering just the electric field component (eq. (2.73)), it is characterised by a wave vector k, with magnitude $k = \lambda^{-1}$ also known as the wavenumber $\tilde{\nu}$, and amplitude $E(x,t)$, with magnitude E. The wavenumber is modified in the wave equation by the complex refractive index, $\hat{n}$, to account for the change in speed and amplitude of the wave in different media.

What is often desired from a spectrum is the wavenumber dependence of the extinction coefficient, $\kappa(\tilde{\nu})$, since this is characteristic of the medium and can be used to identify it. The extinction coefficient can be obtained as follows. The intensity of the electric field can be found from the square of the amplitude (eq. (2.74)). [66] The intensity is seen to decrease exponentially as a function of pathlength x through the material, known as Lambert's Law. To remove the dependence of the incident intensity the transmitted intensity is divided by the incident intensity to provide the transmittance, T (eq. (2.75)). The exponential dependence is removed by taking the logarithm of T and inverting the sign to give the absorbance, A (eq. (2.76)). Often the absorbance is sufficient for identification purposes, but for quantification the extinction coefficient can be obtained through division by the pathlength and wavenumber. [66]

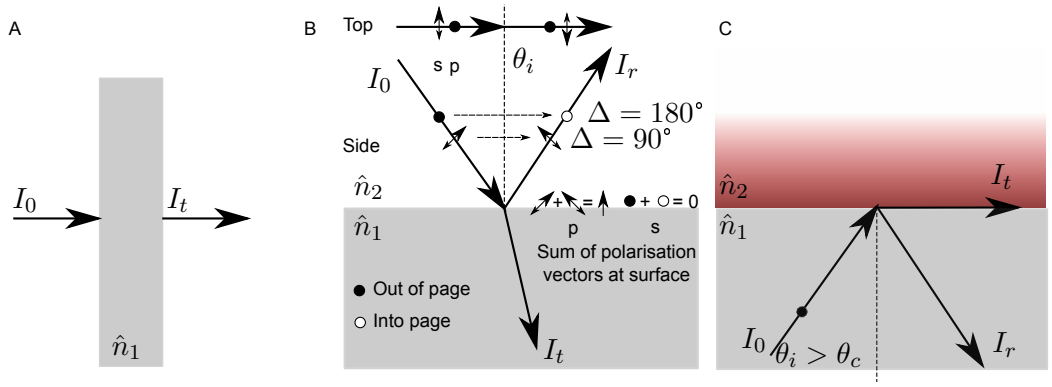

Figure 2.23: Optical geometries for obtaining transmission, external and internal reflection spectra. A: Transmission geometry. B: External reflection (light incident from $\hat{n}_2$). I_0, I_r and I_t are the incident, reflected and transmitted intensities, respectively. θ_i is the angle of incidence. Polarisation of the incident light relative to the plane if incidence is shown as s (*senkrecht*, or perpendicular) and p (parallel). The two polarisation undergo difference changes in phase on reflection, with the change in s-polarised light around 180° at all θ_i, whereas the change in phase of p-polarised light varies with θ_i, reaching $\sim 87°$ at grazing incidence. [67] C: Internal reflection (light incident from $\hat{n}_1$). When $\theta_i > \theta_c$ the reflection is total.

$$E = E_0 \exp[2\pi i \hat{n}(\tilde{\nu})\tilde{\nu}x - i\omega t] \tag{2.73}$$

$$I = E^2 = I_0 \exp[-4\pi\kappa(\tilde{\nu})\tilde{\nu}x] \tag{2.74}$$

$$T = \frac{I}{I_0} = \exp[-4\pi\kappa(\tilde{\nu})\tilde{\nu}x] \tag{2.75}$$

$$A = -\log_{10}(T) = 4\pi\kappa(\tilde{\nu})\tilde{\nu}x \cdot \log_{10}(e) \tag{2.76}$$

$$\kappa(\tilde{\nu}) = \frac{A}{-4\pi\tilde{\nu}x \cdot \log_{10}(e)} \tag{2.77}$$

2.3.3.6 Reflection

In cases where it is not possible to measure transmitted light the reflected light can be used as it also contains information about $k(\tilde{\nu})$, even if indirectly via $n(\tilde{\nu})$. The fractions of incident light reflected at an interface, the Fresnel coefficients, r_s and r_p, are obtained

for the two polarisations s and p, by considering that the magnetic or electric components, respectively, of the wave must be continuous across the interface and are known as the Fresnel equations (eq. (2.78), fig. 2.23). [66] The reflectivity is dependent on the complex refractive indices of the two media and on the angle of incidence, θ_i. To obtain the intensity the square modulus is again taken to give the reflectance R. This quantity can also be converted into absorbance A to obtain a linear dependence on $k(\tilde{\nu})$.

$$r_s(\tilde{\nu}) = \frac{E_r(\tilde{\nu})}{E_i(\tilde{\nu})} = \frac{\cos\theta_i - \sqrt{\hat{n}_{21}(\tilde{\nu})^2 - \sin^2\theta_i}}{\cos\theta_i + \sqrt{\hat{n}_{21}(\tilde{\nu})^2 - \sin^2\theta_i}} \tag{2.78}$$

$$r_p(\tilde{\nu}) = \frac{E_r(\tilde{\nu})}{E_i(\tilde{\nu})} = \frac{-\hat{n}_{21}(\tilde{\nu})^2\cos\theta_i + \sqrt{\hat{n}_{21}(\tilde{\nu})^2 - \sin^2\theta_i}}{\hat{n}_{21}(\tilde{\nu})^2\cos\theta_i + \sqrt{\hat{n}_{21}(\tilde{\nu})^2 - \sin^2\theta_i}} \tag{2.79}$$

$$\hat{n}_{21}(\tilde{\nu}) \equiv \frac{\hat{n}_2(\tilde{\nu})}{\hat{n}_1(\tilde{\nu})} \tag{2.80}$$

$$R = \frac{I}{I_0} = |r|^2 = rr* \tag{2.81}$$

At angles greater than a certain critical angle (eq. (2.82)), the fractions in eq. (2.78) become equal and the reflection coefficient becomes unity; this phenomenon is known as total internal reflection (fig. 2.23C). To understand the nature of the light at the interface the form of the transmitted wave is sought. The tangential and normal components of k_t are written down in terms of the poorly-defined angle of transmission, and then re-written in terms of the well-defined angle of incidence using Snell's law. Insertion of this form of k into eq. (2.73) provides the transmitted wave eq. (2.83). It can be seen that the term in x is of the form $\exp^{i\pi}$, and so is a propagating wave composed of sines and cosines. The term in z, the coordinate normal to the interface, however does not contain i and therefore is not composed of sines and cosines and does not explicitly propagate along this axis, it simply decays away into it. This wave is known as an evanescent wave (illustrated by red shading in fig. 2.23C). The distance at which the amplitude of this wave has reached $1/e$

is defined as the penetration depth, d_p (eq. (2.84)).

$$\theta_c = \sin^{-1} \frac{\hat{n}_1}{\hat{n}_2} \tag{2.82}$$

$$E = E_0 \exp[2\pi n i k_x \sin\theta_i - i\omega t] \exp -2\pi k_z z \sqrt{n_i^2 \sin^2\theta_i - n_t^2} \tag{2.83}$$

$$d_p(z = e^{-1}) = \frac{1}{2\pi k_z \sqrt{n_i^2 \sin^2\theta_i - n_t^2}} = \frac{\lambda}{2\pi \sqrt{n_i^2 \sin^2\theta_i - n_t^2}} \tag{2.84}$$

2.3.3.7 Effective Medium Theories

The behaviour of light at the interface between two pure phases was introduced above, however the interface under investigation in this thesis is not between two pure phases but rather between a pure phase (silicon) and a complex mixed phase (catalyst layer in solution). The mixed phase contains contributions from two distinct solid inclusions, one metallic (platinum) and one semi-metallic (carbon), a solvent (water), a reactant (formic acid), dissolved product (carbon dioxide) and any intermediates (adsorbed or dissolved) in the reaction. The behaviour of light in mixed, *dielectric*, (*i.e.* non-conducting) media can be considered using effective medium theories. These theories attempt to model the scattering of light based on the polarisation of two distinct phases in close proximity. The much greater polarisability of conducting media means these are considered separately.

The effective medium approximation assumes that the dielectric function of a mixture of two phases can be represented as the dielectric function of one effective phase, such that the two are indistinguishable on the length scale of the light used. To generate the effective dielectric function, Mie theory is used to analyse the scattering interactions between the two phases which shows how to combine the two dielectric functions. [68] The earliest theories were from Maxwell-Garnett (1904, eq. (2.85)) and Bruggeman (1935, eq. (2.86)). [68]

In the Maxwell-Garnett model the material is considered to have a separated-grain

structure, with grains of phase A (dielectric function ϵ_A) filling a total fraction f of the material but being well separated by medium B (dielectric function ϵ_B) which takes up the remaining volume $1-f$. In comparison, the Bruggeman theory deals with an aggregate structure, where the material is composed of two grains A and B with relative fractions f and $1-f$, respectively. The suitability of these models for describing porous or nano-strucutured materials is questionable, however; while both theories be used to fit the measured dielectric functions of such materials, the fitted parameters in the two cases are often completely different. [69] More detailed theories have emerged that take into account the porosity of the material, such as the Bergmanan effective medium theory. [69,70] In this theory the combination of the dielectric functions for the two components is parametrised using a new function known as the 'spectral density', $g(f,n)$. The spectral density is a function of both the volume fraction f and a material parameter n which encapsulates the topology of the system. Special significance is attached to $n=0$, which represents the percolation threshold, the point at which bulk connectivity between particles is achieved.

$$\frac{\epsilon_{MG}-\epsilon_B}{\epsilon_{MG}+2\epsilon_B} = f\frac{\epsilon_A-\epsilon_B}{\epsilon_A+2\epsilon_B} \tag{2.85}$$

$$f\frac{\epsilon_A-\epsilon_{Br}}{\epsilon_A+2\epsilon_{Br}} + (1-f)\frac{\epsilon_B-\epsilon_{Br}}{\epsilon_B+2\epsilon_{Br}} = 0 \tag{2.86}$$

$$\epsilon = \epsilon_M\left(1 - f\int_0^1 \frac{g(u,f)}{\epsilon_m/(\epsilon_m-\epsilon)-u}\,du\right) \tag{2.87}$$

2.3.4 Electric Fields at Conducting Surfaces

In terms of spectroscopy the component of most significance is the Pt particles, since they contain significant amounts of mobile electrons. This mobile charge can interact with incident radiation extremely strongly; although there is no absorption peak in the mid-IR region, this interaction is responsible for the relatively high values of platinum's refractive index and makes Pt a good reflector of IR light. This interaction is also sufficient to

modify the electric field of incident light at the surface of Pt which, as will be discussed, has significant implications for spectroscopy. Furthermore, the platinum's mobile electrons can interact with adsorbed molecules extremely well, responding to molecular dipoles in both a constructive and destructive manner, as well as facilitating electronic communication between adsorbates. These phenomena will be introduced briefly in the following sections.

At equilibrium there can be no electric field inside a perfect conductor, otherwise the mobile charge in the conductor would be in motion and equilibrium would not be obtained. To achieve a zero electric field inside the conductor, all mobile charge migrates to the surface in an arrangement that produces zero internal electric field. [71] Under these conditions the electric field at the surface must be entirely normal to the surface. [71]

When a molecule adsorbs formation of bond means either the adsorbate is charged, and the interaction is electrostatic, or that some charge transfer occurs to form a covalent bond in which case a dipole is formed. In either case, this new charge at the surface will induce a redistribution of the metal's own charge and establish a new induced electric field. This induced dipole is constant with time and is known as the static dipole. [54] If the adsorbate is a molecule, then vibration of the molecule may periodically change the molecule's dipole, and therefore also the induced electric field. This is time-dependent dipole is known as the dynamic dipole. [54]

In general, the task of calculating the charge distribution induced in a conductor is non-trivial, however use can be made of the uniqueness theorem which says that there exists only one unique solution to the Laplace equation[1] for a given volume in which the boundary conditions are known. [71] In the case of a grounded conducting plane, in which the potential of the plane is zero and the potential tends to zero at infinity, the electric field of the charge distribution induced in the metal by the molecular dipole is exactly the same as the electric field produced by a dipole positioned as the mirror image of the

[1]The Laplace equation is used to determine the electric field arising from point charges in a region without its own charge. [71]

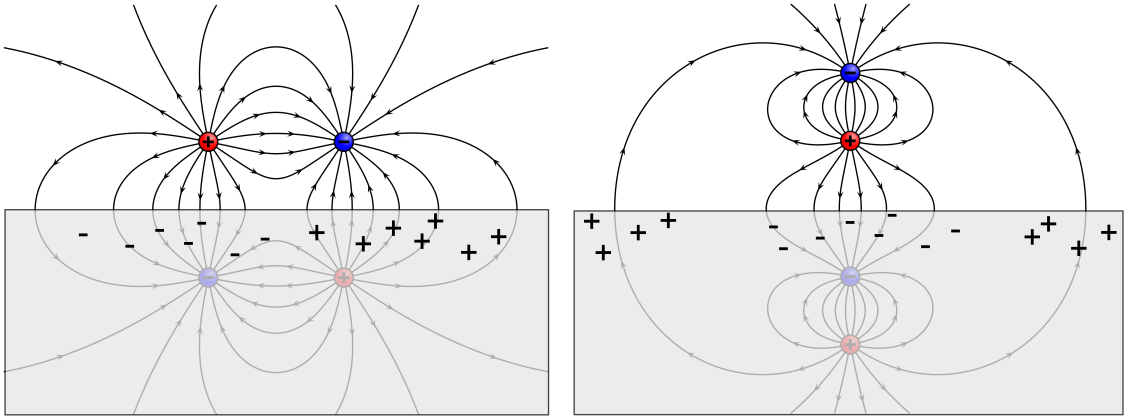

Figure 2.24: The electric field at a metal surface in the presence of a dipole. The field is the sum of that due to the molecular dipole, shown above the surface, and that due to the redistributed surface charge (shown on the figure as + and -), more easily visualised as the hypothetical image dipole, shown inside the metal.

molecular dipole (fig. 2.24). [71]

2.3.4.1 Surface Selection Rule

It can be seen that the image charge introduced above will act to cancel the dipole of an adsorbate if the dipole is oriented parallel to the surface, but enhance the dipole if it is perpendicular to the surface. On the length scale of IR light this effect means that dipoles parallel to the surface do not interact with incident light, whereas the interaction with dipoles perpendicular to the surface is enhanced. This effect is known as the 'surface selection rule' (SSR). [72–74]

In this thesis the metal surfaces of interest are closer to spherical, and definitely not planar, and so the conclusions based on the charge distribution considered in fig. 2.24, such as the SSR, cannot be used directly. In fact, the method of images is only applicable if a simpler arrangement of charges can be found that meets the same boundary conditions. In general such simpler arrangements are not known, however, an alternative view of the SSR is to consider the form of the electric field of the *incident radiation* at the surface of the metal, and then consider if the adsorbate dipole could be excited. [74]

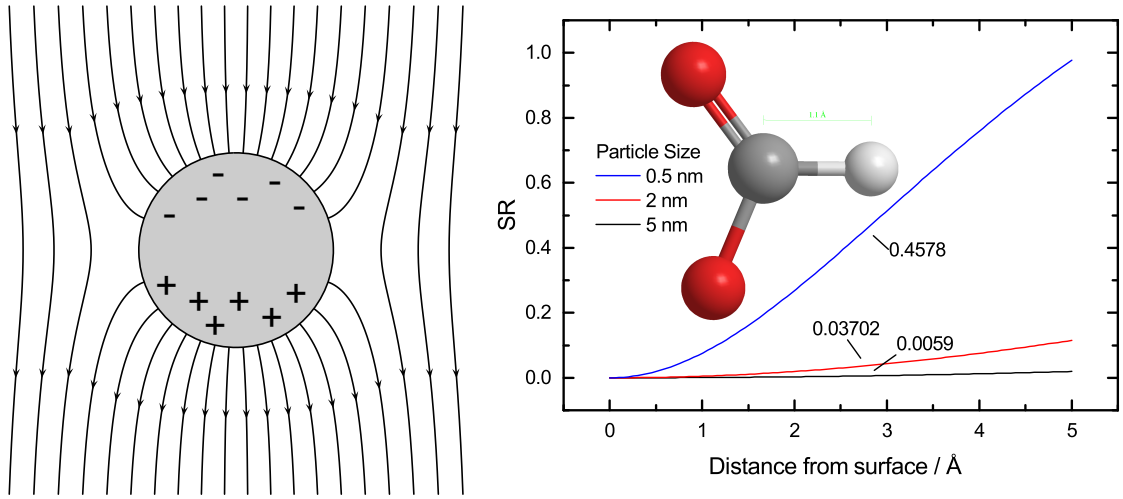

(A) (B)

Figure 2.25: (a) The electric field at a curved metal surface in the presence of an incident electromagnetic field. (b) The surface ratio (SR), the ratio of normal and tangential electric field intensities, as a function of distance from the metal surface. The SR was calculated for spheres of diameter 0.5 nm, 2 nm and 5 nm. A scale model of HCOO, a typical adsorbate, is included for reference.

A mathematical description of the electric field at the surface of a conducting sphere in the presence of a time-varying incident electromagentic wave is also complicated, however in the limit that the particle size (r_0) is much smaller than the wavelength of light, $r_0 \ll \lambda$, and the limit $|\tilde{n}|r_0 \ll \lambda$, the electric field around the sphere reduces to that of the sphere in a static field (fig. 2.25A). [74]

The potential at a position r, θ away from a conducting sphere of radius r_0 and refractive index $\tilde{n}$ is given by [74]

$$V(r,\theta) = E_0 \left[r - \left(\frac{\tilde{n}^2 - 1}{\tilde{n}^2 + 2} \right) \frac{r_0^3}{r^2} \right] \cos\theta \tag{2.88}$$

Differentiation of the potential and averaging over the whole surface yields the electric fields normal and tangential at a distance d from the surface, from which the 'surface

ratio' (SR), the ratio of tangential to normal electric field intensity, can be derived.

$$SR = \frac{\bar{E}_t^2}{\bar{E}_n^2} = 2\left|\frac{1-\left(\frac{\tilde{n}^2-1}{\tilde{n}^2+2}\right)\left(\frac{r_0}{r_0+d}\right)^3}{1+2\left(\frac{\tilde{n}^2-1}{\tilde{n}^2+2}\right)\left(\frac{r_0}{r_0+d}\right)^3}\right|^2 \tag{2.89}$$

The surface ratio can then be determined for different particle sizes at various distances form the particles. Calculated surface ratios for 0.5 nm, 2 nm and 5 nm particles are shown in fig. 2.25B, along with a scale model of a HCOO, a typical adsorbate considered in this thesis. It can be seen that for small particle sizes the surface ratio increases dramatically, such that at around 0.2 nm from the surface, where a typical adsorbate may lie, the ratio of tangential to normal electric field intensities is around 0.25. Furthermore, when Greenler *et al.* added some quantum corrections to their model, the values of the SR increased by over 100% in some cases. For example, at 0.2 nm from a 0.6 nm particle the SR was calculated to increase from 0.2 in the classical model to 0.53 with a fully self-consistent quantum calculation. [74]. This suggests that at small particles there *is* expected to be an appreciable tangential component to the electric field and as a result vibrations tangential to the surface are able to be excited.

2.3.4.2 Infrared Spectra of Rough Metal Surfaces: Enhanced IR Absorption and Distorted Peak Shapes

There exists several differences between IR spectra of species at rough metal surfaces and those of species at smooth metal surfaces. The first difference is that absorbance of the species appears to be much larger when measured on rough metal surfaces than when measured on smooth surfaces, even when the larger amount of species present at rough surfaces is taken into account. This was first reported by Harstein *et al.*, who observed that the IR absorption of a monolayer of 4-nitrobenzoic acid prepared on a silicon IRE increased as sequentially thicker layers of Ag were vacuum deposited onto the monolayer. [75] This

effect became known as surface enhanced IR absorption (SEIRA).

The second difference is that the spectra often show negative absorption for either part (bipolar peak), or all (inverted peak) of the peak envelope. Lu *et al.* first reported anomalous spectra of CO on Pt particles deposited on glassy carbon substrates. [76] They also observed that the IR absorption appeared to be enhanced over that expected, suggesting a common origin for the two phenomena.

The origin of the SEIRA effect was originally attributed to "an electric field enhancement due to collective electron resonances associated with the small islands of metal deposited on the samples".[2] [75] The insensitivity of the enhancement factor to the chemical identity of the monolayer favoured this electromagnetic mechanism over the alternative chemical mechanism, in which changes to a molecule's electronic structure on adsorption increase its absorption of IR light, for example by increasing the transition dipole moment.

Following these reports the SEIRA phenomenon has been used extensively to allow spectroscopic investigation of metal surfaces, with the study of electrode surfaces in situ being particularly well established (see the review in [77] and references therein). Much less attention has been paid to explaining the phenomenon, however, although several models for the observed peak shapes have been proposed, incorporating varying degrees of complexity.

In general the approach has been to simulate the dielectric constant of the rough metal particle/adsorbate layer using an effective medium theory (EMT). The complexity of the approaches used vary from using the Bruggeman EMT directly, where one component is metal and the other is the adsorbate, [78] to using an EMT based on concentric spheroid shells to represent adsorbate covering metal particles of different shapes. [79, 80]

The simplest model reported to explain the inverted peak shapes and SEIRA was that by Su et al. [78] Their study utilised a 3 layer, Pt/porous Pt/solution, model with fraction

[2]Island formation is characteristic of films formed by the vacuum deposition

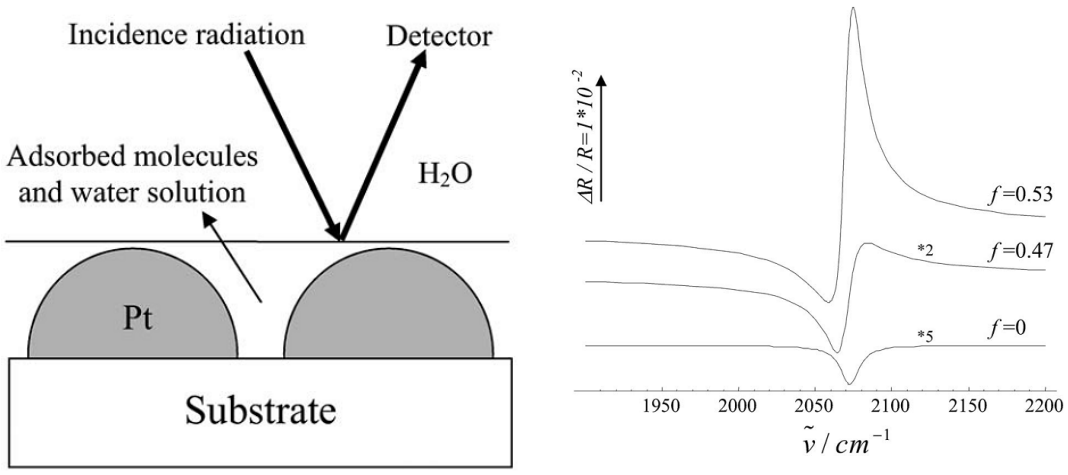

(A) (B)

Figure 2.26: The model of Su *et al.* (a) The model geometry. (b) Spectra simulated using the model. The parameter f is the volume fraction of Pt in the effective medium. Reproduced from reference [78]. Copyright 2008 AIP Publishing LLC.

f of Pt in a middle layer of thickness d_{eff} (fig. 2.26A). The Bruggeman effective medium theory was used to examine the the effect that d_{eff} and f had on the appearance of spectra obtained by external reflection. They observed that the shape of the CO peak and the intensity depended on both f and d_{eff}, although f mainly controlled the shape and d_{eff} the intensity (fig. 2.26B).

A much more complex model was used by Osawa *et al.* to account for SEIRA. [79, 81] Their model was based on earlier work of optical absorption by dyes adsorbed on Ag films. [82] The sophistication, and resulting complexity, of the model arises from the use of concentric oblate spheroids to represent the adsorbate-covered metal particles (fig. 2.27). A spheroid of dielectric function ϵ_1, with long axis a and short axes $b = c$ represents the metal. To account for the adsorbate the spheroid is surrounded by a shell of a second medium, with dielectric function ϵ_2. The dielectric function for such a system has been derived, and to some degree enables the effect of particle shape on the spectrum to be investigated. In this case the origin of the shape-dependence arises from the variation in charge density with the curvature of the surface, with more tightly curved regions of the

surface permitting a greater charge density and therefore a larger polarisability. This is included in the model via the depolarisation factors, which describe how the charge is distributed according to shape, for the long (L_1) and short (L_2) axes in eq. (2.90). [79]

$$\alpha_{\perp,\parallel} = \frac{(\epsilon_2 - 1)[\epsilon_1 L_1 + \epsilon_2(1 - L_1)] + Q(\epsilon_1 - \epsilon_2)[\epsilon_2(1 - L_2) + L_2]}{[\epsilon_2 L_2 + (1 - L_2)][\epsilon_1 L_1 + \epsilon_2(1 - L_1)] + Q(\epsilon_1 - \epsilon_2)(\epsilon_2 - 1)L_2(1 - L_2)_{\perp,\parallel}} \tag{2.90}$$

The effective dielectric constant for the coated particle is calculated by considering the polarisation p of the particles (of volume V) in the presence of the an incident electric field E (eqs. (2.90) to (2.91)). [79] The particle is then treated in the framework of the Maxwell-Garnet effective medium theory (eq. (2.85)) by considering the coated particles to be embedded in a host material ϵ_h, with the particles occupying a fraction F of the total volume.

$$p = \alpha V E \tag{2.91}$$

Values for the dielectric functions of the individual components were obtained using the Drude model for the metal (eq. (2.92)), a Lorentzian oscillator for the adsorbate (eq. (2.71)) and a value of 1.5 for the host medium.

$$\epsilon_1(\omega) = 1 - \frac{\omega_p^2}{\omega(\omega + i/\tau)} \tag{2.92}$$

It can be seen from the ϵ^2 and $\epsilon_1\epsilon_2$ terms in eq. (2.90) that the overall polarisability of the coated particles α is enhanced above that expected by either component alone. The polarisability is also strongly affected by the shape of the particle, with long, thin particles enhancing the polarisation in the direction of their long axis while decreasing it perpendicular to this axis. The distance over which the field enhancement can occur falls of as the cube of distance, confining this effect to species in close proximity to the particles. [79]

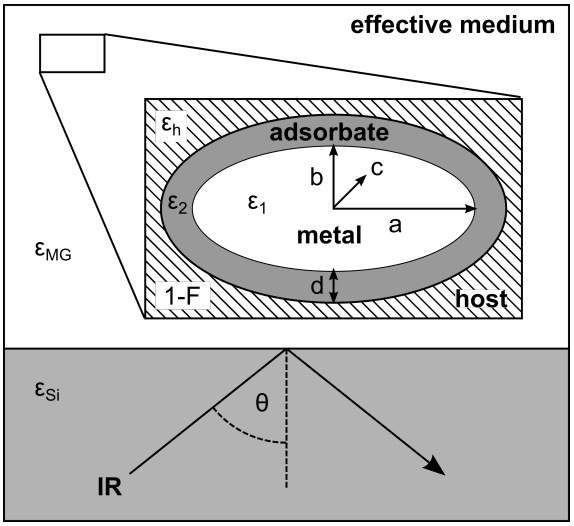

Figure 2.27: The parameters used in Osawa's model of SEIRA. An oblate metal particle with dielectric function ϵ_1 and dimensions a and $b = c$, surrounded by an adsorbate shell with dielectric function ϵ_2 and thickness d, is embedded in a host medium with dielectric function ϵ_h and volume fraction $1-F$. In the effective medium approximation the effective dielectric constant of an array of unit cells is identical to the dielectric constant of an effective medium with dielectric constant ϵ_{MG}. This effective medium sits on top of a silicon crystal, dielectric constant ϵ_{Si}. The IR beam is incident at an angle of θ degrees.

A similar physical model, based on concentric spheroids, was used by Pecharromán *et al.* to explain both the observed distortion of IR peaks and the enhancement in their intensity. [80,83] A different mathematical approach to obtaining the spectrum was taken, however, as it was the change Δ in dielectric function on adsorption of a species, rather than its absolute value, that was modelled. This enabled the reflectance spectrum to be obtained directly. In the model the metal particles were again modelled as spheroids, this time coated in an anisotropic adsorbate. Again the polarisation of the particles, and the depolarisation due to the adsorbate, are calculated in the three dimensions from the fill factor and the depolarisation factors. The model is then simplified by considering spherical particles, with thin, isotropic adsorbate layers. The combined dielectric function is given by the linear combination of the host medium and adsorbate/particle dielectric functions, weighted by the volume fraction. When the effect of volume fraction on the

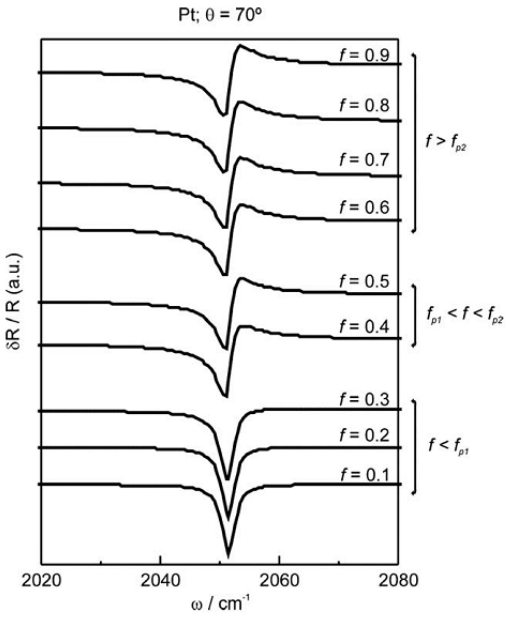

Figure 2.28: The model of Percharroman *et al.* The parameter f is the volume fraction of the effective particle/adsorbate medium in the background medium. Reprinted from from reference [80], Copyright 2004, with permission from Elsevier.

reflection peak shape was investigated, it was observed that only the volume fraction, not particle size, affected the peak shape, with the shape becoming more bipolar as the value of f increased (fig. 2.28).

A similar enhancement factor (≈ 20) is obtained within the framework of the Bergman effective medium theory (fig. 2.29). [84] Since this approach relies on the less intuitive parameter spectral density it provides less insight into the origin of the enhancement. However, it does permit a correlation between the interparticle connectivity and the observed spectra. In this representation both the enhancement factor and the peak shape were controlled by the value of percolation strength, g_0, the value of the spectral density g when bulk conductivity is obtained. The percolation strength is understood as the extent of inter-particle connectivity, and as such is related to the conductivity σ of the material by $\sigma = f g_0 \sigma_0$, where σ_0 is the conductivity of bulk platinum. This apparent dependence on the connectivity is probably more related to the proximity of the metal islands, however, since it is in the small gaps between multiple particles where the electric field is strongest.

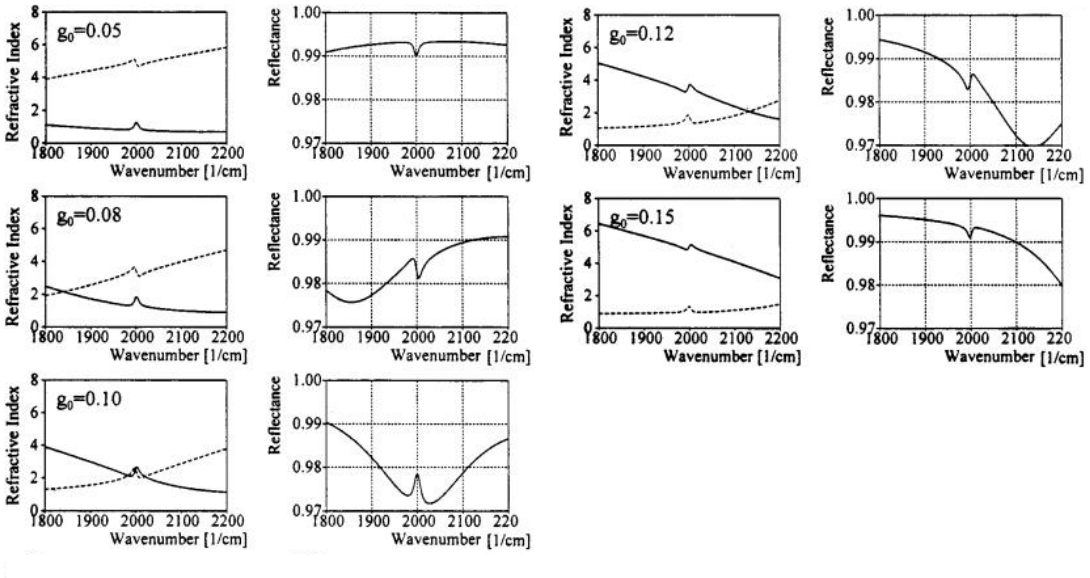

Figure 2.29: The model of Bjerke *et al.* Here g_0 is the spectral density at the volume fraction when bulk conductivity is first obtained. Reprinted with permission from reference [84]. Copyright 1999 American Chemical Society.

The various models proposed to account for the phenomena of anomalous absorption and SEIRA all include the high value of the Pt refractive index as part of their explanation, although the exact procedure, and associated physical justification, for combining it with the indices of the other components differs. Furthermore, it appears that none of the theories have been used to fit experimental spectra, with a view to extracting peak parameters such as centre, width and height. This is not surprising given the mathematical complexity of some of the models, however such a fitting model is required if spectra of realistic catalyst films are to be analysed quantitatively. A much simpler, empirical model for the high refractive index of a film containing metal particles is therefore developed in Chapter 4 (section 4.3.2).

2.3.4.3 The Effect of Electrode Potential on Infrared Spectra

So far the electric fields discussed have arisen from the presence of an adsorbate dipole or from incident electromagnetic radiation, with additional induced fields arising as a result of the both. When the metal surface under consideration is an electrode, an additional

contribution to the local electric field arises from the electrical double layer. The charge distribution giving rise to this field is extremely localised, giving rise to very high electric field strengths on the order of $1 \times 10^9\,\mathrm{V\ m^{-1}}$. [85, 86] During an experiment the local electric field at the electrode can vary, both as a result of the change in adsorbate coverage (*vide infra*) and as a result of an externally applied voltage. The change in local electric field can significantly affect the bonding of adsorbates to the metal and the observed change in bond strength with externally applied potential is known as the Electrochemical Stark Effect [85–89] There are several mechanisms proposed for the Electrochemical Stark Effect, although in general they all relate to the effect the potential has on the filling of bonding and anti-bonding orbitals of the adsorbate. [85] Adsorbed CO is the most common example of Stark tuning with explanations based on the Blyholder model of CO adsorption (section 2.1.2.5). As the electrode potential increases and the metal becomes less electron rich back-donation from the metal into the anti-bonding $\pi*$ orbital decreases and the bond strength increases, causing an increase in $\tilde{\nu}$.

2.3.5 Adsorbate-Adsorbate Interactions

2.3.5.1 Coverage-Dependence of the Static Dipole

Molecules chemisorb to a surface by partially transferring charge to form a chemical bond. This charge transfer gives rise to additional polarisation and hence to an additional dipole moment, known as the static dipole. The synergistic nature of the Pt-CO bond makes the size of the static dipole moment strongly dependent on coverage. At high coverage the large number of charge transfers required will limit the amount of charge that can be transferred to/from each individual adsorbate, decreasing the static dipole moment. This manifests as a change in vibrational frequency with coverage. It can be separated from the effects of dipole-dipole coupling by diluting the adsorbates with an isotopomer, such that the dilute species will not couple to its isotopomeric neighbours due to the difference

in frequency, but will still have to share the available charge transfer with them. On Pt single crystals however this static dipole effect was negligible compared to the effect of dipole-dipole coupling. [90]

2.3.5.2 Dipole-Dipole Coupling

Coupling between oscillators is not limited to those interacting via chemical bonds, neighbouring oscillators can also interact via through-space dipole-dipole interactions. [91, 92] In this case the coupled vibrations are best discussed in terms of normal modes, as for the vibrations of polyatomic molecules (eq. (2.45)). As before, the normal modes can be found by solving the matrix equation eq. (2.93), where V is the potential energy for a system of N parallel dipoles located on a plane at location R_{ij}, oriented normal to this plane and interacting via through-space dipole-dipole forces, Q_i is the normal coordinate of mode i and μ_i is the dipole moment of the normal mode. [93] The first term on the right hand side represents the normal modes already found for the molecular vibrations, the original uncoupled frequency being known as the singleton frequency $\tilde{\nu}_s$, and the second term on the right representing the additional contributions due to coupling.

$$2V = \sum_{i=1}^{N} \lambda_i Q_i^2 + 2 \sum_{i>j=1}^{N} \frac{Q_i Q_j}{R_{ij}} \left(\frac{\partial \mu_i}{\partial Q_i}\right) \left(\frac{\partial \mu_j}{\partial Q_j}\right) \tag{2.93}$$

Applying this model to an adsorbed molecule coupled to its $N-1$ neighbours, solution of the secular equation gives

$$\tilde{\nu} = \tilde{\nu}' + \frac{1}{L^3} \left(\frac{\partial \mu}{\partial Q}\right)^2 \sum_{j=2} \frac{L^3}{r_{ij}^3} \tag{2.94}$$

where $\tilde{\nu}'$ is the wavenumber of the uncoupled, singleton normal mode and L is an arbitrary nearest neighbour distance. In the case where the adsorbed molecule has a different frequency to its neighbours, but the same force constant, solution of the secular equation

provides two IR active modes. [94]

$$\tilde{\nu} = \tilde{\nu}'_1 + \left(\frac{1}{L^6} \left(\frac{\partial \mu}{\partial Q} \right)^4 \sum_{j=2} \frac{L^6}{r_{ij}^6} \right) / (\tilde{\nu}'_1 - \tilde{\nu}'_2) \tag{2.95}$$

$$\tilde{\nu} = \tilde{\nu}'_2 - \left(\frac{1}{L^6} \left(\frac{\partial \mu}{\partial Q} \right)^4 \sum_{j=2} \frac{L^6}{r_{ij}^6} \right) / (\tilde{\nu}'_1 - \tilde{\nu}'_2) \tag{2.96}$$

A more sophisticated model was introduced by Hammaker, Francis and Eischens to take into account the polarisation of the metal by the dipoles. [94] By including the effect of the metal polarisation, the effect of the dipole's own image charge, and the images of the surrounding dipoles, on the overall dipole moment can be taken into account. In general the effect is to lower the potential energy of the system, decreasing the total dipole moment.

A simple example illustrates some of the features of dipole-dipole coupling. Figure 2.30 shows the 2 IR active normal modes for a system of 7 CO molecules on the (111) surface. One CO is on a linear site, its dipole moment represented by a red arrow, and is surrounded by 6 molecules on bridging sites, their dipole moments represented as green arrows. The wavenumber of linear CO molecules is higher than that of bridging molecules, as is found experimentally. The dipole of the central CO can couple to the surrounding dipoles in two IR active combinations: the in phase mode has all dipole moving in phase, with the 6 bridging CO dipoles changing slightly and the linear CO dipole changing considerably, while the anti-phase mode has the linear CO dipole out of phase with the bridging CO dipoles, and much smaller individual motions.

In the in phase mode, the linear CO dipole has the largest coefficient and its wavenumber therefore contributes most to the wavenumber of the normal mode. Conversely, in the anti-phase mode all the coefficients are small and so it is the wavenumber of the bridging CO dipoles, as the most prevalent species, which dominate the wavenumber. Furthermore, because the in phase mode has the largest total dipole moment, it has the greatest

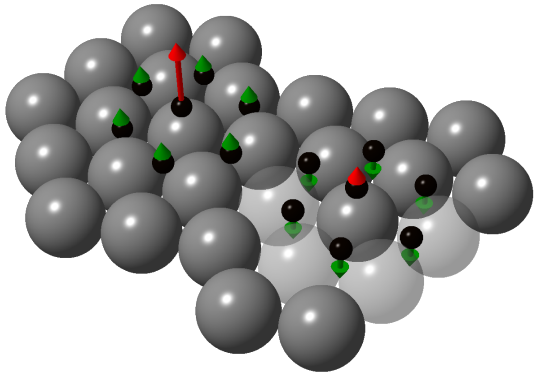

Figure 2.30: Normal modes arising from dipole-dipole coupling of adsorbed oscillators. The two normal modes for a system of 7 coupled oscillators are shown, using arrows to represent the species' dipoles. In this system one species is adsorbed on a linear site (red arrow), and is surrounded by 6 nearest neighbours on bridging sites (green arrows). Note that some surface atoms have been made transparent for clarity.

intensity in the spectrum, while the opposing directions of the linear and bridging dipoles in the anti-phase mode lead to a weaker intensity.

Dipole coupling has far reaching implications for the interpretation of IR spectra of adsorbed species. The previous example demonstrated that the wavenumber and intensity of absorption peaks is a collective property of the adlayer, and cannot be easily assigned to individual species; in the previous example the largest intensity peak had a wavenumber close to that of the central dipole, yet the central species only constituted 1/7 of the adlayer, while conversely the peak closest to the wavenumber of the majority species is the weaker of the two.

Larger scale simulations have been carried out using the model described above. Figure 2.31A shows the effect that changing the CO coverage has on the simulated spectra. [95] The intensity and position of each normal mode contributing to the spectrum is shown as a bar on the spectrum. The spectra were calculated by summing Lorentzian curves generated from each position and intensity, assuming a constant full width half maximum of $7\,\mathrm{cm}^{-1}$. It can be seen how at extremes of coverage the spectra are dominated by

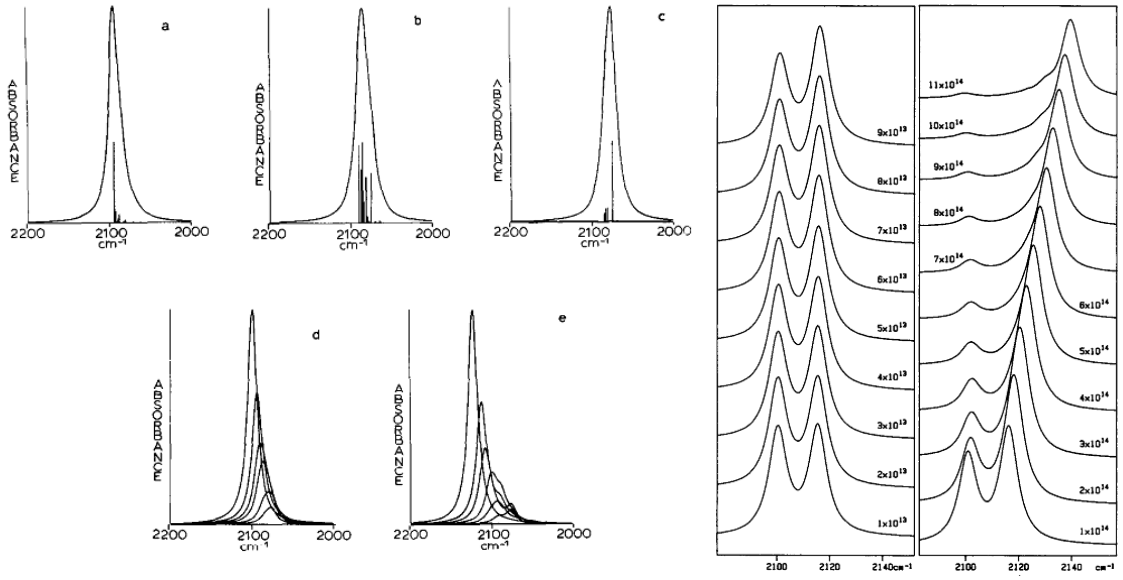

(A) (B)

Figure 2.31: Simulated spectra involving coupled adlayers. A: Spectra of CO on the (100) fcc face calculated for coverages of 0.69, 0.39 and 0.1 (panels a-c). Overlaid spectra at coverages of 0.1, 0.21, 0.39, 0.51, 0.69 and 1.0, scaled according to coverage and calculated with coupling constant $f = 0.1\,\mathrm{Ncm}^{-1}$ (panel d) and $f = 0.2\,\mathrm{Ncm}^{-1}$ (panel e). Reprinted from reference [95]. Copyright 1978, with permission from Elsevier. B: Spectra simulated for different random coverages of equimolar amounts of two CO species with singleton frequencies of $2100\,\mathrm{cm}^{-1}$ and $2115\,\mathrm{cm}^{-1}$. The coverage of each spectrum is shown on the figure. Note the reversed direction of the wavenumber axis. Reprinted from reference [91]. Copyright 1992, with permission from Elsevier.

individual normal modes, while at intermediate coverages each mode tends to contribute, leading to inhomogeneous broadening.

The effect on the spectra where two distinct oscillators are involved can be seen in fig. 2.31B. At low coverage the two oscillators are easily discerned and appear at their singleton frequencies. As the coverage increases the higher wavenumber peak appears to both increase in intensity and shift to higher wavenumber, while the lower wavenumber peak decreases in intensity while remaining in the same position. At the highest coverage the low wavenumber peak is almost invisible.

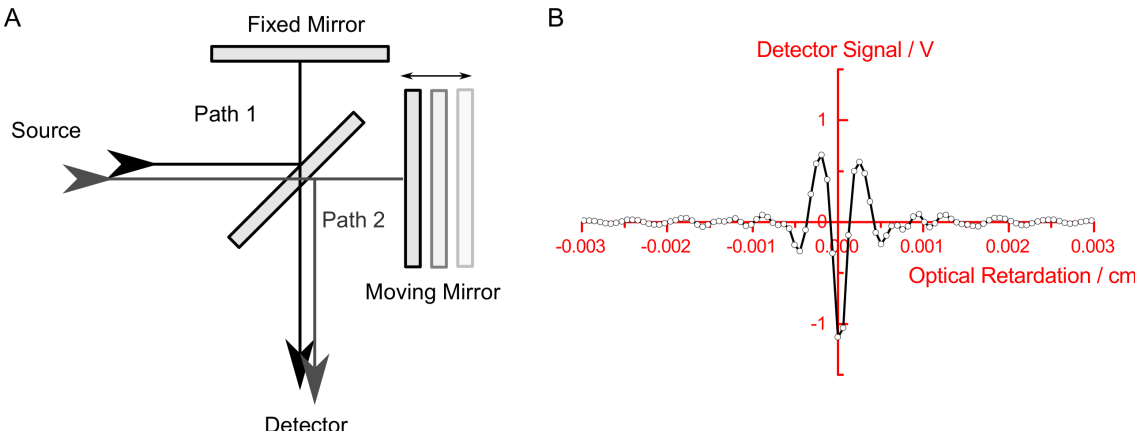

Figure 2.32: Recording an interferogram. A: The optical path in a Michaelson interferometer. Paths 1 and 2 represent the reflected then transmitted beam, and the transmitted then reflected beam, respectively. They paths are offset for clarity. B: An interferogram at small values of optical retardation.

2.3.6 Fourier Transform Infrared (FTIR) Spectroscopy

In conventional spectrometers a light source is monochromated, interacts with a sample and is then detected. A plot of the observed light intensity as a function of wavelength provides the spectrum. An alternative method for measuring a spectrum is to use interferometry. Here a polychromatic beam of light is split into two paths by a beamsplitter, each hitting a mirror at normal incidence before returning to the beamsplitter and recombining (fig. 2.32A). Where the optical path length of the two beams is identical the two beams remain in phase over all wavelengths and constructively interfere. When the resulting intensity is measured it is found to be equal to the incident intensity. The optical path length of one of the beams can be varied by moving its mirror further away from the beamsplitter, creating an optical path difference or retardation. In this case when the beams recombine at the beamsplitter they are no longer in phase, with wavelengths equal to half the optical retardation completely cancelled and the resulting measured intensity being much lower. A plot of the intensity as a function of optical retardation is known as an interferogram (fig. 2.32)B.

Modern FTIR spectrometers have rapidly moving mirrors enabling a wide range of

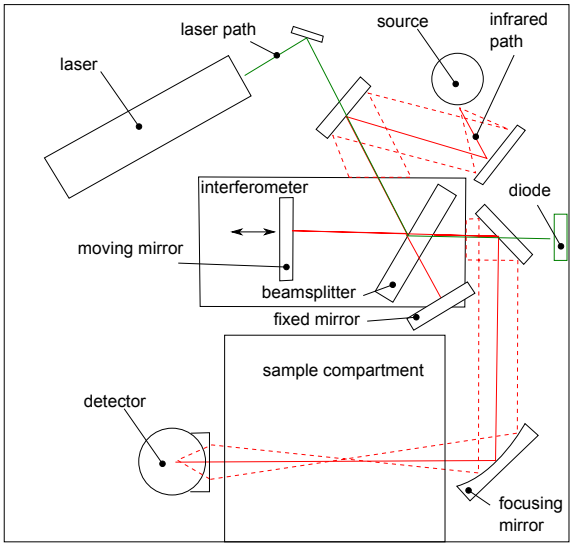

Figure 2.33: Optical layout of a typical Fourier transform IR spectrometer.

retardations to be sampled in a short amount of time. To plot the interferogram the optical retardation must be known accurately however. This is accomplished by also passing light from a well defined, monochromatic light source, commonly a HeNe laser, through the interferometer (fig. 2.33). Modulation of the laser light by the interferometer is detected by a photodiode. Since the wavelength of the laser is known, points of zero intensity detected by the diode provide an accurate trigger for the detector to sample the IR intensity.

Sampling can occur at every zero crossing, or less frequently, known as undersampling; commonly an undersampling ratio of 2 is used. The zero crossing frequency is directly related to the speed of the moving mirror, and so the mirror speed is often reported in the equivalent laser modulation frequency. Choice of mirror speed is determined by the response time of the IR detector. The most common high sensitivity detector used in the IR is a HgCdTe detector, which can operate at frequencies up to 1 MHz, beyond the limitations of commonly available analogue-digital converters. The main limitation on mirror speed is therefore the signal to noise ratio, SNR given by eq. (2.97). Here $U(T)$ is the brightness of the source, Θ is the throughput, $\Delta\tilde{\nu}$ is the resolution, t is the measurement time; ξ, the detector efficiency and NEP, the noise equivalent power are

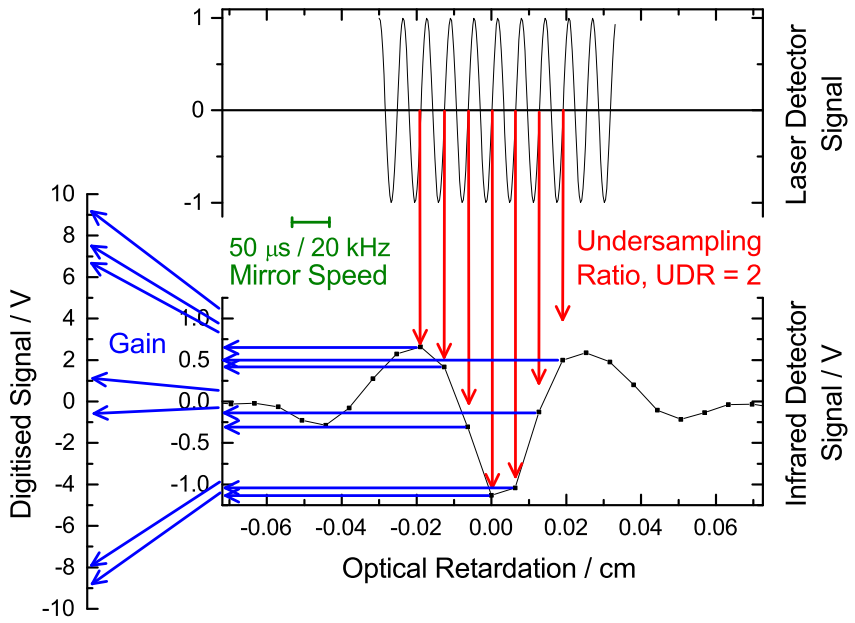

Figure 2.34: Sampling an interferogram. The detector is triggered to record the intensity when the laser intensity crosses zero. Undersampling involves recording less frequently than at every zero-crossing. The frequency of the variation in laser intensity is controlled by the mirror velocity and is chosen to suit the response of the detector.

both properties of the detector. [67] It can be seen that the use of shorter measurement times, by using a faster mirror speed, will significantly decrease the SNR. Therefore it is common to sample at a frequency of 20 kHz when HgCdTe detectors are used. The detector signal should be amplified using the gain control so that the linear range of the detector fills the whole ±10 V range of the analogue-digital converter.

$$\mathrm{SNR} = \frac{U(T)\Theta\Delta\tilde{\nu}t^{\frac{1}{2}}\xi}{\mathrm{NEP}} \tag{2.97}$$

To help decrease the noise level, and to stop the undersampling process digitizing high frequency noise, different band-pass filters in the detector electronics are selected at the various frequencies. The final step in recording an interferogram is to sample the detector signal. To account for the wide variation in signal levels many instruments include amplifiers to increase the detector signal before analogue-digital conversion occurs, with this signal amplification being referred to as gain.

Once collected, Fourier transformation of the interferogram provides the spectrum (fig. 2.35). This has the effect of transforming a plot of the intensity as a function of retardation, in units of length (*e.g.* cm), to a plot of the intensity as a function of wavenumber, in units of reciprocal length (*e.g.* cm^{-1}). [3] Such single channel IR spectra obtained in this way generally look like the spectrum in fig. 2.35B, showing a broad hump with various dips in intensity. The shape of the spectrum is determined by the emission spectrum of the source (calculated for a black body source at a typical temperature of SI1300K in fig. 2.35B, red line), the transparency/reflectivity of the optics, the sensitivity of the detector (see table 3.1 for the components used in this work) and to some extent by absorption due to atmospheric species. To obtain absorption spectra of a sample the ratio of the response with and without a sample must be calculated. Two such single channel spectra are shown in fig. 2.35C, where the change in response due top the sample is indicated by an arrow. Taking the logarithm of the ratio of the sample spectrum to the reference spectrum (eqs. (2.75) and (2.76)) provides the absorbance spectrum shown in fig. 2.35D.

[3]Note that while the Fourier transform is defined for a continuous function with limits of $\pm\infty$, the measured interferogram is necessarily discrete and has a finite range. This is formally equivalent to carrying out the Fourier transform on the convolution of the theoretical infinite interferogram with a delta function, which is zero everywhere outside of the measured range. The peaks in the resulting spectrum are consequently distorted, with lobes either side of the main peak. Such effects can be minimised by multiplying the measured interferogram by a more smoothly varying function than the delta function, a process known as apodization. The choice of apodization function is most significant for peaks with widths on the order of the resolution [67] and thus a simple triangle function was used in this work.

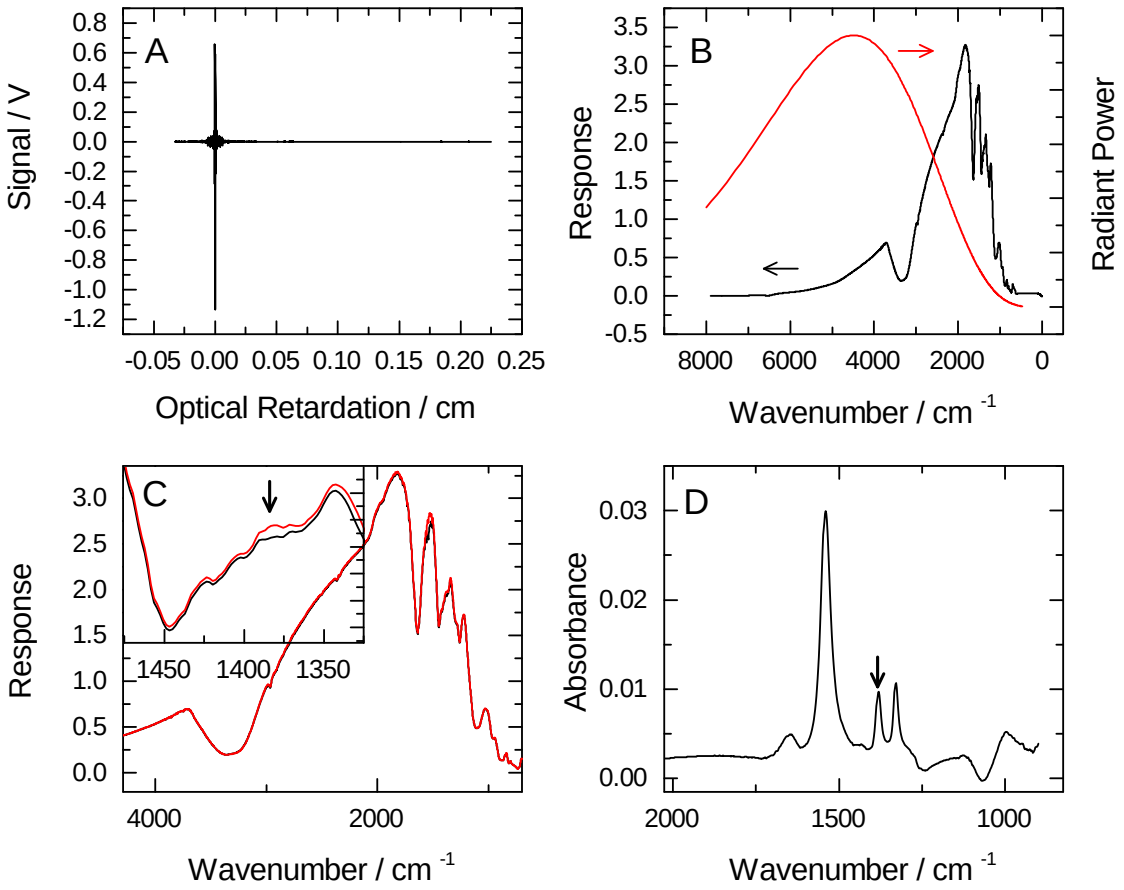

Figure 2.35: The process of collecting IR spectra with FTIR. A: An interferogram is collected. B: Fourier transformation of the interferogram results in the throughput spectrum of the spectrometer. The radiant power calculated for a blackbody source at a typical mid IR source temperature (1300 K) is shown in red. C: To measure an absorbance spectrum the process is repeated with and without sample (black and red spectra, respectively). Differences between the two are indicated by an arrow. D: The logarithm of the ratio of the sample spectrum to the background yields the absorbance.

References

[1] A. J. Bard and L. R. Faulkner, *Electrochemical Methods: Fundamentals and Applications*. New York: Wiley, 2 edition ed., 2000.

[2] A. R. Mount, "Hydrodynamic Electrodes," in *Encyclopedia of Electrochemistry*, Wiley-VCH Verlag GmbH & Co. KGaA, 2007.

[3] B. E. Conway and B. V. Tilak, "Behavior and Characterization of Kinetically Involved Chemisorbed Intermediates in Electrocatalysis of Gas Evolution Reactions," in *Advances in Catalysis* (H. P. D.D. Eley and P. B. Weisz, eds.), vol. 38, pp. 1–147, Academic Press, 1992.

[4] B. E. Conway and G. Jerkiewicz, "Relation of energies and coverages of underpotential and overpotential deposited H at Pt and other metals to the 'volcano curve' for cathodic H2 evolution kinetics," *Electrochimica Acta*, vol. 45, no. 25–26, pp. 4075–4083, 2000.

[5] T. Bligaard, J. Nørskov, S. Dahl, J. Matthiesen, C. Christensen, and J. Sehested, "The Brønsted–Evans–Polanyi relation and the volcano curve in heterogeneous catalysis," *Journal of Catalysis*, vol. 224, no. 1, pp. 206–217, 2004.

[6] V. R. Stamenković, B. S. Mun, M. Arenz, K. J. J. Mayrhofer, C. A. Lucas, G. Wang, P. N. Ross, and N. M. Marković, "Trends in electrocatalysis on extended and nanoscale Pt-bimetallic alloy surfaces," *Nature Materials*, vol. 6, no. 3, pp. 241–247, 2007.

[7] P. Quaino, F. Juarez, E. Santos, and W. Schmickler, "Volcano plots in hydrogen electrocatalysis – uses and abuses," *Beilstein Journal of Nanotechnology*, vol. 5, pp. 846–854, 2014.

[8] P. L. J. Gunter, J. W. H. Niemantsverdriet, F. H. Riberio, and G. A. Somoraji, "Surface Science Approach to Modeling Supported Catalysts," *Catalysis Reviews*, vol. 39, no. 1-2, pp. 77–168, 1997.

[9] C. R. Henry, "Surface studies of supported model catalysts," *Surface Science Reports*, vol. 31, no. 7–8, pp. 231–325, 1998.

[10] N. M. Marković and P. N. Ross Jr., "Surface science studies of model fuel cell electrocatalysts," *Surface Science Reports*, vol. 45, no. 4–6, pp. 117–229, 2002.

[11] G. A. Somorjai, R. L. York, D. Butcher, and J. Y. Park, "The evolution of model catalytic systems; studies of structure, bonding and dynamics from single crystal metal

surfaces to nanoparticles, and from low pressure (<10-3 Torr) to high pressure (>10-3 Torr) to liquid interfaces," *Physical Chemistry Chemical Physics*, vol. 9, no. 27, pp. 3500–3513, 2007.

[12] B. Lang, R. W. Joyner, and G. A. Somorjai, "Low energy electron diffraction studies of chemisorbed gases on stepped surfaces of platinum," *Surface Science*, vol. 30, no. 2, pp. 454–474, 1972.

[13] V. Grozovski, V. Climent, E. Herrero, and J. M. Feliu, "Intrinsic activity and poisoning rate for HCOOH oxidation on platinum stepped surfaces," *Physical Chemistry Chemical Physics*, vol. 12, no. 31, pp. 8822–8831, 2010.

[14] N. P. Lebedeva, A. Rodes, J. M. Feliu, M. T. M. Koper, and R. A. van Santen, "Role of Crystalline Defects in Electrocatalysis: CO Adsorption and Oxidation on Stepped Platinum Electrodes As Studied by in situ Infrared Spectroscopy," *The Journal of Physical Chemistry B*, vol. 106, no. 38, pp. 9863–9872, 2002.

[15] G. D. Barmparis, Z. Lodziana, N. Lopez, and I. N. Remediakis, "Nanoparticle shapes by using Wulff constructions and first-principles calculations," *Beilstein Journal of Nanotechnology*, vol. 6, pp. 361–368, 2015.

[16] A. S. Barnard and L. Y. Chang, "Thermodynamic Cartography and Structure/Property Mapping of Commercial Platinum Catalysts," *ACS Catalysis*, vol. 1, no. 2, pp. 76–81, 2011.

[17] M. L. Sattler and P. N. Ross, "The surface structure of Pt crystallites supported on carbon black," *Ultramicroscopy*, vol. 20, no. 1–2, pp. 21–28, 1986.

[18] L. Jones, K. E. MacArthur, V. T. Fauske, A. T. J. van Helvoort, and P. D. Nellist, "Rapid Estimation of Catalyst Nanoparticle Morphology and Atomic-Coordination by High-Resolution Z-Contrast Electron Microscopy," *Nano Letters*, vol. 14, no. 11, pp. 6336–6341, 2014.

[19] K. J. J. Mayrhofer, B. B. Blizanac, M. Arenz, V. R. Stamenković, P. N. Ross, and N. M. Marković, "The Impact of Geometric and Surface Electronic Properties of Pt-Catalysts on the Particle Size Effect in Electrocatalysis," *The Journal of Physical Chemistry B*, vol. 109, no. 30, pp. 14433–14440, 2005.

[20] K. Bergamaski, A. L. N. Pinheiro, E. Teixeira-Neto, and F. C. Nart, "Nanoparticle Size Effects on Methanol Electrochemical Oxidation on Carbon Supported Platinum Catalysts," *The Journal of Physical Chemistry B*, vol. 110, no. 39, pp. 19271–19279, 2006.

[21] D. Geng and G. Lu, "Size effect of gold nanoparticles on the electrocatalytic oxidation of carbon monoxide in alkaline solution," *Journal of Nanoparticle Research*, vol. 9, no. 6, pp. 1145–1151, 2007.

[22] M. Arenz, K. J. J. Mayrhofer, V. Stamenković, B. B. Blizanac, T. Tomoyuki, P. N. Ross, and N. M. Marković, "The Effect of the Particle Size on the Kinetics of CO Electrooxidation on High Surface Area Pt Catalysts," *Journal of the American Chemical Society*, vol. 127, no. 18, pp. 6819–6829, 2005.

[23] X. Feng, K. Jiang, S. Fan, and M. W. Kanan, "Grain-Boundary-Dependent CO2 Electroreduction Activity," *Journal of the American Chemical Society*, vol. 137, no. 14, pp. 4606–4609, 2015.

[24] K. Kinoshita, "Particle Size Effects for Oxygen Reduction on Highly Dispersed Platinum in Acid Electrolytes," *Journal of The Electrochemical Society*, vol. 137, no. 3, pp. 845–848, 1990.

[25] K. Yahikozawa, Y. Fujii, Y. Matsuda, K. Nishimura, and Y. Takasu, "Electrocatalytic properties of ultrafine platinum particles for oxidation of methanol and formic acid in aqueous solutions," *Electrochimica Acta*, vol. 36, no. 5–6, pp. 973–978, 1991.

[26] G. Kim and S.-H. Jhi, "Carbon Monoxide-Tolerant Platinum Nanoparticle Catalysts on Defect-Engineered Graphene," *ACS Nano*, vol. 5, no. 2, pp. 805–810, 2011.

[27] C. Nethravathi, E. A. Anumol, M. Rajamathi, and N. Ravishankar, "Highly dispersed ultrafine Pt and PtRu nanoparticles on graphene: formation mechanism and electrocatalytic activity," *Nanoscale*, vol. 3, no. 2, pp. 569–571, 2011.

[28] Z. Jusys, J. Kaiser, and R. J. Behm, "Methanol Electrooxidation over Pt/C Fuel Cell Catalysts: Dependence of Product Yields on Catalyst Loading," *Langmuir*, vol. 19, no. 17, pp. 6759–6769, 2003.

[29] Y. E. Seidel, A. Schneider, Z. Jusys, B. Wickman, B. Kasemo, and R. J. Behm, "Transport effects in the electrooxidation of methanol studied on nanostructured Pt/glassy carbon electrodes," *Langmuir*, vol. 26, no. 5, pp. 3569–3578, 2009.

[30] J. K. Nørskov, T. Bligaard, B. Hvolbæk, F. Abild-Pedersen, I. Chorkendorff, and C. H. Christensen, "The nature of the active site in heterogeneous metal catalysis," *Chemical Society Reviews*, vol. 37, no. 10, p. 2163, 2008.

[31] B. Hammer and J. K. Nørskov, "Why gold is the noblest of all the metals," *Nature*, vol. 376, no. 6537, pp. 238–240, 1995.

[32] T. Bligaard and J. K. Nørskov, "Ligand effects in heterogeneous catalysis and electrochemistry," *Electrochimica Acta*, vol. 52, no. 18, pp. 5512–5516, 2007.

[33] B. Hammer, O. H. Nielsen, and J. K. Nørskov, "Structure sensitivity in adsorption: CO interaction with stepped and reconstructed Pt surfaces," *Catalysis Letters*, vol. 46, no. 1-2, pp. 31–35, 1997.

[34] A. Nilsson and L. G. M. Pettersson, "Chapter 2 - Adsorbate Electronic Structure and Bonding on Metal Surfaces," in *Chemical Bonding at Surfaces and Interfaces* (A. N. G. M. P. K. Nørskov, ed.), pp. 57–142, Amsterdam: Elsevier, 2008.

[35] L. G. M. Pettersson and A. Nilsson, "A Molecular Perspective on the d-Band Model: Synergy Between Experiment and Theory," *Topics in Catalysis*, vol. 57, no. 1-4, pp. 2–13, 2014.

[36] R. K. Brandt, R. S. Sorbello, and R. G. Greenler, "Site-specific, coupled-harmonic-oscillator model of carbon monoxide adsorbed on extended, single-crystal surfaces and on small crystals of platinum," *Surface Science*, vol. 271, no. 3, pp. 605–615, 1992.

[37] P. Atkins and J. de Paula, *Atkins' Physical Chemistry*. Oxford ; New York: OUP Oxford, 10 edition ed., 2014.

[38] G. Blyholder, "Molecular orbital view of chemisorbed carbon monoxide," *The Journal of Physical Chemistry*, vol. 68, no. 10, pp. 2772–2777, 1964.

[39] A. Föhlisch, M. Nyberg, P. Bennich, L. Triguero, J. Hasselström, O. Karis, L. G. M. Pettersson, and A. Nilsson, "The bonding of CO to metal surfaces," *The Journal of Chemical Physics*, vol. 112, no. 4, pp. 1946–1958, 2000.

[40] K. J. Laidler, *Chemical kinetics*. New York ; London: McGraw-Hill, 2nd ed. ed., 1965.

[41] I. Mills and International Union of Pure and Applied Chemistry, eds., *Quantities, units, and symbols in physical chemistry*. Cambridge, UK: RSC Pub, 3rd ed ed., 2007.

[42] J. O. Bockris, *Modern Electrochemistry 2A: Fundamentals of Electrodics*. Modern electrochemistry ; v.2A, New York: Kluwer, 2nd ed. ed., 2002.

[43] T. J. Smith and K. J. Stevenson, "4 - Reference Electrodes," in *Handbook of Electrochemistry* (C. G. Zoski, ed.), pp. 73–110, Amsterdam: Elsevier, 2007.

[44] E. Laborda, M. C. Henstridge, C. Batchelor-McAuley, and R. G. Compton, "Asymmetric Marcus–Hush theory for voltammetry," *Chemical Society Reviews*, vol. 42, no. 12, pp. 4894–4905, 2013.

[45] R. Guidelli, R. G. Compton, J. M. Feliu, E. Gileadi, J. Lipkowski, W. Schmickler, and S. Trasatti, "Defining the transfer coefficient in electrochemistry: An assessment (IUPAC Technical Report)," *Pure and Applied Chemistry*, vol. 86, no. 2, 2014.

[46] S. Srinivasan and E. Gileadi, "The potential-sweep method: a theoretical analysis," *Electrochimica Acta*, vol. 11, no. 3, pp. 321–335, 1966.

[47] J. Solla-Gullón, P. Rodríguez, E. Herrero, A. Aldaz, and J. M. Feliu, "Surface characterization of platinum electrodes," *Phys. Chem. Chem. Phys.*, vol. 10, no. 10, pp. 1359–1373, 2008.

[48] B. E. Conway, H. Angerstein-Kozlowska, W. B. A. Sharp, and E. E. Criddle, "Ultrapurification of water for electrochemical and surface chemical work by catalytic pyrodistillation," *Analytical Chemistry*, vol. 45, no. 8, pp. 1331–1336, 1973.

[49] S. Trasatti and O. A. Petrii, "Real surface area measurements in electrochemistry," *Journal of Electroanalytical Chemistry*, vol. 327, no. 1–2, pp. 353–376, 1992.

[50] S. Rudi, C. Cui, L. Gan, and P. Strasser, "Comparative Study of the Electrocatalytically Active Surface Areas (ECSAs) of Pt Alloy Nanoparticles Evaluated by Hupd and CO-stripping voltammetry," *Electrocatalysis*, vol. 5, no. 4, pp. 408–418, 2014.

[51] Metrohm Autolab B.V., "Basic overview of the working principle of a potentiostat/-galvanostat (PGSTAT) – Electrochemical cell setup," Application Note EC08.

[52] P. T. Kissinger, "Introduction to Analog Instrumentation," in *Laboratory Techniques in Electroanalytical Chemistry, Second Edition, Revised and Expanded*, p. 165, 1996.

[53] P. W. Atkins and R. S. Friedman, *Molecular Quantum Mechanics*. Oxford University Press, fifth edition ed., 2010.

[54] J. T. Yates and T. E. Madey, *Vibrational spectroscopy of molecules on surfaces*. Methods of surface characterization ; v. 1 Y, New York ; London: Plenum, 1987.

[55] E. M. S. Maçôas, P. Myllyperkiö, H. Kunttu, and M. Pettersson, "Vibrational Relaxation of Matrix-Isolated Carboxylic Acid Dimers and Monomers†," *The Journal of Physical Chemistry A*, vol. 113, no. 26, pp. 7227–7234, 2009.

[56] S. T. Shipman, P. C. Douglass, H. S. Yoo, C. E. Hinkle, E. L. Mierzejewski, and B. H. Pate, "Vibrational dynamics of carboxylic acid dimers in gas and dilute solution," *Physical Chemistry Chemical Physics*, vol. 9, no. 32, pp. 4572–4586, 2007.

[57] B. N. J. Persson and M. Persson, "Vibrational lifetime for co adsorbed on cu(100)," *Solid State Communications*, vol. 36, no. 2, pp. 175–179, 1980.

[58] M. Born, *Principles of optics : electromagnetic theory of propagation, interference and diffraction of light*. Cambridge: Cambridge University Press, 7th (expanded) ed. ed., 1999.

[59] C. F. Klingshirn, *Semiconductor Optics*. Graduate Texts in Physics, Berlin, Heidelberg: Springer Berlin Heidelberg, 2012.

[60] A. Lipson, S. G. Lipson, and H. Lipson, *Optical physics*. Cambridge ; New York: Cambridge University Press, 4th ed ed., 2011.

[61] A. D. Rakić, A. B. Djurišić, J. M. Elazar, and M. L. Majewski, "Optical Properties of Metallic Films for Vertical-Cavity Optoelectronic Devices," *Applied Optics*, vol. 37, no. 22, pp. 5271–5283, 1998.

[62] C. D. Salzberg and J. J. Villa, "Infrared Refractive Indexes of Silicon Germanium and Modified Selenium Glass," *Journal of the Optical Society of America*, vol. 47, no. 3, pp. 244–246, 1957.

[63] C. W. Peterson and B. W. Knight, "Causality calculations in the time domain: An efficient alternative to the Kramers—Kronig method," *Journal of the Optical Society of America*, vol. 63, no. 10, p. 1238, 1973.

[64] K. Ohta and H. Ishida, "Comparison among several numerical integration methods for Kramers-Kronig transformation," *Applied Spectroscopy*, vol. 42, no. 6, pp. 952–957, 1988.

[65] M. Popović, "ECEN5645 HW2, P2. Kramers-Kronig relationship example using FFTs," 2011.

[66] M. Milosevic, *Internal Reflection and ATR Spectroscopy*. Wiley, 1 edition ed., 2012.

[67] P. R. Griffiths, *Fourier Transform Infrared Spectrometry*. Wiley-Interscience, 2 edition ed., 2010.

[68] G. A. Niklasson, C. G. Granqvist, and O. Hunderi, "Effective medium models for the optical properties of inhomogeneous materials," *Applied Optics*, vol. 20, no. 1, pp. 26–30, 1981.

[69] W. Theiβ, S. Henkel, and M. Arntzen, "Connecting microscopic and macroscopic properties of porous media: choosing appropriate effective medium concepts," *Thin Solid Films*, vol. 255, no. 1–2, pp. 177–180, 1995.

[70] D. J. Bergman, "The dielectric constant of a composite material—A problem in classical physics," *Physics Reports*, vol. 43, no. 9, pp. 377–407, 1978.

[71] D. J. Griffiths, *Introduction to electrodynamics*. Harlow: Pearson Education, fourth edition, pearson new international edition. ed., 2014.

[72] R. G. Greenler, "Infrared Study of Adsorbed Molecules on Metal Surfaces by Reflection Techniques," *The Journal of Chemical Physics*, vol. 44, no. 1, p. 310, 1966.

[73] H. A. Pearce and N. Sheppard, "Possible importance of a "metal-surface selection rule" in the interpretation of the infrared spectra of molecules adsorbed on particulate metals; infrared spectra from ethylene chemisorbed on silica-supported metal catalysts," *Surface Science*, vol. 59, no. 1, pp. 205–217, 1976.

[74] R. G. Greenler, D. R. Snider, D. Witt, and R. S. Sorbello, "The metal-surface selection rule for infrared spectra of molecules adsorbed on small metal particles," *Surface Science*, vol. 118, no. 3, pp. 415–428, 1982.

[75] A. Hartstein, J. R. Kirtley, and J. C. Tsang, "Enhancement of the Infrared Absorption from Molecular Monolayers with Thin Metal Overlayers," *Physical Review Letters*, vol. 45, no. 3, pp. 201–204, 1980.

[76] G.-Q. Lu, S.-G. Sun, S.-P. Chen, and L.-R. Cai, "Novel properties of dispersed Pt and Pd thin layers supported on GC for CO adsorption studied using in situ MS-FTIR reflection spectroscopy," *Journal of Electroanalytical Chemistry*, vol. 421, no. 1–2, pp. 19–23, 1997.

[77] M. Osawa, "Dynamic Processes in Electrochemical Reactions Studied by Surface-Enhanced Infrared Absorption Spectroscopy (SEIRAS)," *Bulletin of the Chemical Society of Japan*, vol. 70, no. 12, pp. 2861–2880, 1997.

[78] Z.-F. Su, S.-G. Sun, C.-X. Wu, and Z.-P. Cai, "Study of anomalous infrared properties of nanomaterials through effective medium theory," *The Journal of Chemical Physics*, vol. 129, no. 4, p. 044707, 2008.

[79] M. Osawa and K.-i. Ataka, "Electromagnetic mechanism of enhanced infrared absorption of molecules adsorbed on metal island films," *Surface Science*, vol. 262, no. 3, pp. L118–L122, 1992.

[80] C. Pecharromán, A. Cuesta, and C. Gutiérrez, "Calculation of adsorption-induced differential external reflectance infrared spectra of particulate metals deposited on a substrate," *Journal of Electroanalytical Chemistry*, vol. 563, no. 1, pp. 91–109, 2004.

[81] M. Osawa, K.-i. Ataka, K. Yoshii, and T. Yotsuyanagi, "Surface-enhanced infrared ATR spectroscopy for in situ studies of electrode/electrolyte interfaces," *Journal of Electron Spectroscopy and Related Phenomena*, vol. 64–65, pp. 371–379, 1993.

[82] H. G. Craighead and A. M. Glass, "Optical absorption of small metal particles with adsorbed dye coats," *Optics Letters*, vol. 6, no. 5, pp. 248–250, 1981.

[83] C. Pecharromán, A. Cuesta, and C. Gutiérrez, "Comments on the paper by M.-S. Zheng and S.-G. Sun entitled 'In situ FTIR spectroscopic studies of CO adsorption on electrodes with nanometer-scale thin films of ruthenium in sulfuric acid solutions' [J. Electroanal. Chem. 500 (2001) 223]," *Journal of Electroanalytical Chemistry*, vol. 529, no. 2, pp. 145–154, 2002.

[84] A. E. Bjerke, P. R. Griffiths, and W. Theiss, "Surface-Enhanced Infrared Absorption of CO on Platinized Platinum," *Analytical Chemistry*, vol. 71, no. 10, pp. 1967–1974, 1999.

[85] S. A. Wasileski, M. T. M. Koper, and M. J. Weaver, "Field-Dependent Chemisorption of Carbon Monoxide on Platinum-Group (111) Surfaces: Relationships between Binding Energetics, Geometries, and Vibrational Properties as Assessed by Density Functional Theory," *The Journal of Physical Chemistry B*, vol. 105, no. 17, pp. 3518–3530, 2001.

[86] F. Vidal, B. Busson, A. Tadjeddine, and A. Peremans, "Effect of a static electric field on the vibrational and electronic properties of a compressed CO adlayer on Pt(110) in nonaqueous electrolyte as probed by infrared reflection–absorption spectroscopy and infrared-visible sum-frequency generation spectroscopy," *The Journal of Chemical Physics*, vol. 119, no. 23, pp. 12492–12498, 2003.

[87] D. K. Lambert, "Vibrational Stark effect of adsorbates at electrochemical interfaces," *Electrochimica Acta*, vol. 41, no. 5, pp. 623–630, 1996.

[88] S. A. Wasileski, M. T. M. Koper, and M. J. Weaver, "Field-Dependent Electrode-Chemisorbate Bonding: Sensitivity of Vibrational Stark Effect and Binding Energetics to Nature of Surface Coordination," *Journal of the American Chemical Society*, vol. 124, no. 11, pp. 2796–2805, 2002.

[89] A. Rodes, J. M. Pérez, and A. Aldaz, "Vibrational spectroscopy," in *Handbook of Fuel Cells* (W. Vielstich, A. Lamm, H. A. Gasteiger, and H. Yokokawa, eds.), Chichester, UK: John Wiley & Sons, Ltd, 2010.

[90] B. E. Hayden, "Reflection absorption infrared spectroscopy," in *Vibrational spectroscopy of molecules on surfaces* (J. T. Yates and T. E. Madey, eds.), vol. 1 of *Methods of surface characterization*, pp. 267–344, New York ; London: Plenum, 1987.

[91] P. Hollins, "The influence of surface defects on the infrared spectra of adsorbed species," *Surface Science Reports*, vol. 16, no. 2, pp. 51–94, 1992.

[92] P. Hollins and J. Pritchard, "Infrared studies of chemisorbed layers on single crystals," *Progress in Surface Science*, vol. 19, no. 4, pp. 275–349, 1985.

[93] P. Hollins, "Coupling effects in the vibrational spectra of adsorbed layers with island structures," *Surface Science*, vol. 107, no. 1, pp. 75–87, 1981.

[94] R. M. Hammaker, S. A. Francis, and R. P. Eischens, "Infrared study of intermolecular interactions for carbon monoxide chemisorbed on platinum," *Spectrochimica Acta*, vol. 21, no. 7, pp. 1295–1309, 1965.

[95] M. Moskovits and J. E. Hülse, "Frequency shifts in the spectra of molecules adsorbed on metals, with emphasis on the infrared spectrum of adsorbed CO," *Surface Science*, vol. 78, no. 2, pp. 397–418, 1978.

Chapter 3

Development of an *in situ* Infrared Spectroelectrochemical Cell for Supported Nanoparticle Catalysts

Infrared (IR) spectroscopy is the most widely used *in situ* characterisation technique in electrocatalysis. [1–8] It can provide molecular information about both adsorbed and desorbed species at the electrode using routine laboratory instrumentation. As with many of the *in situ* techniques, the majority of *in situ* IR studies have been on model systems rather than real catalyst materials. The reasons for this include not only the desire to study very well characterised systems, which motivated the electrochemical studies on, for example, single crystal electrodes, but also the need to find systems amenable to measurement by the *in situ* technique. This has been especially challenging in the case of IR reflection spectroscopy, where the requirements for collecting IR spectra often conflict with the requirements for electrochemical measurement. The compromises needed to make such measurements have made it difficult to study real catalysts, especially under conditions relevant to fuel cells. There remains a need for such study, however, and so the aim of this chapter is to develop an *in situ* IR flow cell capable of sampling real carbon-supported fuel cell catalysts during catalysis under fuel flow conditions.

Existing *in situ* cell designs are briefly reviewed before the requirements for a new cell are specified. A new cell is then developed based on this specification, using electrocat-

alytic formic acid oxidation at carbon-supported Pt as a test system. Along with the cell, an integrated measurement system is developed with hardware synchronisation and computer control over the electrochemical and spectroscopic measurements and the pumping of solution. Finally a Matlab routine is developed to aid in processing and analysing the data.

3.1 Survey of Spectroelectrochemical Cell Designs

At present dedicated IR spectroelectrochemical cells are not widely available and are generally designed and fabricated on an individual basis. As a result no one design exists for any of the sampling geometries introduced in section 1.2, although the basic designs show similarities. Some of the cell designs reported for the two most common sampling geometries will be introduced: those based on the reflection-absorption geometry used in IRRAS (IR reflection absorption spectroscopy) and the attenuated total reflection (ATR) geometry used in ATR-SEIRAS (ATR surface enhanced IR absorption spectroscopy).

3.1.1 IRRAS Cells

The most straightforward geometry for recording IR spectra of electrodes is that of reflection-absorption. The electrode is placed in an electrochemical cell possessing an IR transparent window at its base. Light enters the cell through the window, travels through the electrolyte to the electrode from which it is then reflected, travelling back through the electrolyte and out via the window. [4, 6, 8] A typical cell using such a geometry is shown in fig. 3.1. [9]

The main advantage of this approach is its simplicity - any electrode can be used, as long as it is relatively reflective. This enables both macroscopic electrodes, for example single crystals, [9] and nanoparticle electrodes, supported on inert glassy carbon, [10] to be studied. It can also be used in tandem with complementary techniques such as scanning

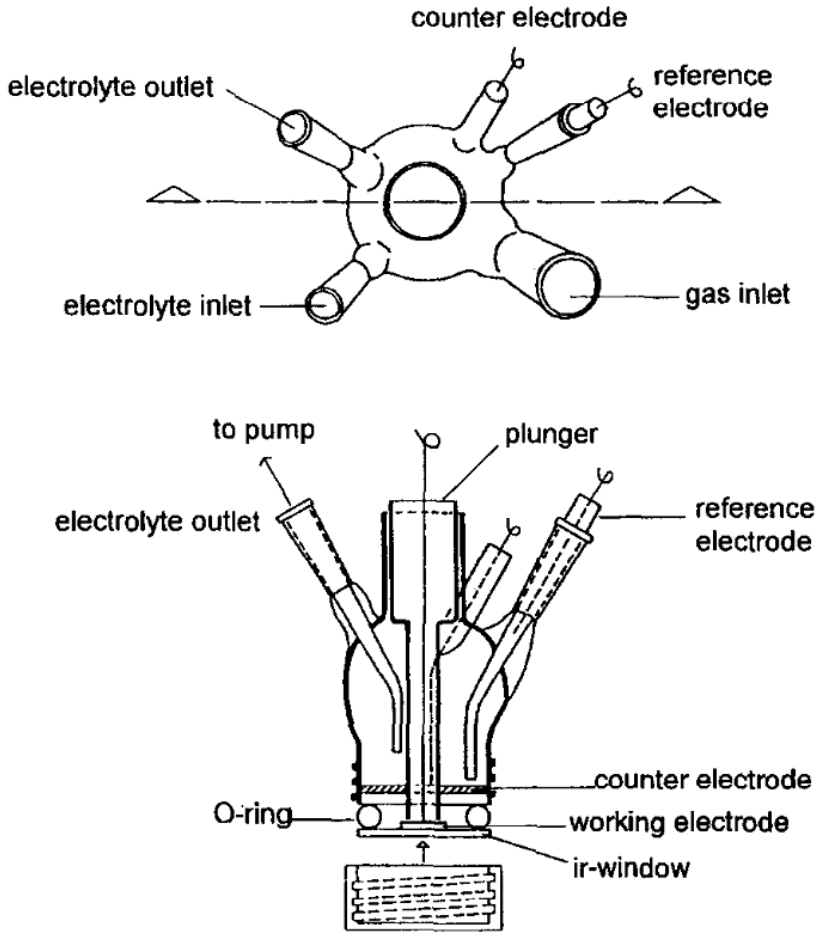

Figure 3.1: A typical IR reflection absorption cell. Reprinted from reference [9]. Copyright 1997, with permission from Elsevier.

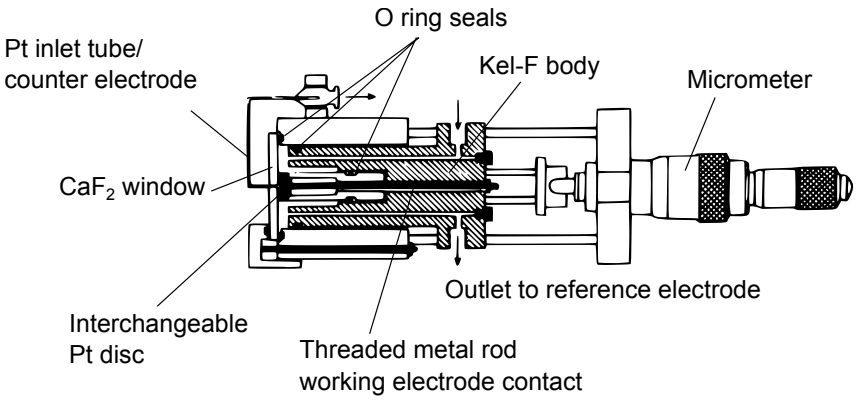

Figure 3.2: An IR reflection absorption flow cell. Adapted with permission from reference [16]. Copyright 1991, American Chemical Society.

tunnelling microscopy [11] and mass spectrometry. [12]

A major problem with this approach, however, is the strong attenuation of the incident radiation by water during the multiple passes through the electrolyte. To minimise this attenuation the distance between the electrode and the IR window is kept below around 10 µm. This can have major implications for studies of very active electrocatalysts which rely on large fluxes of reactant to, and product away from, the electrode. The limited mass transport in the thin layer can distort electrochemical measurements and lead to build up of intermediates, which may re-adsorb and undergo further reaction. The surface species and product distribution observed would then be time dependent and not necessarily reflect the steady state reaction. [13, 14]

The problem of mass transport in the thin layer was address by Roe *et al.* who designed an external reflection flow cell in which solution flowed over the electrode surface from left to right. [15] This design was taken further by Weaver and co-workers who added the option of radial flow from the outside of the electrode to its centre (fig. 3.2). [16] The Weaver cell used a Pt tube epoxied into a hole drilled in the centre of a CaF_2 optical window as the outlet. In this case the Pt tube could also function as the counter electrode. The reference electrode was situated out of the thin layer in the outlet stream.

Mass transport limitations are not the only downside of the thin layer design, however;

the thin layer will also produce a large solution resistance, which in combination with high catalytic currents will lead to a significant potential drop through the solution and a significant deviation of the electrode potential from that applied.

3.1.2 ATR Cells

An alternative approach to IRRAS is to use attenuated total reflection (ATR) spectroscopy. The principle behind ATR spectroscopy is that of total internal reflection; when light incident from a high refractive index material reaches an interface with a material of lower refractive index above a certain angle the light is totally reflected. As described in section 2.3.2 total internal reflection gives rise to an evanscent wave at the interface which samples the region just past the interface. Any species close to the interface can absorb energy from the evanescent wave, leading to attenuation of the reflection around the energy of the absorption.

To ensure that the total internal reflection condition is met, high refractive index, IR transparent, materials are cut into prisms, hemispheres or half-cylinders to make internal reflection elements (IREs). If the entry face of the IRE lies in the plane normal to the incident radiation minimal light is lost by reflection on entering the element. In the case of convex surfaces the beam is also focused onto the interface.

There are several advantages to using ATR spectroscopy for *in situ* spectroelectrochemistry. The first advantage is that the IR beam does not have to propagate through the electrolyte, as it is confined to the interface. This eliminates the need to keep the electrolyte layer thin, improving mass transport to and from the electrode and increasing the conductivity across the electrochemical cell. The second advantage is that the reflection is generated by the IRE/electrode interface, which is totally reflecting, as opposed to the solution/electrode interface which may be much less reflective. This provides a larger signal to measure, particularly in cases where catalysts supported on strongly IR

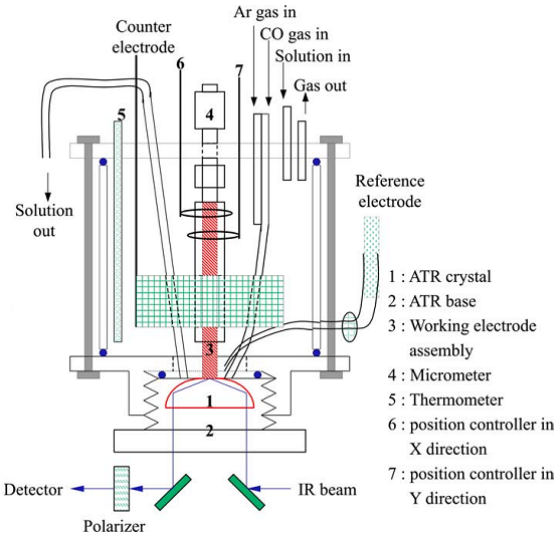

Figure 3.3: A thin layer cell for ATR measurements in the Otto configuration. Reprinted from reference [18]. Copyright 2004, with permission from Elsevier.

absorbing materials (*e.g.* carbon) are studied.

The ATR method can be used in two ways: in the so-called 'Otto' configuration the IRE forms the bottom of an electrochemical cell, just as in IRRAS. [17] The evanescent wave samples an area just above the IRE into which an electrode can be placed. While this allows any electrode to be sampled, without any requirements on its reflectivity, this geometry still suffers from problems with the thin layer, since the penetration depth of the evanescent wave in aqueous solution is on the order of 1 µm (eq. (2.84)). A cell used in such a setup is shown in fig. 3.3. [18] To mitigate the effects of the thin layer resistance a Luggin capillary is used to bring the reference electrode close to the thin layer.

In the second configuration, known as the 'Kretschman' configuration, a metal layer of around 100 nm thickness is deposited directly onto the IRE. [19] Due to its small thickness the metal layer does not significantly affect the total internal reflection condition of the interface, and the evanescent wave penetrates through the metal layer to sample the metal layer/solution interface. The benefit of this geometry is clear: as the IR light comes from within the electrode, there is no limitation on the depth of the electrolyte phase. Most reports of ATR cells involve static electrolyte, possibly agitated by gas sparging

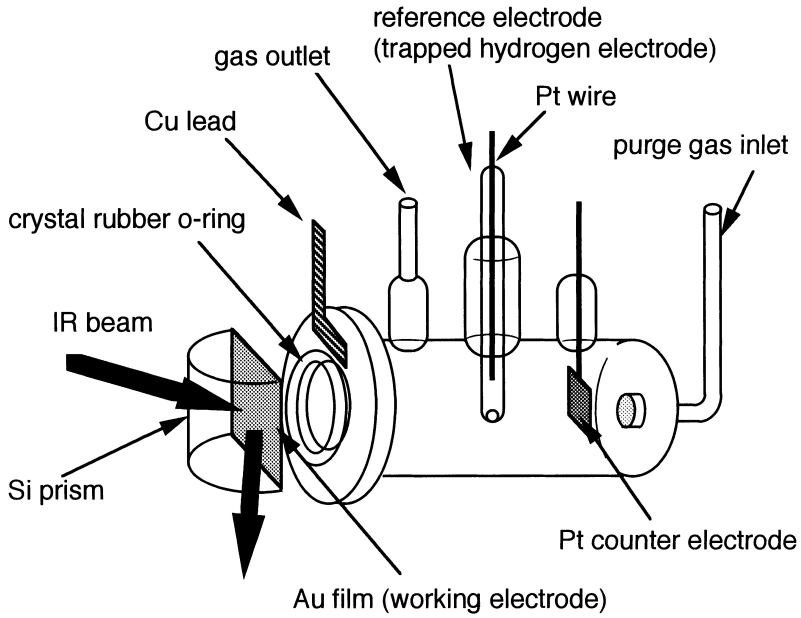

Figure 3.4: Cell used for ATR spectroelectrochemistry in the Kretschman configuration. Reprinted with permission from reference [22]. Copyright 1996 American Chemical Society.

(fig. 3.4), [20] however 'thin' layer flow cells have been developed. [21]

An additional benefit of the Kretschman configuration arises from the morphology of the metal films deposited onto the IRE. Such films are rough on the nanometer scale, [23] and can support plasmonic interactions which couple to the dipoles of surface species, amplifying their absorption of the evanescent wave by a factor of between 10^1 to 10^2 (chapter 2). [24, 25] The increased signal to noise ratio provided by this technique has enabled the time resolution of spectroscopic experiments to be decreased, allowing investigation of reactions down to the µs timescale. [5] To make use of this enhancement it is necessary to be able to deposit suitable metal films of catalytically relevant metals, such as Pt and Pd. The practical issues surrounding the deposition of such films were overcome primarily by the group of Osawa. [23] As a result the ATR surface enhanced IR absorption (ATR-SEIRA) approach has proven extremely useful in the study of electrocatalytic reactions. [5, 26]

3.1.3 Limitations of Existing Spectroelectrochemical Cells for Studies on Nanoparticles

The cells discussed above, being designed for bulk electrodes, suffer from some limitations when they are used to study nanoparticle catalysts. Any IRRAS measurement of an electrocatalytic reaction will always suffer from problems associated with the thin layer, making ATR measurements preferable. Yet to date detection of adsorbed species in the ATR configuration has only been demonstrated with metal underlayer electrodes, the metal layer possibly leading to complications if it also adsorbs species in the reaction. For example, Nesselberger *et al.* designed a thin layer ATR cell based on wall jet flow (section 2.1.1) explicitly for the study of the oxygen reduction reaction at nanoparticle electrocatalysts. [27] The cell used a thin film of Au deposited onto a Si hemisphere as the working electrode. While Au is relatively inert towards oxygen reduction, when similar cell designs have been applied to the study of formic acid oxidation at nanoparticles, only the high-wavenumber CO region was discussed, [28] possibly due to ambiguity in the origin of any lower wavenumber peaks.

To make full use of the information available from *in situ* IR spectroscopy it is desirable to find an approach which combines the inert electrical connection provided by carbon materials, with the mass transport provided by the ATR configuration. The development of such an approach is discussed in the rest of this chapter.

3.2 Existing Cell Design

3.2.1 ATR Accessory

The starting point for the cell design was an existing commercial ATR accessory (GladiATR, Pike Technologies), customised to provide 5 reflections from the top face of the IRE. The accessory consisted of a mirror unit, a demountable baseplate and the IRE.

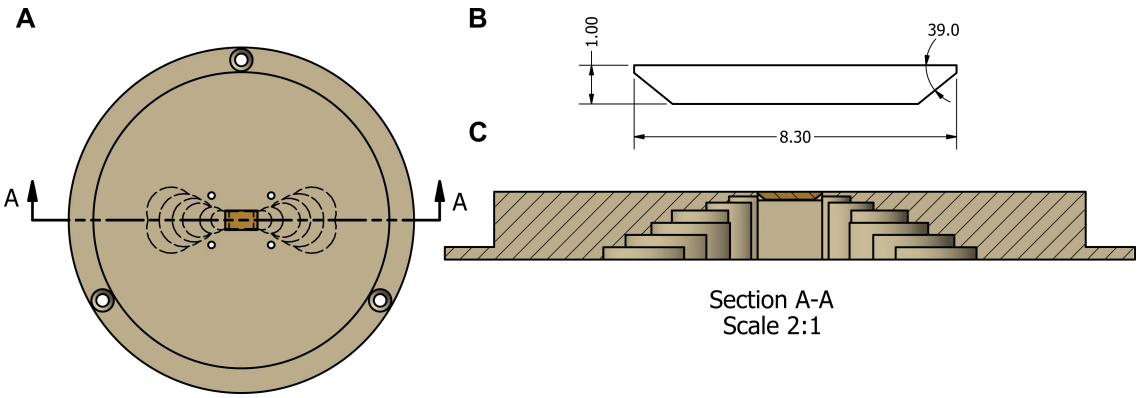

Figure 3.5: The ATR accessory baseplate and IRE used in this work. A: Top view of IRE in baseplate. B: Side view of IRE showing dimensions (in mm). C: Cross section through IRE in baseplate. Drawings not to scale.

The IRE fitted snugly into the baseplate, which in turn screwed into the mirror unit, allowing reproducible positioning of the IRE after removal for cleaning. The underside of the baseplate was scalloped to allow the beam to reach the IRE, while the top had four threaded holes drilled to allow an existing cell to be screwed down onto it. The IRE used throughout this work was a silicon trapezium (Crystal GmbH, Germany), approximately 8 mm long, 5 mm wide and 1 mm thick, with entry and exit faces polished to 39°. The baseplate and IRE are shown in fig. 3.5.

3.2.2 Existing Spectroelectrochemical Cell

An approach to ATR spectroelectrochemistry using carbon materials was recently demonstrated by Healy *et al.*, who developed a spectroelectrochemical cell for looking at metalloproteins adsorbed on high surface area carbon materials. [29,30] The concept is shown in fig. 3.6: metalloproteins were supported on carbon black which was subsequently applied directly onto the face of the IRE. To make electrical contact with the film a sheet of porous carbon paper followed by a coil of Au wire, or latterly carbon fibre, were pressed down onto the film. The carbon paper ensured lateral conductivity while the Au wire provided an electrical connection out of the cell. An electrochemical cell had been designed around

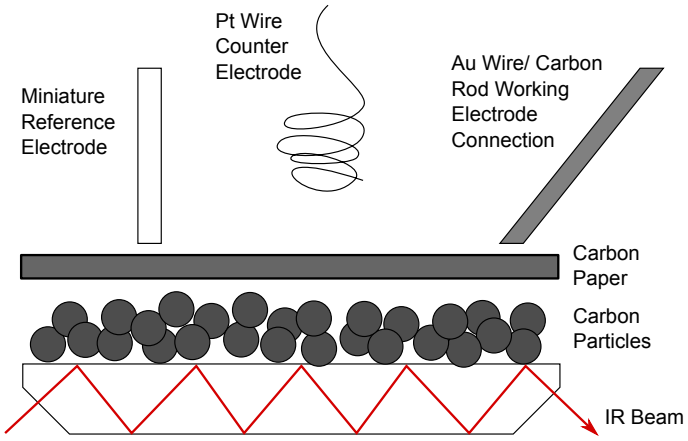

Figure 3.6: The original concept for *in situ* measurement of catalyst films.

this setup to house a reference and counter electrode, as well as inlet and outlet ports to enable solution to be exchanged.

Inspired by this approach, the same cell design was used to study CO and HCOOH oxidation on the surface of carbon-supported nanoparticles. [31, 32] In both cases the distinctive cyclic voltammograms were well reproduced and IR signals from adsorbed CO were observed. The IR peaks (to be discussed later) tracked the potential in the expected way and could be completely removed at a suitable oxidising potential (fig. 3.7). Although these initial results were promising, the were several aspects of the cell design which were either not optimised, or entirely unsuitable, for studying such organic electrooxidation reactions in acidic media.

The first problem encountered was the connection to the catalyst layer, which was made via a thin Au wire. While Au does not strongly adsorb CO (table 1.3), it is an active catalyst for many of the other electrooxidations of interest and significant current was observed even in the absence of catalyst. To correlate catalyst activity with the species observed by IR, it is imperative that current only arises from the catalyst. Even when the the thin Au wire was exchanged for carbon fibre, the poorly defined contact with the catalyst layer led to unreliable results and affected the reproducibility of the experiment.

The second area for improvement was in the mass transport provided by the cell.

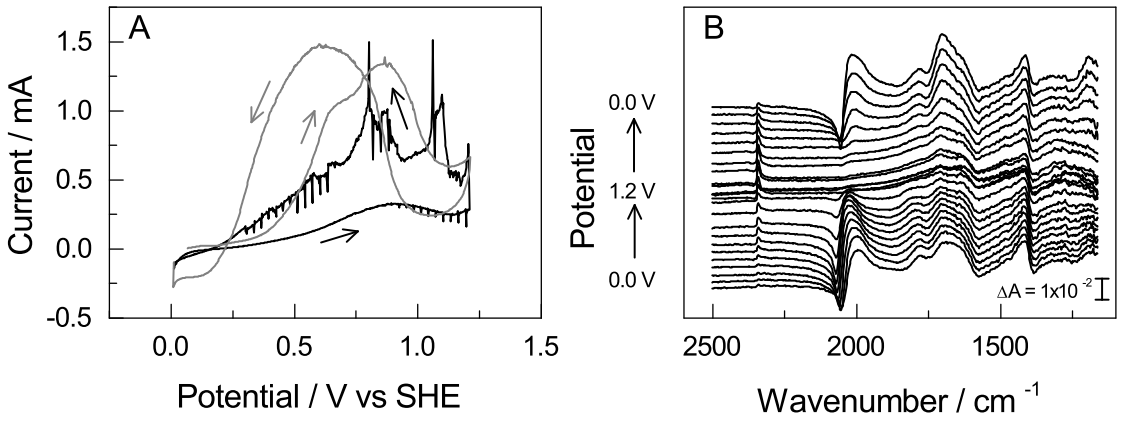

Figure 3.7: Spectroelectrochemical data obtained in the original cell. A: Cyclic voltammetry of Pt/C in 0.5 M HCOOH + 0.5 M $HClO_4$. Flow rate 2 mL min^{-1}. Scan rate: 1 mV s^{-1}. Black line: In situ cell with Au wire working electrode. Grey line: Ex situ glass cell with Pt/C on a glassy carbon electrode. B: IR spectra obtained over 50 s = 50 mV windows during the cycle. Background: initial potential before introduction of HCOOH.

The design of the cell was initially taken from a flow-through liquid cell and as such the inlets were not explicitly designed to provide solution flow over the IRE, just to exchange the contents of the entire cell. To better understand the flow of solution in the cell, computational fluid dynamics software (Autodesk Simulation CFD 2013) was used. A 3D CAD model of the original cell was converted into a mesh for the simulation. An inlet volumetric flow rate of 2 mL min^{-1} and an outlet pressure of 0 bar gauge formed the boundary conditions, along with zero velocity at the cell walls. The magnitude of the solution velocity in the mid plane of the cell is shown in fig. 3.8. It can be seen that in their present arrangement flow occurs between the inlet and outlet without significantly disturbing the solution at the surface of the IRE.

Another important consideration in the design of electrochemical cells is the relative position of the working, reference and counter electrodes. The original design was limited in the number of inlet ports it could support, necessitating the counter and reference electrodes to be positioned together. By sensing the solution/reference electrode potential difference in the vicinity of the counter electrode, rather than in the vicinity of the working

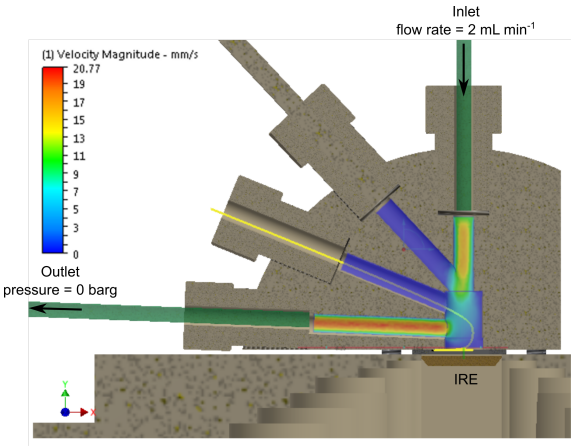

Figure 3.8: Liquid flow in the original spectroelectrochemical cell. The velocity magnitude in the central plane of the cell is shown overlaid on a cross-section of the cell. The velocity is represented on a colour gradient where blue is 0 mm s^{-1} and red is 21 mm s^{-1}.

electrode, the measured working electrode potential will be underestimated due to the voltage loss from the large uncompensated resistance iR_u (section 2.2.3).

More pragmatically, the way the original cell sealed onto the IRE caused a lot of problems. The seal was made using hand-cut rubber gaskets; gaskets are flat pieces of elastomer that need to have a considerable amount of pressure applied to deform them and seal the two surfaces together. The need to apply such pressure quite often cracked the IRE, or led to the cell leaking if insufficient pressure was applied. Furthermore, the rubber gasket was difficult to clean effectively and hard to replicate accurately. Sealing directly onto the IRE also used up valuable sampling area.

Finally, it became apparent that a higher degree of synchronisation between the measurements than was possible via independent manual control through software, was required, especially if dynamic methods such as cyclic voltammetry were to be used.

3.2.3 Design Criteria

Rather than solve each individual problem with the original cell, a new cell design was sought. To inform the design a set of criteria were established. It was decided that the cell must:

1. provide a reliable, inert electrical connection to the catalyst particle film;

2. provide sufficient flow of solution to the catalyst particle film to avoid the depletion of reactant or accumulation of intermediate or product species;

3. allow accurate measurement and control of the catalyst film potential up to currents of $\approx 5\,\mathrm{mA}$;

4. be inert to the aggressive solutions used (pH 0-12, 1 M $HClO_4$, H_2SO_4, HCOOH);

5. tolerate small overpressures (1 mbar) without leaking solution or vapour.

3.3 New Cell Design: 1. The Interdigitated Flow Field

The majority of the components discussed in this chapter were fabricated by the author in the research workshop under the supervision of Mr Charles Jones.

Inspiration for the cell design was initially sought in the literature of fuel cell design, as perhaps the most challenging design criteria - that of enforced mass transport to supported catalyst films - has been researched extensively in this field. Here the objective is to supply a relatively large area of catalyst with fuel as evenly as possible, while simultaneously collecting the current from the catalyst layer with minimal voltage losses. This is achieved using a bipolar plate or flow field - a plate of conducting material with channels machined into one face (fig. 3.9). A layer of porous carbon material called the gas diffusion layer (GDL) is sandwiched between the catalyst layer and the flow field. During operation the gaseous or liquid fuel is flowed through the channels, which spread it evenly over the GDL, the GDL in turn permitting the fuel to diffuse into the catalyst layer. Several patterns for the channels are used. The most simple design is a serpentine pattern of channels, with one long channel weaving back and forth along the flow field connecting the outlet to the inlet. The problem with this design is that the long channel leads to a

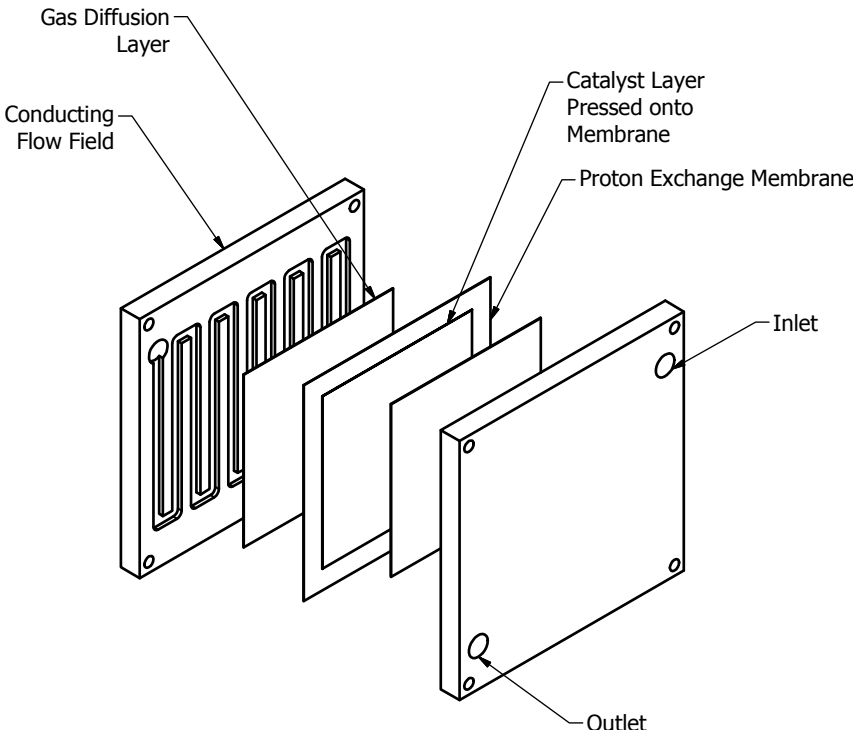

Figure 3.9: The elements of a proton exchange membrane fuel cell.

large pressure drop from inlet to outlet, with significant transport occurring only close to the inlet. To overcome this a different design is often used which has an interdigitated pattern of short, unconnected inlet and outlet channels. [33] The pressure drop in this interdigitated flow field (IFF) is more evenly distributed and diffusion is more even across the catalyst layer. [34]

3.3.1 Flow Field

Based on the fuel cell literature the IFF concept was taken forward as the basis for a new cell design. The flow field was produced from a graphite disc by machining in two unconnected sets of channels each with an inlet hole drilled through the disc (fig. 3.10). The IFF would press a disc of carbon paper GDL onto the catalyst layer, forming a thin layer cell but with effective mass transport. It was envisaged that an IRRAS type 'plunger' cell geometry would be adopted to enable the pressure applied to the flow field/GDL/catalyst layer to be varied. To achieve this the cell was produced by machining a shallow well the

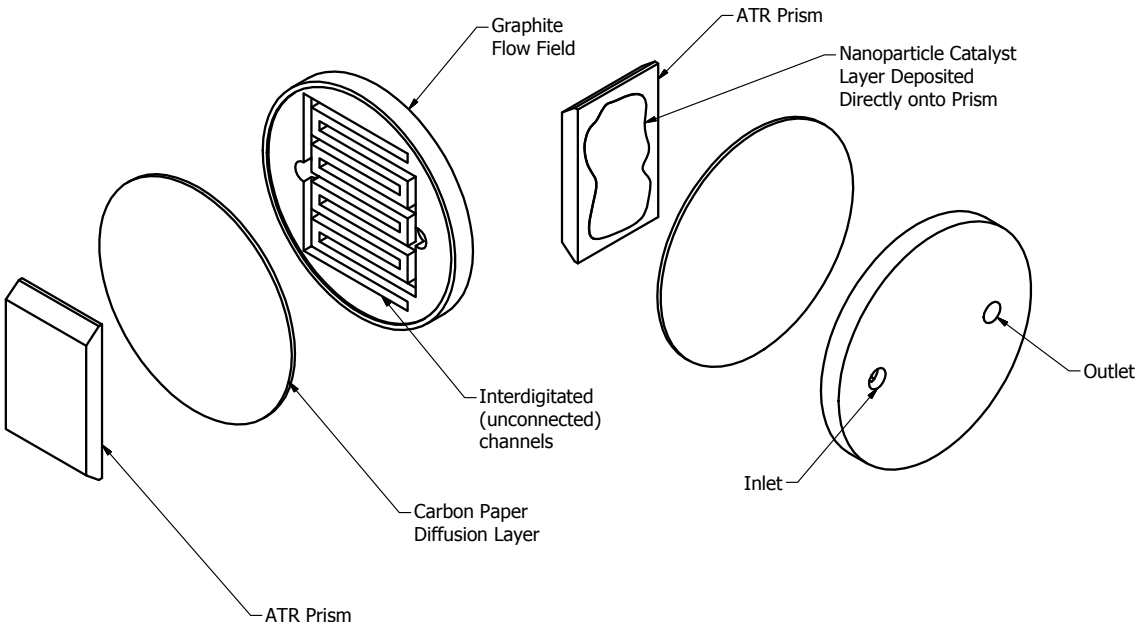

Figure 3.10: Application of the interdigitated flow field concept to an *in situ* ATR cell.

depth of the IFF into a polyether ether ketone (PEEK) plastic body, where PEEK was chosen due to its chemical resistance and mechanical strength. The body consisted of a narrow cylindrical section, which would act as the 'plunger' allowing movement of the flow field perpendicular to the IRE, and a larger head which provided access for the electrodes and solution inlet/outlet connections (fig. 3.11).

Inlet and outlet channels were drilled through the body to line up with the inlet and outlet holes in the flow field. The outlet channel was drilled much wider than the inlet to produce a cavity in which the reference and counter electrodes could sit. Electrical connection to the flow field was made by a metal rod which contacted the back side of the flow field. The counter electrode was a Pt wire set into a length of tubing with epoxy resin. The counter and reference electrodes, along with the inlet and outlet tubing, were connected to the cell using commercially available 1/16 inch liquid chromatography fittings (Kinesis Inc.).

This design was tested using cyclic voltammetry of a Pt/C catalyst film in both supporting electrolyte and formic acid solution. The initial tests revealed several major issues,

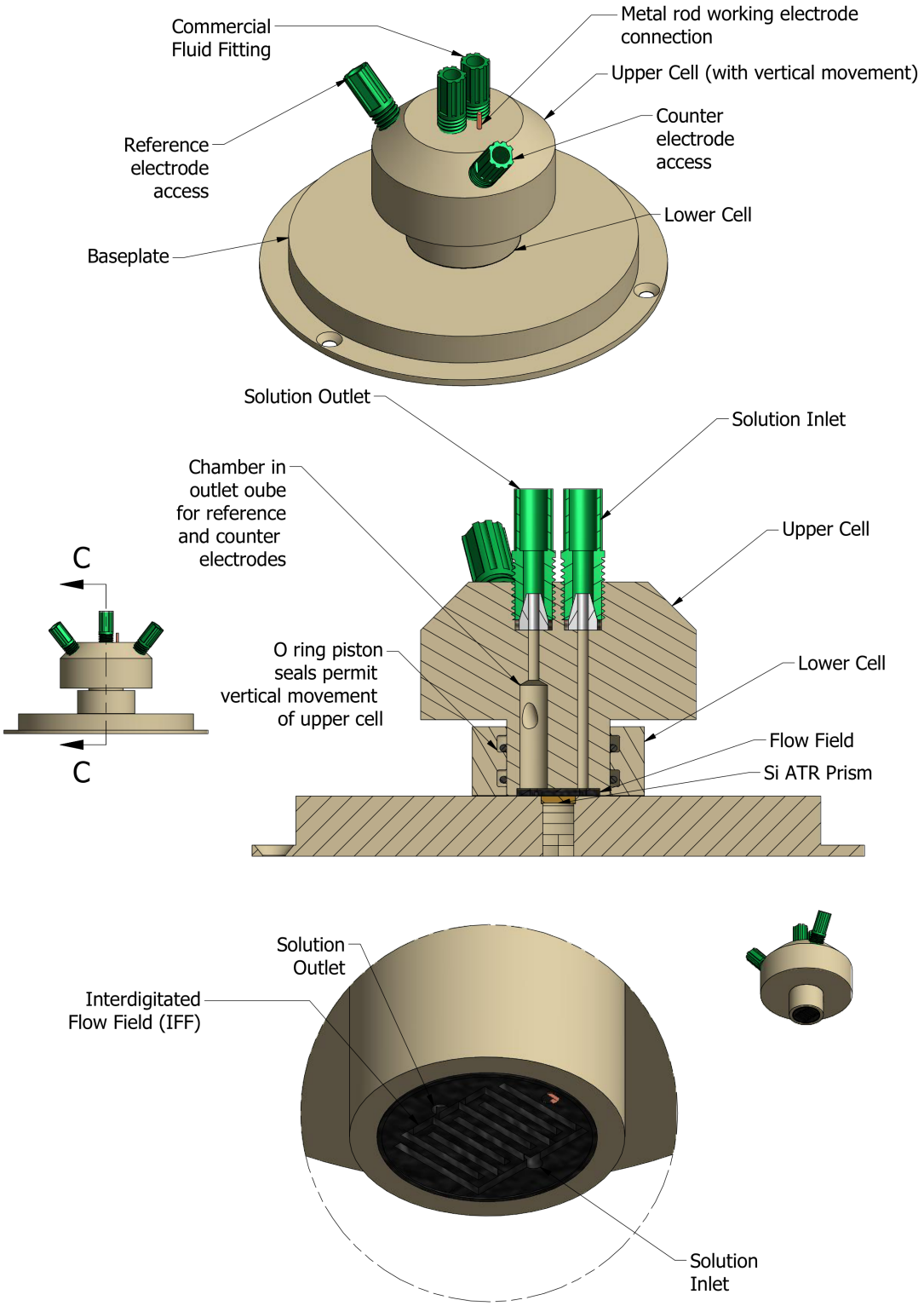

Figure 3.11: The initial new cell design with the interdigitated flow field (IFF).

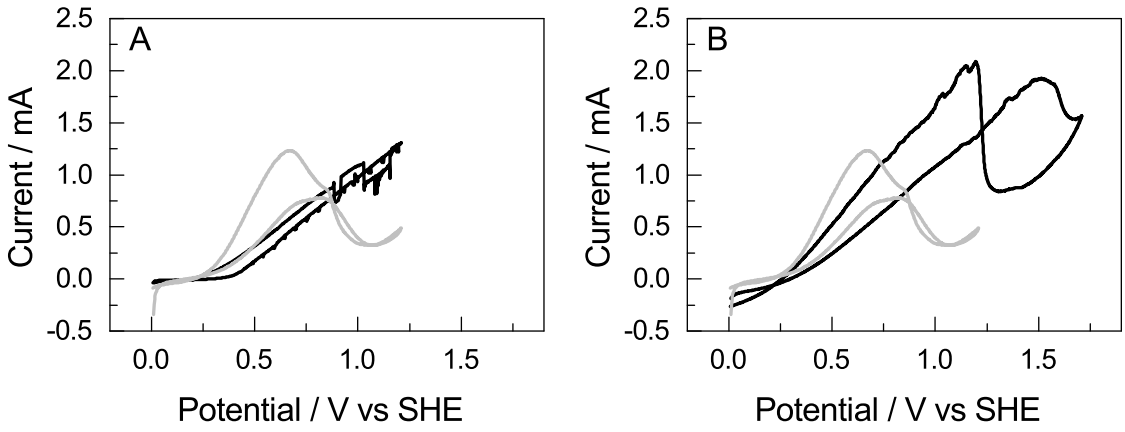

Figure 3.12: Cyclic voltammetry of Pt/C in the IFF cell. Solution: 0.5 M HCOOH + 0.5 M $HClO_4$. Flow rate: 2 mL min^{-1}. Scan rate: 10 mV s^{-1}. Black lines: voltammograms collected in the IFF cell with a carbon rod electrode connection and a Pt gauze counter electrode. Grey lines: voltammogram collected in the original cell with a carbon fibre connection.

starting with potential control. The current-potential behaviour observed in 0.5 M formic acid is shown in fig. 3.12A. The relationship is highly linear, indicating that a factor other than the electrochemical reaction of HCOOH is limiting the current. When the anodic potential limit is increased a peak in the current eventually occurs (fig. 3.12B), although it is displaced around 0.7 V from that expected for formic acid oxidation. A similarly displaced peak is seen in the return sweep. The shift of peaks to higher potential is indicative of a significant uncompensated potential drop between the reference electrode and the working electrode (section 2.2.3). In this case only part of the potential applied between the working electrode and reference electrode is dropped across the working electrode/solution interface, as desired, with the remaining part lost driving the current of ions through the solution. This resistance is probably due to the thin layer of electrolyte formed by the flow field, and the large distance between the reference electrode and the catalyst layer.

An additional problem was the backpressure developed by pumping through the cell, which became very high, reaching 6 bar at one point before the pump automatically shut

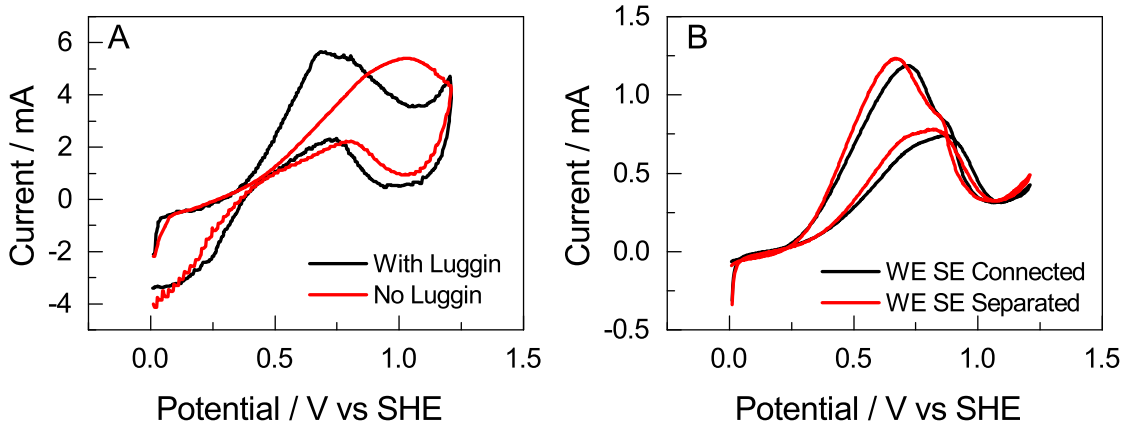

Figure 3.13: Further effects of resistance on the shape of cyclic voltammetry. A: The effect of using a Luggin capillary to sample the solution closer to the catalyst film. The catalyst layer and cell were unchanged between voltammograms, except for the presence of the Luggin. B: The effect of separating sense and working electrode connections when using carbon-loaded epoxy for making electrical connections.

off. This is likely due to the fact that the channels in the flow field were narrow and while there were several of them, there was only one outlet which was also quite narrow. Clearly the much higher viscosity of aqueous solutions compared to gases makes the interdigitated design inappropriate for a low pressure solution electrochemical cell.

Finally, the method for making electrical contact to the flow field was not suitable. Silver-loaded epoxy was used to make the connection, but the join was not sufficiently isolated from the solution and leaching of the Ag into the solution was observed. An alternative approach using carbon-loaded epoxy was found to work (section A.2), although with a slight error due to the iR drop arising from the increased contact resistance (fig. 3.13). The carbon-loaded expoxy connections were very brittle and broke on disassembling the cell, however, and so this approach was not continued.

3.4 New Cell Design: 2. The Radial Flow Field

In light of the initial problems the design of the flow field was revised, with the channels in the IFF replaced by an array of holes: a single central hole as the inlet, a radial array of 6 outlets, and an off-centre hole to allow access by a reference electrode (fig. 3.14). The increased number of outlets allowed an increase in flow rate while keeping the inlet pressure relatively low and the added reference electrode hole allowed the solution potential to be sampled much closer to the catalyst layer. Electrical connection to the flow field was made via PTFE-coated wire bonded to the flow field using Ag-loaded epoxy, leading to a resistance of $\approx 3\,\Omega$. This time special care was taken to isolate all conductive surfaces of the flow field, except the bottom face, from the solution using Araldite resin (figs. 3.14A to 3.14C). Failure to do so not only led to leaching of Ag into the solution, but also to the gradual oxidation of the internal carbon surfaces that could not be routinely polished, such as the interior of the flow holes, and the concomitant appearance of a significant surface redox couple observed in the cyclic voltammogram (fig. 3.15).

To avoid using the gasket found in the original design, a different approach must be found to seal the IRE into the baseplate. The most common seal for use in corrosive solutions, where conventional seals made by braising with an indium or lead-based flux are inappropriate, is an O ring seal. [35] An O ring seal is made using a ring of elastomer with a circular cross section partially housed in a groove in one surface being pressed against a second flat surface. The O ring deforms filling the groove and making a tight seal between the two surfaces. In the present case the small size of the IRE ($8\,\text{mm} \times 5\,\text{mm}$) and its rectangular shape, means that making a seal with an O ring , which typically has a 1 mm cross section, would only leave a 3 mm diameter circle on the face of the IRE for catalyst. As well as wasting around 80 % of the IRE surface, it would be very challenging to machine a flow field this small. Instead, the IRE must be first sealed into the baseplate

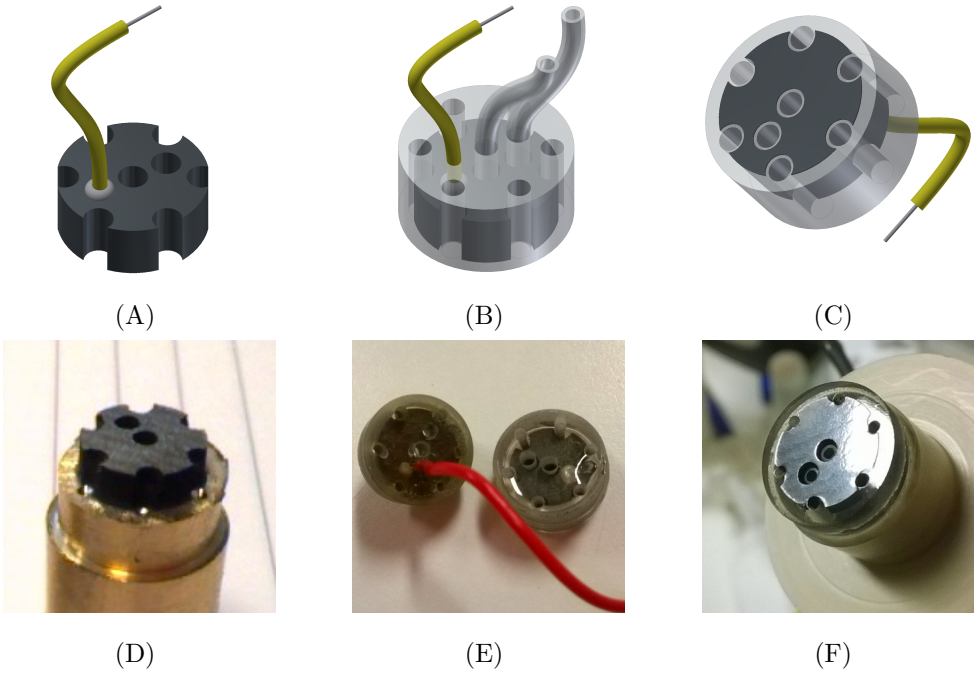

Figure 3.14: Design (top) and production (bottom) of the revised flow field. The graphite was glued to a brass support, turned to diameter and drilled (A), before a collar was made and the graphite encapsulated in resin. The holes were then redrilled (E) before the flow field was removed from the support and polished (F).

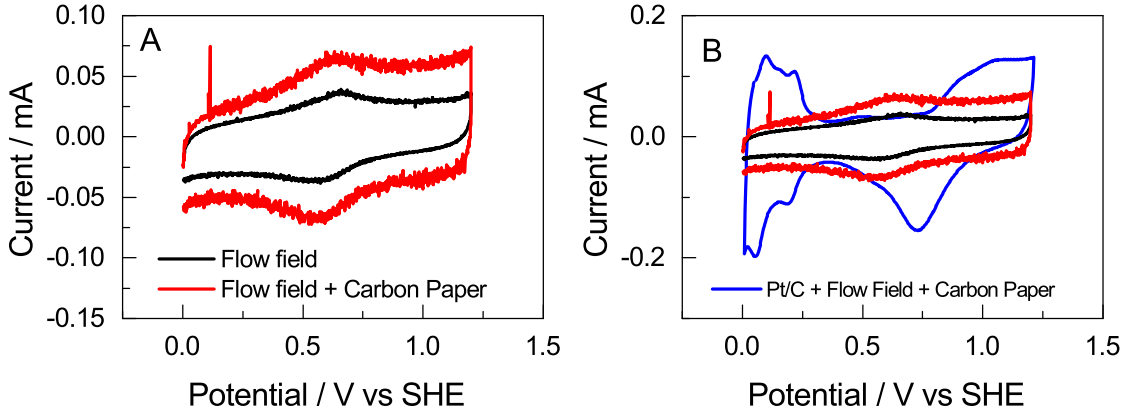

Figure 3.15: Cyclic voltammetry of the radial flow field with and without the carbon paper gas diffusion layer in 0.5 M $HClO_4$ solution (left). A cyclic voltammogram in acid solution including the catalyst layer is shown for comparison (right).

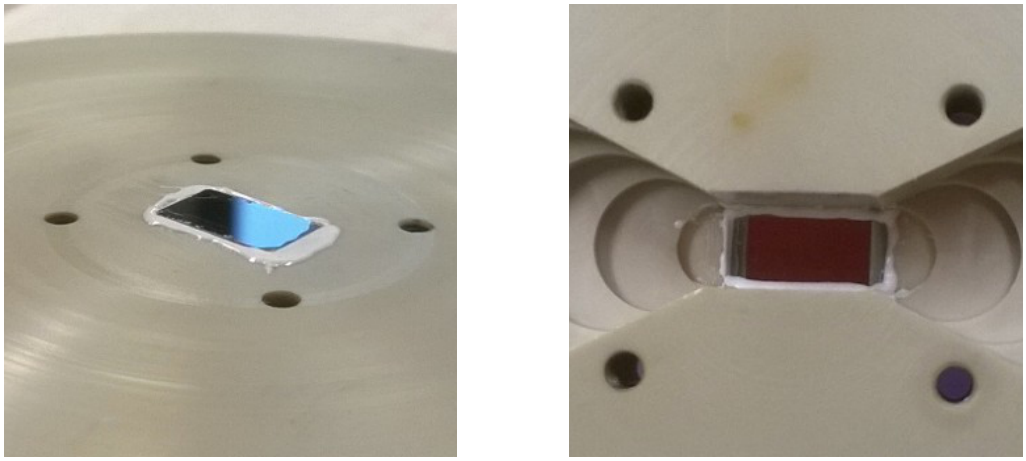

(A) Top (B) Bottom

Figure 3.16: Using silicone to seal the IRE into the baseplate.

by some other means, and then an O ring used to seal the cell onto the baseplate.

A number of methods for sealing the IRE into the baseplate were trialled, including direct bonding of the IRE to a Si wafer to create an IRE with a larger face but with the same reflections (section A.1.0.6), setting the IRE into the baseplate using epoxy followed by polishing the face back to a mirror finish (section A.1.0.4), and sealing with Apiezon wax (section A.1.0.5). The most successful approach however utilised a fast curing silicone sealant (SE4486CV, Dow Corning). It was applied to both the edges of the IRE and the baseplate before the IRE was inserted (fig. 3.16). The low viscosity of the silicone allows it to fill in small gaps to make good seals but it does not flow so readily as to contaminate the angled faces of the IRE. It is easily removed from the IRE using plastic tools followed by washing in concentrated H_2SO_4. Due to its reliable sealing, easy application and subsequent removal it was chosen as the method for sealing the IRE into the mounting plate.

To decrease the error in potential measurement the nature and position of the reference electrode in the cell was reconsidered. The existing spectroelectrochemical cell design used a commercial 2 mm PEEK Ag/AgCl electrode (Harvard Apparatus) as the reference electrode. Subsequently home made versions were fabricated by housing a AgCl-plated

wire in a length of PFA tubing with a 13X molecular sieve on the end. The choice of 13X sieves was made due to their similar pore size to the commercial Vycor glass frits, which were not used here as they are unavailable in narrow diameters. These home made electrodes were flexible, facilitating easy incorporation of the electrode into the flow field. However, electrodes made in this was had relatively unstable potentials, presumably due to the leakage of Cl^- solution through the molecular sieve. To overcome this the same tubing was used to create a Luggin-style capillary that went from the catalyst layer, via an additional hole in the radial flow field, to an outlet port. Here a separate reference electrode compartment was made by connecting a threaded glass tube (#7 Thread, Ace Glass) to the cell using a home made O ring fitting. The use of separate compartment minimised Cl^- contamination of the electrolyte as well as enabling the use of a commercial reference electrode (Ag/AgCl electrode RE-5B, BAS Inc.) which had a more stable potential.

The final cell design used for the experiments described in the following chapters is shown in fig. 3.17. In general the upper cell, lower cell and baseplate were separated after each experiment and cleaned without further disassembly.

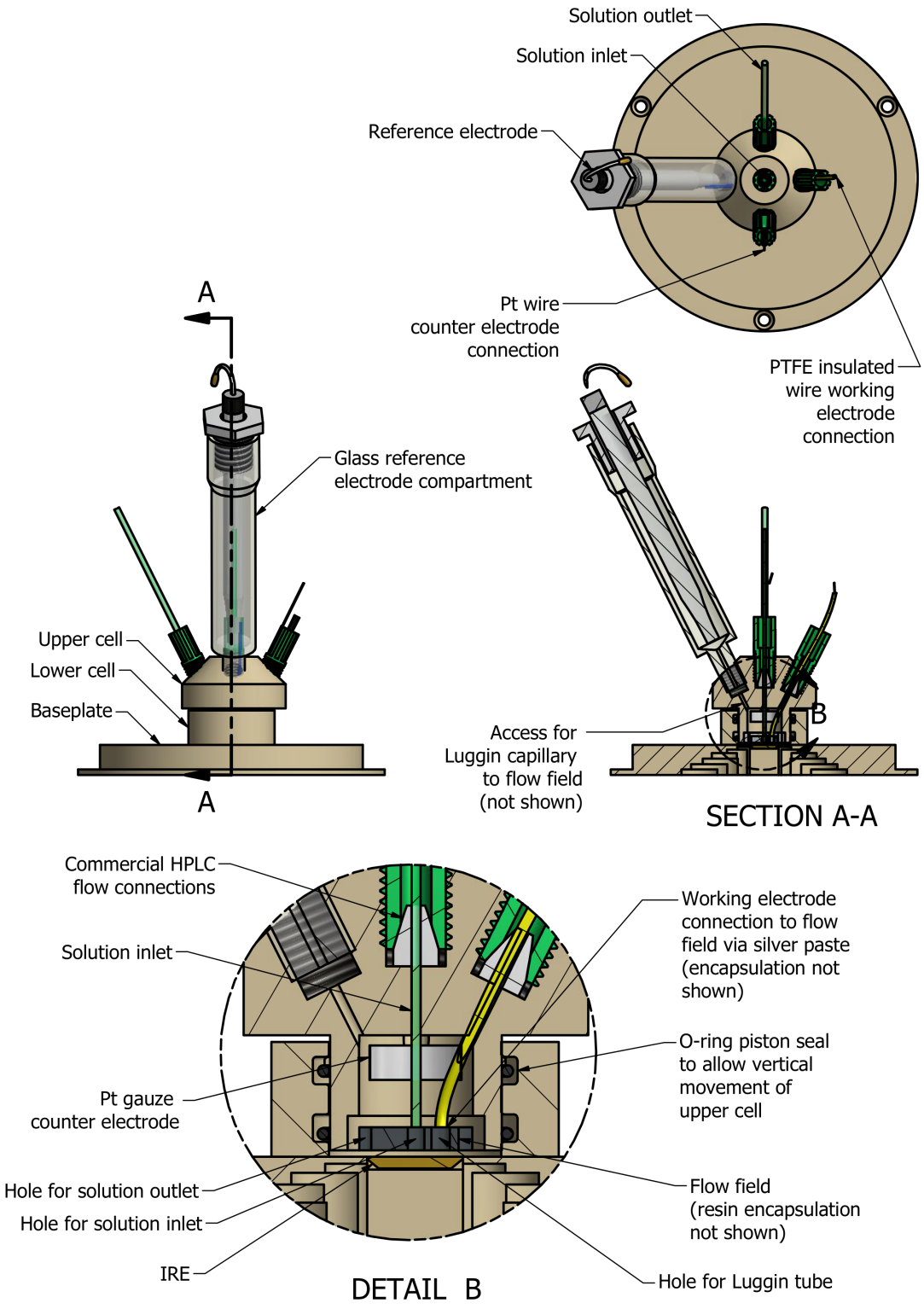

Figure 3.17: The radial flow field cell.

3.5 Catalyst Film Preparation

It is important to understand the morphology of the catalyst layer since it can significantly affect both the electrochemistry, via mass transport effects, and the observed spectroscopy, via the formation of strong local electromagnetic fields. In general there are several stages to preparing a catalyst layer: dispersion of the catalyst powder in a suitable solvent to produce a catalyst ink, application of the ink to the desired substrate and removal of the solvent to leave a stable catalyst layer. These stages have been investigated extensively by those producing whole proton exchange membrane fuel cells, as well as by those looking to replicate the conditions of PEM fuel cells in more analytical spectroscopic and electrochemical settings. In particular, there is a lot of interest in being able to replicate the conventional voltammetric measurements, made on flat metal discs, on nanoparticle films, since analytical expressions exist in these cases which enable kinetic parameters to be calculated. Different preparation methods for catalyst films and their equivalence with conventional electrodes are reviewed in reference [36].

At each of the stages in catalyst layer preparation several methods were investigated. In the first stage, production of the catalyst ink, two different approaches were taken: dispersion in a mixture of water/isopropanol/Nafion, and dispersion in ethanol alone. Initially ethanol alone was used as the solvent, and so it is films prepared from ethanol inks which have been characterised in most detail, however after some problems with the reliability of these films, a water/isopropanol/Nafion mixture was trialled as well. In the end few differences in the spectroscopy were observed between the two inks, although the presence of Nafion seems to lead to broader features in the CV.

There exist several complex application protocols to carry out the remaining steps (application of catalyst ink to the substrate and removal of the solvent), for example spin coating or screen printing. However, the small surface area of the IRE means that the

drop casting technique is the most practical. Previous reports of drop casting catalyst films have suggested heating the substrate or drying in an inert gas flow followed by rinsing. [37, 38] These methods were attempted, however when used in the present setup neither method seemed to provide any benefits over drying at room temperature in air.

In general, catalyst films were prepared by adding a known amount of catalyst powder to a sufficient amount of ethanol to reach a concentration of 10 mg mL^{-1}. The mixture was then dispersed using alternate shaking and ultransonication for a period of 1 h. Then 15 µL of ink was added dropwise to the IRE and allowed to dry. In some cases the rate of solvent evaporation was decreased by covering the wet film with a beaker; films dried in this way appeared shiny and more uniform to the eye, however no difference from films dried quickly was observed experimentally.

A composite image of a catalyst film prepared as described is shown in fig. 3.18. The light microscope images reveal that the film is composed of several regions: dark patches are separated by cracks and smaller, lighter regions. More detail on the nature of the films was sought using scanning electron microscopy (SEM), kindly carried out by Jonathan Quinson. Several SEM images of different parts of a similar film are shown in fig. 3.19. The top row of images shows a top-down view of a film at different magnifications. The incomplete coverage of the film can already be seen in the lowest magnification image (Panel A) although it is more apparent at higher magnification (Panel C), where lighter areas represent catalyst and the darker, uniform grey shows the silicon substrate. A closer view of the catalyst area reveals that even in the well-covered regions, the density of particles is not uniform, with many holes appearing (shown by an arrow in Panel B). To understand the thickness of the films, side-on images were collected and are shown on the bottom row of fig. 3.19. In some regions the film was up to 2 µm thick (Panel D), while in others the thickness was closer to 200 nm (Panel F). The thicker regions are assigned to the darker regions of the light microscope image, while the thinner ones are assigned

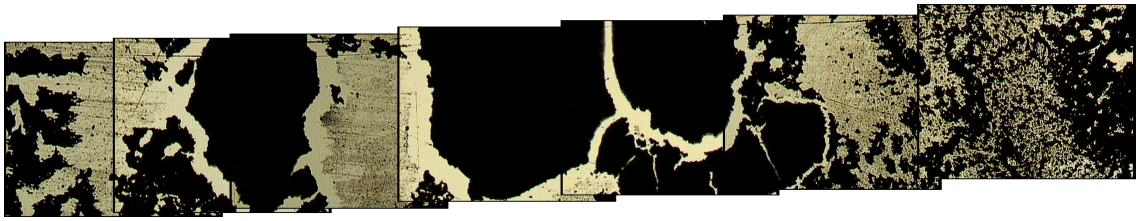

Figure 3.18: Composite micrograph showing film morphology on the IRE. The width of the composite image corresponds roughly to the width of the IRE (ca 5 mm).

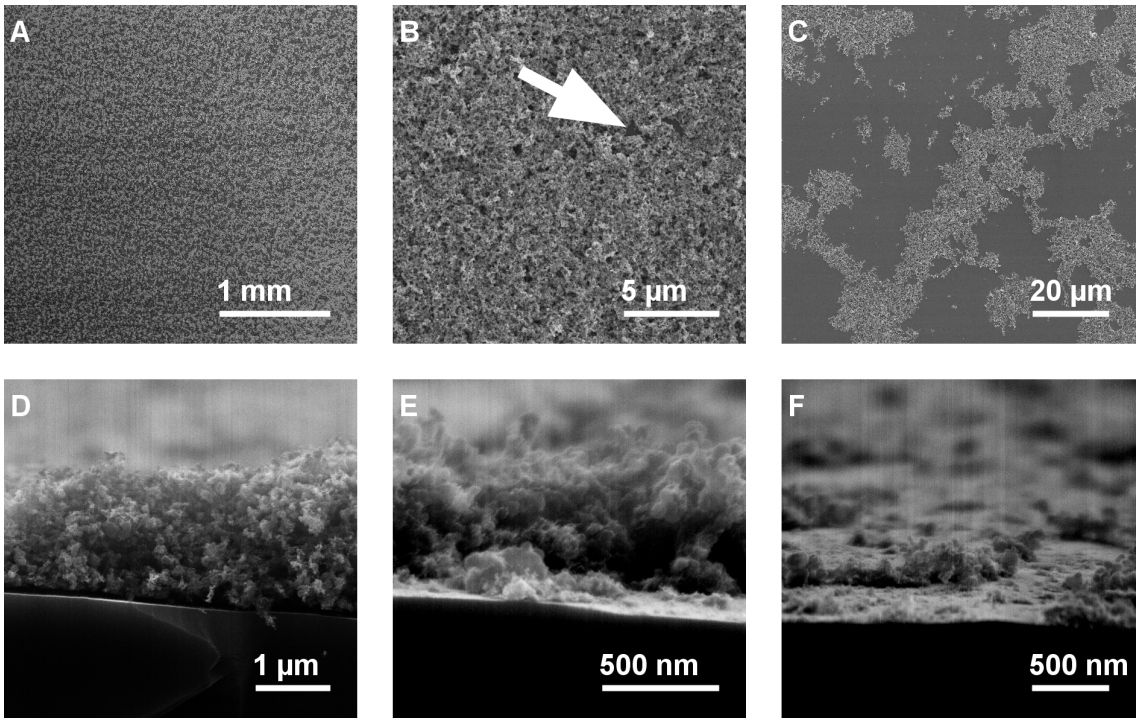

Figure 3.19: Scanning electron microscope images of different regions of a catalyst film. A-C: Birds-eye view, D-F: Side view. Images courtesy of Jonathan Quinson, Department of Materials, Oxford.

to the lighter regions.

These observations can be put into perspective by considering the length scales over which the processes occurring in the electrochemistry and IR spectroscopy experiments operate. The fundamental distance in electrochemistry is the diffusion layer thickness, the distance over which diffusion operates to bring reactant to the electrode surface. Even when forced convection is used to provide mass transport, such as in rotating disc or wall jet experiments, there remains a stagnant layer of solution through which diffusion must

operate. In a typical rotating disc experiment the diffusion layer is often considered to be around 50 µm thick. [36] Since the maximum film thickness observed in the present case is around an order of magnitude smaller than the typical diffusion layer thickness, it is assumed that transport in the film will not be significantly more limited than in the case of a rotating disc experiment.

Of greater significance for the spectro-electrochemical experiment is the effect of film thickness on the IR absorption of the film. There are several reports of the effect of nanoparticle coverage on IR spectra of adsorbates. [37–39] The most simple effect of film thickness is to increase the number of oscillators present and therefore increase the observed absorption. There are also additional effects that arise from increased film thickness. As discussed in Chapter 2 (section 2.3.4.2), the appearance of reflection spectra are strongly determined by the absorption of the reflecting material, with greater absorption correlating with stronger distortion. The strategies for obtaining the 'unipolar spectra' described in references [37] and [38] are both based on the same principle of obtaining thin films, minimising their absorption to minimise the distortion. No such attempt is made here, as peak fitting will be used to interpret the spectra irrespective of shape. In fact, the converse is true: thick films are used to maximise the effective concentrations of any surface species. The film thickness may also affect the shape of the spectra via the strong electric fields induced at the surface of the catalyst particles; the induced field can augment the incident field and enhance the observed absorption. [24, 40] Since this field is highly localised, falling off as the cube of distance, [24] the distance between particles is important in determining the extent of this effect. However, this is the difference between metal particles, not carbon support particles and so this effect will be less important if the metal particles are diluted by the support.

3.6 Electrochemical Cell Characterisation

So far the spectroelectrochemical cell has been tested using cyclic voltammetry in formic acid at moderate scan rates and medium flow rates. It is important to understand the conditions at which the assumptions of accurate potential control and absence of mass transport limitations break down.

Figure 3.20 shows the effect of scan rate on the shape of cyclic voltammograms obtained in $HClO_4$ and HCOOH. When the catalyst layer was cycled at 100 mV s^{-1} in $HClO_4$ the features of hydrogen adsorption and desorption (section 2.2.1)) are seen (fig. 3.20A). The scan rate was then increased to 500 mV s^{-1}, 1000 mV s^{-1} and 10 000 mV s^{-1}, with the resulting current normalised by division by the scan rate. [41, 42] Examination of the voltammograms show that the H peaks (shown enlarged in fig. 3.20B) remain at the same potential for scan rates up to 1000 mV s^{-1}, as expected for a surface redox process. At 10 000 mV s^{-1} the peaks are much broader and have shifted to higher potential, suggesting that at this scan rate the potential of the catalyst layer was not at equilibrium with the applied potential.

Figure 3.20C shows the voltammogram in HCOOH at 100 mV s^{-1}, in which the usual four peaks attibuted to oxidation are seen. [43] At higher scan rates the shape changes however (fig. 3.20D). In this regime the scan rate is much greater than the rate of oxidation and so negligible reaction current is measured. [44] Instead, the only processes fast enough to contribute to the observed current are adsorption and desorption, hence the voltammogram shows the same H adsorption/desorption peaks as $HClO_4$. Also observed in this regime is the adsorption of reactant such as HCOOH, which adsorbs as $HCOO^-$. That this regime is accessible in the cell is significant as in theory it enables these adsorption processes to be examined spectroscopically. To realise this would require developments in the time resolution of the IR measurement, however, for example by using step scan

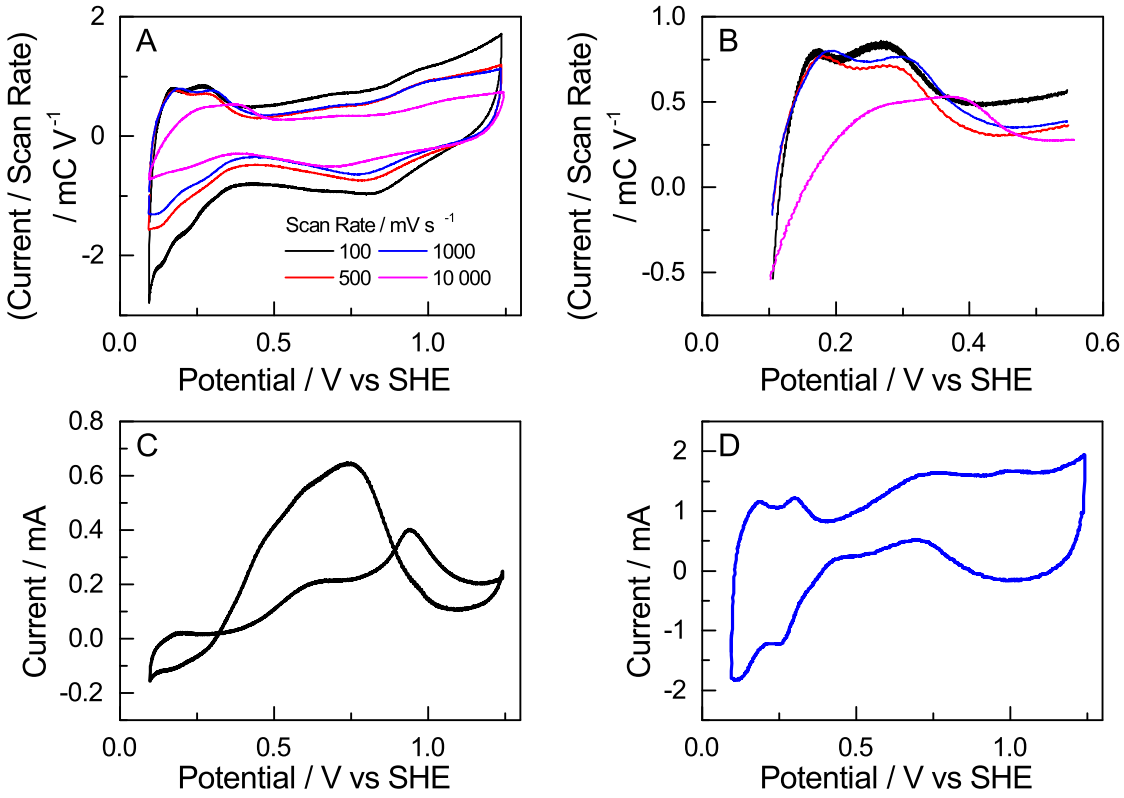

Figure 3.20: The effect of scan rate on voltammetry measured in the RFF cell. A: Cyclic voltammograms of the catalyst layer in 0.5 M $HClO_4$ at different scan rates, normalised to the scan rate. B: An enlargement of the H desorption region in A. C: Voltammogram recorded in 0.5 M HCOOH + 0.5 M $HClO_4$ at a scan rate of 100 mV s^{-1}. D: Voltammogram recorded in 0.5 M HCOOH + 0.5 M at a scan rate of 2000 mV s^{-1}.

FTIR. [5]

Mass transport in the cell was compared to that observed at a rotating disc electrode (fig. 3.21). A 2 µL catalyst film was cast onto both a glassy carbon disc (diameter 7 mm, area 38.5 mm^2) and the IRE (area 5 mm × 8 mm). After cycling in $HClO_4$ to produce a clean catalyst surface and measure the H desorption charge, formic acid (10 mM + 0.5 M $HClO_4$) was introduced and the potential cycled between 0.0 V and 1.2 V at scan rates of 10 mV s^{-1} and 100 mV s^{-1}. This was carried out over a range of flow rates, where the flow rate normal to the electrode is proportional to the square root of the electrode angular frequency ω, in the case of a rotating disc, and proportional to the power $\frac{3}{4}$ in the case of the ATR cell (section 2.1.1). [45] To examine the mass transport limited current in the absence of any catalyst poisoning effects only the backwards, negative-going sweep from high potential was used. The backward sweeps at 10 mV s^{-1} are shown in Panels A and B while the sweeps at 100 mV s^{-1} are shown in C and D. In each case the current has been normalised to the electrochemically active surface area using the H desorption charge measured in Panels E and F, along with a standard charge density for H desorption of 210 µC cm^{-2}. [46]

At 10 mV s^{-1} it can be seen that in the absence of flow the current is negligible in both the RDE and ATR cell cases, suggesting that the HCOOH concentration was depleted in the forward scan. With flow of solution significant current is seen, with the current appearing to be relatively insensitive to the magnitude of the flow rate in both cases. The current density in the ATR cell, however, is around twice that observed on the RDE. These observations suggest that at slow scan rates mass transport in the ATR cell is not significantly limiting the current, and that perhaps the diffusion layer in the cell is smaller than that at the RDE.

The sweeps at 100 mV s^{-1} show different behaviour, with a significant dependence on flow rate observed in both ATR and RDE cases. The peak current was taken to be

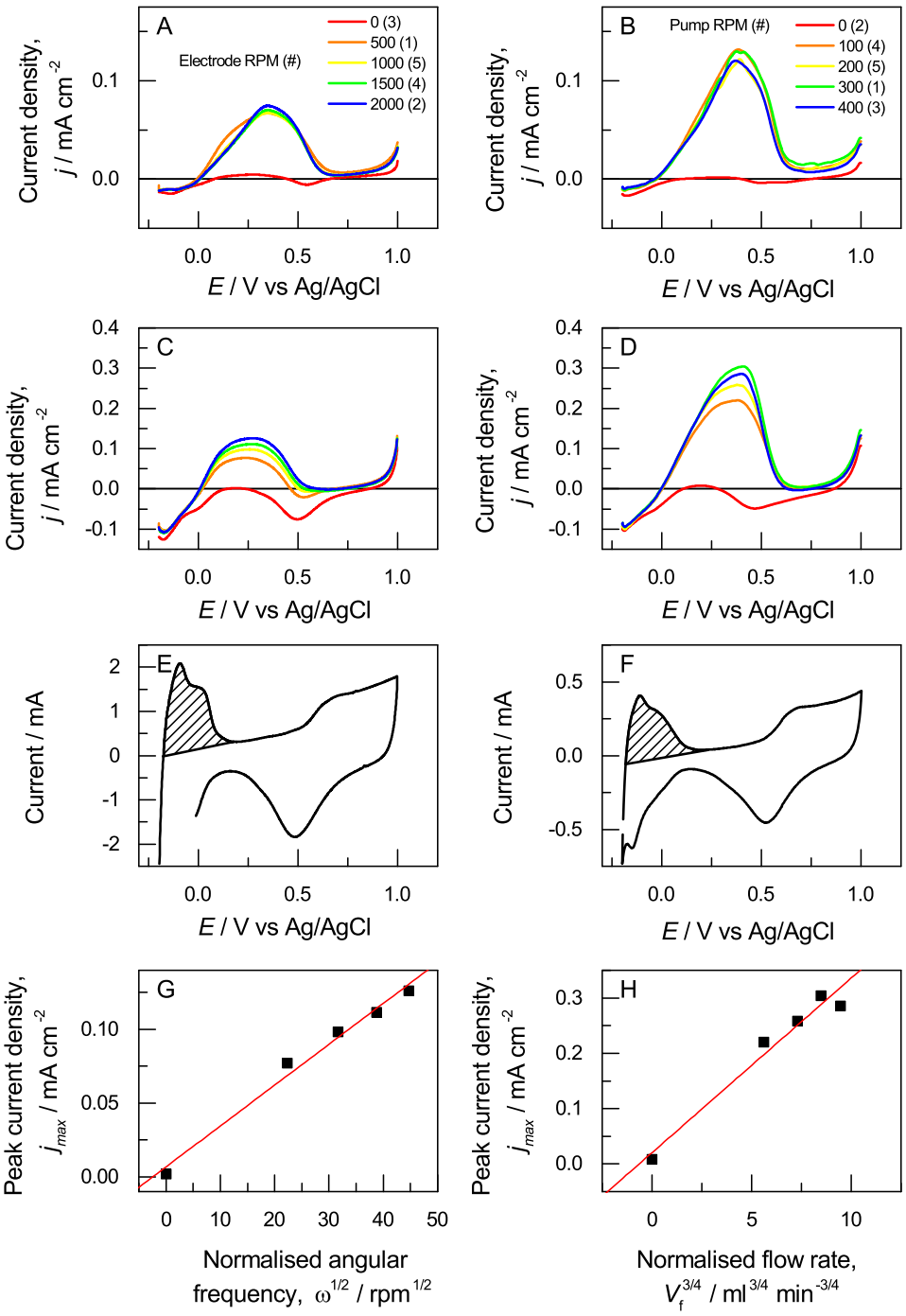

Figure 3.21: Comparison of the flow rate-dependence of cyclic voltammetry obtained at a rotating disc electrode (A, C, E, G) with that obtained in the *in situ* cell (B, D, F, H). Solution: 10 mM HCOOH + 0.5 M $HClO_4$. A and B: Effect of flow rate on the reverse sweep of cyclic voltammetry at 10 mV s^{-1}. Angular frequency and flow rare varied out of sequence, indicated by #. C and D: As in A and B, but with a scan rate of 100 mV s^{-1}. E and F: voltammograms obtained in $HClO_4$. G and H: Peak current density obtained from C and D as a function of normalised flow rate. The red lines are linear fits to the data.

the limiting current in each case and was plotted as a function of normalised flow rate (Panels G and H). The flow rate, obtained from the angular frequency of the electrode ω and the volumetric flow rate, V_f, respectively was normalised using the expressions given in section 2.1.1 for the rotating disc and wall jet electrodes. For the rotating disc the limiting current is given by eq. (2.1) and is expected to be proportional to the square root of ω, while for the wall jet the limiting current is given by eq. (2.2) and is expected to be proportional to $V_f^{3/4}$. [45] In both cases the data show a linear relationship with the normalised flow rate, with $R^2 = 0.993$ and $R^2 = 0.982$ for the RDE and *in situ* cell, respectively.

3.7 Protocol Development

The preceding section dealt with the production of suitable spectro-electrochemical cell for studying supported nanoparticle catalysts. To use the cell effectively, protocols must be developed that enable the reproducible observation of surface species and their correlation with the observed electrochemistry. This requires a reproducible method for preparing well-defined catalyst layers and a method for synchronising the two measurements. Development of these procedures are discussed below.

3.7.1 Instrument Control and Synchronisation

The cell design has been shown to permit cyclic voltammetry at a range of scan rates, with realistic timescales of 10 mV s^{-1} to 100 mV s^{-1}, even up to 1000 mV s^{-1} (see fig. 3.20). Research grade FTIR spectrometers are capable of recording spectra on these timescales in rapid scan mode, without resorting to more involved step scan techniques, and so are easily capable of following these dynamic electrochemical processes. In practice, to do this requires a good level of synchronisation between the measurements, such that the potential range of each spectrum is known. To achieve synchronisation on the order of milliseconds

Table 3.1: Components of the FTS-7000 spectrometer used in this work.

Item	Component Used	Notes
Source	Resitively heated SiC rod (Globar)	Black body source with temperature around 1300 K (see fig. 2.35B for emission spectrum)
Detector	Linearised HgCdTe	Liquid nitrogen-cooled photoconductive detector, 6000 cm^{-1} to 450 cm^{-1}
Optics		
Beamsplitter	KBr	Range 43 500 cm^{-1} to 400 cm^{-1}
Mirrors	Au-coated reflective optics	
ATR Accessory	Al reflective optics	
IRE	Si trapezium	5 reflections, window: 8350 cm^{-1} to 600 cm^{-1}, absorbance around 1100 cm^{-1} due to surface oxide.

requires electronic, hardware-based triggering, as opposed to manual or software based approaches.

To achieve the triggering in the present experimental setup, a program of potential steps and pump controls was set up in the potentiostat's Nova software, such that once started the timing of each event was well-defined. The program was preceded by a command to wait for a high TTL (5 V) signal at one of the potentiostat's digital input ouput ports. The signal was provided by the spectrometer's KTRIG output, which the spectrometer uses to signal the start of a kinetics experiment (available on pin 12 of J340). This signal in turn is controlled by the user starting the kinetics experiment through the spectrometer's Resolutions Pro software. During the experiment signals representing the pump speed are sent as 8 bit bytes from the second DIO port of the potentiostat to an analogue-digital converter (Labjack U3HV) which then outputs an analogue voltage to the pump controller. The complete experimental setup is shown in fig. 3.22.

The configuration of the spectrometer used in this work is shown in table 3.1 and the parameters chosen are shown in table 3.2.

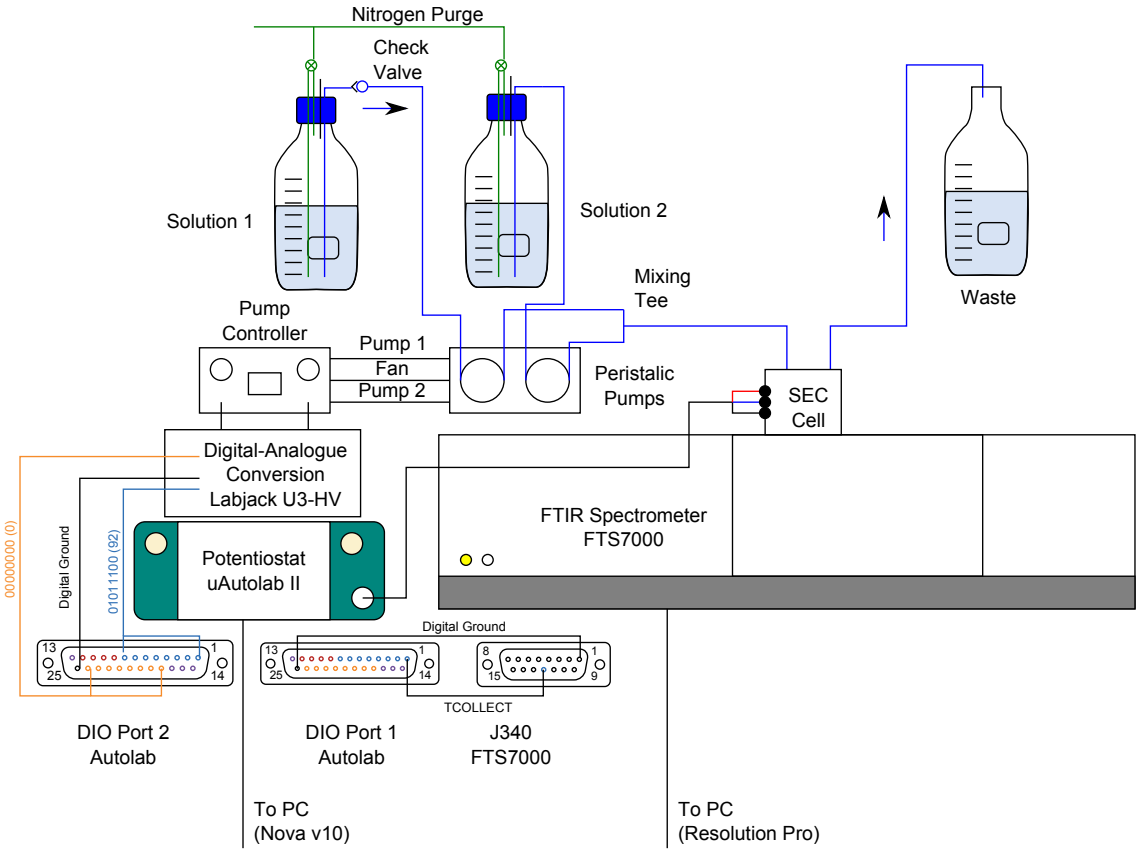

Figure 3.22: Schematic diagram of the experimental setup.

Table 3.2: Collection parameters for the FTS-7000 used in this work.

Parameter	Value	Notes
Resolution	$4\,\mathrm{cm}^{-1}$	Typical peak widths $\gg 4\,\mathrm{cm}^{-1}$
Aperture	Open	
Gain	4-16 ×	Chosen to make signal at zero retardation between 8 V and 10 V
Undersampling Ratio	2	
Mirror Velocity	20 kHz or 40 kHz	40 KHz used in rate experiments.
Electronic Band-pass Filter	5 (0.064 kHz to 5 kHz) or 30 (0.3 kHz to 30 kHz)	Dependent on mirror velocity
Apodization Function	Triangular	

3.7.2 Data Handling and Analysis

A typical spectroelectrochemical experiment, a cyclic voltammogram between 0.0 V and 1.2 V at 10 mV s^{-1} where spectra are recorded at 10 mV intervals between 4000 cm^{-1} to 800 cm^{-1} at 4 cm^{-1} resolution, for example, will produce $240 \times 1600 = 384\,000$ spectral data points and $984 \times 3 = 2952$ electrochemical data points. Correlating and then further processing these data manually would be possible, however automating the tasks would greatly simplify the process and enable more data to be collected and analysed. The technical computing environment Matlab was chosen for ease of use and emphasis on matrix manipulation. By considering the electrochemical and spectral data as matrices with dimensions of time, potential and current, and time, wavenumber and absorbance, respectively, analysis is readily performed, since transformations such as background subtraction and co-addition can be carried out on all spectra simultaneously, as opposed to sequentially. Furthermore, use of matrices enables ready visualisation of any combination of parameters such as absorbance at a particular wavenumber as a function of potential, or the relationship between current and absorbance over time. The script used to import, correlate and co-add the electrochemical and spectroscopic data can be found in section B.1.

3.8 Experimental Procedures

3.8.1 Chemicals

The catalyst used throughout this work was Pt supported on Vulcan XC72R carbon black (60 wt.%, HiSPEC 9000, Alfa Aesar). Pure Vulcan XC72R for control experiments was provided by Cabot Corp. Formic acid (puriss. p.a., $\sim$ 98%, Fluka), Ethanol (puriss. p.a., absolute, $\geq$ 99.8% (GC)), Isopropanol (puriss., $\geq$ 99.5% (GC)), Nafion (perfluorinated resin, aqueous dispersion 10 wt. % in H_2O, eq. wt. 1,100), Sodium phosphate monobasic

monohydrate (puriss. p.a., ACS reagent, $\geq$ 99.0%) and Sodium phosphate dibasic dihydrate (puriss. p.a., 98.5-101.0% (calc. to the dried substance)) were purchased from Sigma Aldrich. Perchloric acid (ca 70% solution in water, for analysis) was purchased from Acros Organics. Sulphuric acid ($\geq$ 98%, Certified AR, for analysis) and Phosphoric acid ($\geq$ 85%, extra pure, SLR) was purchased from Fisher Scientific. Isotopically labelled formic acids, ^{2}HCOOH (98% ^{2}H, $<$ 5% H_2O) and H^{13}COOH (99% ^{13}C, $<$ 5% H_2O) were purchased from Cambridge Isotope Laboratories. All chemicals were used as received. Aqueous solutions were prepared from fresh Milli-Q water (18.2 MΩcm, Millipore). Where necessary solution were purged of O_2 before use by sparging with N_2 from cryogenic boil-off overnight.

3.8.2 Catalyst Inks

3.8.2.1 Ethanol Dispersion

The ethanol dispersion was prepared by adding 25 mg of catalyst powder to 1 mL of ethanol and sonicating for 2 hours until an even dispersion was achieved.

3.8.2.2 Nafion-stabilised Isopropanol Dispersion

The Nafion-stabilised catalyst ink was prepared by adding 4 mg of catalyst powder to a 400 µL mixture of isopropanol, water and Nafion in the ratio 300:100:1. The mixture was mixed and then sonicated for several hours to obtain a homogeneous mixture.

3.8.3 Catalyst Films

A catalyst film was cast by pipetting 10 µL of the ink onto the substrate (electrode or IRE) and drying in air. Films prepared in this way gave a Pt loading of *circa* 150 μg_{Pt} cm^{-2}. This is higher than the 28 μg_{Pt} cm^{-2} loading recommended by Gasteiger et al. to ensure 100% catalyst utilisation during oxygen reduction, [47] however it can be justified by the

increased concentration of reactant used (10 mM to 100 mM HCOOH) as compared to the equilibrium concentration of O_2 in water at atmospheric pressure (ca 1 mM). [48]

3.8.4 Cleaning

The spectroelectrochemical cell components were sonicated and then rinsed thoroughly in Milli-Q water before each use. The silicon IRE was cleaned ultrasonically in concentrated H_2SO_4 to remove traces of silicone sealant before rinsing in water and drying in a stream of N_2. Etching in an O_2 plasma was also used periodically. Before use fresh silicone sealant was applied sparingly to the baseplate and allowed to cure slightly before the IRE was inserted. The graphite flow field was polished to a mirror finish, if necessary starting from abrasive paper (grades 400 up to 2400), using a 1 µm Al_2O_3 slurry (Buehler). The flow field was then rinsed in Milli-Q water, sonicated to remove residual Al_2O_3 and dried using N_2. Tubing was flushed with Milli-Q water before and after each experiment.

References

[1] A. Bewick and S. Pons, "Advances in infrared and raman spectroscopy.," vol. 12 of *Advances in infrared and Raman spectroscopy.*, pp. 1–63, London: Wiley and Heyden, 1985.

[2] S.-G. Sun, "Studying Electrocatalytic Oxidation of Small Organic Molecules with In-Situ Infrared Spectroscopy," in *Electrocatalysis* (J. Lipkowski and P. N. Ross, eds.), John Wiley & Sons, Apr. 1998.

[3] C. Korzeniewski, "Infrared Spectroscopy in Electrochemistry: New Methods and Connections to UhV Surface Science," *Critical Reviews in Analytical Chemistry*, vol. 27, pp. 81–102, July 1997.

[4] J.-M. Léger and F. Hahn, "Contribution of In-situ Infrared Reflectance Spectroscopy in the Study of Nanostructured Fuel Cell Electrodes," in *In-situ Spectroscopic Studies of Adsorption at the Electrode and Electrocatalysis* (Shi-Gang Sun, Paul Andrew Christensen, and Andrzej Wieckowski, eds.), pp. 63–98, Amsterdam: Elsevier Science B.V., 2007.

[5] M. Osawa, "Electrocatalytic Reactions on Platinum Electrodes Studied by Dynamic Surface-Enhanced Infrared Absorption Spectroscopy (SEIRAS)," in *In-situ Spectroscopic Studies of Adsorption at the Electrode and Electrocatalysis*, pp. 209–246, Amsterdam: Elsevier Science B.V., 2007.

[6] C. Korzeniewski, "Ir spectroelectrochemistry: instrumentation and applications of external reflection, atr and transmission sampling," in *In-situ spectroscopic studies of adsorption at the electrode and electrocatalysis* (S.-G. S.-G. Sun, P. A. Christensen, and A. Wieckowski, eds.), Amsterdam ; London: Elsevier, 2007.

[7] A. Rodes, J. M. Pérez, and A. Aldaz, "Vibrational spectroscopy," in *Handbook of Fuel Cells* (W. Vielstich, A. Lamm, H. A. Gasteiger, and H. Yokokawa, eds.), Chichester, UK: John Wiley & Sons, Ltd, Dec. 2010.

[8] P. A. Christensen, "In-situ Fourier transform infra red spectroelectrochemistry as a probe of electrocatalysis," in *Spectroscopic Properties of Inorganic and Organometallic Compounds*, vol. 41, pp. 125–165, 2010.

[9] T. Iwasita and F. C. Nart, "In situ infrared spectroscopy at electrochemical interfaces," *Progress in surface science*, vol. 55, no. 4, pp. 271–340, 1997.

[10] O. Cherstiouk, P. Simonov, and E. Savinova, "Model approach to evaluate particle size effects in electrocatalysis: preparation and properties of Pt nanoparticles supported on GC and HOPG," *Electrochimica Acta*, vol. 48, pp. 3851–3860, Nov. 2003.

[11] I. Villegas and M. J. Weaver, "Carbon monoxide adlayer structures on platinum (111) electrodes: A synergy between in-situ scanning tunneling microscopy and infrared spectroscopy," *The Journal of Chemical Physics*, vol. 101, pp. 1648–1660, July 1994.

[12] M. Heinen, Y.-X. Chen, Z. Jusys, and R. J. Behm, "Room Temperature COad Desorption/Exchange Kinetics on Pt Electrodes—A Combined In Situ IR and Mass Spectrometry Study," *ChemPhysChem*, vol. 8, pp. 2484–2489, Dec. 2007.

[13] Y. E. Seidel, A. Schneider, Z. Jusys, B. Wickman, B. Kasemo, and R. J. Behm, "Transport effects in the electrooxidation of methanol studied on nanostructured Pt/glassy carbon electrodes," *Langmuir*, vol. 26, no. 5, pp. 3569–3578, 2009.

[14] D. Zhang, O. Deutschmann, Y. E. Seidel, and R. J. Behm, "Interaction of Mass Transport and Reaction Kinetics during Electrocatalytic CO Oxidation in a Thin-Layer Flow Cell," *The Journal of Physical Chemistry C*, vol. 115, pp. 468–478, Jan. 2011.

[15] D. Roe, J. Sass, D. Bethune, and A. Luntz, "Prospects for transient IR reflection-absorption spectroscopy of adsorbed species on electrode surfaces," *Journal of Electroanalytical Chemistry and Interfacial Electrochemistry*, vol. 216, pp. 293–301, Sept. 1987.

[16] J. D. Roth and M. J. Weaver, "The electrooxidation of carbon monoxide on platinum as examined by surface infrared spectroscopy under forced hydrodynamic conditions," *Journal of Electroanalytical Chemistry and Interfacial Electrochemistry*, vol. 307, pp. 119–137, June 1991.

[17] A. Otto, "Excitation of nonradiative surface plasma waves in silver by the method of frustrated total reflection," *Zeitschrift für Physik*, vol. 216, pp. 398–410, Aug. 1968.

[18] S. M. Moon, C. Bock, and B. MacDougall, "Setup, sensitivity and application of thin electrolyte layer ATR-FTIR spectroscopy," *Journal of Electroanalytical Chemistry*, vol. 568, pp. 225–233, July 2004.

[19] E. Kretschmann, "Die bestimmung optischer konstanten von metallen durch anregung von oberflächenplasmaschwingungen," *Zeitschrift für Physik*, vol. 241, pp. 313–324, Aug. 1971.

[20] K. Ataka, Y. Hara, and M. Osawa, "A new approach to electrode kinetics and dynamics by potential modulated Fourier transform infrared spectroscopy," *Journal of Electroanalytical Chemistry*, vol. 473, pp. 34–42, Sept. 1999.

[21] Z. Jusys, H. Massong, and H. Baltruschat, "A New Approach for Simultaneous DEMS and EQCM: Electro-oxidation of Adsorbed CO on Pt and Pt-Ru," *Journal of The Electrochemical Society*, vol. 146, pp. 1093–1098, Jan. 1999.

[22] K.-i. Ataka, T. Yotsuyanagi, and M. Osawa, "Potential-dependent reorientation of water molecules at an electrode/electrolyte interface studied by surface-enhanced infrared absorption spectroscopy," *The Journal of Physical Chemistry*, vol. 100, no. 25, pp. 10664–10672, 1996.

[23] H. Miyake, S. Ye, and M. Osawa, "Electroless deposition of gold thin films on silicon for surface-enhanced infrared spectroelectrochemistry," *Electrochemistry Communications*, vol. 4, pp. 973–977, Dec. 2002.

[24] M. Osawa and K.-i. Ataka, "Electromagnetic mechanism of enhanced infrared absorption of molecules adsorbed on metal island films," *Surface Science*, vol. 262, pp. L118–L122, Feb. 1992.

[25] Y. Nishikawa, K. Fujiwara, K. Ataka, and M. Osawa, "Surface-enhanced infrared external reflection spectroscopy at low reflective surfaces and its application to surface analysis of semiconductors, glasses, and polymers," *Analytical Chemistry*, vol. 65, pp. 556–562, Mar. 1993.

[26] M. Osawa, "In-situ Surface-Enhanced Infrared Spectroscopy of the Electrode/Solution Interface," in *Advances in Electrochemical Sciences and Engineering*, vol. 9, pp. 269–314, Weinheim, Germany: Wiley-VCH Verlag GmbH, July 2006.

[27] M. Nesselberger, S. J. Ashton, G. K. H. Wiberg, and M. Arenz, "Design, development, and demonstration of a fully LabVIEW controlled in situ electrochemical Fourier transform infrared setup combined with a wall-jet electrode to investigate the electrochemical interface of nanoparticulate electrocatalysts under reaction conditions," *Review of Scientific Instruments*, vol. 84, p. 074103, July 2013.

[28] H.-X. Zhang, S.-H. Wang, K. Jiang, T. André, and W.-B. Cai, "In situ spectroscopic investigation of CO accumulation and poisoning on Pd black surfaces in concentrated HCOOH," *Journal of Power Sources*, vol. 199, pp. 165–169, Feb. 2012.

[29] A. J. Healy, H. A. Reeve, and K. A. Vincent, "Development of an infrared spectroscopic approach for studying metalloenzyme active site chemistry under direct electrochemical control," *Faraday Discussions*, vol. 148, p. 345, 2011.

[30] A. J. Healy, P. A. Ash, O. Lenz, and K. A. Vincent, "Attenuated total reflectance infrared spectroelectrochemistry at a carbon particle electrode; unmediated redox control of a [NiFe]-hydrogenase solution," *Physical Chemistry Chemical Physics*, vol. 15, pp. 7055–7059, Apr. 2013.

[31] E. Ong, *Developing methods for understanding catalytic specificity of hydrogenases and metal nanoparticle fuel cell catalysts*. Thesis submitted for the honour school of chemistry: Chemistry part ii, University of Oxford, Oxford, 2010.

[32] I. J. McPherson, *IR Spectroelectrochemistry for Understanding Energy-related Catalysis*. Thesis submitted for the honour school of chemistry: Chemistry part ii, University of Oxford, Oxford, June 2011.

[33] D. L. Wood III, J. S. Yi, and T. V. Nguyen, "Effect of direct liquid water injection and interdigitated flow field on the performance of proton exchange membrane fuel cells," *Electrochimica Acta*, vol. 43, pp. 3795–3809, Aug. 1998.

[34] L. Chen, H.-B. Luan, Y.-L. He, and W.-Q. Tao, "Pore-scale flow and mass transport in gas diffusion layer of proton exchange membrane fuel cell with interdigitated flow fields," *International Journal of Thermal Sciences*, vol. 51, pp. 132–144, Jan. 2012.

[35] J. H. Moore, C. C. Davis, M. A. Coplan, and S. C. Greer, *Building Scientific Apparatus*. Cambridge, UK ; New York: Cambridge University Press, 4 edition ed., June 2009.

[36] T. J. Schmidt and H. A. Gasteiger, "Rotating thin-film method for supported catalysts," in *Handbook of Fuel Cells*, John Wiley & Sons, Ltd, 2010.

[37] V. Stamenković, M. Arenz, P. N. Ross, and N. M. Marković, "Temperature-Induced Deposition Method for Anchoring Metallic Nanoparticles onto Reflective Substrates for in Situ Electrochemical Infrared Spectroscopy," *The Journal of Physical Chemistry B*, vol. 108, pp. 17915–17920, Nov. 2004.

[38] S. Park, Y. Tong, A. Wieckowski, and M. J. Weaver, "Infrared reflection-absorption properties of platinum nanoparticle films on metal electrode substrates: control of anomalous optical effects," *Electrochemistry Communications*, vol. 3, pp. 509–513, Sept. 2001.

[39] K. A. Friedrich, F. Henglein, U. Stimming, and W. Unkauf, "In-situ vibrational spectroscopy on Pt electrocatalysts," *Electrochimica Acta*, vol. 47, pp. 689–694, Dec. 2001.

[40] A. Hartstein, J. R. Kirtley, and J. C. Tsang, "Enhancement of the Infrared Absorption from Molecular Monolayers with Thin Metal Overlayers," *Physical Review Letters*, vol. 45, pp. 201–204, July 1980.

[41] S. Srinivasan and E. Gileadi, "The potential-sweep method: a theoretical analysis," *Electrochimica Acta*, vol. 11, no. 3, pp. 321–335, 1966.

[42] A. J. Bard and L. R. Faulkner, *Electrochemical Methods: Fundamentals and Applications*. New York: Wiley, 2 edition ed., Dec. 2000.

[43] H. Okamoto, W. Kon, and Y. Mukouyama, "Five Current Peaks in Voltammograms for Oxidations of Formic Acid, Formaldehyde, and Methanol on Platinum," *The Journal of Physical Chemistry B*, vol. 109, no. 32, pp. 15659–15666, 2005.

[44] J. Xu, D. Yuan, F. Yang, D. Mei, Z. Zhang, and Y.-X. Chen, "On the mechanism of the direct pathway for formic acid oxidation at a Pt(111) electrode," *Physical Chemistry Chemical Physics*, vol. 15, pp. 4367–4376, Feb. 2013.

[45] A. R. Mount, "Hydrodynamic Electrodes," in *Encyclopedia of Electrochemistry*, Wiley-VCH Verlag GmbH & Co. KGaA, 2007.

[46] S. Trasatti and O. A. Petrii, "Real surface area measurements in electrochemistry," *Journal of Electroanalytical Chemistry*, vol. 327, pp. 353–376, June 1992.

[47] T. J. Schmidt, H. A. Gasteiger, G. D. Stäb, P. M. Urban, D. M. Kolb, and R. J. Behm, "Characterization of High-Surface-Area Electrocatalysts Using a Rotating Disk Electrode Configuration," *Journal of The Electrochemical Society*, vol. 145, pp. 2354–2358, Jan. 1998.

[48] J. Speight, *Lange's Handbook of Chemistry, 70th Anniversary Edition*. McGraw-Hill Professional, 16 edition ed., Jan. 2005.

Chapter 4

Carbon Monoxide Electrooxidation by Carbon-supported Platinum

4.1 Carbon Monoxide in Electrocatalysis

4.1.1 Carbon Monoxide Formation

The oxidation of CO is one of the central reactions in electrocatalysis, both from a practical perspective, since it is a common impurity in H_2 feedstocks and must therefore be oxidised alongside H_2 in PEM fuel cells, and from a fundamental perspective, since it is comparatively easy to study and may therefore offer insight into the mechanism of oxidation of larger molecules. [1–5]

Carbon monoxide is a strong field ligand due to its low lying $\pi*$ molecular orbitals (chapter 2); consequently it can adsorb strongly to many metal surfaces, poisoning catalysts by blocking surface sites. Such poisoning is relevant to fuel cells for a variety of reasons. For H_2 fuel cells, poisoning occurs due to the carbon monoxide present in H_2 gas produced by steam reforming and subsequent water-gas shift reaction of methane (eqs. (4.1) and (4.2)).

$$CH_4 + H_2O \rightleftharpoons CO + 3\,H_2 \tag{4.1}$$

$$H_2O + CO \rightleftharpoons H_2 + CO_2 \tag{4.2}$$

For fuel cells running on small organic molecules, the process of breaking down the molecule into a one carbon (C_1) fragment usually requires addition of O atoms, resulting in the formation of CO species. [6] Even for C_1 fuels such as formic acid or methanol, which already have a C−O bond, the strength of CO bonding to the surface results in at least one pathway producing adsorbed CO. [7, 8] For example formic acid decomposes to form CO in a process of dehydration (eq. (4.3)). [9]

$$\mathrm{HCOOH} \longrightarrow \mathrm{CO} + \mathrm{H_2O} \tag{4.3}$$

4.1.2 Carbon Monoxide Oxidation

In electrocatalysis the poisoning effect of CO adsorption can be overcome by increasing the electrode potential to oxidatively remove the CO. On metals such as Pt the oxidation of CO follows a Langmuir-Hinshelwood mechanism, in which the adsorbed CO reacts with an adsorbed oxygen-containing species such as OH (eq. (5.32)). [1] These are formed from H_2O at high potentials just below the oxygen evolution potential ($E^\circ(O_2/H_2O) = 1.23\,\mathrm{V}$). However, in a fuel cell such high polarisation of the anode decreases the cell voltage and therefore the efficiency of the fuel cell. As a result there is a concerted effort to find catalysts for fuel cells which can oxidatively remove CO at low potentials.

$$\mathrm{CO(g)} \longrightarrow \mathrm{CO(ads)} \tag{4.4}$$

$$\mathrm{H_2O(l)} \longrightarrow \mathrm{OH(ads)} + \mathrm{H^+} + \mathrm{e} \tag{4.5}$$

$$\mathrm{CO(ads)} + \mathrm{OH(ads)} \longrightarrow \mathrm{CO_2} + \mathrm{H^+} + \mathrm{e} \tag{4.6}$$

The main strategy currently used to decrease the potential for CO oxidation is to make bifunctional catalysts. These catalysts have a certain fraction of their surface sites replaced by a second metal which is more oxophillic, and thus has a lower overpotential

for OH formation. [10] Commonly used oxophillic metals include Sn, Ru and Ni. [11, 12] Another significant parameter when designing CO-tolerant catalysts is surface structure. As discussed in Chapter 2, the coordination number of surface sites can dramatically affect their adsorption properties. Both catalyst composition and surface structure have been studied using single crystal models, [11, 13, 14] however to fully understand the CO oxidation reaction at different nanoparticle catalysts the reaction must be studied at the nanoparticles themselves. The strong IR absorption of adsorbed CO, along with the high sensitivity of the absorption spectrum to local coordination number, electrode potential and CO coverage, make *in situ* infrared spectroscopy a useful tool in such studies.

In this chapter the experimental procedures and apparatus developed in Chapter 3 are demonstrated in a study of CO oxidation at a commercial carbon-supported Pt fuel cell catalyst. In order to correlate the observed electrochemical and spectroscopic data with the structure of the catalyst, scanning transmission electron microscopy (STEM) and cyclic voltammetry (CV) will first be used to characterise the catalyst. The interaction of CO with the catalyst will then be studied using *in situ* IR spectroscopy. Analysis of the absorption spectra will be carried out by modelling the IR absorption of the catalyst layer. Fitting of the model to the experimental spectra will then be used to extract peak properties such as centre, width and intensity. The variation in peak properties with potential and time will then be used to probe the mechanism of CO oxidation on the catalyst.

4.2 Structural Characterisation

4.2.1 Scanning Transmission Electron Microscopy

The electron microscopy and particle size analysis in this section was performed by Dr L. Jones and A. Varambhia, Department of Materials, University of Oxford.

The catalyst morphology was characterised using high angle annular dark field scanning transmission electron microscopy (HAADF-STEM). The dark field signal in STEM arises from electrons scattered by the sample, so that the catalyst appears bright and the background appears dark. Furthermore, by collecting high angle scattering the intensity is predominantly determined by the atomic number, allowing light elements such as carbon to be readily distinguished from heavier elements such as Pt. [15, 16] Samples are studied by depositing them onto metal grids covered in a thin layer of carbon, with the carbon there to support the sample in regions between the grid bars. To avoid interference from carbon, 'holey carbon' layers can be used, in which the carbon layer has many small holes over which the sample can be suspended.

To prepare the sample several mg of catalyst powder was ground up with a drop of ethanol using a pestle and mortar to form a suspension. The suspension was then diluted in ethanol and further dispersed by ultrasonication. A droplet of this dilute suspension was then applied to a holey carbon Cu TEM grid and allowed to dry in air. The grid was then mounted on the microscope probe and further dried under vacuum with heating from an incandescent light source before insertion into the microscope.

Images of the catalyst obtained using STEM are shown in figs. 4.1 and 4.2. For orientation a low magnification (50 000×) image of the catalyst on the grid is shown in fig. 4.1A; to highlight the different parts of the image, a coloured version of the image is shown in panel B. The darkest regions in A, highlighted in red in panel B, represent regions of vacuum: the holes in the holey carbon. The carbon layer itself is shown in dark blue in panel B. The lighter blue regions shows the amorphous carbon of the catalyst support, while the brighter pinks and yellows show the location of metal. The only elements detected by energy dispersive X-ray spectroscopy were Pt, C and Cu (from the TEM grid).

The low magnification image suggests a certain amount of connectivity between the

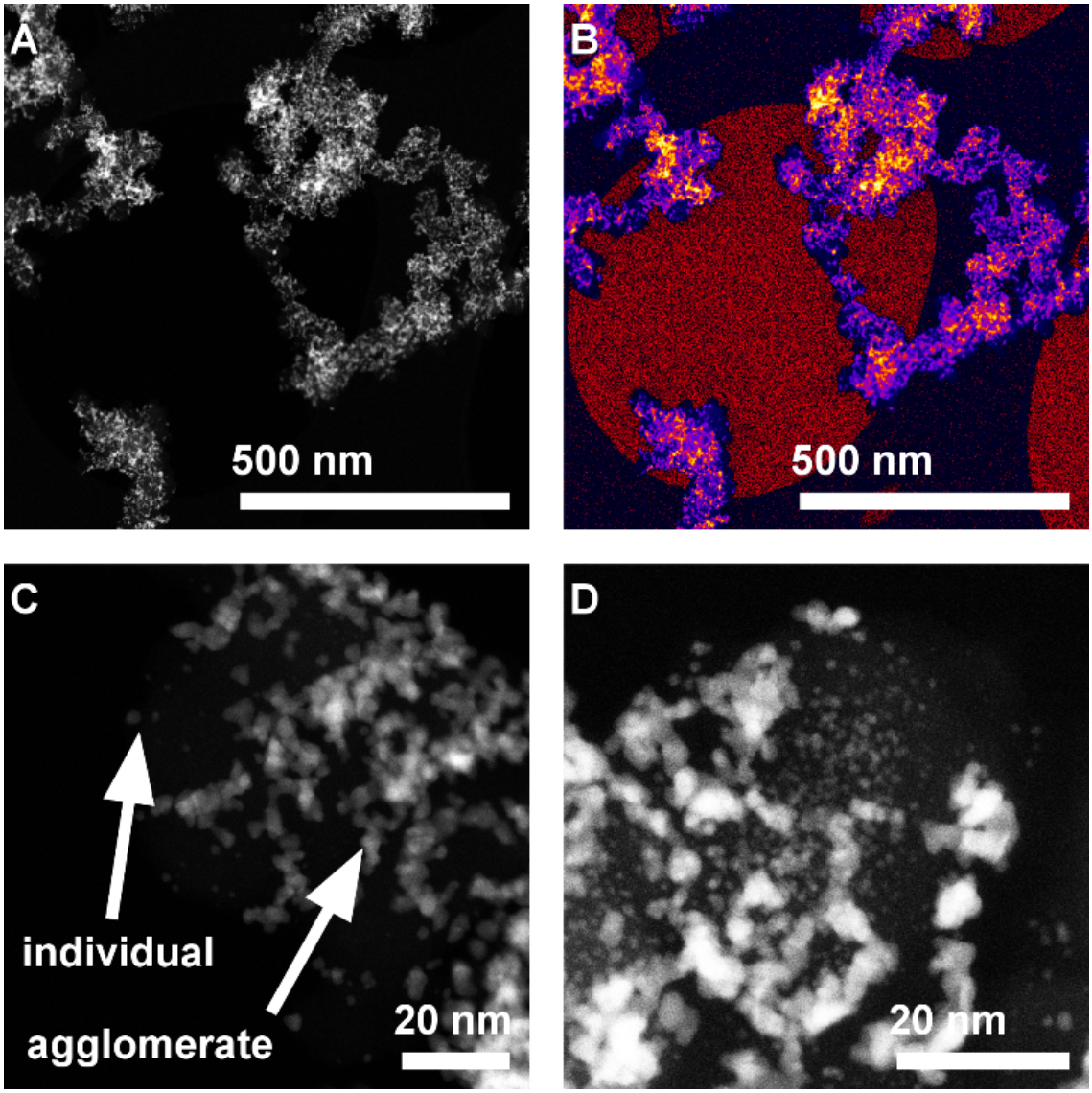

Figure 4.1: Distribution and morphology of Pt in the carbon-supported Pt catalyst. A: Low magnification (50 000×) image of one region of the grid. B: Panel A coloured to emphasise different components: red - vacuum, dark blue - holey carbon, light blue - amorphous carbon catalyst support, pink and yellow - Pt. C: Higher magnification (500 000×) image of the catalyst. Two distinct morphologies are indicated by arrows: individual particles and agglomerates. D: High magnification (800 000×) image of a different region of the catalyst.

particles and this is confirmed at higher magnification. Panels C and D show the extent of what appears to be agglomeration of the particles; visual inspection suggests that its is predominantly larger particles that form the agglomerates, leaving smaller particles well separated on the carbon support. Similar morphologies have been reported for unsupported nanoparticles. [17]

Higher magnification was used to examine the morphology of the catalyst particles in more detail (fig. 4.2). Lattice fringes, which occur when crystalline material lies with one of its crystallographic axis aligned in the beam direction, such that electrons are alternately transmitted through and scattered by the atomic lattice, were observed in a number of cases. Furthermore, some particles were observed to posses well-defined shapes (panel D), suggesting the possibility that the catalyst may contain some extended atomic terraces. Interestingly fringes were observed for both agglomerated catalyst and individual particles (Panel D), with the fringes of some agglomerated particles appearing to be in register (panel B). Thus the catalyst can be considered as a mixture of single and polycrystalline particles.

Automated particle size analysis was attempted from the (50) images collected, although its implementation was complicated by the significant amount of agglomeration. At first the agglomerated particles were removed from the images to enable the individual particles to be sized. This was accomplished by manually masking off regions of the image containing agglomerated particles. An edge finding algorithm was used to automatically detect individual particles and then calculate their effective diameter, assuming them to be circular. The size distribution obtained in this way is shown as a histogram in fig. 4.3A. Effective diameters less than 0.2 nm were not included and each bar represents a range of 0.2 nm.

A size analysis of the agglomerates was also attempted, by considering the diameter of the constituent particles. In this case the images were not masked and the edge finding

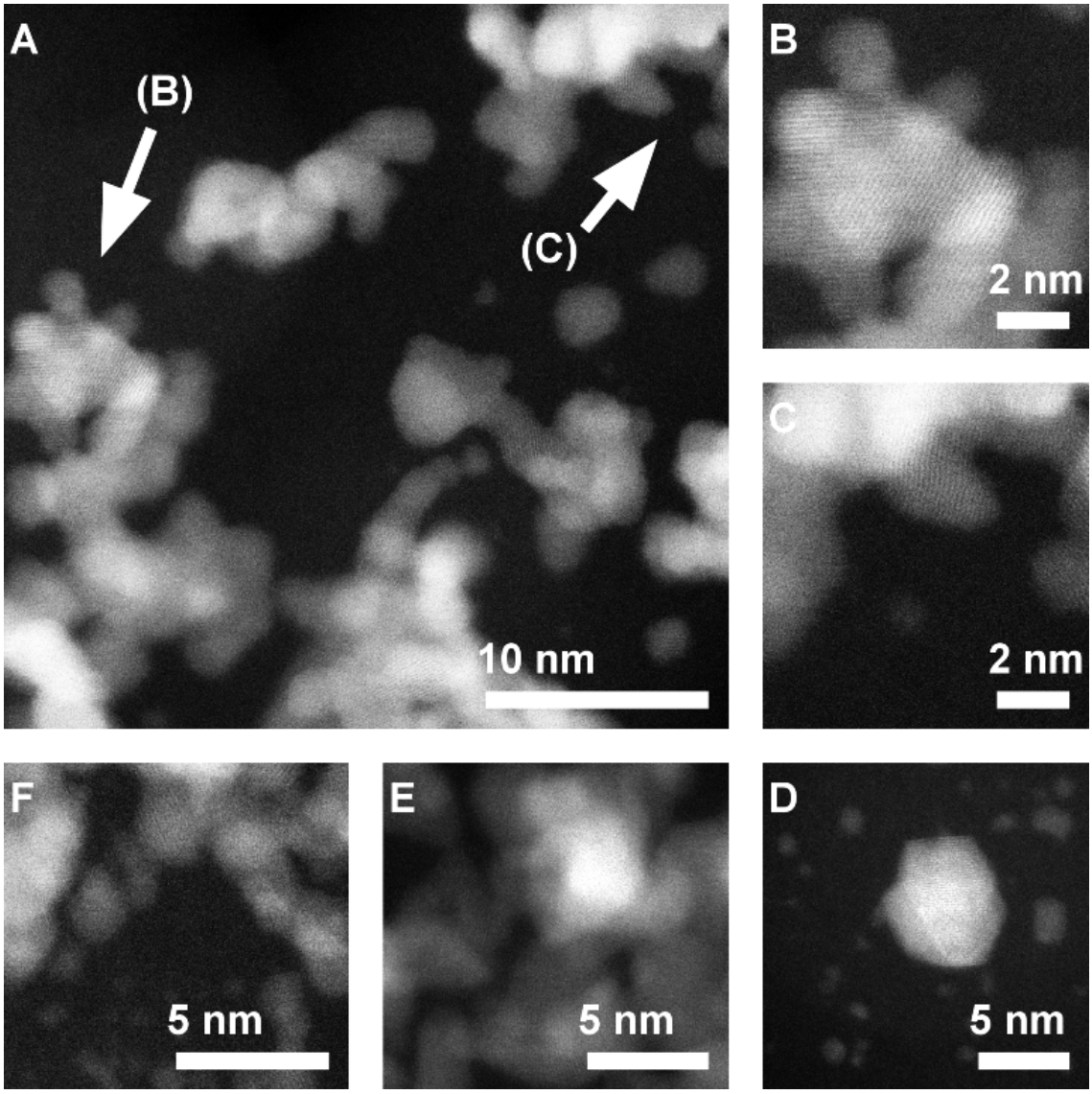

Figure 4.2: High magnification STEM images of both agglomerated and individual catalyst particles showing lattice fringes. A: region showing multiple particles with lattice fringes; B,C: magnified regions in A. D: larger particle showing both lattice fringes and a well defined shape; E,F: further regions showing lattice fringes.

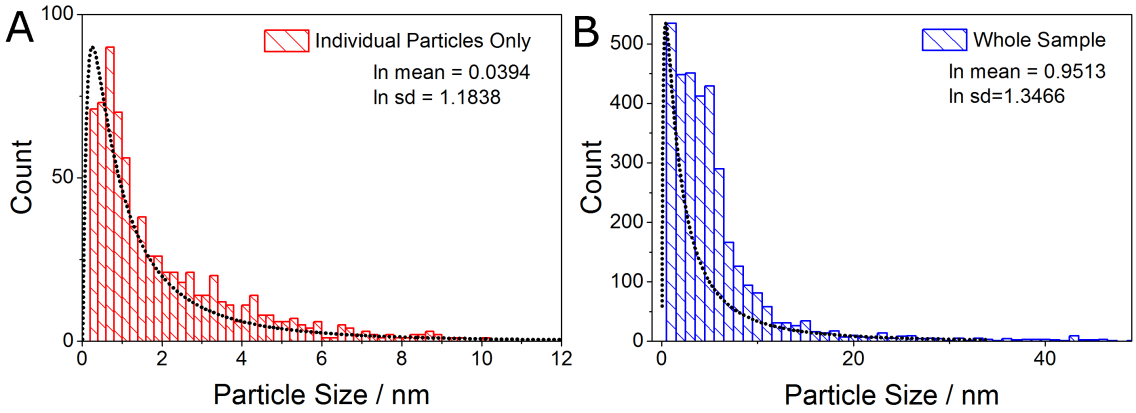

Figure 4.3: Size distribution analysis of the catalyst particles. A: Histogram of calculated sizes for individual catalyst particles, excluding agglomerates. B: Histogram of calculated particle sizes including agglomerated particles. Particle size cut-off size: 0.2 nm, bin size: 1 nm. Dashed line: fitted lognormal distribution.

procedure was used to separate areas of high intensity into multiple parts. The effective diameter of these parts was then calculated. The size distribution of the whole sample, including both individual and agglomerated particles, is shown in fig. 4.3B. Again effective diameters less than 0.2 nm were not included and each bar represents 1 nm.

The size distribution of the individual particles displays a maximum around 1 nm and a broad tail reaching out to around 6 nm. The particle size can be compared to a lognormal distribution (black dashed line), however the peak appears broader than that predicted by the lognormal distribution. Similarly the histogram for the whole sample, including the aggregates, shows a maximum in the range 0.2 nm to 5 nm, although the there are a significant number of particles in the range 5 nm to 10 nm and a tail which falls to less than 10% around 20 nm. When compared to the lognormal distribution, it can be seen again that the width of the distribution is too narrow as it still does not appear to take into account the number of particles in the 10 nm range.

4.2.2 Cyclic Voltammetry

Whereas the STEM analysis reveals local structure and microscopic detail on the level of individual particles, electrochemistry provides macroscopic characterisation, with all of the catalyst particles contributing to the observed current. The microscopy suggests that a significant fraction of the catalyst is highly crystalline and is therefore likely to present well-ordered surfaces to the solution. This can be verified with cyclic voltammetry in H_2SO_4 solution, using the well-defined features of hydrogen adsorption and desorption (Chapter 2). From work on single crystal Pt electrodes, it is known that in H_2SO_4 desorption of H and adsorption of $(H)SO_4$ from the (110)-(1×2) surface gives rise to a large current peak between 0.05 and 0.35V, while on the (100)-(1×1) plane two current peaks are observed, the largest at 0.4 V from the (100) terrace, and the smaller one at 0.25 V attributed to step edges resulting from adsorption-induced surface reconstruction (fig. 4.4(a)-(c)). [11, 18]

A catalyst film was prepared in the *in situ* cell as described in Chapter 3 and 0.5 M H_2SO_4 was introduced. The potential was held at 0.05 V for 5 s and then cycled 10 times between 0 V and 1.2 V at 10 mV s^{-1} (fig. 4.4(d)). The voltammogram reveals 3 positive peaks in the positive potential sweep and 2 negative peaks in the negative sweep. Such a voltammogram was well reproduced from subsequent catalyst films. The positive/negative peaks are at: Peak 1, 0.09 V/0.07 V, Peak 2, 0.16 V and Peak 3, 0.22 V/0.20 V. In general all the peaks are at slightly lower potentials than observed on massive Pt electrodes (both poly and single crystalline, fig. 2.17), perhaps unsurprising given the likely differences between terraces on single crystals and those on small nanoparticles. Thus, these peaks are assigned to the adsorption (negative peaks) and desorption (positive peaks) of H on/from the (110) terrace, (100) step and (100) terrace, respectively. Such clearly defined peaks are taken as an indication that a significant fraction of the catalyst surface is composed of low index planes of Pt.

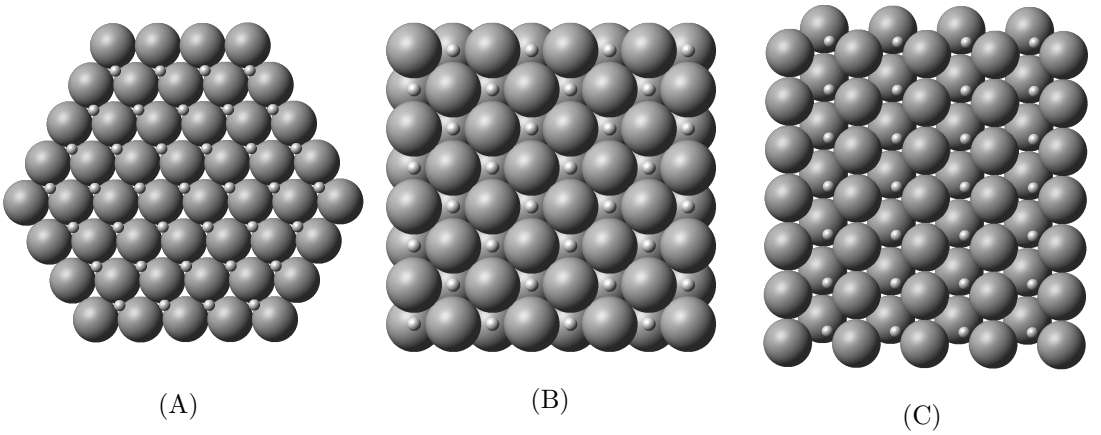

(A) (B) (C)

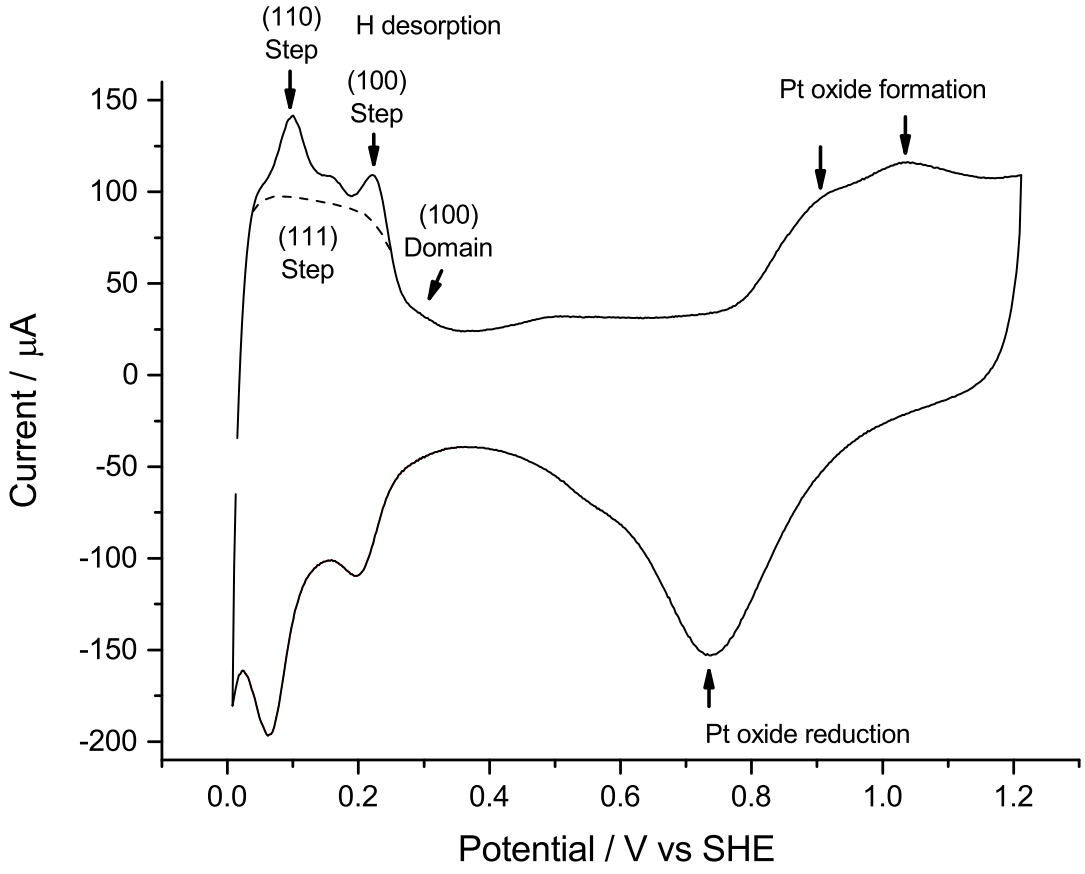

(D)

Figure 4.4: Characterisation of the Pt surface structure using H adsorption. Most likely sites for H adsorption (white) are shown for the (a)(111), (b)(100) and (c)(110) planes of Pt (grey). [11] (d) Cyclic voltammetry of Pt/C in 0.5 M H_2SO_4, obtained in the *in situ* cell. Potential cycled between 0.0 V and 1.2 V 10 times, final cycle shown. Current peaks assigned to H desorption from (110) and (100) planes marked by arrows. Dotted line indicates contribution of desorption from (111) steps.

4.3 Carbon Monoxide Adsorption Studied by *in situ* Infrared Spectroscopy

Following analysis of the catalyst structure, the adsorption of CO was investigated using IR reflection spectroscopy. As discussed in Chapter 2, the reflectivity measured in reflection spectra is a function of the refractive indices of the media at the interface. Under certain conditions, such as those found in ATR-SEIRA measurements, the reflectivity is dominated by absorption, and reflection spectra are composed of peaks. However, under the conditions used in this work the reflectivity is determined by a combination of the materials' refractive indices and their extinction coefficients. As a result the spectra are composed of first derivative-like signals, resembling the anomalous dispersion seen in the refractive index in the region of an absorption peak. To extract values for the peak position, intensity and width from such data, the refractive index and extinction coefficient of the catalyst layer must be modelled and then fit to the observed data. To enable a quantitative analysis, the effect of CO coverage on these parameters must also be investigated to establish a calibration curve.

4.3.1 The IR Reflectance Spectrum of CO Adsorbed on Pt Nanoparticles

To investigate the adsorption of CO on the catalyst, a catalyst layer was first prepared and cycled in H_2SO_4 until a stable voltammogram was obtained. As described in section 4.2.2, this procedure leaves a clean catalyst surface with a well defined surface area. Following the cyclic voltammetry the potential was set to 0.05 V and a background spectrum collected. Spectra were then obtained during the adsorption and subsequent oxidation of CO at a rate of $5\,s^{-1}$.

To introduce CO, H_2SO_4 was saturated with CO gas and then flowed through the cell

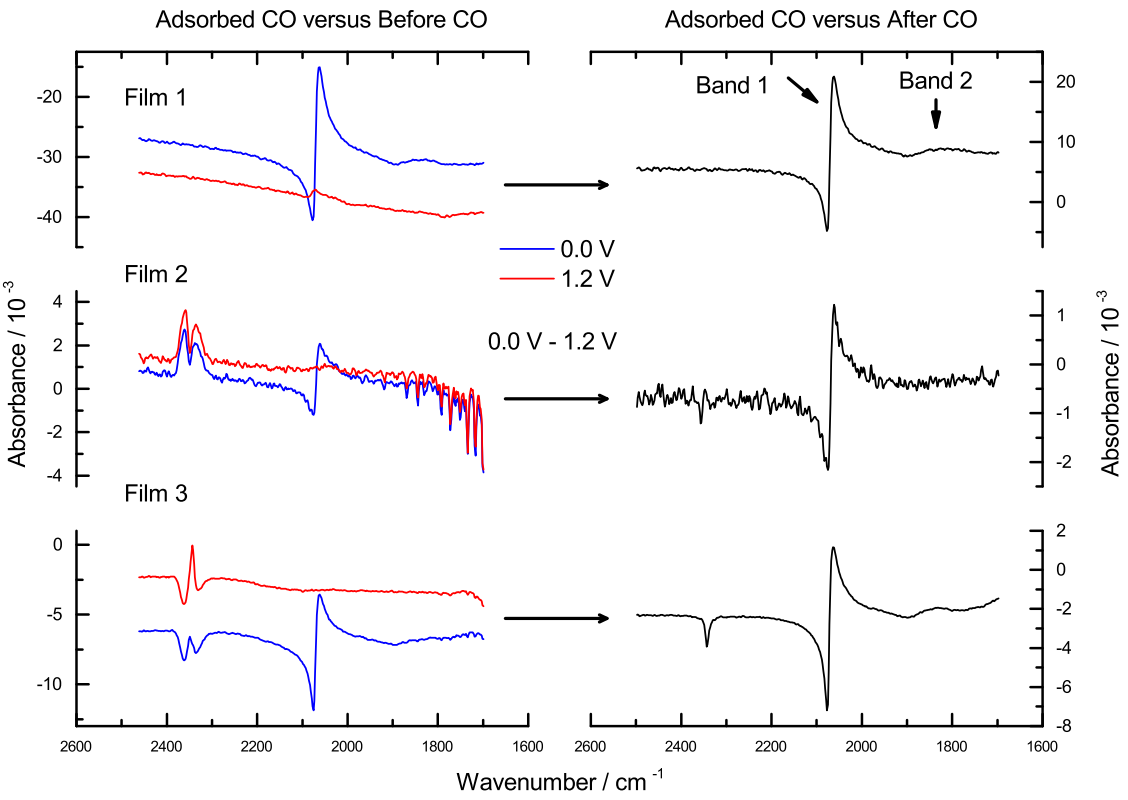

Figure 4.5: Infrared spectra of identical catalyst layers after CO adsorption from CO-saturated H_2SO_4 solution at 0.0 V. Left: Spectra of catalyst layers at 0.0 V after adsorption of CO (blue) and 1.2 V after oxidative removal of CO (red). Background: 0.0 V before introduction of CO. Right: Spectra reprocessed as 0.0 V-1.2 V.

for 300 s. No change in the observed band intensity was observed after 200 s, indicating that a saturated CO adlayer had formed. To remove any interference from bulk CO left in solution, N_2-saturated H_2SO_4 was flushed through the cell for a further 300 s. Again, no change in CO band intensity was observed during this process, confirming that CO adsorption is irreversible. Following adsorption the CO was oxidatively removed during a potential sweep (to be discussed in the next section) leaving a CO-free surface.

Spectra obtained during this process are shown for three independent catalyst layers on the left hand side of fig. 4.5, processed against the initial pre-CO background. The blue spectra were obtained after adsorption, while the subsequent red spectra were recorded following oxidative removal of CO. The blue spectra show a large band around 2070 cm^{-1} and a smaller hump around 1800 cm^{-1}, which are both absent from the higher potential

spectra. Films 2 and 3 also show contributions from atmospheric gases CO_2 and H_2O whose concentrations fluctuate inside the spectrometer, and the 1.2 V spectrum in Film 3 also has a contribution from dissolved CO_2 which has accumulated during the CO oxidation and has not been fully removed by the flow of H_2SO_4. The slope of the baseline and interference from atmospheric H_2O and CO_2 complicate the spectra, particularly in the low wavenumber region, and so these contributions were removed by subtraction of the corresponding high potential spectra. The reprocessed spectra are shown on the right hand side of the fig. 4.5, with the location of the two CO bands indicated.

The higher wavenumber band present in all of these spectra is clearly bipolar, with both positive and negative lobes, while the lower wavenumber band is much broader, making its shape hard to discern. In both cases determination of the band centre, height and width is complicated by the band shape. To extract parameters from this type of spectrum, and allow quantitative analysis of the adsorbed CO, the spectrum must be modelled.

4.3.2 A Model for the IR Reflection Spectrum of CO Adsorbed on Pt Nanoparticles

To develop a suitable model for the bipolar band shapes observed in the previous section, the spectrum of the catalyst layer with adsorbed CO must be simulated. To do this it is necessary to have a model for the refractive index of the catalyst layer. This is non-trivial since the catalyst layer is a strongly inhomogeneous medium composed of metal catalyst in various forms of agglomeration, carbon support particles, water, supporting electrolyte as well as the adsorbed CO (fig. 4.6).

There are several ways to develop such a model. One approach is to derive the refractive indices of all of the components of the catalyst layer, using physical models for each component's interaction with the incident light, and then to combine them using an

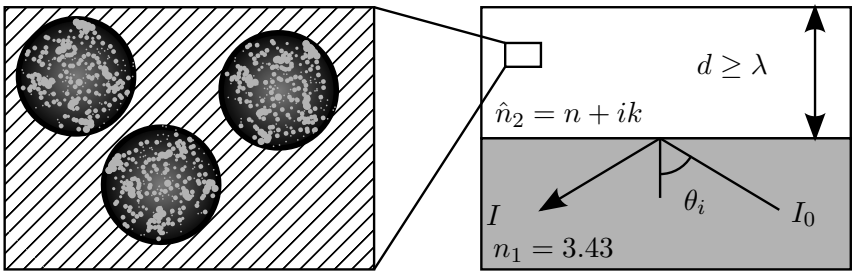

Figure 4.6: Schematic representation of the catalyst layer and the optical arrangement used to measure its reflectance. The relationship between the microscopic composition of the layer and the homogeneous effective medium which approximates it is shown by the rectangular enlargement. The metal catalyst is shown in grey, the carbon in black and the electrolyte solution as hatching. Adsorbed CO is not shown but is assumed to cover the metal surface.

appropriate effective medium theory (discussed in Chapter 2). This approach has been demonstrated for similar systems, [19–24] and has the benefit of affording insight into the underlying physics. However, application of effective medium theories to systems as complex as a multi-component catalyst layer mean many assumptions have to be made, especially with regards to interactions between the components. Furthermore, the complexity of the resulting models prohibits the routine application of this method to spectral analysis.

An alternative, empirical approach is to consider the catalyst layer as one homogeneous medium from the outset and attempt to find parameters which can reproduce the observed spectra. To proceed with this approach it will be assumed that in the medium representing the catalyst layer the only component possessing a wavelength dependent refractive index is the adsorbed CO. The refractive index of the CO component will be modelled as a Lorentzian function, where f is the strength of the oscillator, $\tilde{\nu}_0$ is the resonant wavenumber of the oscillator and γ is the damping constant, which determines the width of the resulting absorption band (eq. (4.7)). The remaining components of the layer, in particular the Pt, represent a constant component of the refractive index which is included in the baseline refractive index, n_∞. Formally, n_∞ accounts for the weak in-

teraction of lower energy CO vibrations far away from the peak centre with the incident light, however it is used here as an adjustable parameter to take into account the large, constant contributions to the refractive index from other components of the catalyst layer such as Pt (section 2.3.3.3).[1]

$$k(\tilde{\nu}) = \mathrm{Im}\left(\frac{f}{\tilde{\nu}_0^2 - \tilde{\nu}^2 - i\tilde{\nu}\gamma}\right) \tag{4.7}$$

To a first approximation the corresponding real part of eq. (4.7) represents $n(\tilde{\nu}) - n_\infty$, although it is formally given by the Kramers-Kronig transformation.[2]

$$n(\tilde{\nu}) = n_\infty + \frac{1}{\pi}\mathcal{P}\int_{-\infty}^{\infty}\frac{k(\tilde{\nu})d\tilde{\nu}}{(\tilde{\nu}_0 - \tilde{\nu})} \tag{4.8}$$

The pole at $\tilde{\nu} = \tilde{\nu}_0$ is dealt with by taking the principal value of the integral, indicated by $\mathcal{P}$. [26, 27] Together $n(\tilde{\nu})$ and $k(\tilde{\nu})$ enable the reflectivity $R(\tilde{\nu})$ to be calculated using the Fresnel coefficient for s-polarised light $r_s(\tilde{\nu})$(eqs. (4.9) and (4.10)). The parameter $\hat{n}_{21} = \hat{n}_2/n_1$, where $n_1 = 3.43$ for the Si ATR crystal and $\hat{n}_2 = n(\tilde{\nu}) + ik(\tilde{\nu})$ for the simulated catalyst layer. The angle of incidence $\theta_i = 39°$ (fig. 4.6).

$$r_s(\tilde{\nu}) = \frac{\cos\theta_i - \sqrt{\hat{n}_{21}(\tilde{\nu})^2 - \sin^2\theta_i}}{\cos\theta_i + \sqrt{\hat{n}_{21}(\tilde{\nu})^2 - \sin^2\theta_i}} \tag{4.9}$$

$$R(\tilde{\nu}) = |r_s(\tilde{\nu})|^2 = r_s(\tilde{\nu})r_s(\tilde{\nu})^\star \tag{4.10}$$

Note that although unpolarised light was used for all experiments, the contribution of p-polarised light, which is much smaller than that of s-polarised light, has been neglected

[1] Note that while it is the imaginary part of the refractive index that dominates Pt, rather than the real part, because the complex refractive index is squared when the reflectivity is calculated, the real and imaginary parts are mixed allowing large baseline values of either part to modify the overall reflectivity.

[2] Strictly it is the antisymmetric combination of imaginary parts $k(\tilde{\nu}) = \frac{k_{\max}(\gamma/2)^2}{(\tilde{\nu}-\tilde{\nu}_0+(\gamma/2)^2} - \frac{k_{\max}(\gamma/2)^2}{(\tilde{\nu}+\tilde{\nu}_0+(\gamma/2)^2}$ that has the Kramers-Kronig transform given by the real parts $n(\tilde{\nu}) - n_\infty = k_{\max}\left\{-\frac{(\tilde{\nu}-\tilde{\nu}_0)(\gamma/2)}{(\tilde{\nu}-\tilde{\nu}_0)+(\gamma/2)^2} + \frac{(\tilde{\nu}+\tilde{\nu}_0)(\gamma/2)}{(\tilde{\nu}+\tilde{\nu}_0)+(\gamma/2)^2}\right\}$. [25]

for simplicity. Once the reflectivity is known the absorbance A can be calculated as for transmitted light. In the model the background reflectivity is arbitrary, but was taken to be that obtained at $2000\,\mathrm{cm}^{-1}$ from an experimental spectrum of a catalyst layer processed against a prism/air spectrum, $R_0(\tilde{\nu}) = 0.68$.

$$A = -\log_{10} \frac{R(\tilde{\nu})}{R_0(\tilde{\nu})} \tag{4.11}$$

Using this model the effect of increasing n_∞ on the reflectance spectrum can be investigated. In terms of the present model, increasing the value of n_∞ can be loosely associated with increasing the amount of Pt in the catalyst layer. The values of the other parameters were taken as: $f = 1$, $\tilde{\nu}_0 = 2000\,\mathrm{cm}^{-1}$ and $\gamma = 15\,\mathrm{cm}^{-1}$. For $n_\infty = 1.5$, a typical value for an organic molecule and used here to represent a catalyst layer with negligible Pt, the absorption spectrum resembles that of a conventional transmission spectrum, that is one containing a unipolar peak centred at $\tilde{\nu}_0$ (fig. 4.7). As the value of n_∞ is increased, the CO band height also increases, up to a value of around $n_\infty = 2.15$, at which point a dramatic change in band shape is observed. The Lorentzian peak shape from $k(\tilde{\nu})$ is replaced by the dispersive shape found in $n(\tilde{\nu})$, indicating that reflectivity is now dominating the wavelength-dependence of the reflected intensity, rather than absorption.

4.3.3 Infrared Band Fitting

The model described above can be used to fit the observed spectrum through non-linear optimisation of the 4 parameters n_∞, f_j, $\tilde{\nu}_{0,j}$, γ_j, where n_∞ is a property of the catalyst layer and the remaining parameters are properties of the j^{th} band. These values form a vector of initial values, $\mathbf{X}$, with corresponding vectors representing the upper and lower bounds of these values, $\mathbf{UB}$ and $\mathbf{LB}$, respectively.

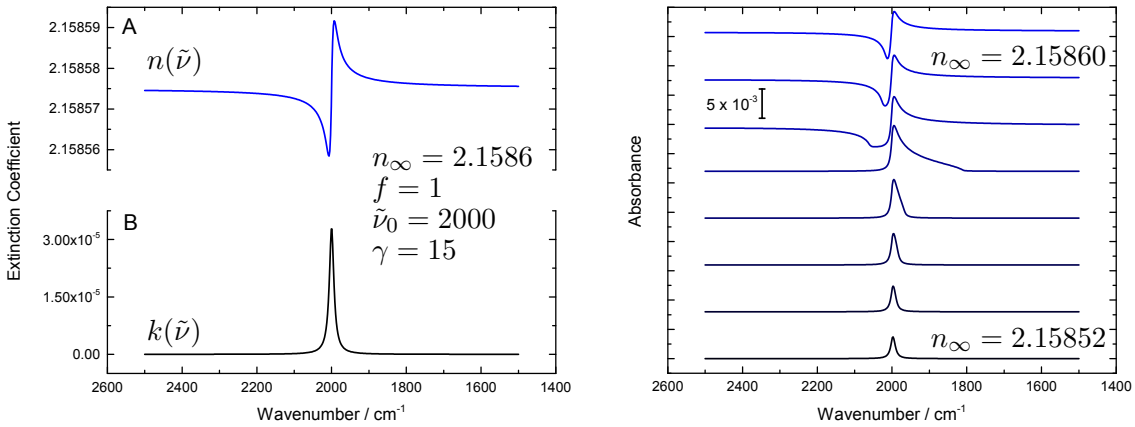

Figure 4.7: Simulation of the refractive index and absorbance spectra of a catalyst film. A: Index of refraction $n(\tilde{\nu})$. B: the index of absorption $k(\tilde{\nu})$. C: Absorbance spectra calculated for a range of different constant baseline refractive indices, n_∞, shown on the figure.

$$\mathbf{X} = \begin{pmatrix} n_\infty \\ f_j \\ \tilde{\nu}_{0,j} \\ \gamma_j \end{pmatrix} \quad \mathbf{LB} = \begin{pmatrix} 1 \\ 0 \\ 1950 \\ 10 \end{pmatrix} \quad \mathbf{UB} = \begin{pmatrix} 10 \\ 1 \times 10^3 \\ 2150 \\ 50 \end{pmatrix} \tag{4.12}$$

Equations (4.7) to (4.11) are formulated into a function $\mathbf{F}(\mathbf{X}, \mathbf{x})$ that accepts the vector of initial values $\mathbf{X}$ and the wavenumber vector $\mathbf{x}$ and outputs the simulated spectrum $\mathbf{y}$. The objective function for the minimisation is given by the sum of the differences between the simulated and experimental points (eq. (4.13)). The trust-region-reflective algorithm in the Matlab function lsqcurvefit is used to search for the value of $\mathbf{X}$ which minimises the objective function.

$$\sum_i (\mathbf{F}(\mathbf{X}, x_i) - y_i)^2 \tag{4.13}$$

The process of fitting series of spectra was accelerated by writing a script to use the fitted parameters of the previous spectrum as the initial parameters for the next spectrum (referred to here as the point-by-point method). Each time this approach was used it was compared to the results from fitting with only a constant set of initial parameters to ensure that minimisation did not stop at a local minimum. This fitting procedure was

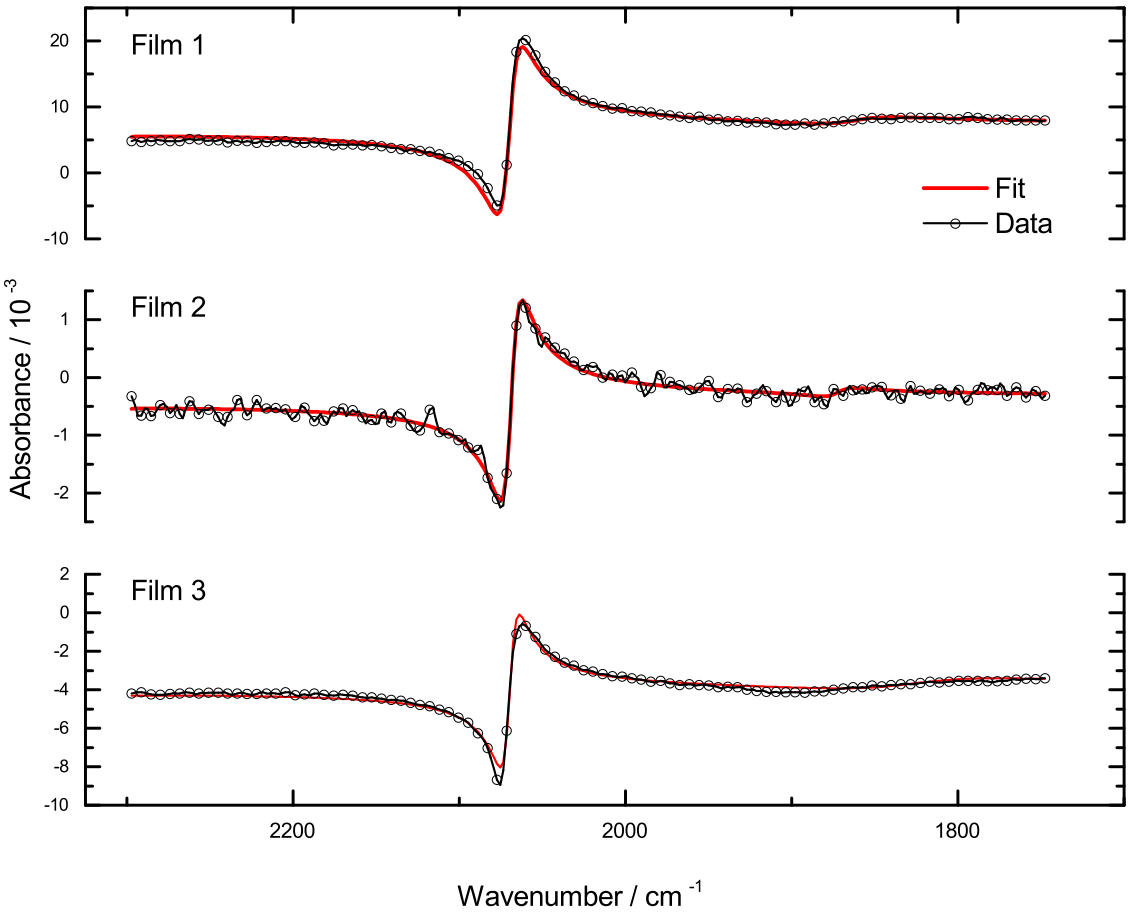

Figure 4.8: Least-squares fits of the refractive index model to the spectra of 3 identical catalyst films shown in fig. 4.5.

incorporated into a Matlab script called fitPeak which can be found in section B.2.

Initially the spectra shown in fig. 4.5 were fitted over the entire CO wavenumber range ($2300\,\mathrm{cm}^{-1}$ to $1750\,\mathrm{cm}^{-1}$) to enable the $2070\,\mathrm{cm}^{-1}$ and $1860\,\mathrm{cm}^{-1}$ bands to be fitted simultaneously. This produced the fits shown in fig. 4.8 and the fitted parameters shown in the Combined Fit column of table 4.1. In all three spectra the model fits the general shape of the data extremely well and provides reproducible band centres and widths, as reflected in the small values of the respective standard deviations. The standard deviation in oscillator strength, f is much larger, however. This variation reflects differences in the absolute value of the measured absorbance, rather than an uncertainty in the fitting, and must arise due to differences in the amount of catalyst layer sampled. The origin of this difference is not obvious, as the same catalyst ink was used in each case and the films were

Table 4.1: Fitted infrared band parameters for adsorbed CO.

	Combined Fit		Separate Fit	
Parameter	Band 1	Band 2	Band 1	Band 2
n_∞	2.174 ± 0.001		2.174 ± 0.001	2.174 ± 0.000
f	32 ± 34	7.1 ± 5.7	31 ± 33	3.8 ± 2.3
$\tilde{\nu}_0$ / cm^{-1}	2071 ± 1	1858 ± 23	2065 ± 1	1837 ± 33
γ / cm^{-1}	13 ± 2	59 ± 42	13 ± 1	70 ± 43
$\|$residuals$\|$	3.23×10^{-5}		8.82×10^{-6}	1.54×10^{-6}

prepared in an identical manner. Furthermore, electrochemical measurements show highly reproducible H desorption charges, indicating that the amount of catalyst in the catalyst layer is well reproduced. The differences in absolute absorbance are therefore ascribed to differences in the microstructure of the deposited catalyst layer (section 2.3.6). In general this variation in the absolute value of f is not a problem, as it is normally the relative change in f with potential which is of interest.

Closer inspection of the whole spectra fits reveals deviations in the model away from the data, such as in the negative lobe of band 1. In addition the fitting to band 2 is relatively poor. The bands were therefore fitted individually to see if any improvement to the fit was obtained (fig. 4.9). Fitting the bands individually did lead to a small decrease in the normalised residual ($\|$ residuals $\|$ in table 4.1) and slight differences in the fitted parameters were obtained. The fitted values of the band 1 center shifted 6 cm^{-1} lower compared to the whole spectrum fit, although the deviations remained similar. The fitted centre of band 2 shifted down by 21 cm^{-1}, although this difference is within the rather large deviation. The curved tail observed on the high wavenumber side of the fit to band 2 is an artefact arising from the finite range over which the Fast Fourier Transforms used in the Kramers-Kronig Transform were computed; when then Kramers-Kronig Transform was not used the tail disappears (dashed blue line).

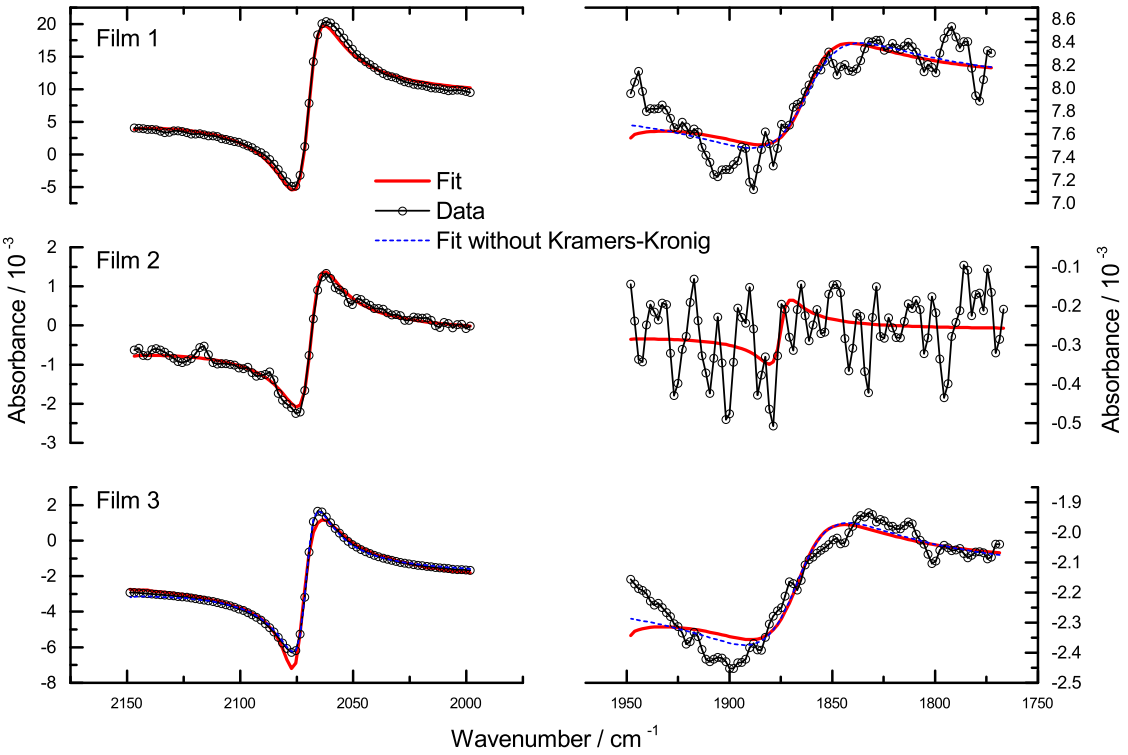

Figure 4.9: Least-squares fits as in fig. 4.9, with bands 1 and 2 considered separately.

4.3.3.1 Infrared Band Assignment

The fitted band parameters for the saturated CO adlayer measured here can be compared to values measured for adsorbed CO on other electrode surfaces at similar potentials (table 4.2). The centre of band 1, observed here at $(2071 \pm 1)\,\mathrm{cm}^{-1}$, agrees well with the value of $2063\,\mathrm{cm}^{-1}$ from linear CO adsorbed on a 60% Pt/C catalyst, and is also close to the value for linear CO observed on Pt(111) single crystals. Significantly the band width is also close to that measured on Pt(111), as opposed to the $20\,\mathrm{cm}^{-1}$ to $40\,\mathrm{cm}^{-1}$ often reported for nanoparticle catalysts. The broad bandwidth is usually taken to indicate a broad distribution of adsorption sites and so the narrow width here could suggest that the catalyst surface is relatively uniform compared to other catalysts. Another trend apparent from the data in table 4.2 is the trend towards higher wavenumbers for both large particles and higher metal loading, which may explain the relatively high wavenumber observed here.

Table 4.2: Typical wavenumbers for CO adsorbed on different Pt sites.[a]

Electrode	Wavenumber (FWHM)[b]/ cm^{-1}			Ref.
	Linear or Atop	Bridging	Threefold	
polycrystalline Pt	2077			[28]
60% Pt/C NP (8.8 nm)	2063	1820 ∼ 1850		[28]
SEIRA Film	2071	1872	1768	[29]
(111) single crystal	2057 (14)	1828 (23)		[30]
	2066		1773	[14]
(100) single crystal	2048 (21)	1872 (44)		[30]
(110) single crystal	2069 (11)			[30]
1 nm Pt NP	2049 (∼ 20)			[31]
30 nm Pt NP	2062 (∼ 20)			[31]
2 nm Pt NP (low loading)	2015			[32]
2 nm Pt NP (high loading)	2046 (∼ 20)			[32]
1.7 nm and 3.6 nm Pt/C NP	2046 (42)	∼ 1850		[33]

[a] Measured at ∼ 0 V
[b] Full width at half maximum

The lower wavenumber band, band 2, is observed around 1840 cm^{-1}. Adsorbed CO stretches in this region are usually assigned to bridging CO, [28–30,33] and it can be seen that the value observed here again agrees well with that previously reported for bridging CO on 60% Pt/C, although it is apparent that the much lower intensity of the band affects the fitting. The reason for this lower intensity could reasonably be assigned to the lower coverage of this species, although intensity transfer to higher wavenumber bands in close proximity is another possibility (*vide infra*). [14] Due to the greater uncertainty in the band parameters, the bridging CO band will not be discussed in the same detail as the main peak. In some cases no distinction is observed in the reactivity of bridging and linear CO geometries, although this is still a matter of debate. [11,29] No evidence for CO adsorbed on a threefold site was observed, however it may be below the detection limit of the experiment.

It has been shown how the bipolar shapes of IR bands from adsorbed CO can be fitted using an empirical model for the catalyst layer refractive index. Furthermore, two such bands have been observed from CO saturated catalyst layers, and have been assigned to linear and bridging CO. The behaviour of these species on the catalyst during oxidation can now be investigated. However, to be able to discuss the behaviour quantitatively, the observed band parameters must be calibrated with the surface coverage of CO. This is required due to both the strong lateral interactions amongst adsorbed CO molecules (section 2.3.5.2), and the strong dependence of their vibrational properties on the electrode potential (section 2.3.4.3).

4.3.4 Calibration

To calibrate the oscillator strength with coverage a potentiostatic dosing strategy was adopted. [30,34] It was observed in section 4.3 that at 0.05 V CO from saturated solution was adsorbed over the course of 200 s, after which the surface became saturated. To

prepare fractional CO coverages, therefore, CO-saturated solution was introduced under potential control for time periods less than 200 s before being flushed out. This process was automated to provide repeatable timings using the dual peristaltic pump controlled by the potentiostat described in Chapter 3. One pump provided flow of N_2-saturated H_2SO_4, while the second pump introduced controlled amounts of CO-saturated H_2SO_4 into the flow. Following the addition of CO-saturated H_2SO_4 the N_2-saturated solution was pumped for a further 120 s to remove CO from the solution. Then, following a 5 s equilibration at 0 V, the potential was cycled between 0 V and 1.2 V at 10 mVs^{-1} for two cycles.

Typical cyclic voltammetry resulting from the dosing procedure is shown in fig. 4.10A. The first cycle (solid line) reveals the coverage of CO, θ_{CO}, in two ways. First, the coverage is revealed indirectly via the suppression of H adsorption, which is observed as a decrease in the H desorption charge Q_H^{CO} between 0 V and 0.3 V. Secondly the coverage is revealed directly via the CO oxidation charge Q_{CO}, between 0.3 V and 0.8 V. The second cycle reveals the full extent of the H desorption Q_H^{max}, and confirms the complete removal of CO via the absence of the CO oxidation peak.

From these data, and the assumptions that 1 H or CO adsorbs per site, H desorption releases 1 electron and CO oxidation releases 2 electrons, the CO coverage can be calculated in two ways. [35, 36] The first way uses the fractional change in the H desorption charge before and after CO is removed, abbreviated to Q_H^{2-1} (eq. (4.14)).

$$\theta_{CO}^{H} = \frac{Q_H^{max} - Q_H^{CO}}{Q_H^{max}} = \frac{Q_H^{2-1}}{Q_H^{max}} \tag{4.14}$$

The second way uses the ratio of the CO charge to the maximum H desorption charge

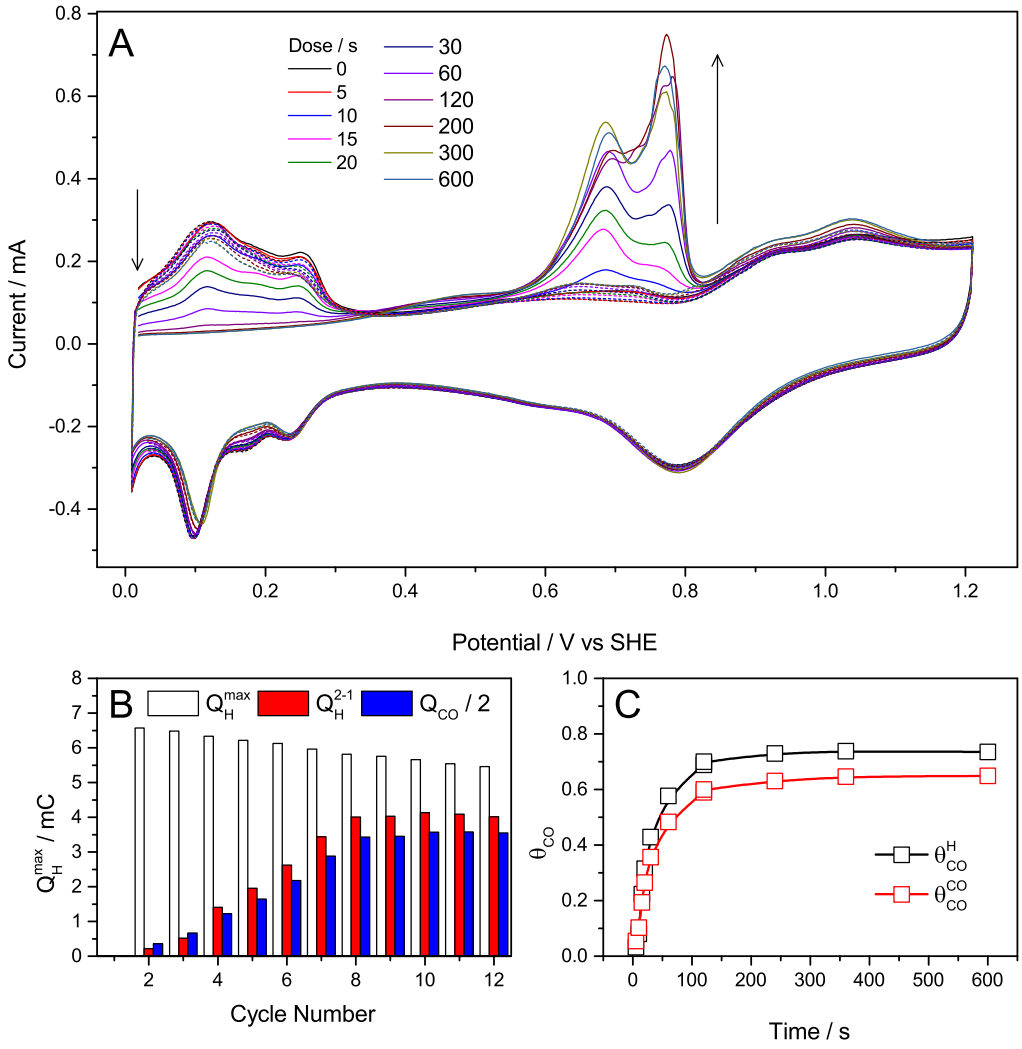

Figure 4.10: Electrochemical determination of CO coverage. A: Cyclic voltammograms following CO adsorption. Cycle 1: solid line, Cycle 2: dashed line. Flow rate: mL min^{-1}. Scan rate 10 mV s^{-1}. Solution: 0.5 M H_2SO_4. Solid line: scan 1; dashed line: scan 2. B: Bar chart representing charge under the H desorption and CO oxidation peaks. C: Surface coverage of CO, θ_{CO} calculated from Q_{CO} or Q_H.

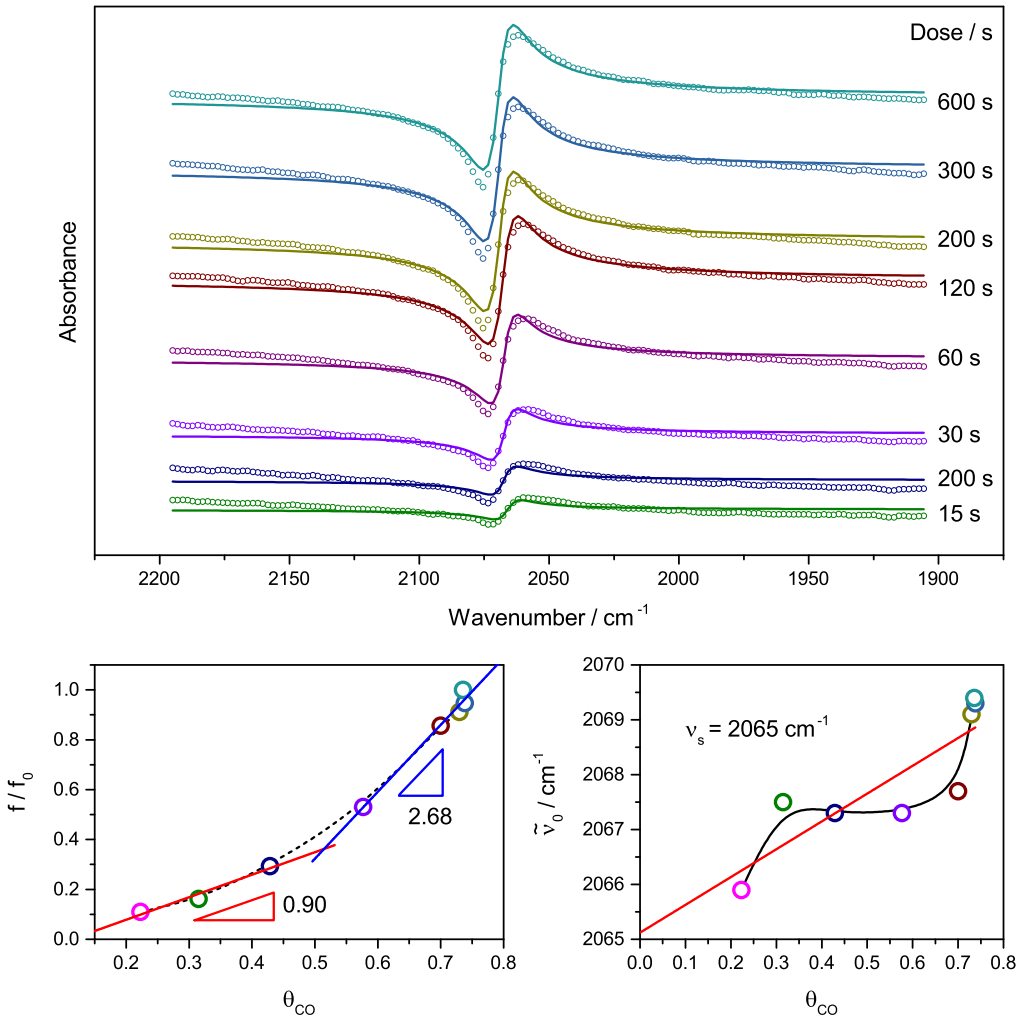

Figure 4.11: Calibration of oscillator strength with coverage for adsorbed CO. A: IR spectra obtained at 0.05 V immediately after dosing CO for a set time. Data: points, Fits: solid line. B: Relative CO band intensity (f/f_0) as a function of CO coverage. Independent lines of best fit are shown for points 1-3 and points 4-8. C: CO band centre as a function of CO coverage. Line of best fit: red. ν_s = band centre in the limit of zero coverage.

divided by 2 to account for the $2\,e^-$ process(eq. (4.15)).

$$\theta_{\mathrm{CO}}^{\mathrm{CO}} = \frac{Q_{\mathrm{CO}}}{2Q_{\mathrm{H}}^{\mathrm{max}}} \tag{4.15}$$

These quantities are shown together in Panel B. A slight decrease in $Q_{\mathrm{H}}^{\mathrm{max}}$ is observed over the course of the experiment, arising perhaps from loss of low index planes on the particle [37] or even loss of Pt surface area through dissolution or sintering. [38] This will not significantly affect the calculation of coverage, however, as it is calculated as a fraction of the charge measured in the respective cycle. The values of $Q_{\mathrm{CO}}/2$ and Q_{H}^{2-1} agree relatively well, although the coverage as measured by $\mathrm{Q}_{\mathrm{H}}^{2-1}$ is slightly greater. Figure 4.12 shows the reproducibility of the dosing approach, which becomes significant when differences in coverage are compared between experiments, and suggests that an error of around 0.1 monolayers should be considered when coverages derived in this way are discussed.

The values of θ_{CO} evaluated from both the H and CO areas are shown in Panel C. The plots show classic isotherm behaviour, with a rapid increase in coverage at first which becomes smaller and smaller until no further increase is observed and saturation is reached. At this point the coverage is between 0.65 and 0.74, as determined from the CO and H charges, respectively. These values compare well with the value of $\theta = 0.7$ for the 2 nm particles in reference [35], and is similar to the value of 0.64 observed for Pt(111). It should be noted that the the non-close packed (100) and (110) planes support higher coverages of 0.82 and 0.98, respectively. [39]

Infrared spectra were acquired continuously during the dosing process enabling the oscillator strength, f to be extracted by fitting as shown in Panel D. The large film to film variation observed in f, discussed in section 4.3.1, means that f should be normalised before use. This is achieved by dividing it by the value at saturation f_0 to give the

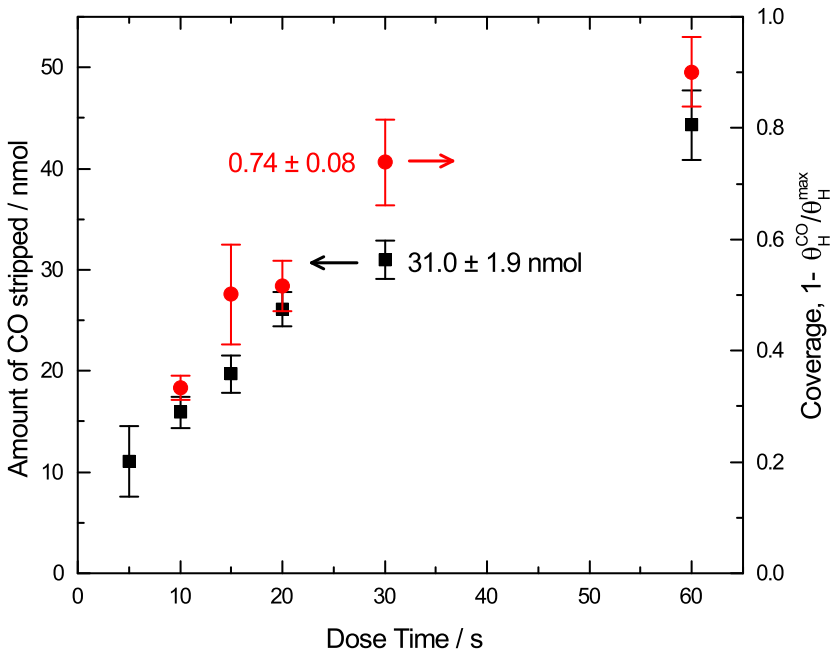

Figure 4.12: Errors in the electrochemical analysis of CO coverage. Black: CO oxidation charge. Red: Fractional coverage calculated from the ratio of CO charge to H desorption charge. Error bars show the standard deviation calculated from 3 measurements.

relative oscillator strength, f/f_0. A plot of f/f_0 as a function of coverage is shown in Panel E, where it is observed to have a non-linear dependence on coverage. Similarly, a plot of wavenumber as a function of θ, shown in Panel F, also exhibits a small, non-linear dependence on coverage. The origin of this coverage dependence lies in the strong lateral interactions amongst adsorbed CO molecules, mediated via dipole-dipole coupling. [40]

4.3.4.1 Dipole-dipole Coupling Effects

As discussed in section 2.3.5.2 the dipole of an adsorbed CO molecule is affected by the electric fields of neighbouring dipoles, as well as by the electric field it induces itself by displacing charge on the metal surface. [41, 42]). The coupling between adsorbed CO molecules means that their vibrations cannot be considered independently, instead they must be understood in terms of normal modes, as for polyatomic molecules. The result of this is that the observed absorption band centre and intensity are properties of the whole

adlayer, not of individual molecules, and may therefore vary with adlayer composition.

In light of the coupling effects, the dependence of the CO parameters on coverage can be compared between the supported nanoparticles used here and other Pt surfaces. While the absolute values of $\tilde{\nu}_0$ agree relatively well with those on bulk surfaces, the θ-dependence of $\tilde{\nu}_0$ on bulk Pt surfaces appears to be much greater than in the present case. For example, the $5\,\mathrm{cm}^{-1}$ variation in wavenumber here contrasts with the $20\,\mathrm{cm}^{-1}$ to $50\,\mathrm{cm}^{-1}$ shift observed for a strongly coupled adlayer on Pt(111). [30, 42] The absence of significant change in coupling with changes to the coverage is an indication of island formation. [30] In this case the CO forms a segregated phase on the surface, such that changes to the coverage only occur at the edges of the island, leaving the average local environment of a CO molecule largely unchanged by changes in coverage. The formation of islands, and the effect they have on the dynamics of reactions with CO, are considered further in the conclusions.

A final point is that to make use of f/f_0 when fitting spectra it is useful if the relationship with θ can be considered as linear. To this end, two regimes were chosen which can be approximated as linear: $0.2 < \theta < 0.5$ and $0.5 < \theta < 0.74$, and linear fits carried out for each. In the low coverage regime the slope is close to 1 (0.90 ± 0.16), and the intercept is close to 0. In the high coverage regime however the slope is much greater (2.68 ± 0.23), meaning that a change in coverage at high coverages will have a larger effect on f/f_0 than a similar change at low coverage. This relationship will be used in later sections when discussing CO coverage during oxidation.

4.4 Carbon Monoxide Electrooxidation Followed with *in situ* Infrared Spectroscopy

After the catalyst layer had been structurally characterised using microscopy and electrochemistry, and the link established between coverage and band intensity for adsorbed CO, the CO electrooxidation reaction was investigated. Cyclic voltammetry was used to strip a saturated CO adlayer from the surface of the catalyst, as carried out for calibration, while spectra were obtained throughout the oxidation process.

Figure 4.13A shows the current recorded in the first and second potential sweeps after the formation of a saturated CO adlayer (black and red lines, respectively). At low potential in the first sweep it can be seen that the H desorption peaks are completely suppressed, confirming the formation of saturated adlayer. As the potential is increased the current is seen to increase forming a broad peak around 0.4 V, labelled (i), before a larger, asymmetric set of peaks are observed between 0.5 V and 0.8 V, labelled (ii)-(iv). Finally, a small peak is observed at high potential, around 1.04 V labelled (v). The second cycle sees the return of H desorption and the loss of the majority of CO oxidation current, although a small peak remains around (iv).

Figure 4.13B is a plot of the normalised fitted linear CO oscillator strength f/f_0 during the first cycle of voltammetry. As with the voltammogram, the plot of f/f_0 shows several distinct regions. An initial, relatively flat region is observed from 0.0 V to 0.5 V which encompasses the region of peak (i). Following this f/f_0 decreases dramatically during the main asymmetric peak region, up until 0.8 V, at which point it stops decreasing, having reached around 17% of its original value. The value of f/f_0 then remains constant until around 1.0 V after which it slowly decreases, correlating with peak (v), finally reaching zero on the return sweep.

The three distinct peak regions require individual discussion. The separation in po-

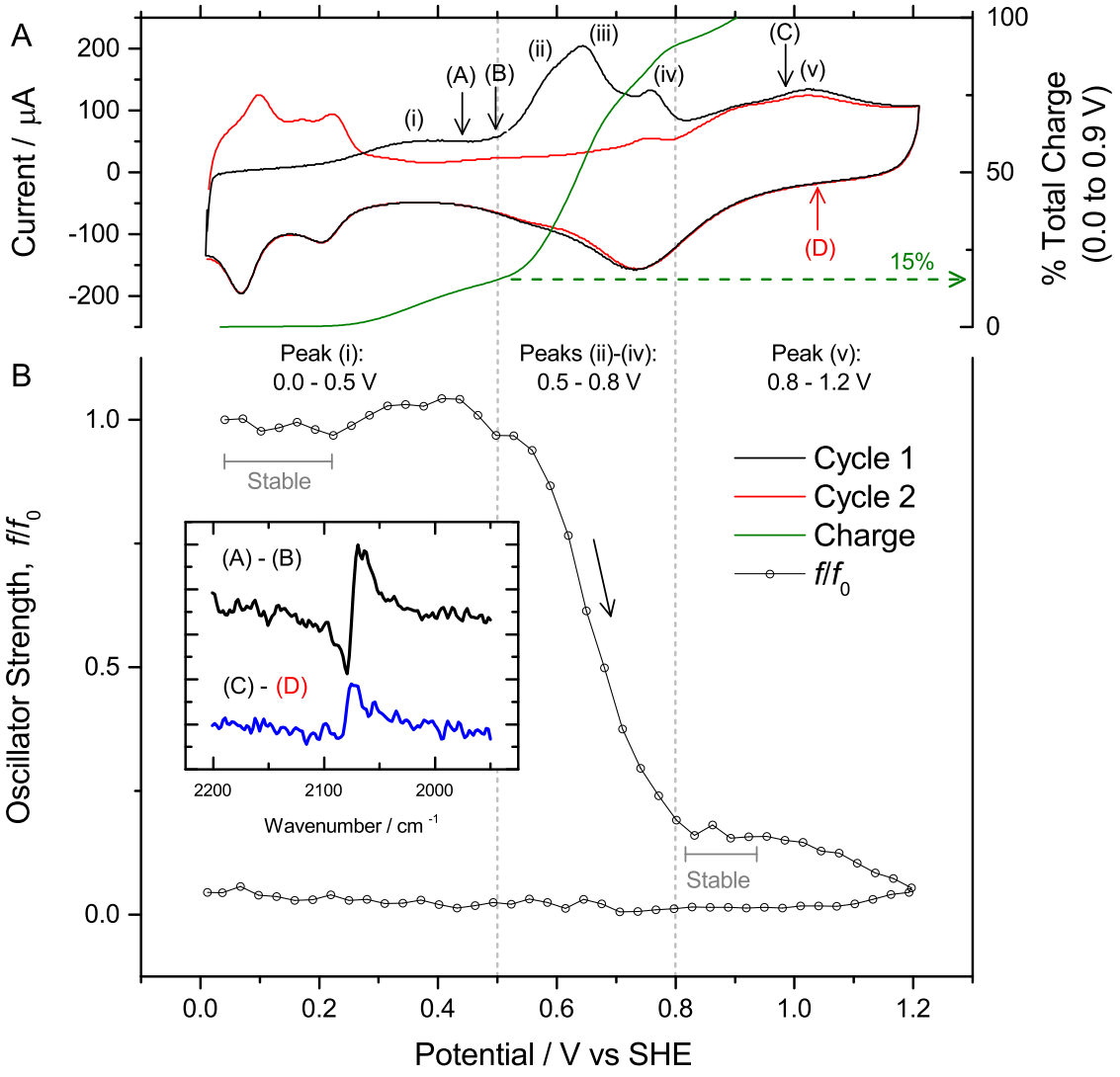

Figure 4.13: Oxidative stripping of a saturated CO adlayer by cyclic voltammetry. A: Cyclic voltammogram. First cycle (black), second cycle (red), percentage charge passed between 0.0 V to 0.9 V (green). Current peaks labelled (i)-(v). Selected spectra obtained at positions (A), (B), (C) and (D). B: Relative oscillator strength f/f_0 obtained from fitting spectra obtained throughout the voltammogram. Inset: Difference spectra of CO species present at high and low potentials, calculated as (A)-(B) and (C)-(D).

tential between the regions, especially between the main peaks and the high potential peak, suggest that there exists multiple oxidation potentials, and therefore adsorption environments, for the CO. This is supported by the difference in peak shape for the CO observed in the two potential regions (fig. 4.13, inset). The peak from the CO which is lost in the region of peak (i), calculated as the difference between spectra at (A) and (B), is bipolar, whereas the peak from the CO which is lost in the high potential region, (C)-(D), is unipolar. This difference in peak shape will be discussed in section 4.4.3.

4.4.1 Current peak (i): CO in the region 0.0 V to 0.5 V

Peak (i) is observed in the region from 0.2 V to 0.5 V. Integration of the current reveals the charge passed in the region, which corresponds to oxidation of around 15% of the CO adlayer (fig. 4.13A). The magnitude of peak (i), commonly known as the 'pre-peak', has previously been shown to be significantly influenced by the CO adsorption potential, with the pre-peak oxidation charge increasing as the adsorption potential decreases from the double layer region into the H upd region. [43] Analysis of the CO adlayer on Pt (111) at potentials just below the pre-peak suggests the adlayer possesses long range order, adopting a p(2 × 2)-3CO structure (fig. 4.14) as revealed independently by *in situ* X-ray diffraction and scanning tunnelling microscope (STM) measurements. [14, 43] Detailed analysis of the STM height data suggested that of the 3 CO molecules in the unit cell, 2 were slightly lower and therefore sat on hollow sites while 1 was on an atop site. [14] The STM study also included *in situ* IR spectra which revealed the wavenumbers of the linear and threefold CO species as 2066 cm^{-1} and 1773 cm^{-1}, respectively.

Spectra recorded between 0.0 V and 0.5 V are shown in fig. 4.15. To remove the contribution of the distinct, second unipolar CO peak observed at high potential, the spectra are processed against a background obtained at 0.89 V. The linear CO region of the spectra were then fitted to the model described in section 4.3.2 using the point-

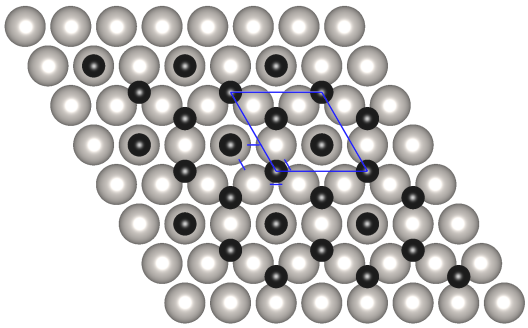

Figure 4.14: Illustration of the Pt(111) p(2 × 2)-3CO adlayer structure. Pt atoms are in grey, C atoms are black and unit cells of both the metal and CO are shown in blue. Note the presence of CO on two of the threefold sites and one of the linear sites.

by-point method (fig. 4.15), while the intensity of the 1840 cm^{-1} band (not shown) was insufficient to obtain a reliable fit. The data show an intense band around 2070 cm^{-1}, with a subtle change in band centre with potential, initially to higher wavenumber and then to lower wavenumber. Comparison of the first and last spectra in the set further suggests that the band intensity has decreased. A more quantitative picture is revealed by inspecting the fitted parameters directly. In general the changes in parameters are much smaller than their absolute value, and so it is the difference Δ, or in the case of f the percentage difference, from the initial value at 0.0 V which is discussed. These differences are plotted as a function of potential, along with the baseline corrected current, in fig. 4.16.

The baseline refractive index, n_∞, which in this model accounts for the large refractive index of Pt, barely changes throughout the region and shows no obvious correlation with potential (fig. 4.16B). The remaining parameters on the other hand show much greater variation. Figure 4.16C shows the percentage change in f as the potential is swept to more positive values. Between around 0.0 V and 0.2 V there is no discernible trend. Above 0.2 V, however, there is a concerted trend upwards towards a 5.2% increase in f, the increase correlating well with the onset of the pre-peak current. Such behaviour can be explained as an effect of dipole-dipole coupling (section 2.3.5.2). For coupled systems, the transition dipole moment μ, and hence intensity, is expected to increase as the coverage

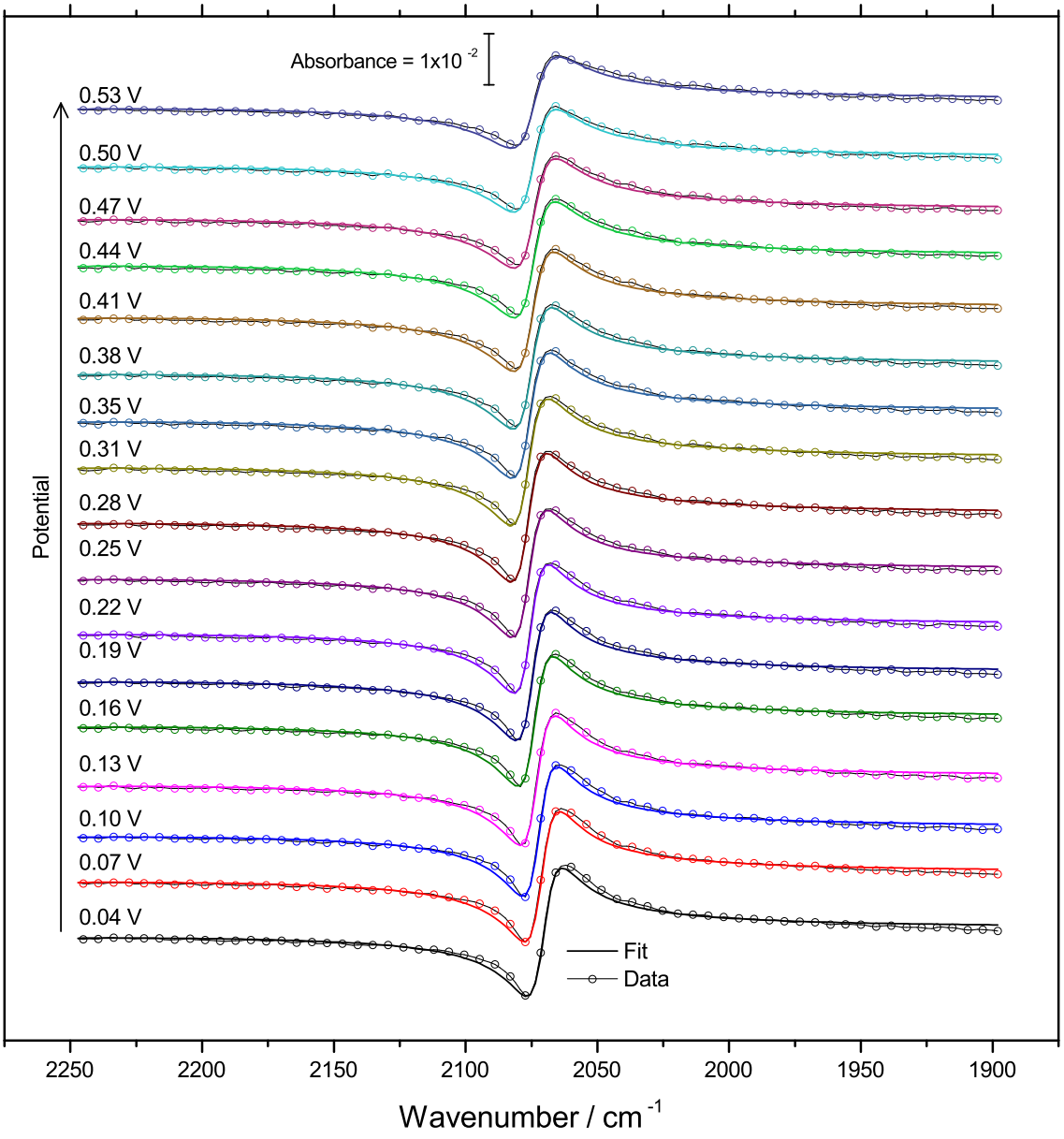

Figure 4.15: IR spectra recorded over the range 0.0 V to 0.5 V during the voltammogram in fig. 4.13. Data: points with fine lines, Fits: bold lines. For clarity only every third data point is shown. Spectra each offset vertically by 0.01 units. Background: 0.89 V.

θ, decreases. [44] This counter-intuitive behaviour, arising from the cumulative effects of all of the dipoles' image charges, must be remembered when measurements are made with reactive species in the bulk. Under these conditions, eg in the presence of formic acid, the CO coverage can increase, as well as decrease, leading to ambiguity in the interpretation of changes in f. In these situations the remaining parameters, band centre $\tilde{\nu}_0$ and width γ, can be used to decide whether dipole coupling effects are significant or not.

The sensitivity of the band centre to potential is shown in Panel D. The fitted band centre at 0.0 V is 2071 cm^{-1}, slightly higher than the band observed on Pt(111) under similar conditions. [14]. The band centre is initially seen to increase with potential, as demonstrated by the linear fit shown on the figure (black line, $\partial\Delta\tilde{\nu}_0/\partial E = 28\,\mathrm{cm}^{-1}\mathrm{V}^{-1}, R^2 = 0.999$). The band centre reaches a maximum of 2077 cm^{-1} around 0.28 V, again slightly higher than that observed on Pt(111). [14] This increase in band centre with potential is attributed to the Electrochemical Stark Effect (section 2.3.4.3). Deviation from the linear trend is observed at the onset of pre-peak current, and the sign of the slope is completely reversed by 0.3 V (grey line, $\partial\Delta\tilde{\nu}_0/\partial E = -18\,\mathrm{cm}^{-1}\mathrm{V}^{-1}, R^2 = 0.995$). This competing trend can be assigned to the effect of dipole-dipole coupling between adsorbed CO species. [45] Coupling is expected to increase the band centre (section 2.3.5.2), [44] such that a decrease in coverage, and the resulting decrease in coupling, leads to an apparent decrease in band centre.

The effect of a lower coverage can also seen in the fitted band width, which increases slightly ($\Delta\tilde{\nu}_0 = 2.6\,\mathrm{cm}^{-1}$) as the potential increases. As discussed in section 2.3.2.1 there are several contributions to inhomogeneous band broadening of adsorbed species, although perhaps the best explanation here would be in terms of the lower frequency CO molecules at the edges of islands, whose contribution to the absorption band would increase as the size of the island decreases and the ratio of edge to centre molecules increases. [46] The exact extent of broadening should be treated with caution, however, as the values of $\Delta\tilde{\nu}_0$

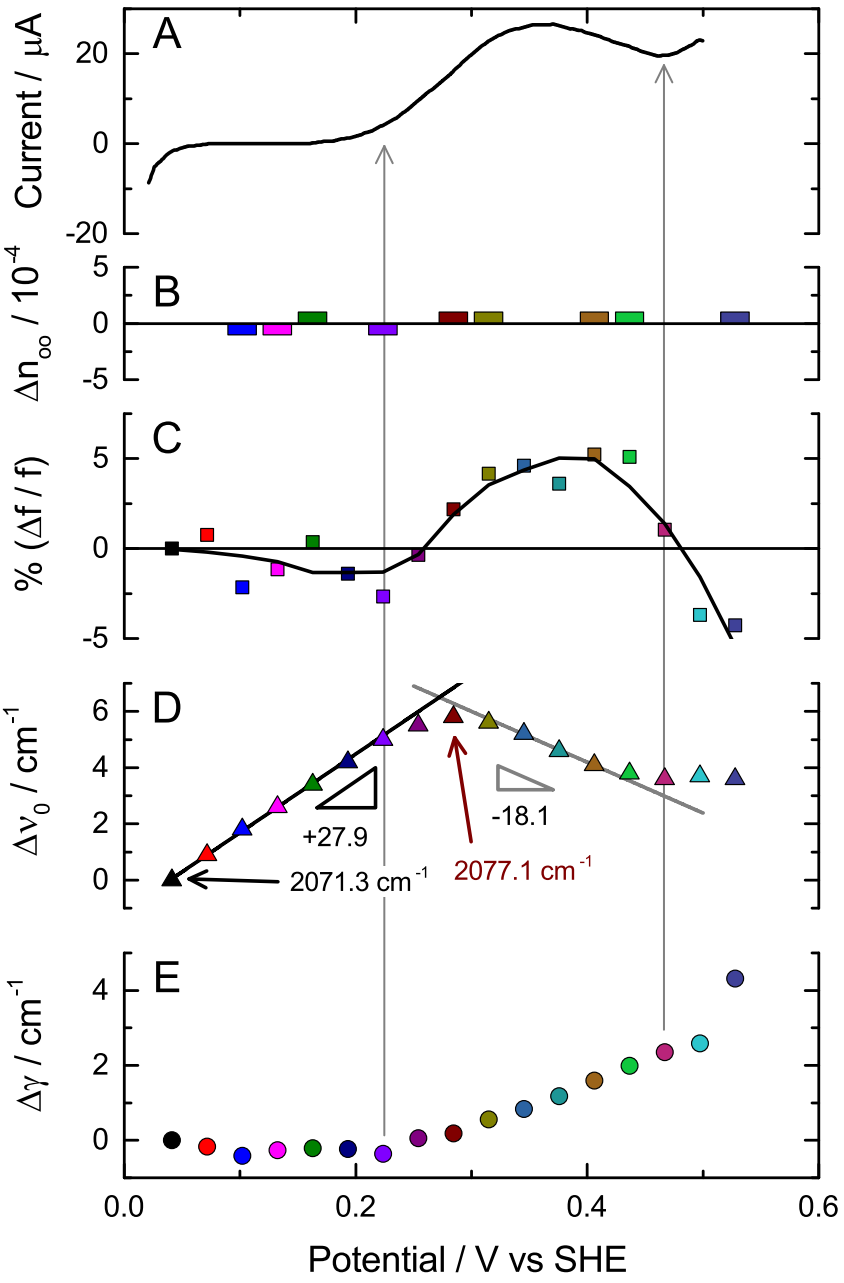

Figure 4.16: Current and fitted parameters from the data in fig. 4.15 plotted as a function of potential. The parameters n_∞, $\tilde{\nu}_0$ and γ are shown as differences Δ from the initial value. Oscillator strength f is shown as the percentage difference, $\%(\Delta f/f)$. Colours correspond to the spectra in fig. 4.15. A moving average of $\%(\Delta f/f)$ and linear fits to regions of $\Delta\tilde{\nu}_0$ are superimposed over the respective data.

lie within the uncertainty in fitted width determined in section 4.3.1.

4.4.2 Current peaks (ii)-(iv): CO in the region 0.5 V to 0.8 V

To investigate the main peaks further the baseline shown in fig. 4.13 (dashed grey line) was subtracted to give the baseline-corrected current (fig. 4.17). The main peak region is seen to consist of a large and a small peak, the first peak being asymmetric. The height of these peaks was observed to increase at different rates during dosing experiments (see fig. 4.10) and so fitting was used to quantify their individual contributions to the overall current. A rigorous model for the current observed during CO stripping must include consideration of the formation, surface diffusion and loss of both of the reacting species, OH and CO, and account for the different rates of these processes at different surface sites. [47] However a qualitative understanding of the shape can be obtained by fitting the current to a simple model which relates the observed current to the time derivative of the coverage of a single species (section 2.2). [48] The model is an oversimplification, and is simply used as an alternative to the Gaussian or Lorentzian functions used elsewhere to extract peak potentials from overlapping peaks. [49]

To account for the asymmetry of the current peaks, the current was modelled as the desorption of 3 species (green line, fig. 4.17). The 3 peaks are labelled ii, iii and iv and occur at 0.58 V, 0.65 V and 0.76 V, respectively. This analysis is consistent with previously reported CO stripping voltammograms, in which a broad initial peak was followed by 2 larger peaks. [43, 50, 51] When sub-saturated CO adlayers were stripped, as in the calibration process, only 2 of the 3 peaks were observed, with peak (ii) seemingly absent. This suggests that CO only adsorbs onto this site at high coverages or after long adsorption times.

Infrared spectra were obtained during the potential sweep to provide further insight into the origin of the current peaks. Spectra recorded at the beginning, middle and end

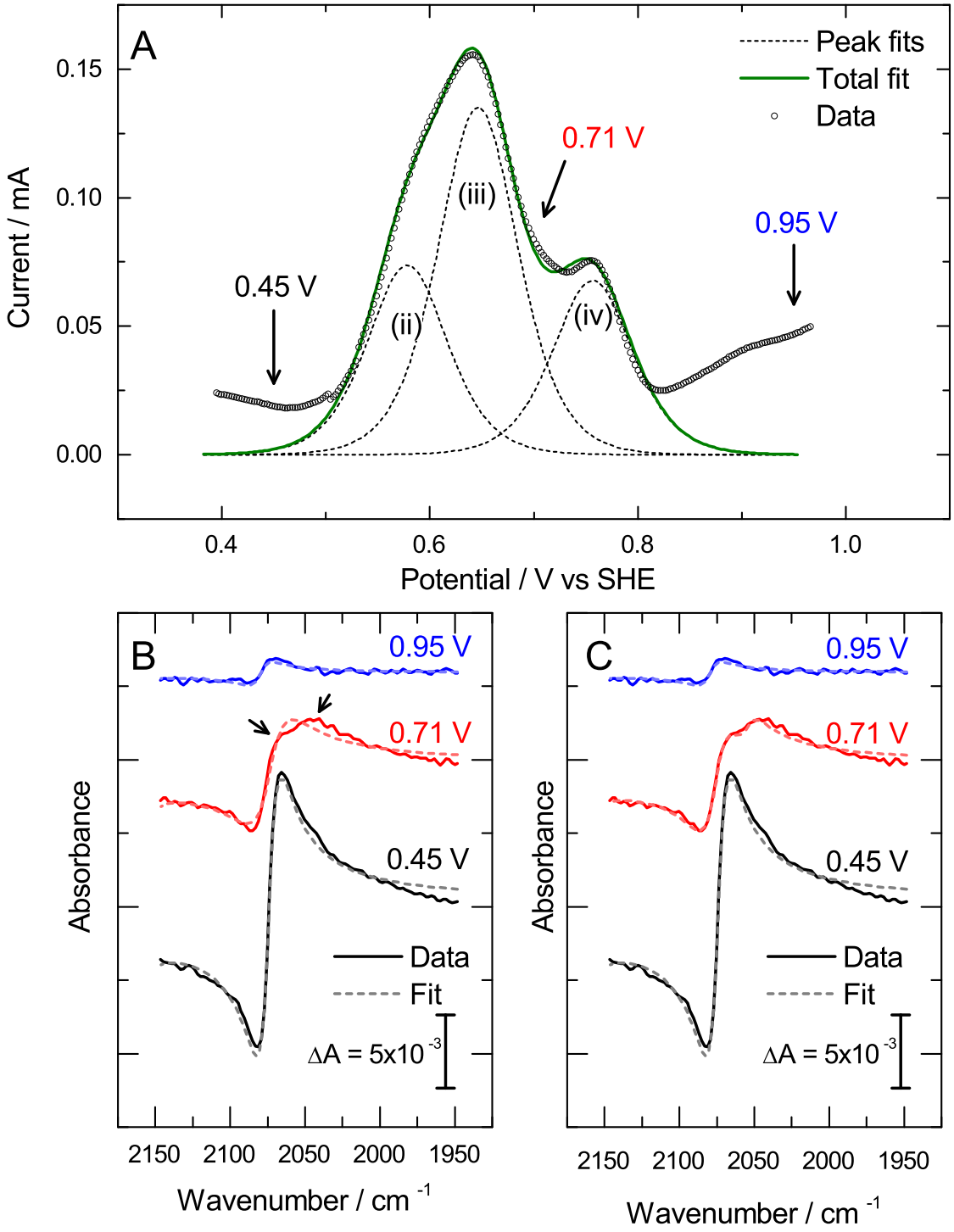

Figure 4.17: Current observed between 0.4 V and 0.95 V with spectra recorded at different points. A: Baseline corrected current (points), fits to current peaks ii, iii and iv (dashed lines), sum of fitted peaks (green line). Arrows mark potentials of selected spectra. B: Selected spectra (solid lines), single oscillator fits (dashed lines). C: Selected spectra (solid lines), two oscillator fits (dashed lines).

of the main peak region are shown in fig. 4.17B, the mid-point potentials being 0.45 V, 0.71 V and 0.95 V, respectively.

The first spectrum (black line, fig. 4.17B) was recorded before the oxidation current starts to increase and unsurprisingly resembles the spectra recorded during the pre-peak region. The second spectrum (red line, fig. 4.17B) was recorded after peaks (ii) and (iii), and has a different shape. As well as being less intense, the spectrum contains a new band, with a maximum at 2043 cm^{-1}, in addition to the existing band that has a maximum at 2065 cm^{-1}. By the final spectrum (blue line, fig. 4.17B), collected after peak (iv), the low wavenumber band had disappeared and only a small band remains at 2065 cm^{-1}.

The spectra were fitted using the same, single oscillator model as used throughout peak (i), and the fits are also shown in fig. 4.17B. The model fits the first spectrum well, as seen when the spectra were fitted throughout peak (i). However, fitting to the second spectrum is not as good, as the model only includes one oscillator and so is unable to account for the additional low wavenumber band. A second oscillator was therefore included in a new model and the subsequent fit, shown in fig. 4.17C, is much closer.

The wavenumber of the second band is still relatively high, suggesting it also arises from linear CO. Such a situation is possible on a nanoparticle surface since it contains many different Pt sites and thus possibilities for linear CO. To understand the sudden emergence of the shoulder band, reference can be made to the stepped single crystal model surfaces discussed in Chapter 2. For example, consider the Pt(332) surface, comprised of (111) terraces separated by (110)-type steps (fig. 4.18). Two linear sites are available: the terrace site (occupied by the brightly coloured CO molecules) and the step sites (occupied by the light coloured CO molecules). The stronger Pt-CO interaction of CO adsorbed on step sites compared to terraces (due to the higher energy of the local d-band, section 2.1.2.4) leads to a decreased $\tilde{\nu}$(C−O) compared to that of CO on terrace sites. [41] The Pt(332) surface has been investigated experimentally using CO stripping, and two

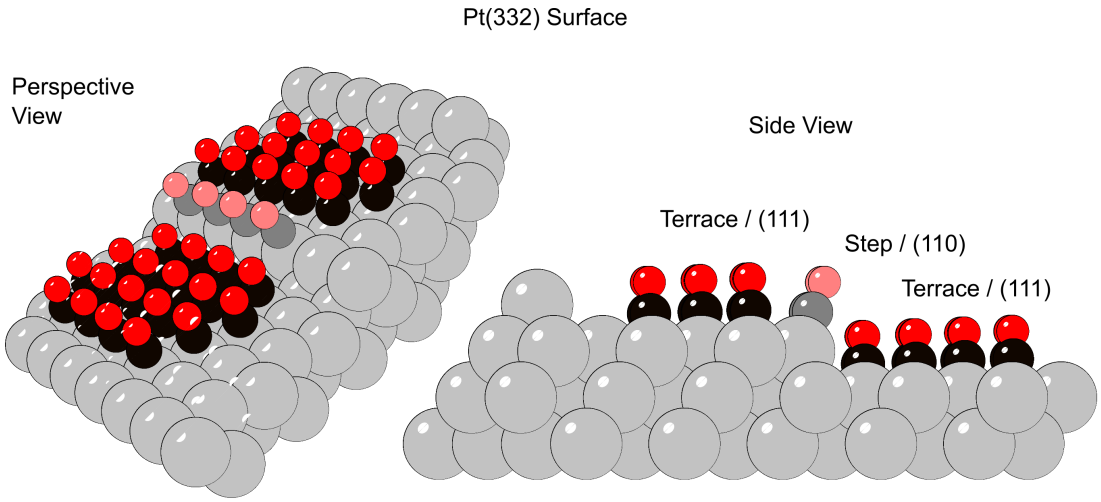

Figure 4.18: CO adsorbed on terrace and step sites on Pt(332).

linear CO stretches were also detected, at 2054 cm^{-1} and 2030 cm^{-1}, and were assigned to terrace and step CO, respectively. [52] The two bands observed here are therefore also tentatively assigned as terrace and step CO.

Fitting was then carried out on all of the spectra obtained during the main peak region, using the improved, two-oscillator model and the spectrum at 0.89 V as the background (fig. 4.19). To account for the absence of the second band in the early spectra, the initial value of the oscillator strength for this band, f_{step}, was set to zero. The second band is then only included when it leads to a better fit (*i.e.* a smaller residual). Both the point-by-point and single initial value methods were used, the latter to check that inclusion of the second band really was necessary.

The fitted oscillator strengths of the two bands, f_{terrace} and f_{step} are shown in fig. 4.20A, plotted as a function of potential along with the observed (baseline corrected) current. Note that the lines are meant only as a guide and the value of f_{step} has been multiplied by 5 for ease of comparison. It can be seen that at first f_{terrace} and f_{step} share an inverse relationship: the decrease in f_{terrace} is mirrored by an increase in f_{step}. At the first current maximum this relationship changes and both f_{terrace} and f_{step} now decrease, the value of f_{step} reaching zero around the potential of the second current maximum while

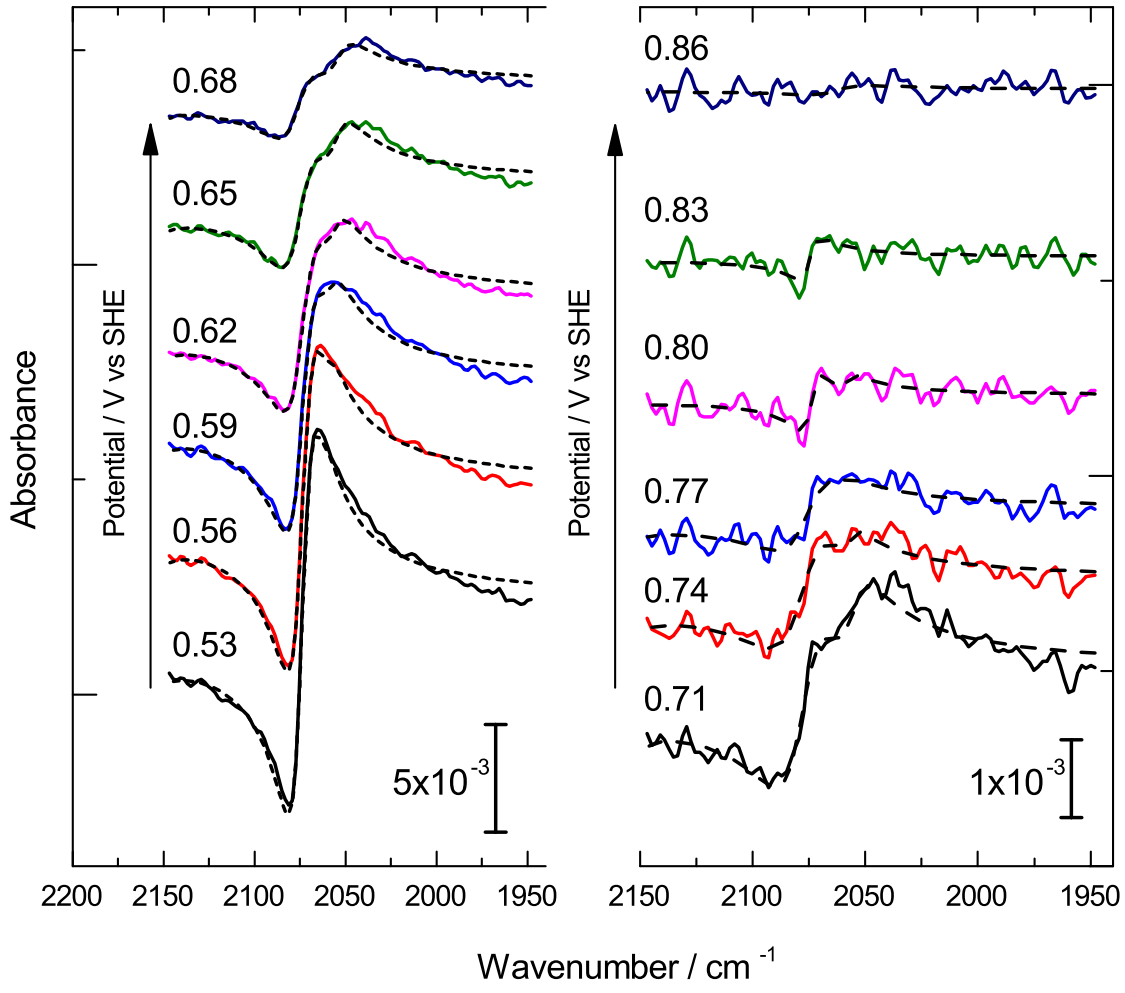

Figure 4.19: Spectra obtained between 0.5 V to 0.9 V during CO stripping in 0.5 M H_2SO_4, with fits to a two-oscillator model. Data are shown as solid lines, fits are shown as dashed lines. Background: 0.89 V

f_{terrace} persists until the current has reached a minimum.

The change in f_{terrace} with potential is readily understood, particularly in terms of the current; oxidation of terrace CO leads to a decrease in coverage of terrace CO and a decrease in its oscillator strength. The relationship between step CO f_{step} and potential is less intuitive, however, although the same anomalous increase in f_{step} with potential has been observed before for CO adsorbed on stepped single crystals, [52] as well as carbon-supported platinum. [17] In neither case was any attempt made to quantify the band intensities.

Based on the close proximity and wavenumber of the step and terrace CO vibrations, the anomalous behaviour was rationalised using dipole coupling (section 2.3.5.2). As discussed in section 5.3.4, when the normal modes of coupled adlayer vibrations are compared to the vibrations expected for isolated molecules, significant intensity transfer can appear to occur. Intensity transfer always occurs from the lower to the higher frequency vibration, [41] which in this case would lead to the transfer of intensity from the step CO to the terrace CO. In cases of moderate coverages of the higher wavenumber species ($\approx 10\%$), this transfer can leave the lower wavenumber vibration almost invisible (fig. 2.31B). [41]

This intensity transfer is believed to be the origin of the present observations. The normal mode dominated by the terrace CO vibration acquires the majority of the band intensity, leaving the normal mode with the band centre closer to the step CO invisible. As the coverage of terrace CO, and f_{terrace}, decreases the extent of dipole-dipole coupling decreases and intensity is 'returned' to the step CO vibration, resulting in its appearance in the spectrum. The subsequent decrease in f_{step} is then simply the result of a decrease in step CO coverage as it gets oxidised.

The correlation between step CO f_{step} and the current is particularly striking; although the correlation with the increase in current is indirect, as discussed above, the correlation with the decrease in current region is not. The correlation suggests that the current in

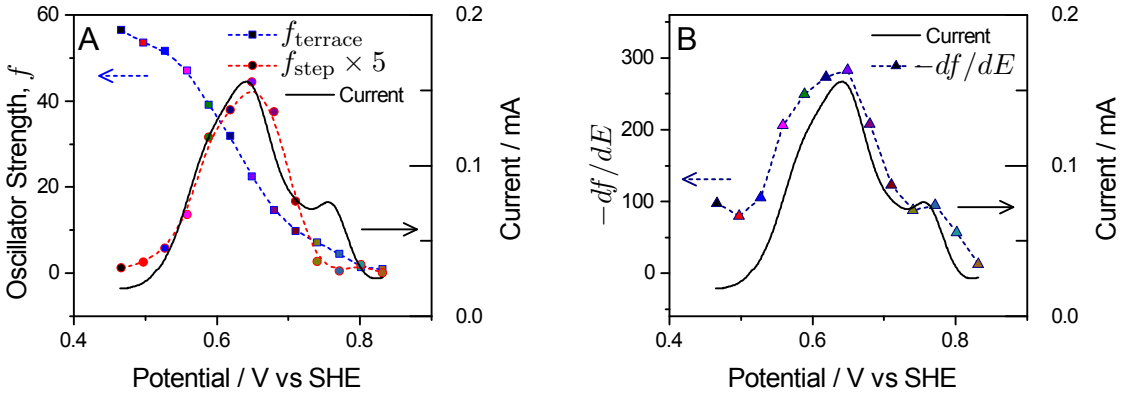

Figure 4.20: Fitted parameters for linear CO in spectra recorded between 0.53 V and 0.89 V shown in fig. 4.19. A: Oscillator strengths of the two bands observed, f_{terrace} and f_{step}, plotted as a function of potential along with the current. f_{step} enlarged by a factor of 5 for clarity. B: Negative time derivative of f_{terrace} plotted as a function of potential.

peaks 1a and 1b arises from oxidation of both step and terrace CO, while the correlation of f_{terrace} with current peak 2 suggests that this current peak arises exclusively from terrace CO.

The relationship between terrace CO and the current was further investigated using the model for the current in a linear sweep described above. In the model the current was assumed to be proportional to the negative time derivative of coverage of the species being oxidised, in this case CO (eq. (4.16)).

$$i \propto \frac{-d\theta_{CO}}{dt} \tag{4.16}$$

It is assumed in the first instance that the change in coverage of CO can be approximated by the change in oscillator strength (eq. (4.17)), although this is only true for small changes (section 5.3.4).

$$i \propto \frac{-df_{\text{terrace}}}{dt} \tag{4.17}$$

The values of $-df_{\text{terrace}}/dt$ are plotted with the current in fig. 4.20B. It can be seen that the derivative has the same shape as the current, including the local minimum before

current peak 2. Such a correlation provides further evidence for the current observed in the main peaks region being dominated by oxidation of the terrace CO. To understand the reason for the apparent preferential loss of terrace CO the mechanism of oxidation must be considered.

4.4.2.1 Mechanisms for CO Oxidation on Pt Nanoparticles

The oxidation of CO(ad) is generally believed to follow a Langmuir-Hinshelwood mechanism, in which CO(ad) reacts with an adsorbed oxygen-containing species. [1] This oxygen-containing species is written here as OH(ad), although H_2O(ad) and O(ad) have also been proposed. [53] The precise details of this mechanism are also still the subject of debate; brief reviews of the literature can be found in references [4] and [49]. Two different mechanisms have been proposed, largely on the basis of two different measurements (fig. 4.21). Electrochemical measurements suggest a mean field (MF) model, in which CO(ad) and OH(ad) are homogeneously distributed in the adlayer, is most suitable. This mechanism is further supported by mathematical modelling of the current transients following potential steps on single crystals. [4,54,55] Meanwhile, *in situ* IR measurements tend to suggest the formation of CO islands, and therefore that a nucleation and growth (NG) mechanism is in operation. [13,56,57] Although in fact this mechanism was originally proposed on the basis of electrochemical measurements alone. [2] A third model, a special case of the nucleation and growth mechanism, has also been suggested: the active site (AS) model. [49] Each model differs in its assumptions about the site of OH(ad) nucleation and the mobility of CO(ad) (table 4.3) and is introduced below.

In the MF model the rate of surface diffusion of CO is much faster than the rate of CO oxidation, such that CO(ad) and OH(ad) can be considered as homogeneously distributed throughout the adlayer. [49] Consequently, CO is oxidised from random sites in the adlayer. The NG model, in contrast, considers the reacting species immobile.

Table 4.3: Assumptions behind different models for CO oxidation.

Parameter	Mean Field	Nucleation and Growth	Active Site
OH adsorption site	Homogeneous distribution	Low coordinate 'defect' sites preferred	Low coordinate 'defect' sites preferred
CO mobility	High	Low	High

Nucleation of OH(ad) species occurs preferentially at low-coordinate surface sites due to to their higher energy d-band centre (see section 2.1.2.4), although formation at any vacant site is possible. Oxidation starts at low coordinate sites, such as corners, with the reaction front then moving inwards to reach fresh CO, since the immobile CO cannot move towards the corners. In this mechanism 'islands' of CO are formed, which is in agreement with IR measurements that shown an apparent insensitivity of CO vibrations to coverage. [13, 56, 57] In the AS model OH(ad) formation still occurs at low-coordinate sites, but the mobile CO can now diffuse to the OH(ad). The effect of this is that CO oxidation occurs at specific 'active sites', with vacant sites forming in the centre of the adlayer.

Figure 4.21 suggests what the surface may look like at several points in time during CO oxidation under the three models. The surface is represented as a 9×9 array of circles, grey representing CO(ad), orange OH(ad) and white vacant sites. The corners and edges of the array are used to represent the corner and edge/step sites of a nanoparticle. It is suggested that the three models are likely to give rise to different distributions of CO on the surface during the oxidation. While the MF model gives rise to a random distribution of CO on the surface, the NG model leads to the formation of islands, with edge CO being lost in preference to terrace CO. This contrasts with the AS model, in which CO is preferentially lost from the centre of the terrace, as CO diffuses up to the OH(ad) at the corners.

These models each give rise to distinct CO distributions during oxidation, which are

likely to have distinct IR signatures. The MF model does not result in island structures, which conflicts with the prior observation that the CO molecules are strongly coupled but relatively insensitive to changes in coverage. This leaves the NG and AS models as the more likely mechanisms. The trend shown in fig. 4.20 was interpreted in terms of initial loss of terrace CO followed by step CO. This trend is qualitatively similar to that expected from the AS model, where mobile CO diffuses to the corner OH(ad) sites, effectively maintaining a large edge CO population at the expense of the terrace population. These preliminary conclusions are similar to those made by Friedrich *et al.*, who considered in more detail the interplay between the particle size and the site and potential of both OH(ad) nucleation and CO oxidation. [17]

4.4.3 Current peak (v): CO above 0.8 V

It was suggested in the introduction to this section that the final oxidation peak occurred from oxidation of a distinct CO species. As well as the current peak occurring at a much higher potential than that required to oxidise the main peak CO, evidence for this distinction also comes from the *in situ* IR spectra. Not only is a plateau in band intensity observed as the current is increased, but two distinct peak shapes are observed (fig. 4.22). When spectra of CO lost during oxidation are generated, by subtracting spectra obtained 100 mV apart during the sweep, it can be seen that the CO lost from the pre-peak region gave rise to a bipolar peak while the CO lost from the high potential peak region showed a unipolar peak.

Evidence for the nature of the two species is first revealed in the voltammogram. The potentials of the CO stripping peaks in the main peak region are similar to those observed on bulk Pt, while the potential observed for the high potential current peak is much closer to that observed for small nanoparticles. [49] [17, 32, 49] This can be interpreted in light of the catalyst morphology, characterised in section 4.2, in which two morphologies were

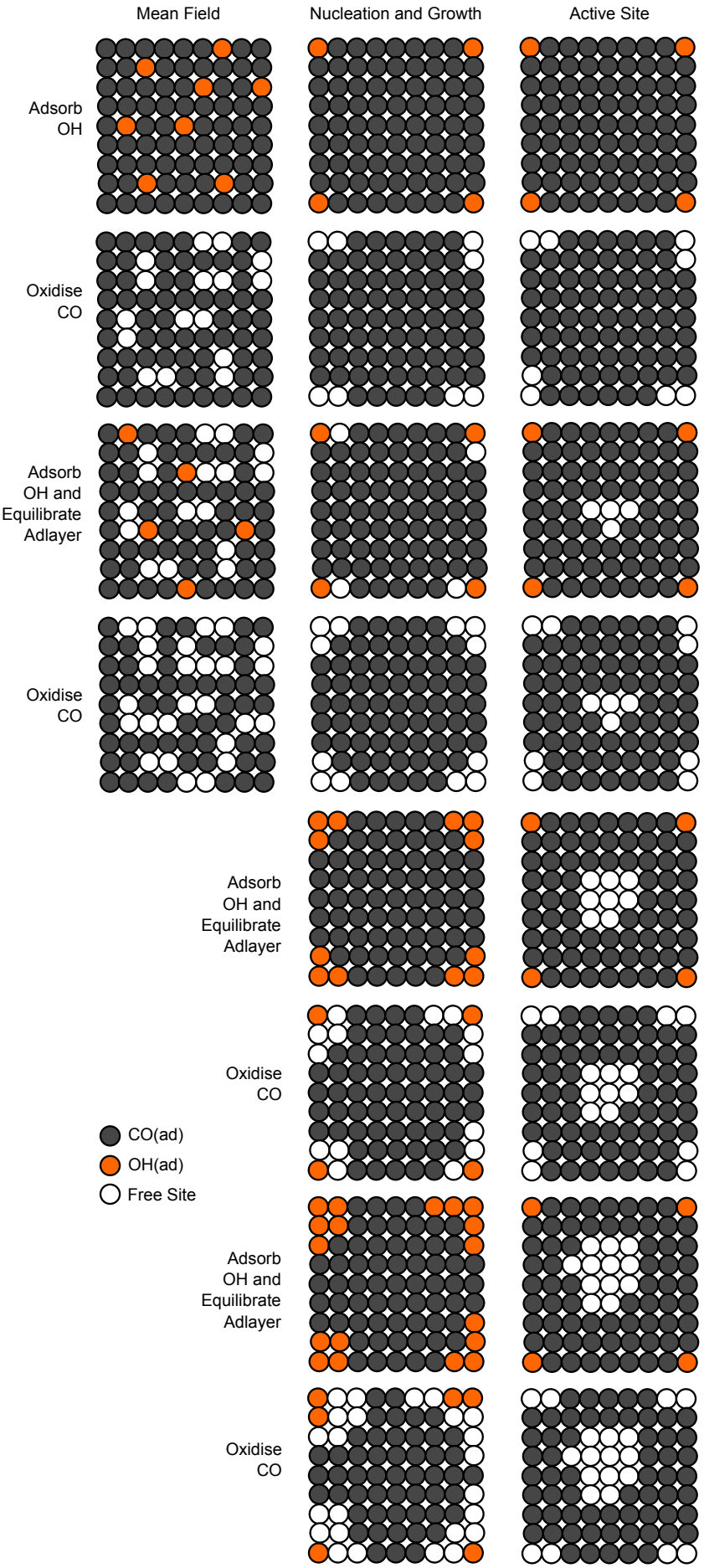

Figure 4.21: Three models for the CO distribution during oxidation on metal surfaces. The corner sites in the illustration represent defect sites. Orange circles = OH(ad); grey circles = CO(ad); white circles = vacant site.

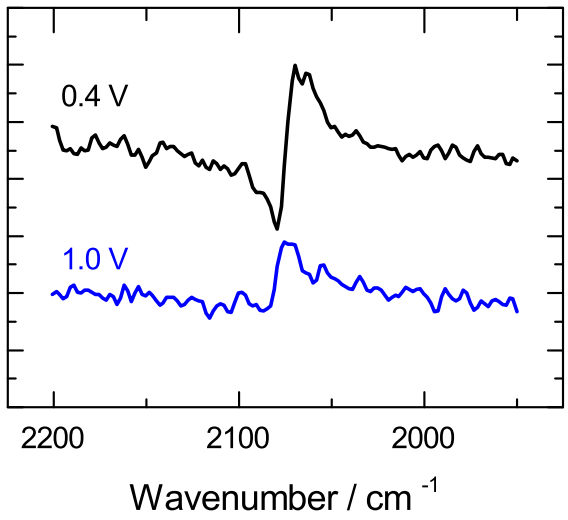

Figure 4.22: Comparison of the CO peaks lost at low and high potential. The difference spectra of CO calculated from spectra 100 mV apart in fig. 4.13 is shown for initial potentials of 0.4 V and 1.0 V. Further details can be found in the original discussion of fig. 4.13.

observed: agglomerated catalyst and individual catalyst. The agglomerated catalyst is likely to provide an environment closer to bulk Pt, while the individual catalyst particles will give rise to stripping characteristic of small particles. This interpretation accounts for the stability of the CO up to high potential, since it is known that in general small particles require higher potentials for CO stripping, due to the fewer defect sites available to nucleate the OH formation necessary for CO oxidation. [17, 35]

The difference in band shape between the two CO species can also be understood in light of the two different morphologies. Comparing the shape and size of the bands, it can be seen that the high potential band is smaller and predominantly unipolar, while the main CO band is larger and bipolar. Such differences have been observed previously in studies of surface roughening. [21, 24] When the correlation between the surface structure of a Pt electrode and the shape of the CO(ad) peak observed in IR reflection spectra was studied it was found that when the surface was roughened, to produce a more fragmented surface composed of nanometer islands, the peak shape of the adsorbed CO changed from unipolar to bipolar, as well as increasing in magnitude. These observations were rationalised using

a variety of effective medium approximations (section 2.3.3.7), although in general it was found that conversion from unipolar to bipolar peaks occurred with an increase in volume fraction of Pt in the layer representing the roughened surface.

4.5 Conclusion

In this chapter the spectroelectrochemical cell developed in Chapter 3 has been used to study the adsorption and oxidation of CO on a commercial fuel cell catalyst. The design of the cell, based around a carbon flow field, has enabled the unequivocal assignment of peaks in the CO region to CO adsorbed on the catalyst, as opposed to the supporting electrode. A peak fitting procedure was developed to enable the observed bipolar CO peaks to be fitted, allowing the peak intensity, centre and width to be reported for the first time. This subsequently enabled calibration of the fitted intensity with the electrochemically determined CO coverage. When CO stripping voltammetry was carried out two linear CO peaks were observed and were assigned to CO on terrace and step/defect sites of the catalyst. The correlation between the two CO species and the observed current is discussed in relation to the mechanisms proposed for the oxidation, and the active site model, in which CO diffuses to OH(ad) formed on defect sites, was suggested to fit the data best. This preliminary study has shown what is possible using the spectroelectrochemical cell, and has developed the fitting techniques to enable further investigation into the relationship between nanoparticle morphology and CO oxidation behaviour.

References

[1] S. Gilman, "The Mechanism of Electrochemical Oxidation of Carbon Monoxide and Methanol on Platinum. II. The "Reactant-Pair" Mechanism for Electrochemical Oxidation of Carbon Monoxide and Methanol1," *The Journal of Physical Chemistry*, vol. 68, no. 1, pp. 70–80, 1964.

[2] C. McCallum and D. Pletcher, "An investigation of the mechanism of the oxidation of carbon monoxide adsorbed onto a smooth Pt electrode in aqueous acid," *Journal of Electroanalytical Chemistry and Interfacial Electrochemistry*, vol. 70, no. 3, pp. 277–290, 1976.

[3] B. Beden, C. Lamy, N. R. de Tacconi, and A. J. Arvia, "The electrooxidation of CO: a test reaction in electrocatalysis," *Electrochimica Acta*, vol. 35, no. 4, pp. 691–704, 1990.

[4] M. T. M. Koper, N. P. Lebedeva, and C. G. M. Hermse, "Dynamics of CO at the solid/liquid interface studied by modeling and simulation of CO electro-oxidation on Pt and PtRu electrodes," *Faraday Discussions*, vol. 121, pp. 301–311, 2002.

[5] A. M. Gómez-Marín and J. P. Hernández-Ortiz, "Langmuir–Hinshelwood Mechanism Including Lateral Interactions and Species Diffusion for CO Electro-Oxidation on Metallic Surfaces," *The Journal of Physical Chemistry C*, vol. 118, no. 5, pp. 2475–2486, 2014.

[6] T. Iwasita and E. Pastor, "A dems and FTir spectroscopic investigation of adsorbed ethanol on polycrystalline platinum," *Electrochimica Acta*, vol. 39, no. 4, pp. 531–537, 1994.

[7] B. Beden, S. Bilmes, C. Lamy, and J. M. Leger, "Electrosorption of carbon monoxide on platinum single crystals in perchloric acid medium," *Journal of Electroanalytical Chemistry and Interfacial Electrochemistry*, vol. 149, no. 1–2, pp. 295–302, 1983.

[8] K. Kunimatsu, "Infrared spectroscopic study of methanol and formic acid adsorbates on a platinum electrode: Part I. Comparison of the infrared absorption intensities of linear CO(a) derived from CO, CH3OH and HCOOH," *Journal of Electroanalytical Chemistry*, vol. 213, no. 1, pp. 149–157, 1986.

[9] B. Beden, A. Bewick, and C. Lamy, "A study by electrochemically modulated infrared reflectance spectroscopy of the electrosorption of formic acid at a platinum electrode," *Journal of Electroanalytical Chemistry and Interfacial Electrochemistry*, vol. 148, no. 1, pp. 147–160, 1983.

[10] M. Watanabe and S. Motoo, "Electrocatalysis by ad-atoms: Part III. Enhancement of the oxidation of carbon monoxide on platinum by ruthenium ad-atoms," *Journal of Electroanalytical Chemistry and Interfacial Electrochemistry*, vol. 60, no. 3, pp. 275–283, 1975.

[11] N. M. Marković and P. N. Ross Jr., "Surface science studies of model fuel cell electrocatalysts," *Surface Science Reports*, vol. 45, no. 4–6, pp. 117–229, 2002.

[12] Y. Zhao, L. Fan, J. Ren, and B. Hong, "Electrodeposition of Pt–Ru and Pt–Ru–Ni nanoclusters on multi-walled carbon nanotubes for direct methanol fuel cell," *International Journal of Hydrogen Energy*, vol. 39, no. 9, pp. 4544–4557, 2014.

[13] S.-C. Chang and M. J. Weaver, "Coverage-dependent dipole coupling for carbon monoxide adsorbed at ordered platinum(111)-aqueous interfaces: Structural and electrochemical implications," *The Journal of Chemical Physics*, vol. 92, no. 7, pp. 4582–4594, 1990.

[14] I. Villegas and M. J. Weaver, "Carbon monoxide adlayer structures on platinum (111) electrodes: A synergy between in-situ scanning tunneling microscopy and infrared spectroscopy," *The Journal of Chemical Physics*, vol. 101, no. 2, pp. 1648–1660, 1994.

[15] J. Liu, "Scanning transmission electron microscopy and its application to the study of nanoparticles and nanoparticle systems," *Journal of Electron Microscopy*, vol. 54, no. 3, pp. 251–278, 2005.

[16] W. Zhou, I. E. Wachs, and C. J. Kiely, "Nanostructural and chemical characterization of supported metal oxide catalysts by aberration corrected analytical electron microscopy," *Current Opinion in Solid State and Materials Science*, vol. 16, no. 1, pp. 10–22, 2012.

[17] K. A. Friedrich, F. Henglein, U. Stimming, and W. Unkauf, "Size dependence of the CO monolayer oxidation on nanosized Pt particles supported on gold," *Electrochimica Acta*, vol. 45, no. 20, pp. 3283–3293, 2000.

[18] J. Solla-Gullón, P. Rodríguez, E. Herrero, A. Aldaz, and J. M. Feliu, "Surface characterization of platinum electrodes," *Phys. Chem. Chem. Phys.*, vol. 10, no. 10, pp. 1359–1373, 2008.

[19] M. Osawa and K.-i. Ataka, "Electromagnetic mechanism of enhanced infrared absorption of molecules adsorbed on metal island films," *Surface Science*, vol. 262, no. 3, pp. L118–L122, 1992.

[20] M. Osawa, K.-i. Ataka, K. Yoshii, and T. Yotsuyanagi, "Surface-enhanced infrared ATR spectroscopy for in situ studies of electrode/electrolyte interfaces," *Journal of Electron Spectroscopy and Related Phenomena*, vol. 64–65, pp. 371–379, 1993.

[21] A. E. Bjerke, P. R. Griffiths, and W. Theiss, "Surface-Enhanced Infrared Absorption of CO on Platinized Platinum," *Analytical Chemistry*, vol. 71, no. 10, pp. 1967–1974, 1999.

[22] C. Pecharromán, A. Cuesta, and C. Gutiérrez, "Comments on the paper by M.-S. Zheng and S.-G. Sun entitled 'In situ FTIR spectroscopic studies of CO adsorption on electrodes with nanometer-scale thin films of ruthenium in sulfuric acid solutions' [J. Electroanal. Chem. 500 (2001) 223]," *Journal of Electroanalytical Chemistry*, vol. 529, no. 2, pp. 145–154, 2002.

[23] C. Pecharromán, A. Cuesta, and C. Gutiérrez, "Calculation of adsorption-induced differential external reflectance infrared spectra of particulate metals deposited on a substrate," *Journal of Electroanalytical Chemistry*, vol. 563, no. 1, pp. 91–109, 2004.

[24] Z.-F. Su, S.-G. Sun, C.-X. Wu, and Z.-P. Cai, "Study of anomalous infrared properties of nanomaterials through effective medium theory," *The Journal of Chemical Physics*, vol. 129, no. 4, p. 044707, 2008.

[25] K. Ohta and H. Ishida, "Comparison among several numerical integration methods for Kramers-Kronig transformation," *Applied Spectroscopy*, vol. 42, no. 6, pp. 952–957, 1988.

[26] F. M. Mirabella, "Specular reflection spectroscopy," in *Modern techniques in applied molecular spectroscopy*, Techniques in analytical chemistry series Y, p. 83, New York ; Chichester: Wiley, 1998.

[27] P. R. Griffiths, *Fourier Transform Infrared Spectrometry*. Wiley-Interscience, 2 edition ed., 2010.

[28] S. Park, S. A. Wasileski, and M. J. Weaver, "Electrochemical Infrared Characterization of Carbon-Supported Platinum Nanoparticles: A Benchmark Structural Comparison with Single-Crystal Electrodes and High-Nuclearity Carbonyl Clusters," *The Journal of Physical Chemistry B*, vol. 105, no. 40, pp. 9719–9725, 2001.

[29] Y.-G. Yan, Y.-Y. Yang, B. Peng, S. Malkhandi, A. Bund, U. Stimming, and W.-B. Cai, "Study of CO Oxidation on Polycrystalline Pt Electrodes in Acidic Solution by ATR-SEIRAS," *The Journal of Physical Chemistry C*, vol. 115, no. 33, pp. 16378–16388, 2011.

[30] S.-C. Chang, J. D. Roth, Y. Ho, and M. J. Weaver, "New developments in electrochemical infrared spectroscopy: adlayer structures of carbon monoxide on monocrystalline metal electrodes," *Journal of Electron Spectroscopy and Related Phenomena*, vol. 54–55, pp. 1185–1203, 1990.

[31] M. Arenz, K. J. J. Mayrhofer, V. Stamenković, B. B. Blizanac, T. Tomoyuki, P. N. Ross, and N. M. Marković, "The Effect of the Particle Size on the Kinetics of CO Electrooxidation on High Surface Area Pt Catalysts," *Journal of the American Chemical Society*, vol. 127, no. 18, pp. 6819–6829, 2005.

[32] K. A. Friedrich, F. Henglein, U. Stimming, and W. Unkauf, "Investigation of Pt particles on gold substrates by IR spectroscopy particle structure and catalytic activity," *Colloids and Surfaces A: Physicochemical and Engineering Aspects*, vol. 134, no. 1–2, pp. 193–206, 1998.

[33] F. Maillard, E. R. Savinova, P. A. Simonov, V. I. Zaikovskii, and U. Stimming, "Infrared Spectroscopic Study of CO Adsorption and Electro-oxidation on Carbon-Supported Pt Nanoparticles: Interparticle versus Intraparticle Heterogeneity," *The Journal of Physical Chemistry B*, vol. 108, no. 46, pp. 17893–17904, 2004.

[34] S. Park, Tong, A. Wieckowski, and M. J. Weaver, "Infrared Spectral Comparison of Electrochemical Carbon Monoxide Adlayers Formed by Direct Chemisorption and Methanol Dissociation on Carbon-Supported Platinum Nanoparticles," *Langmuir*, vol. 18, no. 8, pp. 3233–3240, 2002.

[35] O. V. Cherstiouk, P. A. Simonov, V. I. Zaikovskii, and E. R. Savinova, "CO monolayer oxidation at Pt nanoparticles supported on glassy carbon electrodes," *Journal of Electroanalytical Chemistry*, vol. 554–555, pp. 241–251, 2003.

[36] S. Rudi, C. Cui, L. Gan, and P. Strasser, "Comparative Study of the Electrocatalytically Active Surface Areas (ECSAs) of Pt Alloy Nanoparticles Evaluated by Hupd and CO-stripping voltammetry," *Electrocatalysis*, vol. 5, no. 4, pp. 408–418, 2014.

[37] G.-F. Wei and Z.-P. Liu, "Restructuring and Hydrogen Evolution on Pt Nanoparticle," *Chem. Sci.*, vol. 6, no. 2, pp. 1485–1490, 2015.

[38] Y. Shao-Horn, W. C. Sheng, S. Chen, P. J. Ferreira, E. F. Holby, and D. Morgan, "Instability of Supported Platinum Nanoparticles in Low-Temperature Fuel Cells," *Topics in Catalysis*, vol. 46, no. 3-4, pp. 285–305, 2007.

[39] R. Gómez, J. M. Feliu, A. Aldaz, and M. J. Weaver, "Validity of double-layer charge-corrected voltammetry for assaying carbon monoxide coverages on ordered transition metals: comparisons with adlayer structures in electrochemical and ultrahigh vacuum environments," *Surface Science*, vol. 410, no. 1, pp. 48–61, 1998.

[40] P. Hollins, "Coupling effects in the vibrational spectra of adsorbed layers with island structures," *Surface Science*, vol. 107, no. 1, pp. 75–87, 1981.

[41] P. Hollins, "The influence of surface defects on the infrared spectra of adsorbed species," *Surface Science Reports*, vol. 16, no. 2, pp. 51–94, 1992.

[42] M. W. Severson, C. Stuhlmann, I. Villegas, and M. J. Weaver, "Dipole–dipole coupling effects upon infrared spectroscopy of compressed electrochemical adlayers: Application to the Pt(111)/CO system," *The Journal of Chemical Physics*, vol. 103, no. 22, pp. 9832–9843, 1995.

[43] N. M. Marković, B. N. Grgur, C. A. Lucas, and P. N. Ross, "Electrooxidation of CO and H2/CO Mixtures on Pt(111) in Acid Solutions," *The Journal of Physical Chemistry B*, vol. 103, no. 3, pp. 487–495, 1999.

[44] P. Hollins and J. Pritchard, "Infrared studies of chemisorbed layers on single crystals," *Progress in Surface Science*, vol. 19, no. 4, pp. 275–349, 1985.

[45] V. Stamenković, K. C. Chou, G. A. Somorjai, P. N. Ross, and N. M. Marković, "Vibrational Properties of CO at the Pt(111)-Solution Interface: the Anomalous Stark-Tuning Slope," *The Journal of Physical Chemistry B*, vol. 109, no. 2, pp. 678–680, 2005.

[46] B. E. Hayden, "Reflection absorption infrared spectroscopy," in *Vibrational spectroscopy of molecules on surfaces* (J. T. Yates and T. E. Madey, eds.), vol. 1 of *Methods of surface characterization*, pp. 267–344, New York ; London: Plenum, 1987.

[47] C. A. Angelucci, E. Herrero, and J. M. Feliu, "Modeling CO Oxidation on Pt(111) Electrodes," *The Journal of Physical Chemistry C*, vol. 114, no. 33, pp. 14154–14163, 2010.

[48] S. Srinivasan and E. Gileadi, "The potential-sweep method: a theoretical analysis," *Electrochimica Acta*, vol. 11, no. 3, pp. 321–335, 1966.

[49] F. Maillard, M. Eikerling, O. V. Cherstiouk, S. Schreier, E. Savinova, and U. Stimming, "Size effects on reactivity of Pt nanoparticles in CO monolayer oxidation: The role of surface mobility," *Faraday Discussions*, vol. 125, no. 0, pp. 357–377, 2004.

[50] K. A. Friedrich, F. Henglein, U. Stimming, and W. Unkauf, "In-situ vibrational spectroscopy on Pt electrocatalysts," *Electrochimica Acta*, vol. 47, no. 5, pp. 689–694, 2001.

[51] P. Urchaga, S. Baranton, C. Coutanceau, and G. Jerkiewicz, "Electro-oxidation of COchem on Pt Nanosurfaces: Solution of the Peak Multiplicity Puzzle," *Langmuir*, vol. 28, no. 7, pp. 3658–3663, 2012.

[52] N. P. Lebedeva, A. Rodes, J. M. Feliu, M. T. M. Koper, and R. A. van Santen, "Role of Crystalline Defects in Electrocatalysis: CO Adsorption and Oxidation on Stepped Platinum Electrodes As Studied by in situ Infrared Spectroscopy," *The Journal of Physical Chemistry B*, vol. 106, no. 38, pp. 9863–9872, 2002.

[53] M. van der Niet, A. den Dunnen, L. Juurlink, and M. Koper, "Co-adsorption of O and H2O on Nanostructured Platinum Surfaces: Does OH Form at Steps?," *Angewandte Chemie International Edition*, vol. 49, no. 37, pp. 6572–6575, 2010.

[54] M. T. M. Koper, A. P. J. Jansen, R. A. van Santen, J. J. Lukkien, and P. a. J. Hilbers, "Monte Carlo simulations of a simple model for the electrocatalytic CO oxidation on platinum," *The Journal of Chemical Physics*, vol. 109, no. 14, pp. 6051–6062, 1998.

[55] N. P. Lebedeva, M. T. M. Koper, J. M. Feliu, and R. A. van Santen, "Mechanism and kinetics of the electrochemical CO adlayer oxidation on Pt(111)," *Journal of Electroanalytical Chemistry*, vol. 524–525, pp. 242–251, 2002.

[56] T. Iwasita and F. C. Nart, "In situ infrared spectroscopy at electrochemical interfaces," *Progress in surface science*, vol. 55, no. 4, pp. 271–340, 1997.

[57] C. Korzeniewski, "Infrared Spectroscopy in Electrochemistry: New Methods and Connections to UhV Surface Science," *Critical Reviews in Analytical Chemistry*, vol. 27, no. 2, pp. 81–102, 1997.

Chapter 5

Formic Acid Oxidation

5.1 Introduction

Formic acid is a promising candidate for use in proton exchange membrane fuel cells. [1–7] It has a reasonable practical energy density, high theoretical cell potential and exhibits low fuel crossover (table 1.1). One of the main obstacles to the widespread adoption of the direct formic acid fuel cell, however, is its decrease in performance over time due to catalyst poisoning. [8] Extensive investigations have been carried out over the last 100 years to elucidate the various mechanisms behind formic acid oxidation and the associated catalyst poisoning, however to date there remains uncertainty over the exact pathway the reactions follow. Furthermore, the mechanistic studies which have been carried out have focused on model catalysts, such as planar single crystal electrodes, while real supported nanoparticle catalysts have received less attention. The aim of this work is therefore to resolve some of the outstanding questions surrounding the mechanism of formic acid at Pt, and to do so using a real fuel cell catalyst. The experiments that follow are a combination of methods previously applied to planar electrodes that are now extended to supported nanoparticles, and novel experiments, all carried out in the IR spectroelectrochemical cell developed in Chapter 3.

5.2 Review of Formic Acid Oxidation at Pt Electrodes

A key feature of formic acid electrooxidation at Pt is the gradual decrease in oxidation rate with time. [9] In mechanistic terms this suggests the presence of multiple oxidation pathways, some in which the productive reaction occurs rapidly, and others which proceed via strongly adsorbed intermediates which block the electrode surface and decrease the rate. The simplest scheme, the so-called dual pathway mechanism, involves just 2 pathways, one which occurs rapidly via a reactive species, the other which occurs via formation of a poisoning intermediate (fig. 5.1). [9] This scheme forms the basis of almost all mechanistic studies of formic acid oxidation, where the primary objectives have been to identify the 2 intermediate species and determine the mechanisms associated with their formation and decomposition.

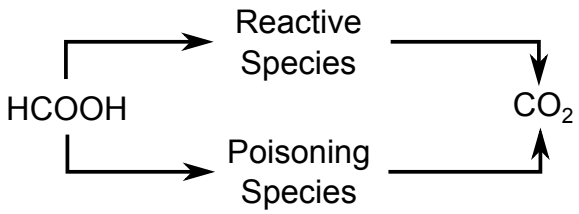

Figure 5.1: The dual pathway reaction scheme for formic acid oxidation.

While 2 intermediates have been well characterised during the reaction, there is not yet consensus on their role in the mechanism, with at least 6 separate mechanisms having been proposed to account for them (*vide infra*). The earliest proposals were made on the basis of electrochemical measurements and chemical intuition, while later proposals relied on the detailed analysis of reactions and spectroscopic characterisation of intermediates afforded by studies in ultra high vacuum (UHV). Most recently in situ studies using IR spectroscopy and differential electrochemical mass spectrometry (section 1.2) have led to further mechanisms being proposed.

There exist many reviews of formic acid oxidation, including the classic series by Parsons *et al.*, [9–13] as well as more recent overviews. [1, 2, 4–7, 14] The majority of these

reviews start from the dual pathway mechanism, however a more fundamental review will be attempted here so as to include all of the mechanisms proposed and the intermediates observed. Since many mechanisms rely on evidence from UHV studies for support, this review will start with a brief survey of the work in this area. A short summary of this literature review is given in section 5.2.3.

5.2.1 Formic Acid Decomposition in Ultra High Vacuum

In general studies in UHV are designed to reproduce aspects of real catalysts, but under very well defined conditions. [15–17] To this end the surfaces studied are usually single crystals of the catalyst material, with a particular Miller index exposed (section 2.1.2.1). The absence of any ambient species in UHV ensures the surface remains pristine, while the vacuum environment also permits a wider range of spectroscopic techniques to be applied than is possible under real reaction conditions. In a typical experiment the temperature of the crystal is initially kept very low and is studied as a gas is introduced. The low temperature ensures that no reaction occurs and allows weakly adsorbed species to be characterised. The temperature of the crystal is then ramped up, initiating reaction of the adsorbed species and eventually leading to desorption of all stable species. Where intermediates are observed, the well defined nature of the surface enables the adsorption site to be suggested, and variable angle experiments even permit the orientation of the species at the surface to be determined. [18]

The reaction of metal surfaces, including Pt, with formic acid has been well studied in UHV and is reviewed by Columbia and Thiele. [19] When the different low index surfaces of Pt were compared, it was found that while Pt(100) is unreactive unless pre-treated with O_2, Pt(111) and Pt(110) both catalyse the decomposition of formic acid. The main reaction occurring was dehydrogenation, to give CO_2 and H_2, while around 10% of the formic acid was dehydrated to yield CO and H_2O.

The reaction steps were studied in detail, starting from the dosing of low temperature Pt crystals with formic acid, which led to molecular adsorption. On the Pt surface the formic acid forms H-bonded chains, adopting either the α or the β geometry (fig. 5.2A). On heating the crystal reaction occurs and adsorbed formate is detected (fig. 5.2B). Analysis of the formate vibrations suggest that it is adsorbed in the bridging geometry (table 5.1). The absence of the δ(C−H) and ν_a(OCO) vibrations was explained using the surface selection rule (SSR, section 2.3.4.1). The image dipole induced in the metal by the formate vibrations will tend to augment the dipole moment of a vibration normal to the surface, but cancel it out if the vibration is parallel to the surface. For the missing modes to be perfectly parallel to the surface HCOO(ad) would have to be sitting in the plane normal to the surface, bridging two Pt sites. This interpretation is supported by a similar study on the Pt(110) surface, where variable angle measurements enabled the effects of the SSR to be minimised and the two modes could be observed. [18] In this case the difference between the ν_a(OCO) and ν_s(OCO) vibrations, known as Δ, can be compared to the values from well characterised molecular formates (table 5.2). The value of $180\,\mathrm{cm}^{-1}$ correlates well with that seen for bridging species. The precise orientation can also be calculated directly from the variable angle measurements, and is shown to be $< 10°$ from the surface normal. [18] This species is referred to as HCOO(ad) throughout this thesis.

A different formate species was initially seen on O-predosed Pt(111), and analysis of the value of Δ suggested this species was monodentate formate. [20] The species was unstable with respect to conversion to the bridging form, however, having a lifetime of around 10 minutes even at 130 K.

Additional bimolecular decomposition pathways have been proposed. It is suggested that the chains of adsorbed acid break up to leave dimers (fig. 5.2C), which then dehydrate to form anhydride or formyl species.

Significant differences were observed when the reaction on Ni and Ru was investigated.

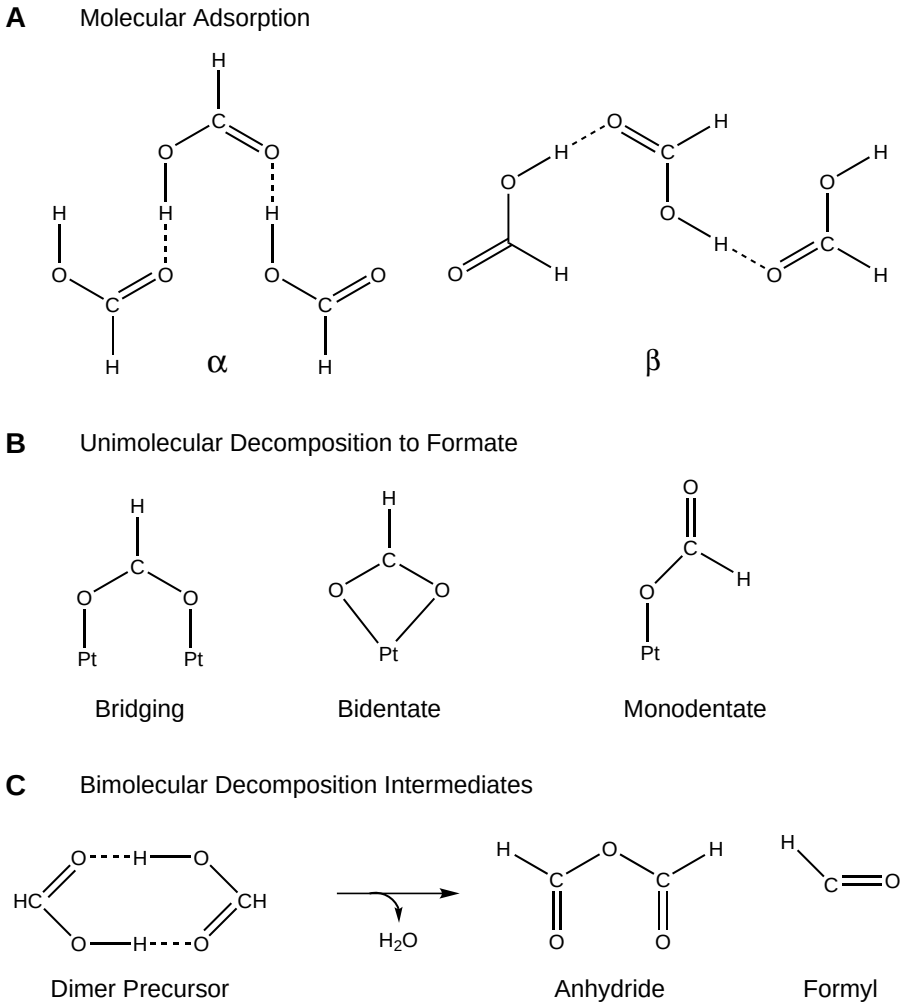

Figure 5.2: Species formed from formic acid adsorption in UHV. A: The α and β geometries adopted by formic acid on adsorption at low temperature. B: Different binding modes of adsorbed formate, bridging, bidentate and monodentate. C: The bimolecular dehydration pathway suggested and the resulting anhydride and formyl products. Figure adapted from reference [19].

Table 5.1: Vibrations assigned to formate species adsorbed on Pt surfaces in UHV.[1]

	Wavenumber / cm^{-1}		
	Pt(111)		Pt(110)
Mode	Monodentate [20]	Bidentate [21]	Bidentate [18]
ν(PtO)	360	360	355
δ(OCO)	780	780	785 (785)
ν_s(OCO)	1290	1330	1340 (1320)
δ(CH)			(1010)
ν_a(OCO)	1620		1560 (1560)
ν(CH)	2920	2920	2950 (2185)
ν(PtO)+ν_s(OCO)		1690	
$2\nu_s$(OCO)		2670	

[1] Deuterated species in brackets.

Table 5.2: The splitting parameter Δ for different formate adsorption geometries.[1]

Mode	Δ / cm^{-1}
Free ion	201
Monodentate	$\sim$ 300
Bidentate	$<$ 80
Bridging	$\sim$ 200

[1] $\Delta = \nu_a(\mathrm{OCO}) - \nu_s(\mathrm{OCO})$. Adapted from reference [20].

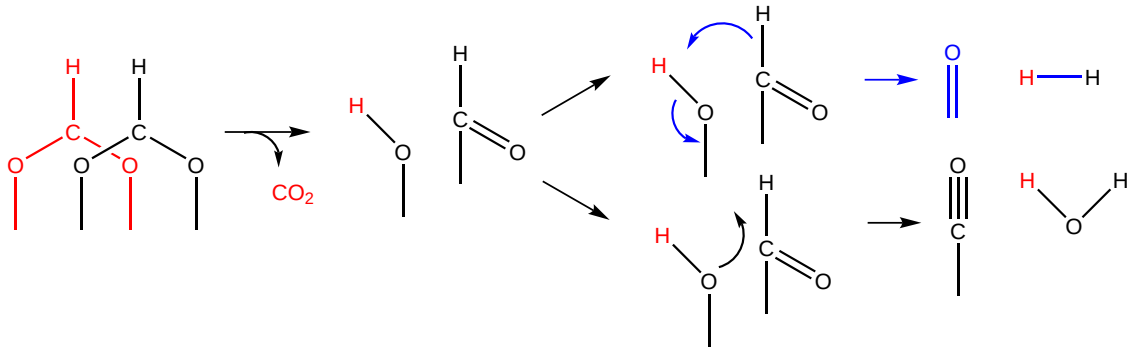

Figure 5.3: The bimolecular mechanism postulated for formate decomposition on Ru. [23]

In both cases a bimolecular reaction was implicated, based on the exclusive formation of H_2O and D_2 from DCOOH. [22,23] In contrast, when DCOOH decompositon is carried out on Pt all species are observed: D_2, HD, H_2 and H_2O, HOD and D_2O. [19] The bimolecular mechanism proposed for Ru is shown in fig. 5.3. The mechanism involves the insertion of an acyl proton from formate into the C−O bond of an adjacent formate.

In addition, for Ni, the reaction was found to be autocatalytic, that is as the coverage of HCOO(ad) decreased the reaction rate increased. [24] This behaviour can be explained if an attractive interaction exists between neighbouring HCOO(ad) species. The interaction leads to the formation of HCOO(ad) islands were the adsorbed species stabilise each other. Loss from just one site destabilises the species on the neighbouring sites and sets off a chain reaction. [19] The presence of autocatalysis on Ni implies that although the mechanism on both Ni and Ru are bimolecular, the reaction mechanisms are distinct.

The observation of HCOO(ad), and the bimolecular and autocatalytic properties of formic acid decomposition at various metals in UHV has heavily informed work on the electrocatalytic oxidation mechanisms.[1]

[1]The validity of comparing results from UHV to those obtained in solution and with applied potential has been discussed. [16, 17]

5.2.2 Formic Acid Electrooxidation

The first comprehensive reports of formic acid oxidation came from Erich Müller in 1923, [25] and were summarised in later work by Brummer and Makrides. [26] Müller observed that the ratio of the charge passed to the amount of CO_2 produced was almost stoichiometric, that there were potential regions in which the current decreased with increasing potential, and that under constant current conditions the potential was observed to oscillate. Following these observations a mechanism was proposed (eqs. (5.1) to (5.6)).

Mechanism 1: The indirect H_2 pathway of Müller *et al.*

$$\mathrm{HCOOH(aq)} \longrightarrow \mathrm{HCOOH(ads)} \tag{5.1}$$

$$\mathrm{HCOOH(ads)} \longrightarrow \mathrm{H_2 + CO_2} \tag{5.2}$$

$$\mathrm{H_2} \longrightarrow \mathrm{2\,H^+ + 2e^-} \tag{5.3}$$

The decrease in current at higher potential was attributed to the formation of Pt oxide. The subsequent increase in current was then ascribed to the increasing rate of the reaction eq. (5.4).

$$\mathrm{HCOO^-(aq)} \longrightarrow \mathrm{HCOO(ad) + e^-} \tag{5.4}$$

$$\mathrm{HCOO(ad)} \longrightarrow \mathrm{H(ad) + CO_2} \tag{5.5}$$

$$\mathrm{H(ad)} \longrightarrow \mathrm{H^+ + e^-} \tag{5.6}$$

This mechanism took into account the observation of open circuit H_2 and CO_2 production by metals such as Rh, Pd and Os in formic acid solution. [26] It presents no obvious mechanism for potential oscillations, however, nor for the dip in reaction rates with increasing potential, since Pt oxide formation occurs at higher potentials than those

at which the current decreases.

Further work on the electrochemical oxidation showed that the oxidation rate at a given potential decreases with time, while there is a steady build-up of a strongly adsorbed intermediate. [26] It was therefore assumed that the adsorbed species interferes with the oxidation. The adsorption behaviour of the adsorbed species was determined and it was found that the coverage decreased with potential after 0.35 V and was fully removed at 0.7 V. There were two candidates proposed for the poisoning species, CO(ad) and adsorbed formyl, −CH=O(ad), however in the absence of in situ characterisation techniques it was impossible to offer a definitive assignment. Irrespective of its identity, the presence of a strongly adsorbed species was enough to suggest a 'dual pathway' mechanism for oxidation, proposed first by Capon and Parsons. [9–12]

Mechanism 2: Capon and Parsons' Dual Pathway Mechanism Capon and Parsons' work utilised cyclic voltammetry to characterise the reaction at different potentials. [9] They made use of the ratio between the H underpotential deposition (upd) charge, and the charge required for the oxidation of the strongly adsorbed species, to determine the number of electrons per Pt site required for the oxidation. Their observation of 1.3 electrons per site suggested a mixture of species and led them to formulate the following mechanism. In it there are two pathways for oxidation, one via a weakly adsorbed intermediate that occurs at low potential (eq. (5.7)), the other via strongly adsorbed intermediate that requires higher potentials for its oxidation (eqs. (5.8) to (5.11)). The presence of the strongly adsorbed species blocks the adsorption of the weakly adsorbed species and gives rise to the multiple peaks observed in the cyclic voltammogram. It should be noted that while the identity of the strongly-bound intermediate was debated there was much less uncertainty surrounding the assignment of −COOH to the weakly

bound reactive intermediate. [27]

$$\mathrm{HCOOH} \longrightarrow \mathrm{COOH(ad)} + \mathrm{H^+} + \mathrm{e^-} \longrightarrow \mathrm{CO_2} + \mathrm{H^+} + \mathrm{e^-} \tag{5.7}$$

$$\mathrm{HCOOH} \longrightarrow \mathrm{COOH(ad)} + 2\,\mathrm{H(ads)} \longrightarrow \mathrm{COH(ads)} + \mathrm{H_2O} \tag{5.8}$$

$$\mathrm{COH(ad)} + \mathrm{H_2O} \xrightarrow{\text{slow}} \mathrm{C(OH)OH(ad)} + \mathrm{H^+} + \mathrm{e^-} \tag{5.9}$$

$$\mathrm{C(OH)OH(ad)} \xrightarrow{\text{fast}} \mathrm{COOH(ad)} + \mathrm{H^+} + \mathrm{e^-} \tag{5.10}$$

$$\mathrm{COOH(ad)} \xrightarrow{\text{fast}} \mathrm{CO_2(g)} + \mathrm{H^+} + \mathrm{e^-} \tag{5.11}$$

Following Capon and Parson's investigations there were two significant developments in the experimental techniques available for fundamental research into electrocatalysis: the introduction of a reproducible method for preparing single crystal electrodes by Clavilier *et al.*, [28] and the demonstration of combined electrochemical and in situ spectroscopic methods which permitted characterisation of adsorbed species during catalysis. [29]

5.2.2.1 Electrochemical Investigation on Single Crystal Electrodes

The introduction of reproducible methods for preparing single crystal electrodes enabled the structure sensitivity of the formic acid oxidation reaction to be studied on different Pt surfaces. [28, 30–32] Cyclic voltammograms showing formic acid oxidation at the 3 basal planes of Pt are shown in fig. 5.4. Cyclic voltammetry on a Pt(111) electrode shows low current but little hysteresis between forward and backward cycles. Conversely, the Pt(100) electrode shows very high currents, but only on the negative-going cycle after excursion to high potential. The Pt(110) electrode shows negligible current until after 0.65 V on the forward scan, at which point the current peaks and falls again, returning over an extended region on the return scan.

The varying extent of hysteresis between the three planes suggests that the rate of

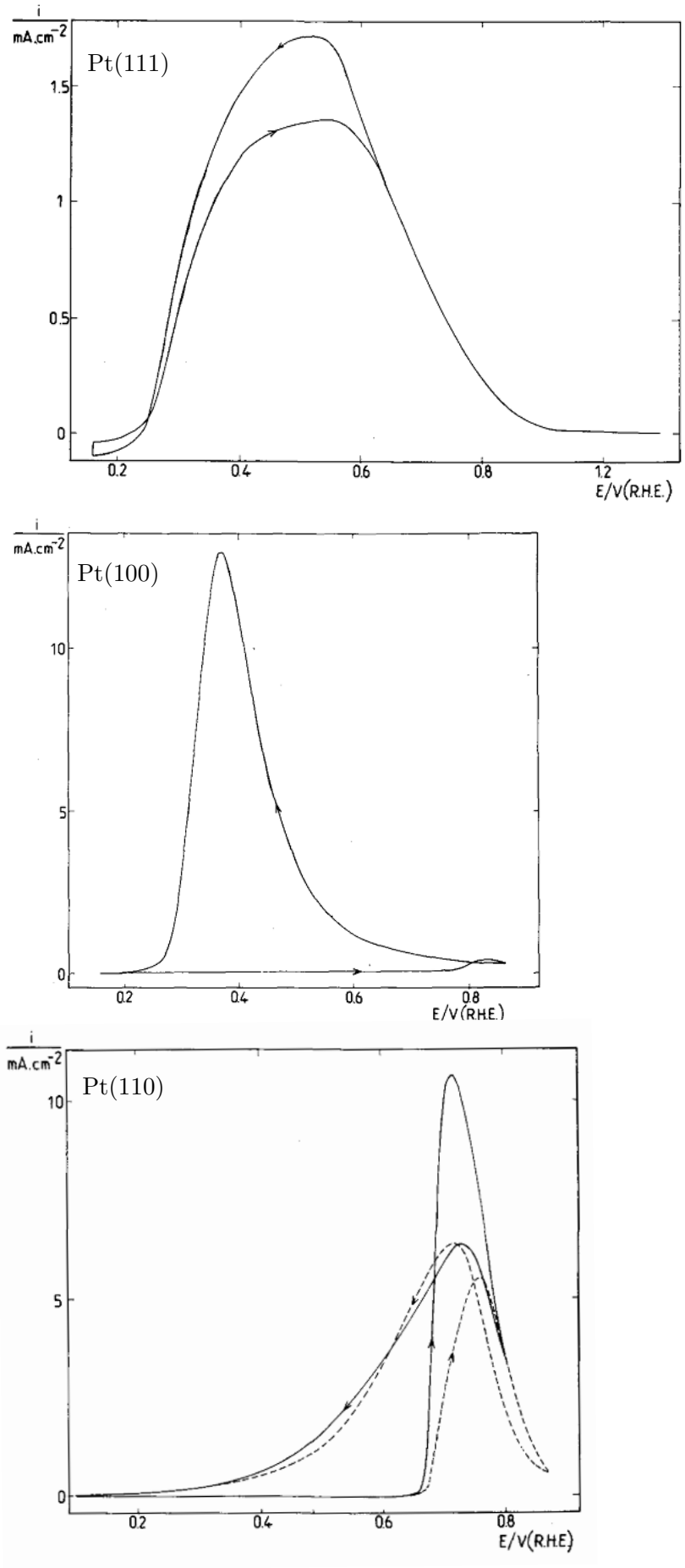

Figure 5.4: Cyclic voltammograms showing formic acid oxidation at the 3 basal planes of Pt. Solution: 0.1 M HCOOH + 0.5 M H_2SO_4. Scan rate = 50 mV s^{-1}. Reprinted from reference [28]. Copyright 1981, with permission from Elsevier.

poisoning is affected by surface structure, with very little poisoning occurring on the (111) surface. This hypothesis is supported by single crystal measurements, in which the rate of HCOOH dehydration to CO was measured directly using pulse experiments and found to be negligible on Pt(111), [33, 34] and by electronic structure calculations using density functional theory (DFT) which predict that HCOOH dehydration should not occur at all on Pt(111). [35] Experiments in which CO formation on Pt(111) *is* observed can be explained by considering the presence of defect sites on any real surface, at which CO could form. The adsorption of a well-defined cyanide (CN^-) adlayer on Pt(111) electrodes was observed to block CO formation and was originally taken as evidence for a specific site requirement for CO formation from HCOOH, due to the characteristic geometry of the free sites left by the CN^- adlayer. [36] In light of other evidence it is more likely that the CO was formed at defect sites on the (111) surface, however, and that CN^- preferentially blocked these sites on adsorption. [33]

Useful catalysts are not composed solely of flat crystal planes, they have edges and corners, junctions where these planes meet to form 3D structures. Stepped single crystal electrodes can be used to investigate the effect of certain aspects of these junctions, such as their symmetry and density, on activity. For electrodes composed of (111) terraces interrupted by steps of (110) orientation it was found that an increase in step density led to an increase in CO formation and a decrease in activity. For (111) electrodes where the step was of (100) symmetry it was also found that an increase in step density decreased the activity, although in this case the poisoning was relatively unaffected by the steps. This suggests the (100) steps have lower activity for both oxidation and CO formation than the (111) terraces. [33] This is significant as it reveals a large difference in behaviour of terrace and step sites of the same symmetry and suggests that the ensemble size, as well as the local symmetry, affects the rate of reaction. This is supported by the observation that on (100) electrodes the presence of (111) steps does not make any difference to

the catalytic activity, implying that the (111) edges have a similar activity to the (100) terraces. It should be noted that when the size of the terrace becomes small, e.g. $n = 3$, large differences are observed as the distinction between terrace and step environments decreases. [33]

The clear differences in current between surfaces of different orientation was further tested by comparison with different shape-controlled nanoparticles. [37, 38] Such a comparison between well-defined nanoparticles and single crystals is especially valid in this case due to the apparent insensitivity of formic acid oxidation to terrace size in the (100) or (111) crystal planes. [33, 39] The results are similar to those seen on stepped single crystals: nanoparticles with many (100) sites are the most active, those with many (111) sites are less active, while spherical particles are the least active. The trend in activity observed for the nanoparticles was also explained via the differing extent of poisoning on the different surfaces. However, rather than use ensemble or direct electronic arguments to rationalise the poisoning, the effects were explained by considering the potential-dependent coverage of ions in the electrolyte. This coverage is related to the potential of zero total charge (pztc) of the surface, which is lower for lower coordinate sites such as edges and corners, and also decreases with size for nanoparticles. [40, 41] Due to these effects, the surface structure, via the pztc, is believed to be of more direct importance in determining activity than other factors such as particle size.

5.2.2.2 In situ Spectroscopic Investigation

Adsorbed carbon monoxide was the first intermediate to be observed, evidence coming from IR spectroscopy. [42] On polycrystalline platinum two peaks were observed, an intense peak at $2061\,\mathrm{cm^{-1}}$ and weaker peak at $1840\,\mathrm{cm^{-1}}$. These peaks shifted to higher wavenumber and increased in amplitude as the potential limit increased from 0.15 V up to 0.45 V, after which they decreased and were not observed above 0.65 V. Similar in situ

results have been obtained on almost all Pt electrodes studied with formic acid oxidation, including polycrystalline, [43] single crystal [44–46] and nanoparticle surfaces. [47]

The assignment of CO(ad) as the poisoning species was confirmed using Differential Electrochemical Mass Spectrometry (DEMS, section 1.2). [48, 49][2] The DEMS data confirmed that the strongly adsorbed intermediate only has one oxygen atom and it comes from formic acid. When it is oxidised to CO_2 the additional oxygen atom comes from the solution. Conversely, the oxygen atoms in the product CO_2 from the direct (that is, non-CO) pathway both come from formic acid.

CO is now widely accepted to be the strongly adsorbed intermediate in the dual pathway mechanism and remains the most commonly used spectroscopic handle on the reaction. [43–47]

The extent to which CO oxidation contributes to the overall oxidation in the so-called 'indirect pathway' was investigated by Chen *et al.* in a series of measurements. They represented the rate of change of CO coverage with time as:

$$\frac{d\theta_{\mathrm{CO}}}{dt} = k_1\theta_{\mathrm{HCOOH}} - k_2\theta_{\mathrm{CO}}\theta_{\mathrm{OH}} \tag{5.12}$$

where θ_{HCOOH} represents the adsorption of HCOOH in the geometry required for dehydration, related to the bulk concentration of HCOOH via a suitable, unspecified isotherm, k_1 represents the rate constant of the dehydration reaction and k_2 represents the rate constant for CO oxidation.

To obtain estimates of the individual rate constants, conditions were chosen to min-

[2]Initially the DEMS results conflicted with the assignment of CO(ad). In the measurement both the Faradaic current and the ion current from the mass spectrometer were recorded during the oxidation of the strongly bound intermediate. These signals were compared to the same signals recorded during the oxidation of a monolayer of CO adsorbed from saturated CO solution, for which the number of electrons required was known to be 2. The comparison suggested that 3 electrons per desorbed intermediate were required for its oxidation. [48] This discrepancy was later explained by the different saturation coverages of CO, θ_{CO}. The saturation coverage obtained from adsorption of CO(aq), $\theta_{\mathrm{CO}} \sim 0.75$, is different from that obtained by dehydration of HCOOH(aq), $\theta_{\mathrm{CO}} \sim 0.5$, as observed by IR spectroscopy, leading to miscalibration of the ion current. [50, 51]

Table 5.3: Turnover frequencies for CO formation and oxidation during formic acid oxidation.[a]

	Turnover Frequency / molecules site^{-1} s^{-1}		
Reaction	0.4 V	0.5 V	0.6 V
HCOOH dehydration	2×10^{-3}	1.8×10^{-3}	3.2×10^{-4}
CO(ad) oxidation	n.d.	6.4×10^{-5}	3.3×10^{-4}
Total HCOOH oxidation	0.3	1.4	2.5

[a] Adapted from reference [52].

imise the contribution of the other constant. One method involved rapid exchange of supporting electrolyte for one containing HCOOH, enabling the measurement of k_1 in the limit $\theta_{CO} = 0$, while the reverse exchange enabled the measurement of k_2 in the absence of HCOOH (which, assuming rapid equilibrium, means $\theta_{HCOOH} = 0$). [52] A similar approach used potential steps to achieve the same results; equilibration at low potential ensured saturation of CO, *ie* $\theta_{HCOOH} = 0$, so that on stepping the potential $d\theta/dt = k_2\theta_{CO}\theta_{OH}$. Conversley, by starting at high potential, where high values of θ_{OH} cause the coverage of CO to be negligible, and stepping down to low potentials, k_1 can be obtained. [50] In both cases θ_{CO} was obtained from the integrated CO peak intensity from *in situ* IR spectroscopy. The relationship between IR peak intensity and θ_{CO} was calculated via the charge observed in electrochemical CO stripping experiments.

From this data, turnover frequencies (TOFs, the rate divided by the number of sites) were calculated for CO. Similar TOFs were calculated for the reaction as a whole, based on the current. Comparison of the two showed that CO oxidation contributes negligibly to the total current (table 5.3).

Around a decade after the assignment of CO to the poisoning intermediate, Miki and Osawa introduced a new Pt ATR-SEIRA methodolgy (section 1.2.1). [53] When this technique was used to study a Pt electrode during formic acid oxidation a new potential-

dependent peak was observed around $1330\,\mathrm{cm}^{-1}$. Based on the UHV literature (section 5.2.1) they assigned this peak to the ν_s(OCO) mode of adsorbed formate, HCOO(ad). The absence of the remaining modes was taken as evidence for the species sitting in the plane of the surface normal, as it was for the UHV measurements. This observation also correlates with similar observations of formate species adsorbed from formic acid solution under potential control on Au [29], Rh [54] and on Ir (111) and (100) during cyclic voltammetry. [55]. The ν_s(OCO) peak of HCOO(ad) on Pt has subsequently been confirmed by several groups using the same ATR-SEIRA methodology. [52, 56, 57] In addition, lower wavenumber modes of adsorbed formate have also been reported on several metals using Raman spectroscopy [58] and Sum Frequency Generation (SFG). [59].

The presence of further intermediates, such as the −COOH long thought of as the reactive intermediate, has been suggested but with the exception of single reports of a peak at $1262\,\mathrm{cm}^{-1}$ by Xia *et al.* [60] and the observation of a very weak band at $1735\,\mathrm{cm}^{-1}$ by Sun *et al.* [27] no other species have been reported. Calculations suggest that −COOH(ad) on Pt(111) in vacuum should have IR active vibrations at $1748\,\mathrm{cm}^{-1}$, $1221\,\mathrm{cm}^{-1}$ and $1124\,\mathrm{cm}^{-1}$, corresponding to the ν(HOC−O), δ(OH) and ν(HO−CO) vibrations, respectively. [61]

While the assignment of the $1330\,\mathrm{cm}^{-1}$ peak to HCOO(ad) has not been disputed, the subsequent role of HCOO(ad) in formic acid oxidation has been. [57,62] The evidence for assigning HCOO(ad) to the reactive intermediate, aside from it being the only species other than CO(ad) to be detected, is based on the following 3 observations [62,63]:

1. The trend in integrated formate intensity resembles the current in the cyclic voltammogram, although the peaks do not perfectly coincide

2. On solution exchange from $H^{12}COOH$ to $H^{13}COOH$ the formate peak also exchanges rapidly, with apparent first order kinetics ($k_1 \approx 5\,\mathrm{s}^{-1}$) and a constant current of 3 mA

3. The formate and CO bands change periodically during potentiostatic oscillation.

5.2.2.3 Oscillations in formic acid oxidation at constant current/potential

The oscillation of potential during constant current formic acid oxidation was first observed by Müller and has since been studies extensively. [63–69] The oscillatory regime arises when two conditions are met: a significant cell resistance which permits the working electrode potential to deviate from the applied potential (section 2.2.3), and surface chemistry which gives rise to abrupt changes in current with small changes in potential, such as stripping of poisoning species. In the case of formic acid oxidation, oscillations can be explained by as follows. At low potentials a layer of CO forms on the electrode and blocks further oxidation, no oscillations are observed. At higher potentials, however:

1. The higher potential will lead to a slow decrease in the coverage of CO
2. The decreased CO coverage leads to an increase in active sites and an increase in current at the same potential
3. The increase in current leads to an increase in iR and therefore a drop in the working electrode potential for the same applied potential
4. The decrease in electrode potential leads to an increase in CO coverage
5. An increased CO coverage leads to a decrease in active sites and a decrease in current
6. A decreased current leads to a decrease in iR and therefore to an increase in working electrode potential
7. The cycle repeats...

A similar effect also occurs in potential sweep experiments, appearing as either as a single sharp peak in potential, as seen later in the cyclic voltammograms in 0.2 M phosphate buffer solution (section 5.3.10), or as a continuing series of oscillations as seen in steady state current measurements (section 5.3.7).

Mechanism 3: The formate pathway after Samjeské *et al.* The original work by Osawa's group focused on explaining the origin of the potential and current oscillations observed during galvanostatic and potentiostatic oxidation. [63, 67] In particular,

they sought an explanation for the decrease in current with increasing potential in the voltammogram, known as negative differential resistance, which gives rises to the feedback mechanism necessary for oscillations (see section 5.2.2.3). They noted the presence of formate in the high potential, high current region, where the CO coverage was small and attributed the observed current to the decomposition of HCOO(ad). They suggested a vacancy-driven mechanism for formate decomposition, in which HCOO(ad) required an adjacent vacant site for it to decompose. This means the current would increase with the coverage of formate up to the point at which the formate coverage was limiting the number of adjacent vacant sites; beyond this point the decomposition rate, and therefore the current, would fall. This mechanism also gives rise to autocatalysis, similar to that suggested for HCOO(ad) on Ni in UHV (section 5.2.1), since removal of one HCOO(ad) enables adjacent species to decompose, setting off a chain reaction.

This can be written as:

$$i \propto -\frac{d\theta_{\mathrm{HCOO}}}{dt} = k\theta_{\mathrm{HCOO}}(1 - \theta_{\mathrm{CO_L}} - 2\theta_{\mathrm{CO_B}} - 2\theta_{\mathrm{HCOO}}) \tag{5.13}$$

where the term in brackets represents the coverage of vacant sites. [63] The potential-dependence can be removed from the equation by dividing the current by the rate constant, which now predicts a bell-shaped dependence of the current on formate coverage, showing a maximum at $\theta_{\mathrm{HCOO}*}$:

$$\frac{di/k}{d\theta_{\mathrm{HCOO}}} = 1 - \theta_{\mathrm{CO_L}} - 2\theta_{\mathrm{CO_B}} - 4\theta_{\mathrm{HCOO}*} = 0 \tag{5.14}$$

$$\theta_{\mathrm{HCOO}*} = \frac{1 - \theta_{\mathrm{CO_L}} - 2\theta_{\mathrm{CO_B}}}{4} \tag{5.15}$$

In this model the current depends on the coverages of both CO(ad) and HCOO(ad), with a high coverage of either species inhibiting the formation and decomposition of

HCOO(ad). While this provides a qualitative explanation of the cyclic voltammogram and oscillation mechanism, quantitative measurements have failed to establish a relationship between HCOO(ad) coverage and current that accounts for all of the observed current. Chen *et al.* place an upper limit of 15% on the total contribution of the HCOO(ad) pathway to the overall current, based on the observed turnover frequencies (table 5.3). [62] Furthermore Okamoto *et al.* show that while the shape of the cyclic voltammogram changes as the scan rate is decreased, the shape of the HCOO(ad) intensity/potential profile hardly changes, indicating that the similarity between the HCOO(ad) intensity and current under the conditions chosen by Samjeské is coincidental. [57]

Mechanism 4: Triple pathway mechanism after Chen *et al.* To account for their observed TOFs, and their further evidence of the non-linear relationship between the current and formate concentration, Chen *et al.* proposed a third pathway proceeding through an as-yet undetected intermediate. [52] This interpretation is supported by HCOO(ad) coverage/current relationships derived purely electrochemically using fast scan rate cyclic voltammetry, which also revealed that HCOO(ad) adsorption occurs at a higher potential than the onset potential of the main formic acid current wave. [70] They expect either a weakly adsorbed HCOOH species or an activated transition state, which because of its low steady state coverage is not detected by spectroscopy. In addition, they suggest that HCOO(ad) may adsorb directly from the anion, $HCOO^-$(aq) rather than the acid, despite its low bulk concentration ($\sim 2 \times 10^{-5}$ M in 0.1 M HCOOH + 0.5 M H_2SO_4).

These ideas were later combined by Osawa, Koper and co-workers who suggested the active pathway actually proceeds via direct reaction of the anion, while conversely HCOO(ad) forms only from the acid. [71, 72] This theory is supported by the pH dependence of the reaction, which shows that the maximum peak current occurs at a pH around the pKa of HCOOH, which is 3.75 (fig. 5.5A). As the pH increases towards the pKa, the

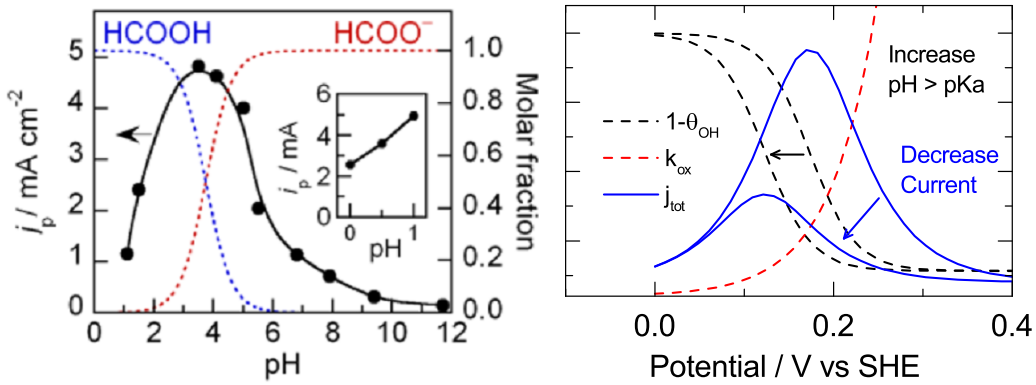

(A) (B)

Figure 5.5: (a) The pH dependence of the peak oxidation current, j_p in cyclic voltammograms obtained at different pH values. Adapted with permission from reference [71]. Copyright 2013 American Chemical Society. (b) Illustration of the pH dependence of the formic acid oxidation current using the model of Joo *et al.* $1 - \theta_{OH}$ = fraction of sites left vacant by OH(ad) (black dashed line). k_{ox} = Butler-Volmer rate law for the direct pathway (red dashed line). j_{tot} = total current (blue line). [71]

anion concentration increases, which in turn should lead to an increase in current if the anion were the active species. The decrease in current at pH values above the pKa, where a further increase in anion concentration, and therefore current, is expected, is explained by considering the decrease in surface sites through competing formation of OH(ad). As the pH increases the onset potential for OH(ad) formation decreases, decreasing the potential window over which vacant Pt sites are available for formic acid oxidation (fig. 5.5B).

A different approach was taken by Cuesta *et al.* who were interested in the formation of HCOO(ad). [51] At most concentrations used in mechanistic studies (1 mM to 1000 mM) HCOO(ad) formation occurs rapidly and reaches saturation in much less than the time it takes to collect an IR spectrum. As a result there have been very few studies relating the HCOO(ad) coverage with other parameters, such as CO(ad) coverage or current. In order to record spectra during HCOO(ad) adsorption, thereby collecting data over a range of HCOO(ad) coverages, concentrated formic acid was added to unstirred supporting electrolyte while spectra were recorded as at the maximum rate permitted by

the instrument ($7\,s^{-1}$). Under these conditions the concentration of formic acid at the electrode, and therefore the coverage of formate, changed slowly enough to be followed spectroscopically. Based on this new information Cuesta *et al.* proposed a mechanism for formic acid oxidation with several novel features.

Mechanism 5: Common formate intermediate after Cuesta *et al.* When the adsorption of HCOO(ad) was followed using the approach described above, both CO(ad) and HCOO(ad) formation were observed. The CO(ad) intensity, I_{CO} increased with time while the HCOO(ad) intensity, I_{HCOO} increased rapidly and then decreased. Based on a plot of dI_{CO}/dt against I_{HCOO}, which showed that the rate of change of CO(ad) was proportional to the HCOO(ad) coverage, the data was interpreted in terms of the formation of CO(ad) from HCOO(ad) (eq. (5.16)). Previous reports of a sudden appearance of linear CO(ad) at potentials above the onset potential of formic acid oxidation were also used to justify this interpretation. [45] Note, however the appearance of linear CO in this report was also correlated with a decrease in bridging CO(ad), suggesting its appearance there was correlated with a sudden interconversion between adsorption modes rather than the onset of formation.

$$HCOOH(aq) \longrightarrow HCOO(ad) + H^+ + e^- \tag{5.16}$$

$$HCOO(ad) + H^+ + e^- \longrightarrow CO(ad) + H_2O \tag{5.17}$$

The mechanism was further justified based on an analysis of the Tafel slopes derived from different models, with the measured Tafel slope found to be closest to that predicted by the formate precursor model in eq. (5.16). A decrease in the rate of CO(ad) formation at higher CO(ad) coverages was taken to imply that HCOO(ad) required adjacent vacant sites for dehydration to CO(ad), in a similar way Samjeské *et al.* suggested HCOO(ad) needed vacant sites for oxidation to CO_2. This conclusion relies on the assumption of

a linear relationship between I_{CO} and coverage up to high coverages, however, and it is suggested that this may not be valid as found for CO in Chapter 4.

This experimental approach towards obtaining I_{HCOO} was taken further to argue for adsorbed formate also being the active intermediate in formic acid oxidation, and that the same mechanism operates on both Pt and Au. [73] It was demonstrated that on both metals a plot of I^2_{HCOO} versus current was linear for relative intensities, and therefore coverages, up to around 0.3. This was taken to imply that the rate determining step was bimolecular and a mechanism based on this was postulated (eq. (5.18), where * represents a vacant surface site), by analogy with the mechanism suggested for formate decomposition on Ru in UHV (section 5.2.1 and fig. 5.3). [23] It should be noted that the relationship between the HCOO(ad) coverage and the current was also derived independently by Xu *et al.* using fast scan rate voltammetry. The relationship they derived was successfully fitted to a different model in which HCOO(ad) simply blocked the surface and the current came from the first order reaction of aqueous formic acid. [70] Thus, a bimolecular mechanism is not the only explanation for such a relationship.

$$2\mathrm{HCOOH} \rightleftharpoons [\mathrm{HCOOH}]_2 + 4\ * \tag{5.18}$$

$$\longrightarrow 2\,\mathrm{HCOO(ad)} + 2\,\mathrm{H^+} + 2\,\mathrm{e^-} \tag{5.19}$$

$$2\,\mathrm{HCOO(ad)} \longrightarrow 2\,\mathrm{CO_2} + \mathrm{H_2} + 4\ * \tag{5.20}$$

$$\mathrm{H_2} \longrightarrow 2\,\mathrm{H^+} + 2\,\mathrm{e^-} \tag{5.21}$$

It should be noted that in the mechanism of Cuesta *et al.* two distinct electron transfer reactions occur, with the second transfer actually being the oxidation of the nascent H_2. This implies that the activity of formic acid oxidation at a catalyst should therefore correlate with the H_2 oxidation activity, providing a simple means with which to test this

hypothetical mechanism. Brimaud *et al.* chose to do just this, and started by examining the similarity of the mechanisms on Au and Pt reported by Cuesta *et al.*. [56] Brimaud *et al.* noted that H_2 oxidation on Au can often be explained by trace levels of platinum group metals. When they used decontaminated Au electrodes they found no H_2 oxidation activity, questioning the validity of the mechanism proposed by Cuesta *et al.* Instead, Brimaud *et al.* proposed a different mechanism, starting from an explanation of the pH dependence reported by Joo *et al.* [71, 72]

Mechanism 6: $HCOOH \cdot HCOO^-$ Interaction To confirm the explanation that the bell-shaped pH dependence of formic acid oxidation derives from the interplay between formate concentration and the onset of OH(ad) formation, Brimaud *et al.* compared the reactivity on Pt with that of Au. Since OH(ad) formation on Au occurs at a higher potential than on Pt, the pH dependence should reflect this, however it resembled the relationship on Pt exactly, with the peak current still observed at pH = pKa. This suggested that OH(ad) formation was not part of the reason for the bell-shape dependence.

Contrary to the observations of Joo *et al.*, however, when the pH dependence was measured on Pt, a plateau in current density as a function of pH was observed, rather than a peak. It is suggested that this effect may be down to the experimental conditions, however. The sulfate solution used by Brimaud *et al.* would not buffer the pH as well as the phosphate buffer used by Joo *et al.* The discrepancy between Au and Pt may then arise as a result of the much greater current density observed for formic acid oxidation on Pt, since a much greater local pH variation would be expected. This conclusion is supported by the difference in behaviour when the electrode was rotated: the initial linear trend became non-linear with the emergence of a peak-like shape. It is suggested that the decreased diffusion layer at the rotating electrode would lead to more rapid removal of the generated H^+, minimising the deviation from bulk pH.

In light of their finding that OH(ad) formation cannot account for the decrease in current with pH, Brimaud *et al.* suggest that in order for the bell-shaped pH dependence to occur with a maximum at the pKa, both HCOOH and $HCOO^-$ must be involved in the mechanism. One possibility is that the reactive intermediate forms from a solution dimer such as [HCOOH · HCOO−](aq) (eq. (5.22)). Alternatively reaction of $HCOO^-$(aq) with HCOO(ad) (eq. (5.25)) would also give rise to a dependence on both the formic acid concentration, as the precursor to adsorbed formate, and the anion concentration.

$$\mathrm{HCOOH} + \mathrm{HCOO^-} \rightleftharpoons [\mathrm{HCOOH} \cdot \mathrm{HCOO^-}](\mathrm{aq}) \tag{5.22}$$

$$[\mathrm{HCOOH} \cdot \mathrm{HCOO^-}](\mathrm{aq}) \longrightarrow [\mathrm{intermediate}](\mathrm{ad}) \tag{5.23}$$

$$\longrightarrow 2\,\mathrm{CO_2} + 3\,\mathrm{H^+} + 4\,\mathrm{e^-} \tag{5.24}$$

$$\mathrm{HCOOH} \rightleftharpoons \mathrm{HCOO(ad)} + \mathrm{H^+} + \mathrm{e^-} \tag{5.25}$$

$$\mathrm{HCOO(ad)} + \mathrm{HCOO^-(aq)} \longrightarrow [\mathrm{intermediate}](\mathrm{ad}) \tag{5.26}$$

$$\longrightarrow \mathrm{CO_2} + \mathrm{HCOOH} + \mathrm{e^-} \tag{5.27}$$

The energetics of these mechanisms were considered using DFT by Gao *et al.* [74] It was concluded that reaction through a [HCOOH · $HCOO^-$]-type complex represented the minimum energy pathway on Au, but only in the potential window $0.9\,\mathrm{V} < E < 1.4\,\mathrm{V}$, while unimolecular formate and direct HCOOH pathways operated on Pt, as will be discussed in section 5.2.2.4.

A similar conclusion to that of Brimaud *et al.* was reached by Perales-Rondón *et al.*, who examined formic acid oxidation at different pHs on the Pt(111) surface. [75] They measured the activation energy of adsorption as a function of pH and found a decrease with increasing pH, and, surprisingly, also in the presence of the more coordinating anion SO_4.

They attribute both effects to the same phenomenon: the presence of an adsorbed species helps favour the C−H-down orientation of H−COO^-(aq) at the surface, which leads to a productive reaction. Thus the increase in pH leads to higher HCOO(aq) concentrations, while the need to form HCOO(ad) from HCOOH requires the pH is not too high. The formation of an OH(ad)-covered surface would also further inhibit the reaction as the pH increased.

$$\mathrm{HCOOH} + * \longrightarrow \mathrm{HCOO(ad)} + \mathrm{H^+} + \mathrm{e^-} \tag{5.28}$$

$$\mathrm{HCOO(ad)} + * + \mathrm{H{-}COO^-(aq)} \xrightarrow{rds} \mathrm{HCOO(ad)} + \mathrm{H(ad)} + \mathrm{CO_2} + \mathrm{e^-} + * \tag{5.29}$$

$$\mathrm{H(ad)} \longrightarrow \mathrm{H^+} + \mathrm{e^-} + * \tag{5.30}$$

5.2.2.4 Theoretical Studies of Formic Acid Oxidation

A theoretical understanding of the energy surface of a reaction can both help determine the likely role of observed species, and suggest the presence of other species which, for experimental reasons, might not be observed. The use of density functional theory (DFT) to calculate such reaction profiles is widespread in gas phase heterogeneous catalysis, and despite the dual added challenges of solvation and electric field effects, can also be applied in electrocatalysis.

In the case of formic acid electrooxidation, only the Pt(111) surface has been studied by DFT. This is presumably for reasons of simplicity, since experimentally observed rate of CO formation on the (111) surface is negligible. The two goals in DFT calculations of formic acid oxidation therefore become a search for the minimum energy pathway (MEP) in the reaction $\mathrm{HCOOH} \longrightarrow \mathrm{CO_2} + 2\,\mathrm{H^+} + 2\,\mathrm{e^-}$ and, if not included in the MEP, the role of the experimentally observed bridging formate.

The first calculations to be reported for formic acid oxidation where by Neurock *et*

al. [76] They compared the two pathways:

1. Initial activation of the O−H bond to yield adsorbed bridging formate (b-HCOO), followed by activation of the C−H bond to release CO_2

2. Initial activation of the C−H bond to produce adsorbed hydroxy carbonyl −COOH, followed by activation of the O−H bond to release CO_2 (the simultaneous activation of C−O and C−H bonds, which provides the same outcome was not calculated but was not discounted either.)

Of these the MEP was pathway 2, via −COOH. Pathway 1 had a lower initial barrier but a much greater second barrier, which would therefore lead to an accumulation of b-HCOO, as observed experimentally. Critically, however, the calculations did not include explicit solvent molecules and therefore neglected the effect of water in, for example, the activation of O−H bonds.

This shortcoming was overcome by Wang *et al.*, who did include explicit solvation. [77] While they also suggest that the barrier to b−HCOO reaction is too high to be relevant, with solvation it was calculated that a MEP including b−HCOO would occur via transformation to monodentate formate (m-HCOO), the transformation aided by the greater solvation of the m-HCOO over b-HCOO. However, this solvent stabilisation of m-HCOO, which is largely absent in the transition state to CO_2, causes too high a barrier for further reaction to CO_2, preventing this formate pathway from contributing to the reaction. This is in contrast to the gas phase, where decomposition of m-HCOO is rapid.

Instead, the reaction is proposed to occur via direct reaction of HCOOH, with the CH-down orientation, required for rapid oxidation, stabilised by the presence of adsorbed formate. The CH-down orientation is favoured as, CH being less solvated than the CO, it incurs a lower desolvation energy penalty. Adsorbed formate favours this orientation by providing a hydrophobic, that is low charge, region of 10 adjacent sites at the surface.

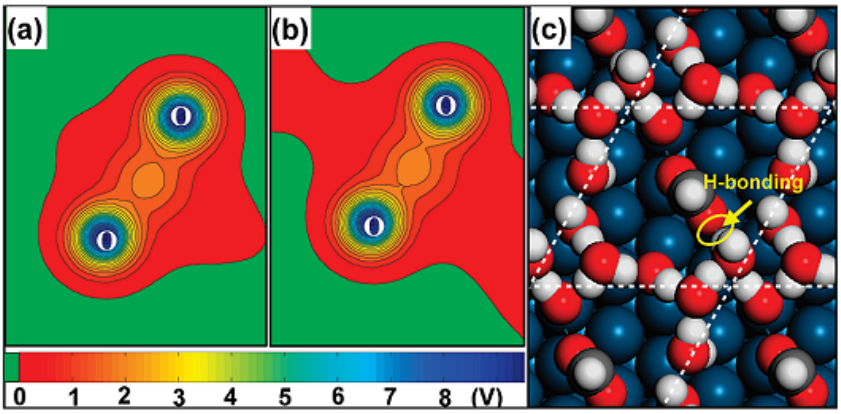

Figure 5.6: Calculations of formate at the Pt(111)/H_2O interface. (a,b) Contour plots of total electrostatic potential for an adsorbed formate on Pt(111) without and with the continuum solvation shell, respectively. The planes are parallel to Pt(111) surface while cutting through the two O-ends of formate. (c) Molecular dynamics snapshot for a formate adsorbed in a Pt(111)/H_2O system. Reprinted with permission from reference [77]. Copyright 2009, American Chemical Society.

This is shown in fig. 5.6, where the electrostatic potential around the formate is calculated both without (a) and with (b) a solvent continuum present, the green shading highlighting the regions of low charge, which panel (c) shows to be disfavoured by adsorbed water molecules, following molecular dynamics simulation. In this theory, it is suggested that the CH-down HCOOH discussed by Wang *et al.* represents the weakly adsorbed formate suggested by Chen *et al.* [52, 77]

The effect of solvation was considered in more detail by Gao *et al.* [35] When the b-HCOO pathway was considered, transformation to the m-HCOO was again found to be the MEP, however in contrast to Wang *et al.* subsequent reaction to CO_2 was found to be energetically feasible and comparable in energy to the direct reaction of HCOOH. It should be noted that in this case the HCOOH reaction was not calculated for a formate-covered surface, and the pathway involved a transient adsorbed CO_2(ad) species. The simultaneous activation of C−H and O−H bonds to release CO_2 directly was discounted.

Gao *et al.* further considered the participation of CO and OH in the *direct* pathway. [78]

They suggest that as well as inhibiting the direct reaction via site blocking, under certain conditions these species may also in fact promote the reaction. One way in which this occurs is by causing changes in the H-bonding network which would increase the activation of the C−H bond of adsorbed HCOOH. A second factor is the positive shift in surface charge caused by the coverage of OH.

5.2.3 Summary

It can be seen from the literature that consensus has not yet been reached on the mechanism of formic acid oxidation. To date two adsorbed intermediates have been reproducibly observed: carbon monoxide and bridging formate; any mechanism for formic acid oxidation must therefore include these species, along with any proposed transient species, whose presence cannot be entirely ruled out.

Two mechanisms have been suggested for the formation of CO, one via adsorbed HCOO, [51] and one via a weakly adsorbed HCOOH, [52, 63] with calculations favouring the latter. [35, 76] In any case it is clear that CO oxidation contributes negligibly to the catalytic current. [50,52] What is also becoming clear is that while formate decomposition cannot account for all of the current observed during formic acid oxidation, [52, 57, 70, 76, 77] a relationship between current and formate coverage certainly exists. [51, 63, 67, 79] Furthermore, the dependence of the current on pH, suggests that $HCOO^-$(aq) plays a role in the reaction, [71, 72] possibly along with HCOOH(aq). [56]

In light of these data, it is suggested that the mechanism proceeds via activation of the C−H bond of the $HCOO^-$(aq) anion, with the necessary CH-down orientation required for reaction promoted by the formation of hydrophobic surface regions around adsorbed b-HCOO or SO_4 species. The dependence on potential in this case is non-linear, with increasing potential favouring adsorption of b-HCOO and oxidative electron transfer, but disfavouring the reactive orientation of $HCOO^-$(aq) due to the preference

for the negatively charged $-COO^-$ moiety to be close to the electrode rather than the C−H bond. The importance of 'spectator' species is also clear, as they can dramtically affect the nature of the surface, inhibiting, and even possibly promoting, the interaction of $HCOO^-$(aq) with the surface.

5.3 In situ IR spectroscopy of Pt/C during formic acid oxidation

A survey of the literature reveals a lack of consensus on the mechanism of formic acid oxidation. Futhermore, the vast majority of mechanistic studies have been carried out on model electrodes. In the remainder of this chapter the IR spectroelectrochemical cell developed in Chapter 3 and already applied to the CO oxidation reaction in Chapter 4 will be applied to a study of the mechanism of formic acid oxidation at a commercial carbon-supported Pt catalyst (HiSPEC 9000, 60% Pt/C, Alfa Aesar).

5.3.1 Carbon Black

Before the catalyst surface is studied it must be remembered that it is the catalyst itself, as opposed to species adsorbed on its surface, that make up the largest fraction of the medium being studied in these experiments. As such, any changes to the catalyst during reaction may give rise to prominent features in the spectra and should therefore be understood. The catalyst consists of Pt nanoparticles supported on Vulcan carbon black (section 4.2.1). While the spectral response of Pt nanoparticles in the region of interest is likely to be insensitive to the applied potential, the same may not be true for carbon black. The surface of carbon blacks (surface area $254\,m^2\,g^{-1}$) is highly oxidised, with oxygen-containing functionalities such as carbonyl and ether groups incorporated into the highly conjugated structure of carbon (fig. 5.7). These functional groups can be strong absorbers of IR

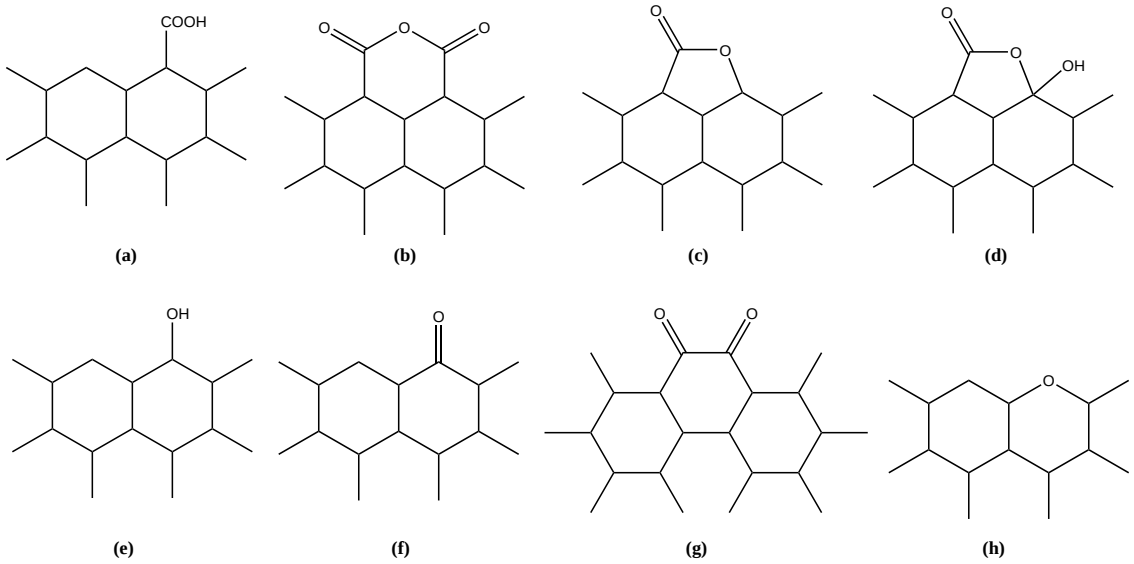

Figure 5.7: Possible structures of oxygen groups on the surface of carbon blacks. Adapted from reference [81].

radiation, in particular the C=O and C−O bonds in quinones, lactones, and carboylic acids, which have characteristic absorptions in the ranges $1712\,\mathrm{cm}^{-1}$ to $1527\,\mathrm{cm}^{-1}$ and $1335\,\mathrm{cm}^{-1}$ to $1000\,\mathrm{cm}^{-1}$, respectively. [80]

The oxidation or reduction of these groups during potential cycles is therefore likely to give rise to changes in absorption around their characteristic wavenumbers. It should be remembered however, when comparing spectra with and without the catalyst present, that the Pt nanoparticles are likely to enhance the IR absorption of species in close proximity (see section 2.3.4.2) and therefore features in the carbon black-only spectra are expected to be weaker than comparable features in catalyst spectra. Changes attributed to the surface of carbon can be seen when a carbon black-only layer was cycled in $HClO_4$(fig. 5.8A) and in HCOOH + $HClO_4$(fig. 5.8B). The spectra show the appearance and disappearance of several broad bands, some of which arise from the carbon ($1572\,\mathrm{cm}^{-1}$ and $1562\,\mathrm{cm}^{-1}$, $1269\,\mathrm{cm}^{-1}$, $1267\,\mathrm{cm}^{-1}$, $1215\,\mathrm{cm}^{-1}$ and $1207\,\mathrm{cm}^{-1}$), [80] others correspond to HCOOH ($1726\,\mathrm{cm}^{-1}$, table 5.4), while the remaining peaks correspond to bands observed in the difference spectrum of aqueous $HClO_4$ against pure water ($2035\,\mathrm{cm}^{-1}$, $1765\,\mathrm{cm}^{-1}$, $1626\,\mathrm{cm}^{-1}$

and 1101 cm^{-1}, see top spectrum). The presence of these latter bands can be explained by the change in interfacial anion concentration with potential. Furthermore, the absence of the multiple peaks around 1350 cm^{-1} show that strong chemisorption of HCOOH to produce HCOO(ad) species does not occur on carbon alone, nor is there any sign of CO(ad) or CO_2, also ruling out dehydration and dehydrogenation on carbon.

5.3.2 Formic Acid Adsorption

The interaction between HCOOH and the catalyst will first be studied at ambient temperature and pressure in the absence of water, solutes or applied potential. In this configuration any changes observed in the spectrum can be attributed entirely to HCOOH and HCOOH-derived species. This step-by-step approach to understanding in situ spectra has not been reported previously for studies of electrocatalysts, with most studies comparing spectra obtained in situ directly with those reported in UHV. The advantage of the present approach is that reference spectra are generated for species adsorbed on the catalyst of interest, providing an additional link between species observed in UHV and those observed during in situ electrochemical experiments.

The experimental procedure was simple: the IRE was sealed into the baseplate of the ATR accessory and a background spectrum obtained. A catalyst film was then deposited onto the crystal and an absorption spectrum recorded. A 5 mL glass beaker was placed upside down over the film and 10 µL of 98% reagent grade formic acid was pipetted in through the spout of the beaker such that no formic acid solution was in contact with the prism. Spectra were subsequently recorded as a function of time, first with and then without the beaker present, in effect changing the partial pressure of formic acid near the film (fig. 5.9A).

In the first spectrum after addition of formic acid, (black line, labelled 0 s) several bands are observed at 2052 cm^{-1}, 2027 cm^{-1}, 1709 cm^{-1}, 1391 cm^{-1}, 1350 cm^{-1},

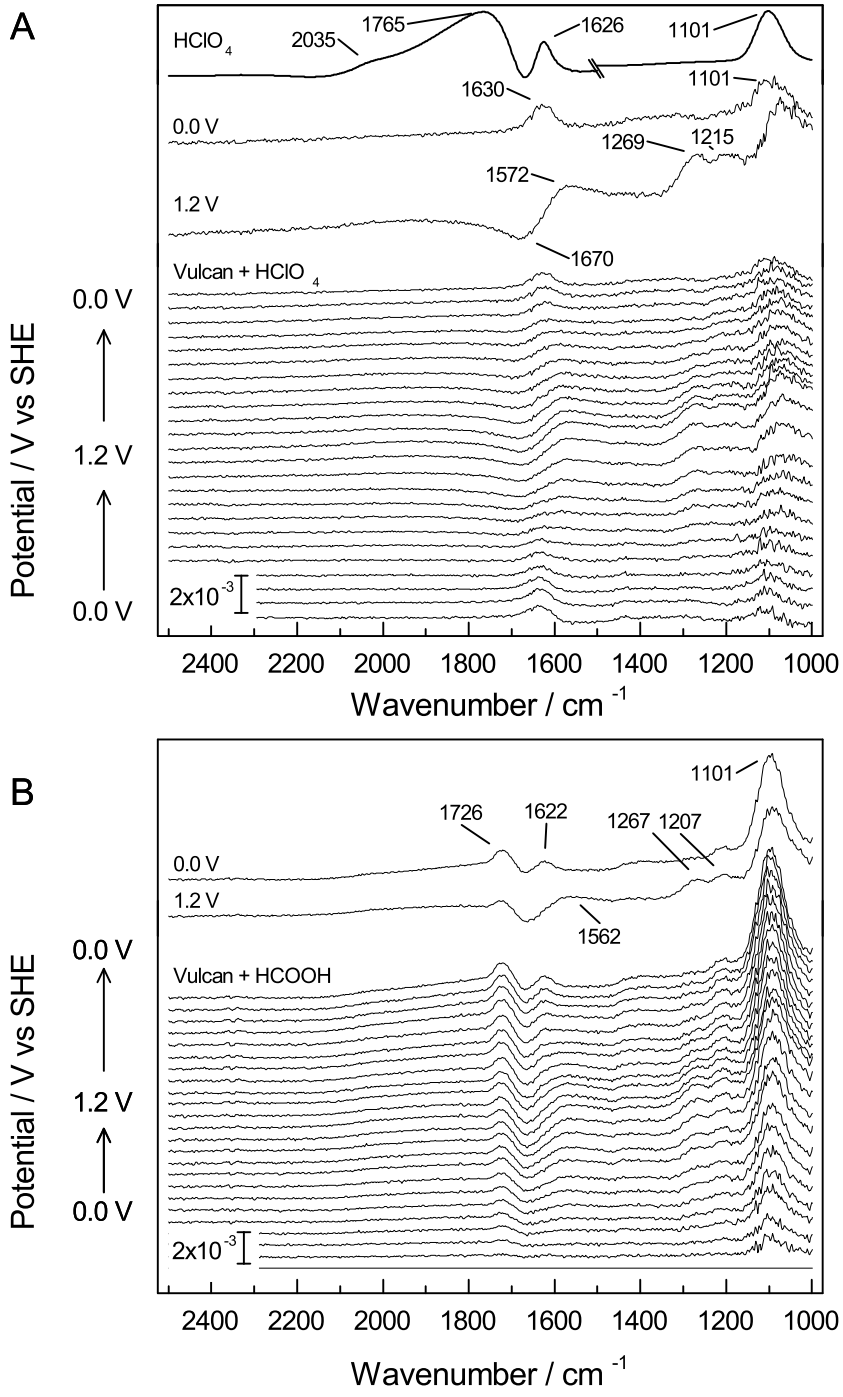

Figure 5.8: In situ spectra of carbon only layers during cyclic voltammetry. A: Carbon black film during cyclic voltammetry in 0.5 M $HClO_4$ solution. Difference spectrum of 1 M $HClO_4$ solution against pure water in the absence of carbon shown above (NB regions above and below 1700 cm^{-1} scaled independently). Spectra at 0.0 V and 1.2 V are shown enlarged above. B: Carbon black film during cyclic voltammetry in 10 mM HCOOH + 0.5 M $HClO_4$. Spectra at 0.0 V and 1.2 V shown above.

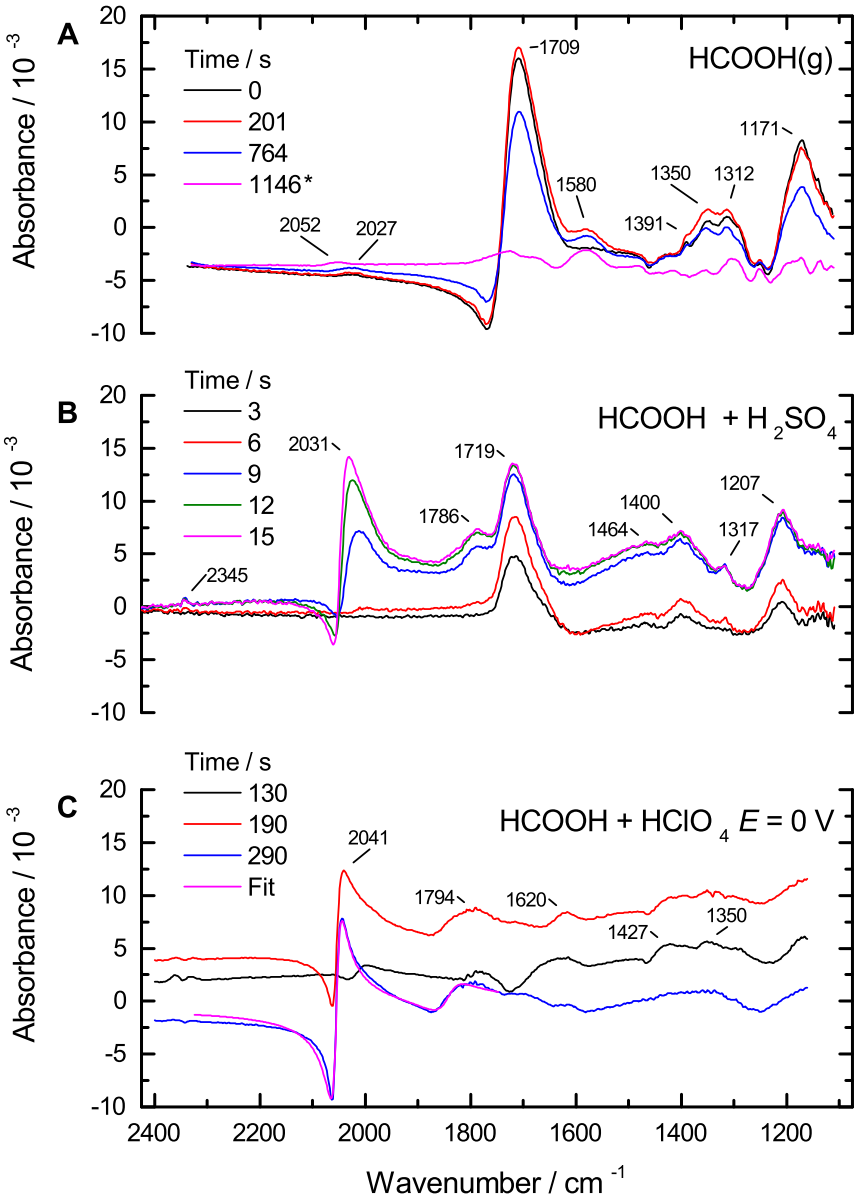

Figure 5.9: The interaction of formic acid with Pt/C under a range of conditions as probed by IR spectroscopy. A: Spectra of the catalyst layer acquired at different times after introduction of formic acid vapour, and * after decreasing the vapour pressure. B: Spectra of the catalyst layer in H_2SO_4 solution at different times after introduction of concentrated formic acid. C: Spectra of the catalyst layer in $HClO_4$ held at 0 V at different times after introduction of formic acid.

Table 5.4: Vibrational modes of formic acid and sodium formate isotopomers measured in the region 1800 cm^{-1} to 1000 cm^{-1}.

Species	Wavenumber / cm^{-1}		
Mode	Backbone Stretch	C-H Wag	C=O Stretch
	ν(HC(O)OH)	δ(CH)	ν(C=O)
	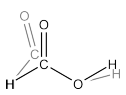	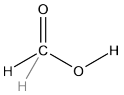	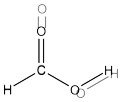
HCOOH	1213	1400	1719
$H^{13}COOH$	1223	1400	1690
DCOOH	1196	1400	1674
Mode	Symmetric OCO Stretch	C-H Wag	Asymmetric OCO Stretch
	ν_s(OCO)	δ(CH)	ν_{as}(OCO)
	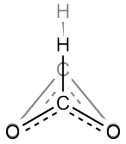	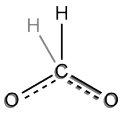	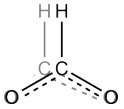
HCOONa	1350	1383	1582
$H^{13}COONa$	1329	1381	1541
DCOONa	1325		1572

Assignments and depictions of individual atomic motions for each normal mode are based on references [82, 83].

1312 cm^{-1} and 1171 cm^{-1}. As time goes on (red and blue lines) a band at 1580 cm^{-1} appears and is accompanied by an increase in the intensity of all bands except the 2027 cm^{-1} band. Based on data in tables 4.2, 5.1 and 5.4 the bands are provisionally assigned as follows: 2052 and 2027 cm^{-1} C−O stretch of linear CO(ad), 1709 cm^{-1} C−O stretch of HCOOH, 1582 cm^{-1} asymmetric O−C−O stretch of $HCOO^-$, 1393 cm^{-1} C−H bend of HCOOH, 1350 cm^{-1} symmetric O−C−O stretch of $HCOO^-$, 1314 cm^{-1} symmetric O−C−O HCOO(ad), 1173 cm^{-1} backbone stretch of HCOOH.

When the vapour pressure of formic acid is decreased by removing the beaker (pink line) the species assigned to HCOOH and $HCOO^-$ are lost, as shown by the absence of the 1719 cm^{-1}, 1393 cm^{-1}, 1350 cm^{-1} and 1173 cm^{-1} bands, although the 1580 cm^{-1}

band remains, suggesting it actually arises from a distinct species. The CO(ad) and HCOO(ad) bands remain, although the wavenumber of the CO(ad) band increases 29 cm^{-1} to 2054 cm^{-1}. This change in CO(ad) peak position is consistent with the decreased lateral repulsion on loss of $HCOO^-$, or similarly with the decreased electron back donation from the metal on loss of the electron donating $HCOO^-$ species (section 2.1.2.5). The small peaks left behind may arise from species adsorbed in the mesopores of the carbon support.

It appears that formic acid strongly interacts with the catalyst in the vapour phase, dissociating to produce multiple formate species along with CO. This dissociative adsorption of formic acid is well known from both the UHV studies discussed previously, and from heterogeneous catalysis, where it occurs readily on Pt-promoted metal oxides such as Pt/CeO_2 at temperatures around 200 °C, with a range of formate species observed by IR spectroscopy. [84, 85] One difference however is the presence of CO(ad); in the case of Pt/CeO_2 a prominent linear CO(ad) peak is observed, whereas on Pt/C only a very small feature is assigned to this species. The fact that some peaks assigned to $HCOO^-$ disappear when the vapour pressure is decreased suggest that these arise from weakly adsorbed species, although no peaks are visible at 1290 cm^{-1} or 1620 cm^{-1}, assigned to the unstable monodentate formate on Pt(111) in UHV. [20]

The interaction of formic acid with Pt/C in the presence of electrolyte yet without potential control was also studied (fig. 5.9B). A catalyst film was prepared on the IRE and immersed in 0.5 M H_2SO_4. Concentrated formic acid was then added to the solution and spectra were recorded continuously. Initially absorption bands were observed only from formic acid (1719 cm^{-1}, 1400 cm^{-1} and 1207 cm^{-1}), then after around 6 s the intensity of the formic acid band had increased and new bands were observed at 1464 cm^{-1} and 1317 cm^{-1}, and finally after 10 s bands at 2345 cm^{-1}, 1786 cm^{-1} and 2031 cm^{-1} were also observed. When compared to the the solution case, it can be seen that a much larger linear CO(ad) band (2031 cm^{-1}) and a new bridging CO(ad) band (1786 cm^{-1}) are observed,

Table 5.5: Values obtained by fitting the CO region in HCOOH.

Parameter	Band 1	Band 2
f	369	149
$\tilde{\nu}_0$	2054	1843
γ	20.9	59.4

along with the presence of CO_2, while the multitude of peaks assigned to formate species are absent. One explanation for this difference could be the ability for formate desorption in solution, as compared to the vapour phase; when formate desorbs it can be replaced with CO, which is much more stable and therefore tends to accumulate. The presence of the solution also acts to trap the CO_2, permitting its observation as a dissolved species at $2343\,\mathrm{cm}^{-1}$.

Finally, the adsorption of formic acid on the catalyst under potential control was studied. A catalyst layer was prepared in the cell and 0.5 M $HClO_4$ introduced. The potential was cycled 10 times between the H_2 and O_2 evolution potentials (0 V to 1.2 V) to clean the surface of any contaminants, before holding at 0 V and flowing in 10 mM HCOOH (in 0.5 M $HClO_4$) for 300 s. At 0 V the surface of the catalyst should be saturated with H(ad) and no oxidation should occur. Spectra recorded during this process are shown in fig. 5.9C. Under potential control two dominant bands are observed at $2041\,\mathrm{cm}^{-1}$ and $1794\,\mathrm{cm}^{-1}$, suggesting they arise from linear and bridging adsorbed CO, respectively. The CO bands were analysed using the fitting procedure developed in Chapter 4. The peak centres, ν_0 of the two CO bands were fitted as $2054\,\mathrm{cm}^{-1}$ and $1843\,\mathrm{cm}^{-1}$ (table 5.5). The region below $1800\,\mathrm{cm}^{-1}$ is not flat, however the sharp features initially observed at $1427\,\mathrm{cm}^{-1}$ and $1350\,\mathrm{cm}^{-1}$ were soon replaced by a broad hump. It is again suggested the gradual loss of features below $1600\,\mathrm{cm}^{-1}$ occurs as a result of slow CO accumulation, which displaces less strongly adsorbed species like HCOO(ad).

It is also interesting to compare the CO peak positions obtained from direct adsorption

of CO from solution (Chapter 4), and from dehydration of formic acid. In the former case the CO peaks at saturation were at 2069 cm^{-1} and 1857 cm^{-1}, while in the latter case they are at 2054 cm^{-1} and 1843 cm^{-1}. These differences in the CO wavenumber are significant in the case of linear CO, although within the uncertainty of the fit for bridging CO. The difference could result from the CO adsorbing at different locations in each case, which would occur if the HCOOH dehydration reaction occurs preferentially on one site over another. It could also arise from differences in the lateral interactions between CO(ad) molecules. Further discussion of this is left until section 5.3.4.

These spectra reveal the IR signatures of species formed via adsorption, dehydration and dehydrogenation of formic acid under non-electrochemical conditions. Of interest in this thesis is how these reactions combine to create a catalytic cycle with the release of electrons and production of CO_2. Insight into this process can be gained by applying a potential to the catalyst layer, observing which adsorbates are present at the different potentials and from this inferring which reactions are occurring.

5.3.3 Quasi-steady state voltammogram in HCOOH

A good starting point for an in situ investigation of electrochemical reaction intermediates is to carry out slow cyclic voltammetry while collecting spectra; by sweeping the potential between two limits the catalyst is characterised over a wide potential range, and if the potential is swept slowly enough the conditions at the surface can be considered as at 'quasi-steady state'. While this approach has certainly been used to study nanoparticle films during small organic molecule electrocatalysis, [86, 87] its dynamic nature and the inherently limited spectral acquisition times has meant that to date the only species adsorbed on a nanoparticle to be studied this way is the strongly infrared-absorbing CO(ad). It was shown above, however, that other adsorbed species, such as formate, can be observed on the relatively thick catalyst layers studied in this work.

To record the quasi-steady state voltammogram a catalyst layer was prepared and the potential swept from 0 V to 1.2 V and back at 1 mV s^{-1} while 25 mM HCOOH in 0.5 M $HClO_4$ was flowed through the cell. The current recorded during the sweep is shown in fig. 5.10A and is seen to exhibit a single peak in both the positive (0.83 V) and negative-going (0.75 V) scans. The degree of hysteresis observed between the two directions shows that steady state was not quite obtained at these scan rates, although the 80 mV difference in peak potentials is much smaller than observed at faster scan rates, [57, 88] indicating steady state is being approached.

IR spectra were recorded continuously during the sweep with a time resolution of 0.5 s. A spectrum recorded at 0.0 V in $HClO_4$ before introduction of formic acid was used as the background. Inspection of one of the spectra, recorded around 0.7 V during the potential sweep, reveals several features (fig. 5.10B). The largest peak, observed around 1109 cm^{-1}, is 2 orders of magnitude larger than the other peaks. It can be assigned to the asymmetric Si−O−Si mode of the native oxide layer on the surface of the Si IRE. [89] As the oxide layer is of no interest in this case, spectra shown in this thesis are cut off below 1150 cm^{-1}. In addition no peaks other than a broad peak in the O−H stretching region were observed above 2500 cm^{-1}, and so this region is also omitted from later spectra. The region 2500 cm^{-1} to 1150 cm^{-1} is shown enlarged above the full spectrum in fig. 5.10B, and the main peaks are marked with the wavenumber maxima. It is remarkable that the peaks are clearly visible at such short acquisition times, especially the peak at lower wavenumber. In fact the observed intensities are similar to those measured in ATR-SEIRA experiments, [53] suggesting that the enhancement of IR absorption by the catalyst particles might be significant. The evolution of these peaks during the cyclic voltammogram was investigated by co-adding the spectra in 100 mV intervals (fig. 5.11).

The spectra show potential-dependent peaks at 2344 cm^{-1}, 2033 cm^{-1} to 2046 cm^{-1}, 1811 cm^{-1} to 1827 cm^{-1}, 1740 cm^{-1}, 1600 cm^{-1} to 1450 cm^{-1}, 1384 cm^{-1}, 1315 cm^{-1} and

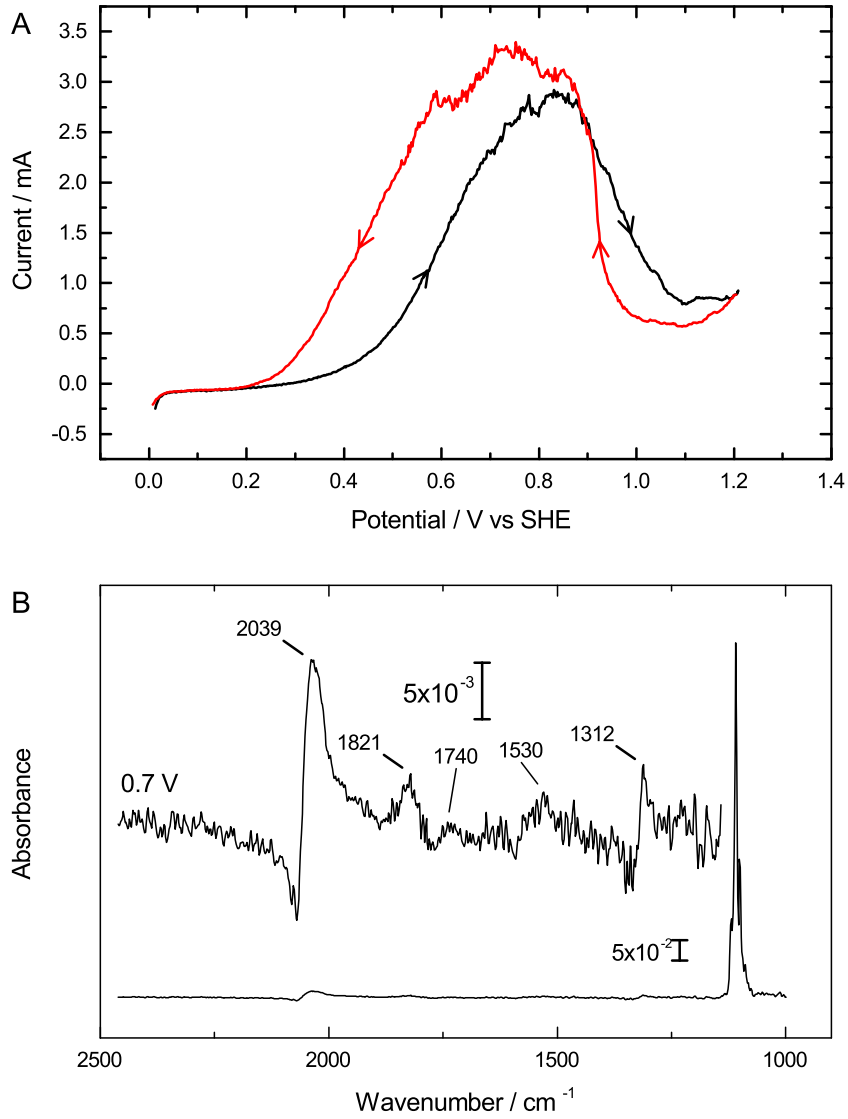

Figure 5.10: Voltammogram and representative spectrum obtained during formic acid oxidation. A: Quasi-steady state voltammogram of a catalyst layer in HCOOH. Scan rate 1 mV s^{-1}. Solution: 25 mM HCOOH in 0.5 M $HClO_4$. Flow rate: 3 mL min^{-1}. B: Individual spectrum obtained at 0.7 V over 0.5 s during the voltammogram. Background: catalyst layer at 0.0 V in $HClO_4$ before introduction of formic acid. The region above 1150 cm^{-1} is shown enlarged above the full spectrum. Labels show the position of the major peaks.

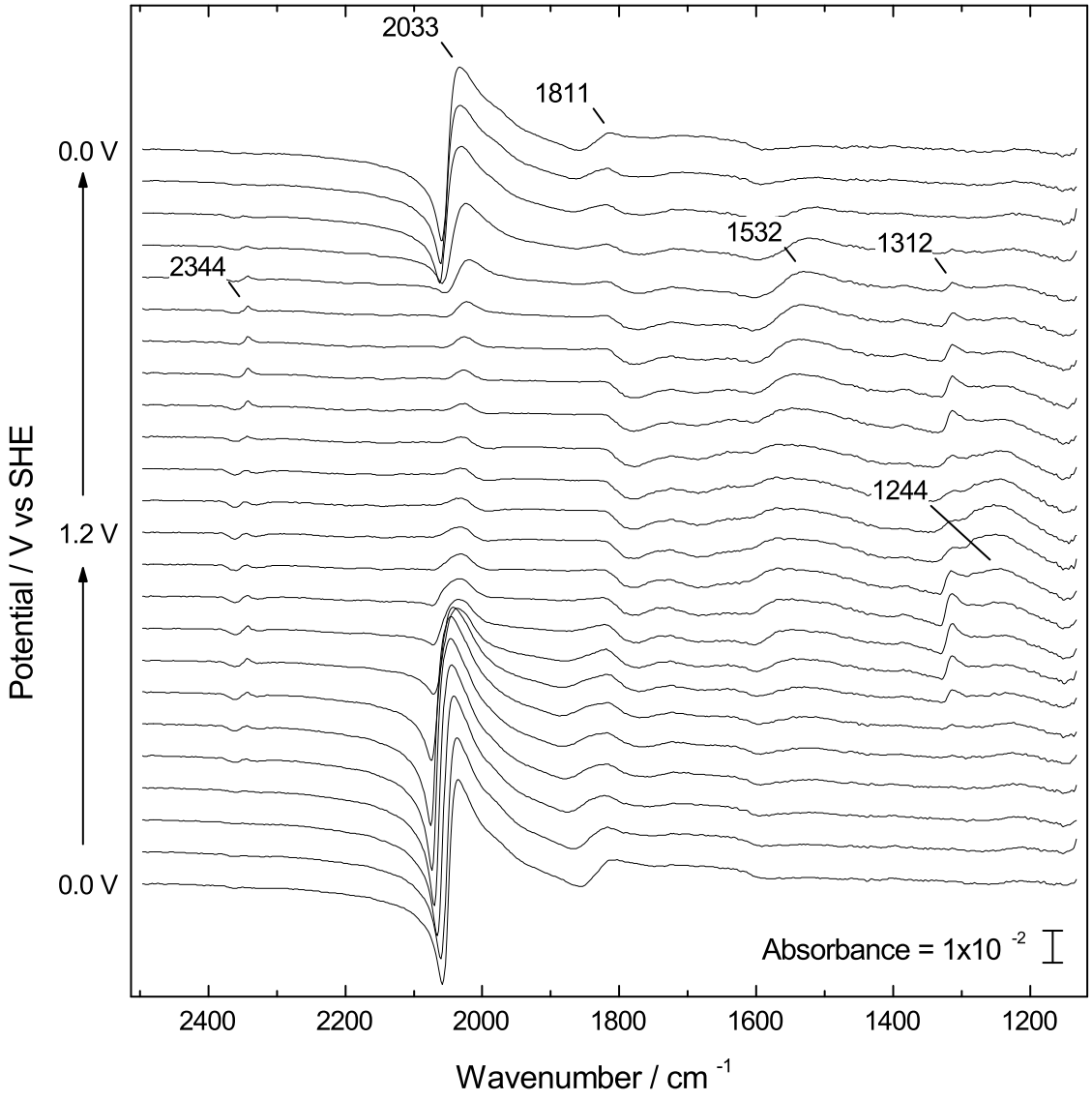

Figure 5.11: Spectra recorded over 100 mV = 100 s windows during a quasi-steady state voltammogram in 25 mM HCOOH + 0.5 M $HClO_4$. Flow rate = 2 mL min^{-1}. Background $HClO_4$ at 0.0 V.

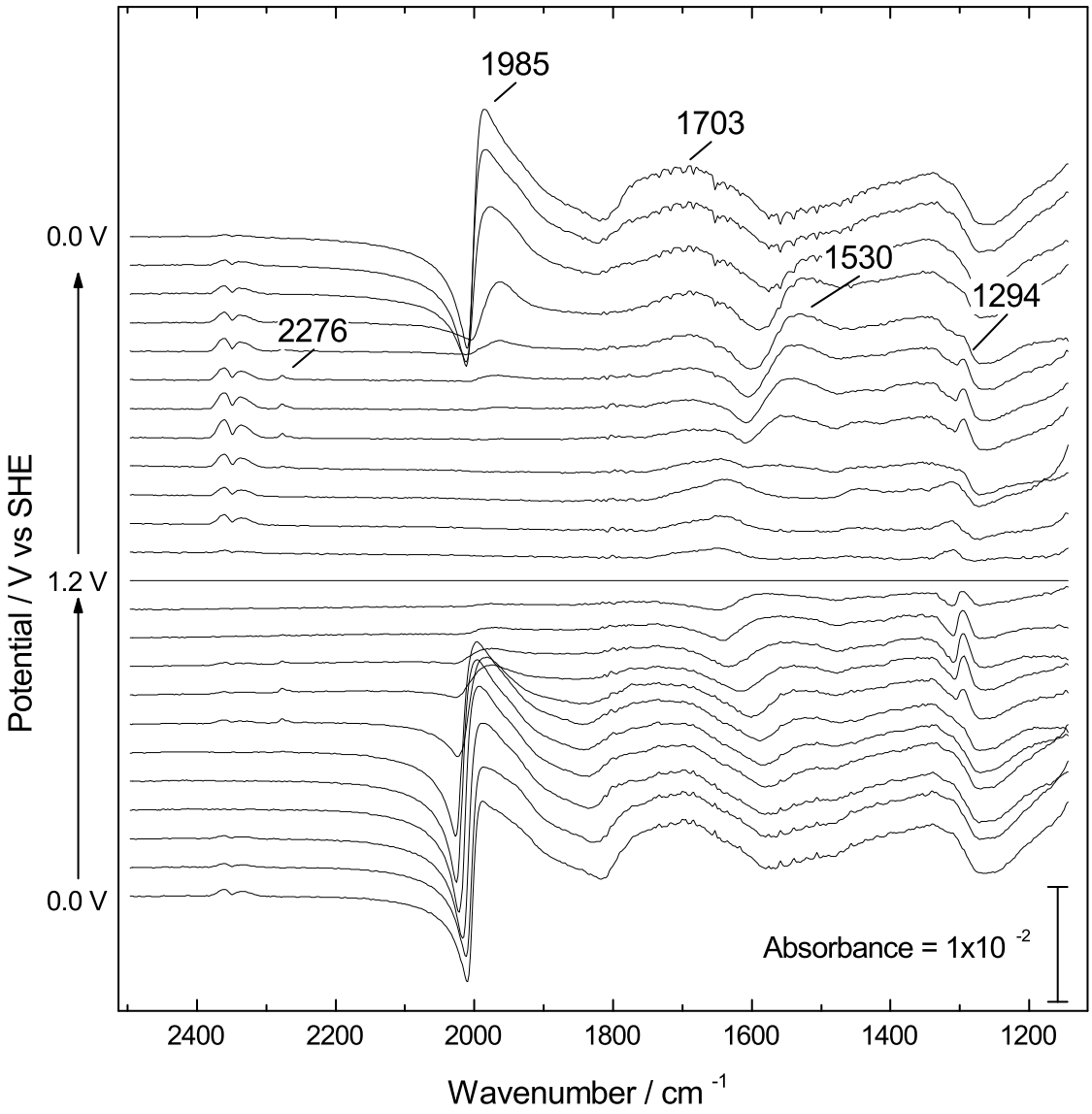

Figure 5.12: Spectra recorded over 100 mV = 100 s windows during a quasi-steady state voltammogram in 10 mM $H^{13}COOH$ + 0.5 M $HClO_4$. Flow rate = 2 mL min^{-1}. Background recorded at 1.2 V during cycle.

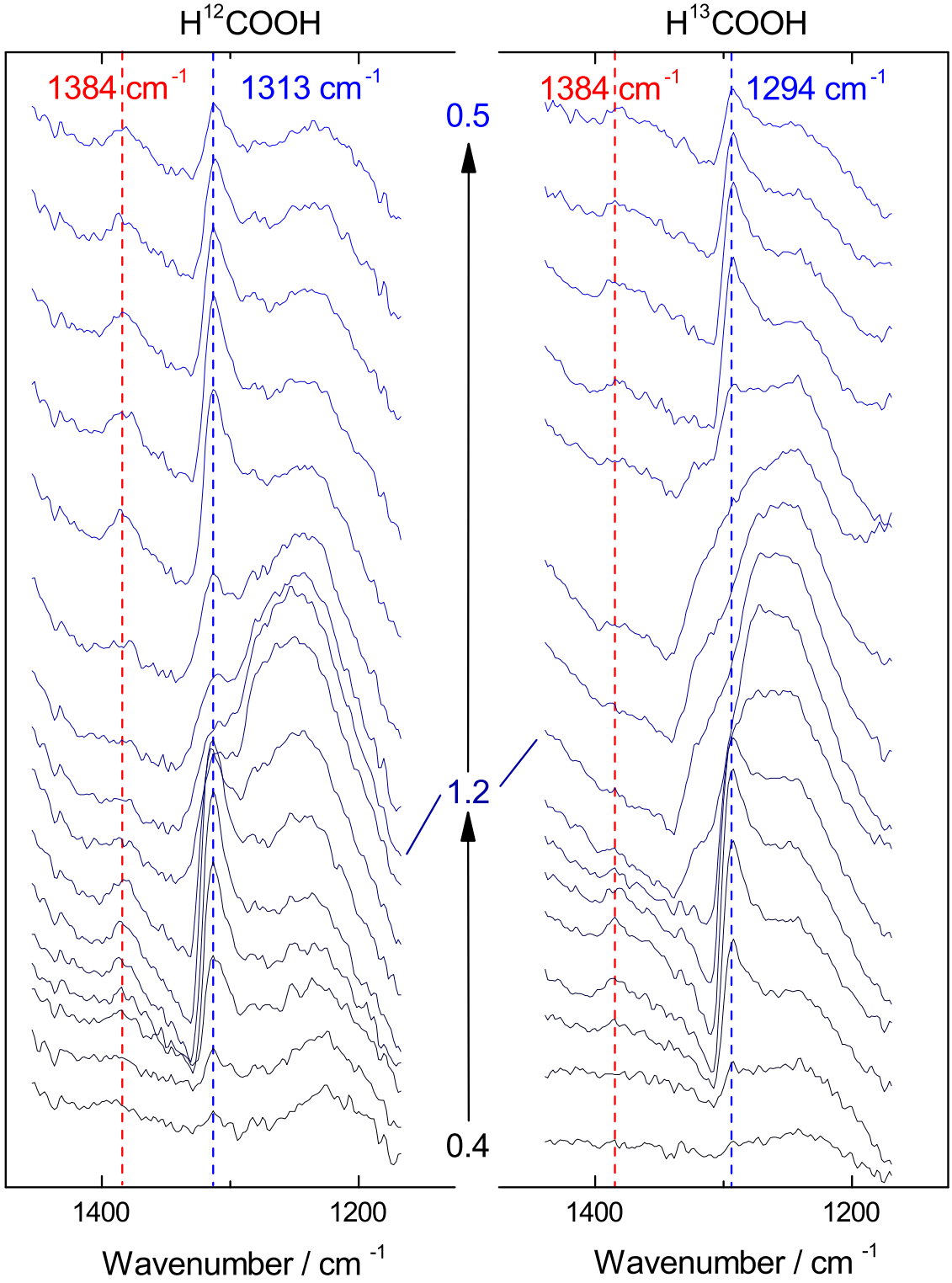

Figure 5.13: Enlargement of 1400 cm^{-1} to 1200 cm^{-1} region in $H^{12}COOH$ and $H^{13}COOH$.

Table 5.6: Peaks assigned to adsorbed species in formic acid oxidation on Pt ATR-SEIRA electrodes and Pt/C.†

	Wavenumber / cm^{-1}	
Mode	Pt ATR-SEIRA	Pt/C
$\nu(CO_L)$	2055-2075	2035-2046
$\nu(CO_B)$	1800-1850	1811-1827
$\nu_s(OCO)$	1323	1315

† Values taken from reference [90].

1250 cm^{-1}. Of these peaks, 1740 cm^{-1} can be assigned to the ν(C=O) stretch of formic acid (table 5.4) while four others can be readily assigned with reference to results reported for SEIRA experiments: the asymmetric stretch of dissolved CO_2, $\nu(CO_2) = 2343\,cm^{-1}$, the C-O stretch of atop or linear adsorbed CO, $\nu(CO_L) = 2035\,cm^{-1}$ to $2046\,cm^{-1}$, the C-O stretch of bridging adsorbed CO, $\nu(CO_B) = 1811\,cm^{-1}$ to $1827\,cm^{-1}$, and the OCO symmetric stretch of adsorbed bridging formate, HCOO(ad), $\nu_s(OCO) = 1315\,cm^{-1}$. [51–53, 90] When these positions are compared to the ATR-SEIRA measurements (table 5.6), it can be seen that the vibrations of species on Pt/C have lower wavenumbers. This suggests a greater occupancy of antibonding states for species on Pt/C, arising perhaps from greater donation of electron density from the nanoparticle surface than the SEIRA surface. [77]

To help confirm these assignments the cyclic voltammogram was repeated in $H^{13}COOH$ (fig. 5.12). To remove the effects of water vapour and provide a suitable baseline for comparison, the spectrum collected at 1.2 V was used as the background and therefore appears as a flat line. It can be seen that the $\nu(CO_L)$, $\nu(CO_B)$ and $\nu_s(OCO)$ peaks have moved to lower wavenumber, while the 1580 cm^{-1} and 1250 cm^{-1} peaks remain unperturbed. Comparison of the catalyst layer spectra with that of carbon at the same potentials suggests that the peaks around 1250 cm^{-1} and 1580 cm^{-1} can be assigned to functional groups on the surface of the carbon support (fig. 5.8). [80, 91]

This leaves the assignment of the remaining peak at 1384 cm^{-1}. Inspection of the

lower wavenumber region of the spectrum suggests that the intensity of the 1384 cm^{-1} peak shares a close relationship with that of the ν_s(OCO) mode (fig. 5.13). Assignment can be made by comparing the catalyst layer spectra at 0.9 V and 1.2 V in both HCOOH and $H^{13}COOH$ with the solution spectrum of NaOOCH and $NaOO^{13}CH$ (fig. 5.14). It can be seen that the presence of the 1384 cm^{-1} peak correlates with that of the ν_s(OCO) peak and does not shift on isotopic substitution. When the spectrum of $HCOO^-$(aq) is examined (fig. 5.14) it can be seen that $HCOO^-$(aq) also has a peak at 1384 cm^{-1} that also doesn't shift on isotopic substitution, and which is assigned to the in-plane C-H bend, δ(CH). [83] The 1384 cm^{-1} peak in the catalyst spectra is therefore tentatively assigned to the δ(CH) mode of HCOO(ad). The δ(CH) assignment is further supported by the correlation between the 1384 cm^{-1} and 1315 cm^{-1} peak intensities as a function of potential (fig. 5.15).

5.3.3.1 δ(CH): The C-H wagging mode of HCOO(ad)

The significance of this final assignment is twofold. First, it represents the first time the δ(CH) mode has been spectroscopically characterised on any metal surface. Although one study of HCOOH adsorption on the Pt(110)(1 × 2) surface in UHV did assign an IRAS peak at 1338 cm^{-1} to the CH wagging mode, [92] this is strikingly close to the 1340 cm^{-1} peak assigned to the symmetric OCO stretch in a previous study of the same system, [20] and thus seems unlikely. Its absence from the many UHV and in situ spectroscopic studies of HCOO adsorption on metal surfaces has always been attributed to the metal surface selection rule (SSR, section 2.3.4.1). [21, 29, 53, 54] However, it was discussed in section 2.3.4.1 how the extent of the SSR is expected to be dependent on the particle size when species adsorbed on nanoparticles are considered. It was calculated that for particle sizes around 0.5 nm the absorption intensity of normal modes with dipole moments tangential to the nanoparticle surface may only be diminished in intensity relative to

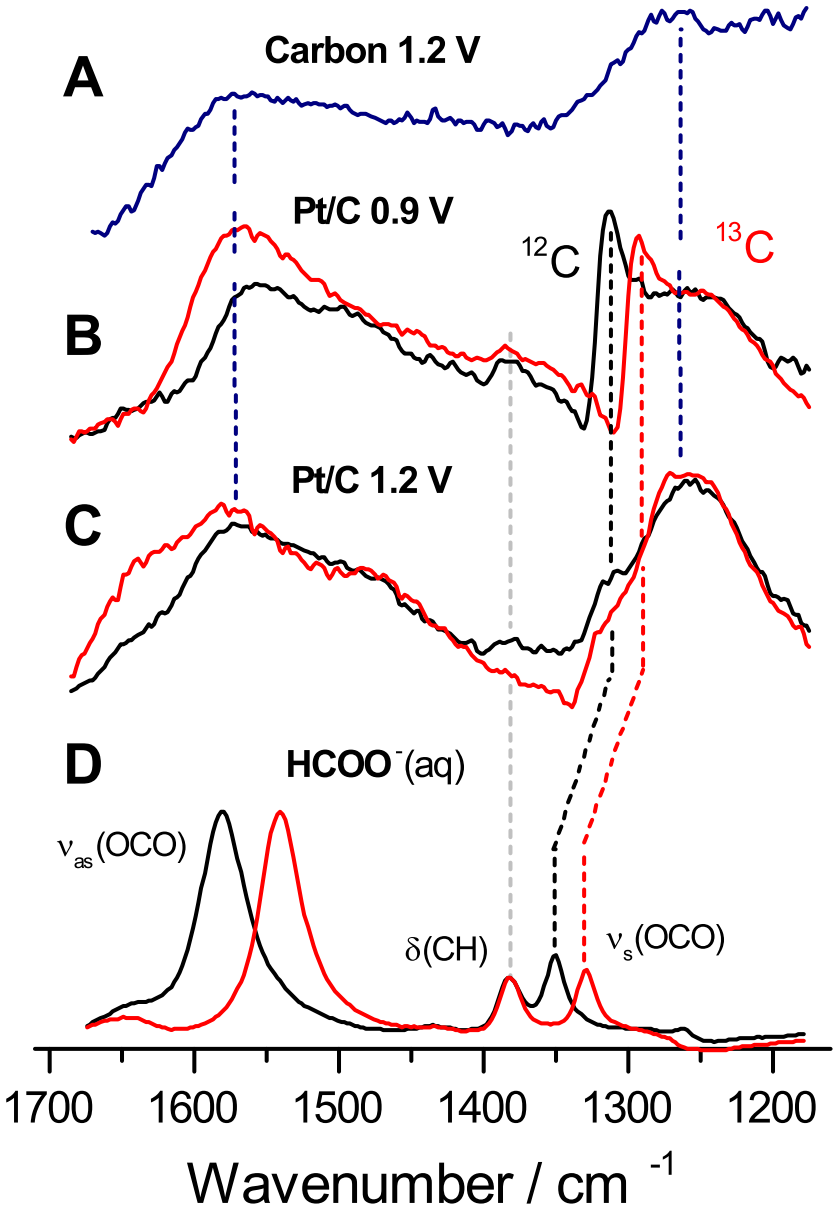

Figure 5.14: A comparison of catalyst spectra in formic acid to the spectra of carbon black only and to the solution spectra of regular abundance and ^{13}C-labelled formic acid. A: The spectrum of carbon black only in $HClO_4$, recorded at 1.2 V (taken from fig. 5.8A). B: Spectra of the catalyst layer in regular (black) and ^{13}C-labelled (red) formic acid at 0.9 V (extracted from figs. 5.11 and 5.12). C: As in B but at 1.2 V. D: Spectra of regular (black) and ^{13}C-labelled (red) NaOOCH solutions (0.1 M), with respect to a water background. For ease of comparison the absorbance of all spectra has been independently scaled.

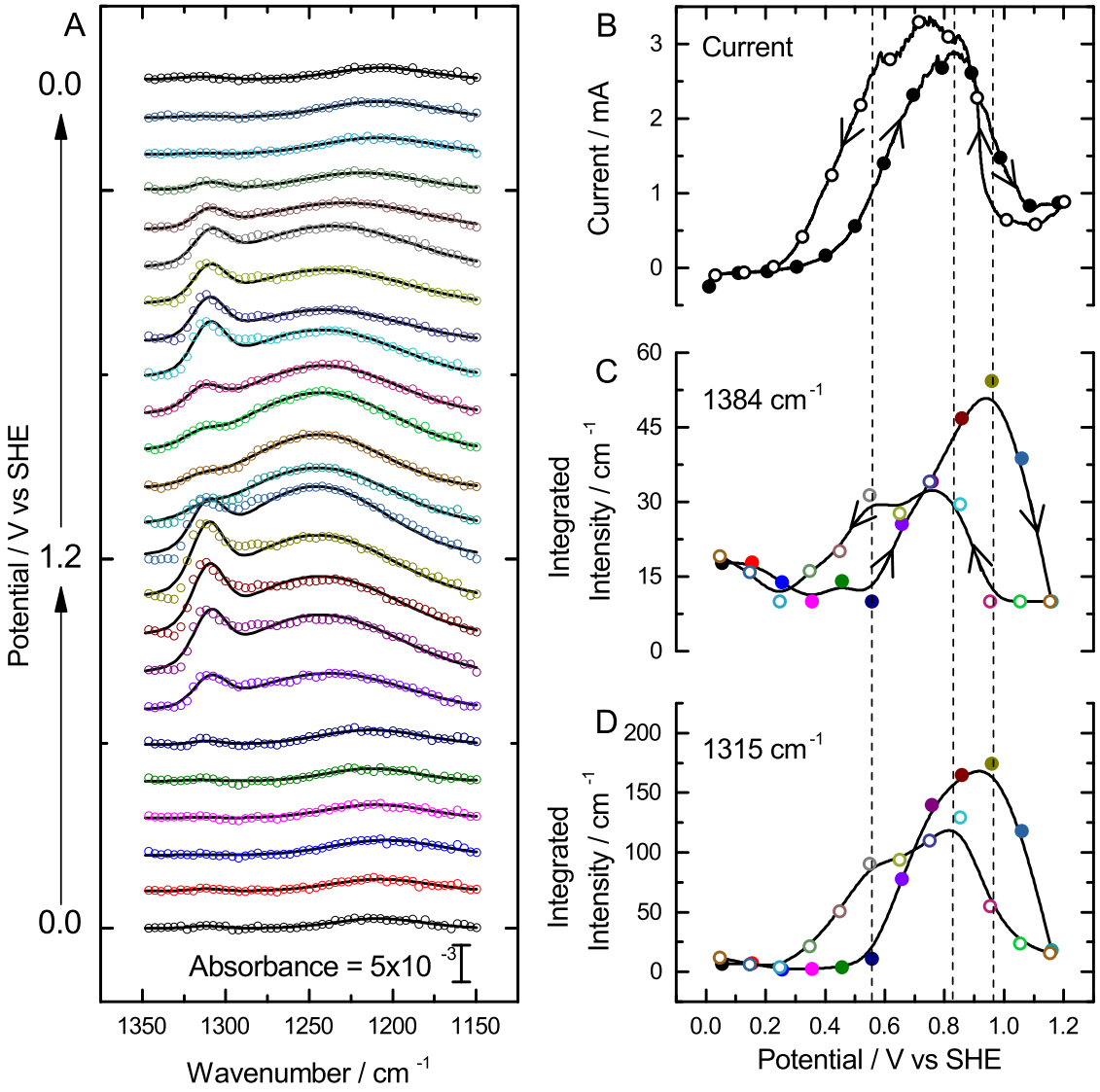

Figure 5.15: The potential dependence of the formate peak intensity. A: The low wavenumber region of fig. 5.11 showing fits to the ν_s(OCO) peak. Note that the carbon peak around 1225 cm^{-1} was fit at the same time. B: The cyclic voltammogram recorded with the spectra. C: Integrated intensity of the 1384 cm^{-1} peak plotted as a function of potential. Data are shown as points, coloured to match the spectra in A. Lines show spline interpolation of the data as a guide. D: Integrated intensity of the 1315 cm^{-1} peak. Data and lines are shown as for C.

modes with dipoles normal to the surface by 50%, with the actual ratio perhaps being much larger when quantum corrections were made to the model. [93] It is worth noting that this suggested weakening of the SSR should also apply to the ν_a(OCO) mode, seen in $HCOO^-$(aq) at 1580 cm^{-1}. Unfortunately this region is dominated by the peaks assigned to species at the surface of carbon, however lower wavenumber shoulders on these features do not rule out the possibility that the ν_a(OCO) peaks are present underneath (fig. 5.14).

The second reason for the significance of the δ(CH) mode is that it provides information on the crucial C−H bond of HCOO(ad). The C−H bond is important as its scission is the final step on route to CO_2 production from HCOO(ad), and as such the barrier to this process helps determine the extent to which HCOO(ad) contributes to the overall reaction. The present finding, that the position of the peak remains unperturbed from its value in dissolved formate, indicates that there is no inherent activation of the C−H bond when formate adsorbs on pure Pt. This observation agrees with DFT calculations which predict that the majority of electron density accepted by formate on adsorption is localised in the conjugated π states of the O−C−O system, [77] leaving the H−COO(ad) bond unperturbed and its breakage the rate determining step for HCOO(ad) oxidation, with a significant activation energy. [35, 76, 77]

The ability to observe this peak should enable further testing of hypotheses involving the activation of the C−H bond. For example, a recent hypothesis to explain the dramatic promotional effect of adsorbed Bi on the rate of formic acid oxidation suggests that $HCOO^-$(aq) adsorbs on Bi as a monodentate formate; the formate is then held at the surface while it rotates around the Bi−O−C axis until a favourable Pt−H distance is obtained and the C−H bond dissociates. [94] In this case it might be expected that the δ(CH) vibration changes wavenumber, possibly decreasing due to a weakening of the C−H bond as it interacts with Pt at the surface.

5.3.3.2 The Potential Dependence of CO(ad)

The behaviour of adsorbed CO with potential can also be examined. The linear CO peak is observed to decrease in intensity, but not disappear, as the potential is swept up from 0.0 V to 1.2 V. Closer inspection reveals that at these high potentials the main, bipolar CO peak, originally at 2054 cm^{-1}, has actually disappeared, and the remaining peak is now unipolar peak and centred around 2036 cm^{-1}. As discussed in Chapter 4 (section 4.4.3), this difference in peak shape suggests this peak arises from CO adsorbed on individual catalyst particles, leaving the main CO peak to arise from CO on agglomerated catalyst.

This conclusion is also supported by the persistence of the peak even at the highest potentials. In contrast to CO stripping experiments, where the coverage of CO is only determined by the rate of removal, since the rate of formation is zero, in formic acid oxidation the coverage of CO is determined by both the rate of removal and the rate of formation. While a CO species may be completely removed in CO stripping, given high enough potential and long enough times, in the presence of formic acid it may never be removed if the rate of formation is always faster than the rate of its oxidation. It was mentioned in section 4.4.3 that CO oxidation on small particles is much slower than on larger particles, due to fewer defect sites available to nucleate the adsorbed OH species required for oxidation. [95, 96] Thus, it seems reasonable to assign the persistent, high potential, unipolar CO peak to CO adsorbed on the small, individual catalyst particles.

To extract the CO peak centre, width and intensity, the spectra were fitted to the same 1-peak model developed for CO in Chapter 4 (section 4.3.2). This approach contrasts with the approach adopted in all other in situ studies, with the exception of work by Sato *et al.*, [97] where the spectral data is numerically integrated rather than fitted. As well as providing a much more reliable measure of the peak intensity when bipolar peaks are used, fitting also provides the peak centre and width, enabling all three peak parameters to be extracted and plotted as a function of potential.

When the fitted peak parameters are examined (fig. 5.16), it can be seen that at the beginning of the voltammogram there is a significant coverage of CO, and no current observed. As the potential, E increases, so does the oscillator strength and the CO wavenumber, $\tilde{\nu}$ ($\partial\tilde{\nu}/\partial E = 49\,\mathrm{cm^{-1}V^{-1}}$). The increase in oscillator strength in this case can be directly attributed to the increase in CO coverage (as opposed to a decrease in coverage as in CO stripping), while the increase in wavenumber can be considered as a combination of Electrochemical Stark Tuning (section 2.3.4.3) and an increase in dipole-dipole interactions (section 2.3.5.2). This latter contribution can also explain the $21\,\mathrm{cm^{-1}\ V^{-1}}$ increase in Stark tuning slope observed in formic acid compared to that observed in CO stripping.

The maximum in oscillator strength (vertical line, fig. 5.16) matches the onset of significant oxidation current in the voltammogram and the onset of deviation from the initially linear trends in peak wavenumber and width. After half of the CO has been removed from the surface the slope of the peak wavenumber-potential relationship returns to the value observed in the stripping of directly adsorbed CO, indicating that most lateral interactions have been lost. As the coverage of CO decreases the peak width increases, [43] perhaps suggesting the CO(ad) that remains is adsorbed in a variety of different environments (section 2.3.2.1).

5.3.3.3 CO(ad) and HCOO(ad) Behaviour on Pt/C Compared to ATR-SEIRA Measurements

In general the inverse relationship with current suggests that CO(ad) acts as a poison for formic acid oxidation on the catalyst, as has been shown for macroscopic Pt electrodes. [50] This correlation with behaviour on macroscopic Pt can be compared directly using results obtained by Okamoto *et al.* in ATR-SEIRA experiments at the same scan rate. [57] The potential dependence of HCOO(ad) and CO(ad) observed here are plotted

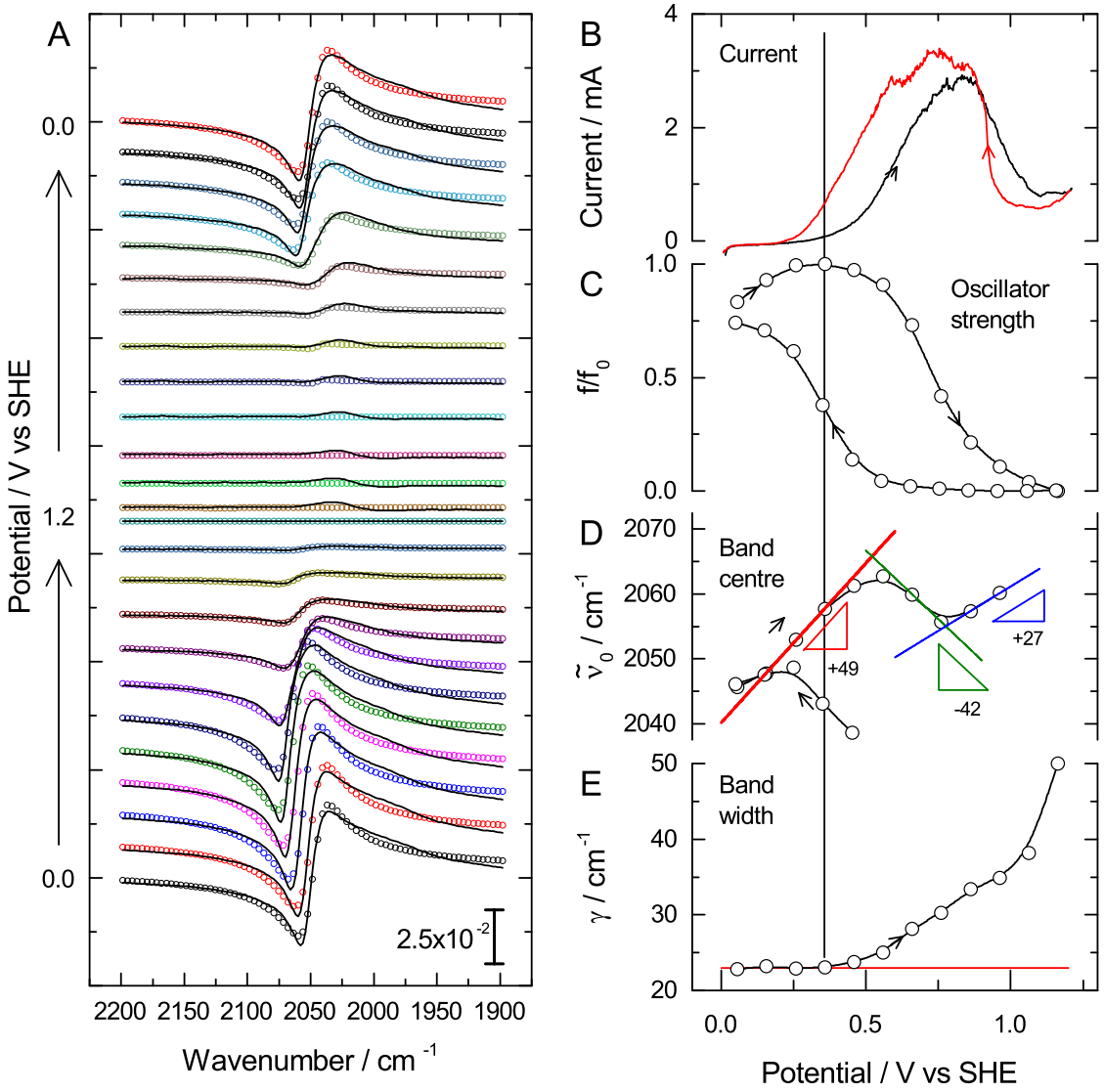

Figure 5.16: Fitting of the CO band region during formic acid oxidation. Solution: 25 mM HCOOH + 0.5 M $HClO_4$. Background: 0.0 V in $HClO_4$. A: Fits (lines) to the spectra (points) in CO band region. B: Cyclic voltammogram obtained in formic acid (1 mV s^{-1}). C: Fitted normalised oscillator strength f/f_0 (points) plotted as a function of potential, with a spline interpolation (line) shown as a guide. D: Fitted band centre as a function of potential (points) with a spline interpolation (black line) and linear fits to regions of the positive sweep (red, green, blue lines). The slope of each linear fit is shown on the figure. E: Fitted band width for the positive sweep, as a function of potential. A horizontal line is shown in red for reference. Data points and interpolation are shown as above.

alongside the data of Okamoto in fig. 5.17. [57] At the beginning of the positive going scan the CO observed in ATR-SEIRA does not appear to increase in intensity with potential to the same extent as observed in the spectra reported here. Furthermore, while the subsequent decrease in intensity occurs at a potential around 0.2 V higher in ATR-SEIRA measurements, the loss is much faster with CO intensity reaching zero by 0.7 V. On the negative-going scan CO is observed to appear at the same potential (around 0.5 V), but again increases much faster in the ATR-SEIRA measurements, returning to its original intensity by 0.2 V, in contrast to the present measurements in which CO has not reached its original absorbance by the end of the scan.

The behaviour of HCOO(ad), on the other hand, is much closer to that observed in ATR-SEIRA measurements, the only significant difference being the more positive onset potential for HCOO(ad) formation in the negative-going scan, and the resulting slightly higher HCOO(ad) intensity for the duration of the plateau region. Due to the difference in experimental conditions it is impossible to say whether this difference is a result of the seemingly stronger interaction between HCOO(ad) and Pt nanoparticles than thin Pt films (as determined from the decrease in the wavenumber of the ν_s(OCO) vibration) or simply the result of a more developed oxide layer arising from the higher anodic potential limit used in the ATR-SEIRA experiment.

This comparison shows that the differences in reactivity between nanoparticles and macroscopic electrodes, such as those used in ATR-SEIRA experiments, are likely to be dominated by differences in the rate of CO formation and oxidation, rather than by differences in the reaction of HCOO(ad). The slower rate of CO formation observed in the negative-going scan on nanoparticles as compared to that measured in ATR-SERIA experiments can be explained by analogy with the particle size-dependence of CO poisoning observed previously on nanoparticles during formic acid oxidation. [98, 99] In these cases the CO intensity was observed to decrease with particle size, and was rationalised by

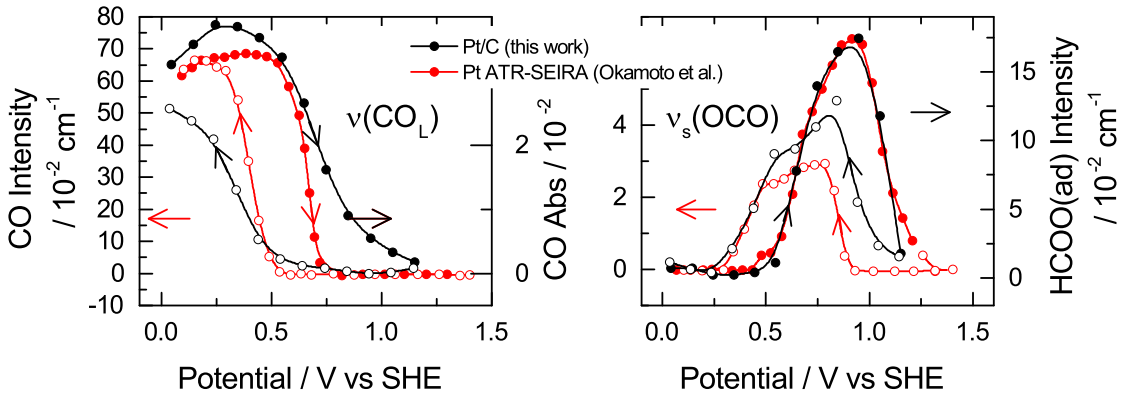

Figure 5.17: Comparison of the potential dependence of the CO and HCOO(ad) peak intensities observed on Pt/C with those observed in ATR-SEIRA experiments reported by Okamoto *et al.* in reference [57].

considering the decrease with particle size in the number of atomic ensembles with the contiguous vacant sites thought to be required for CO formation. Similarly the slower decrease in CO intensity on nanoparticles than in SEIRA experiments can be explained by considering the much higher onset potential for CO oxidation on small nanoparticles than on bulk Pt. [95, 100, 101] Together, these two effects will determine the number of vacant sites on the surface and therefore the rate of formic acid oxidation.

To obtain more quantitative information on the rates of CO formation and oxidation, the CO peak oscillator strength was calibrated to the coverage of CO using the procedure describes in section 5.3.4.

5.3.4 IR Calibration

To allow a quantitative comparison of the CO position and intensity during formic acid oxidation, the relationship between coverage and oscillator strength must be understood and can be obtained from dose-strip spectroelectrochemical experiments. [50,52] Although the oscillator strength coverage relationship was correlated in section 5.3.4, a significant shift in the position of the CO band formed from HCOOH, compared to direct adsorption of CO, suggest that the nature of CO is different in the two cases. Calibration was therefore

carried out again, this time using doses of formic acid to control the CO coverage (figs. 5.18 and 5.19).

The first difference to note from the calibration carried out on directly adsorbed CO, is a difference in the H desorption peaks in the stripping cyclic voltammograms (fig. 5.20). Whereas direct CO adsorption diminished the intensity of the two H desorption peaks equally (fig. 5.20A), CO adsorption from formic acid seems to initially only affect the higher potential peak, assigned to H desorption from 100 sites [102] (fig. 5.20B). With longer adsorption times the low potential H desorption peak, assigned to desorption from (110) sites, [102] decreases in magnitude and shifts to higher potential. This indicates that there is less H adsorbed but it is more strongly bound, this increase in adsorption strength possibly being explained by the decreased lateral repulsive interactions between adsorbed H. At coverages approaching saturation both H desorption peaks have been lost, although there remains a broad current plateau throughout the desorption region (compare the hatched region in fig. 5.20B with the same region in fig. 5.20A). This shape is characteristic of H adsorbed on (111) planes, [102] suggesting that CO adsorption does not take place on these sites at all.

As well as differences in the H desorption current, there are also differences between the CO stripping current. The stripping of the formic acid-derived CO gives rise to one peak, whereas stripping of directly adsorbed CO gives rise to two in the same region. The peak that appears to be missing is the higher potential peak, at around 0.77 V. Coupled with the fact that the (111) H desorption peak remains in the presence of CO from formic acid, the higher potential of the two peaks from direct adsorption is suggested to arise from CO adsorbed on (111) planes. This interpretation is supported by measurements reported on single crystals, in which negligible HCOOH dehydration to CO was found to occur on Pt(111), [33,34] and by DFT calculations which predict that HCOOH dehydration should not occur at all on Pt(111). [35]

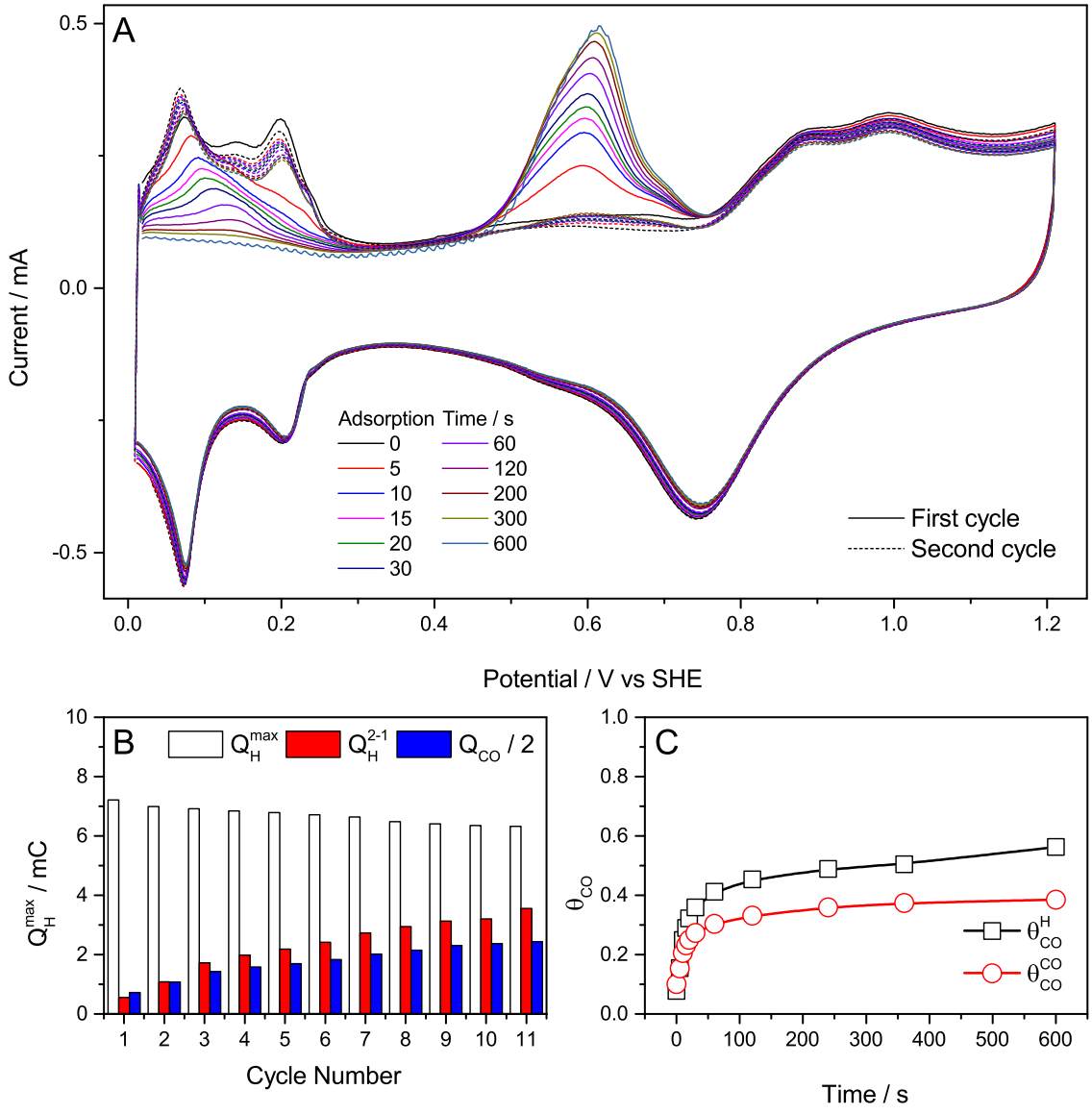

Figure 5.18: Electrochemical determination of CO coverage following HCOOH adsorption. A: Cyclic voltammograms following HCOOH adsorption for different amounts of time. Solution: 0.01 M HCOOH + 0.5 M H_2SO_4. Flow rate: 0 mL min^{-1}. Scan rate: 10 mV s^{-1}. Step potential: 2.44 mV. B: Charge under H desorption (Q_H) and CO oxidation (Q_{CO}) peaks. C: Surface coverage of CO calculated from $Q_{CO}/2Q_H^{max}$ and Q_H^{2-1}/Q_H^{max}.

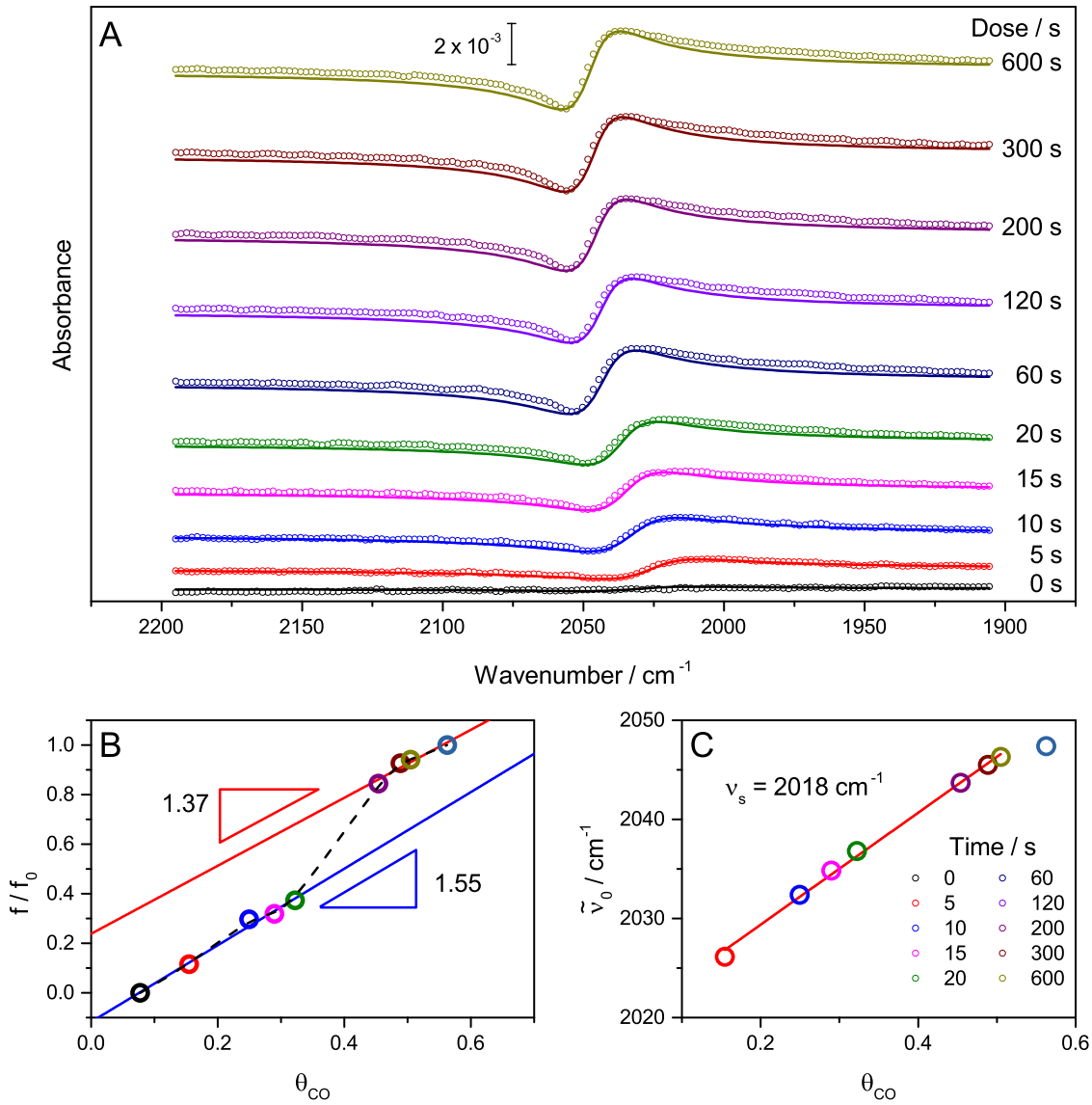

Figure 5.19: Calibration of oscillator strength with coverage for CO adsorbed in fig. 5.18. A: IR spectra and fits of adsorbed CO at 0.0 V after different adsorption times. Background: 0.0 V before introduction of HCOOH. B: Relative CO band intensity as a function of CO coverage. C: CO band centre as a function of CO coverage. Extrapolation of band centre in the limit of zero coverage is shown as ν_s.

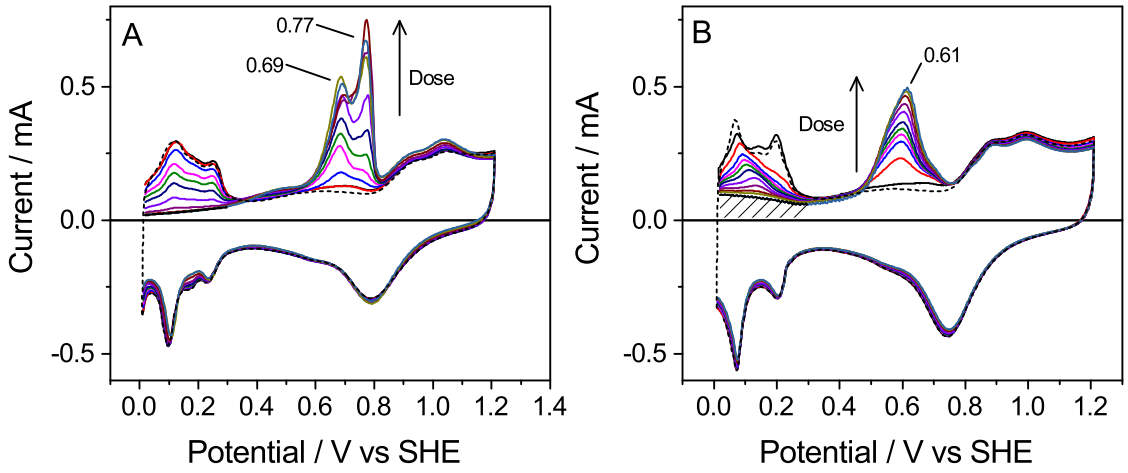

Figure 5.20: CO stripping voltammograms of CO adsorbed directly (A) or from HCOOH dehydration (B), taken from fig. 4.10 and fig. 5.18, respectively. Catalyst dosed with CO or HCOOH for times from 0 s to 600 s. Representative voltammogram obtained after removing CO is shown as a dashed line in each panel.

When the singleton wavenumbers,[3] ν_s of the main adsorbed CO band are compared for direct adsorption (2067 cm^{-1}) and formic acid dehydration (2018 cm^{-1}), both at 0 V, it can be seen that the CO band from dehydration is much lower. [44] Based on the conclusions of Chapter 4, the CO band is therefore assigned to CO adsorbed on step rather than terrace sites.

A significant difference is also observed in the relationship between the fitted band centre, $\tilde{\nu}_0$ and the coverage in the two cases (fig. 5.21B). For directly adsorbed CO the band centre is around 2065 cm^{-1} and is relatively insensitive to coverage, while for formic acid-derived CO the band centre is around 35 cm^{-1} lower and is strongly dependent on coverage. A difference is also seen in the Stark tuning slope, $\partial\tilde{\nu}/\partial E$ which is 49 cm^{-1} V^{-1} for CO from formic acid dehydration, compared to 27 cm^{-1} V^{-1} for direct CO adsorption. The insensitivity of the directly adsorbed CO to coverage was attributed to island formation in Chapter 4, suggesting that stable islands are not formed by CO dosed from formic acid. This can be rationalised if dehydration only occurs on certain sites, for example (100) and

[3]The wavenumber in the limit of zero coverage, used here to remove any influence of dipole-dipole coupling.

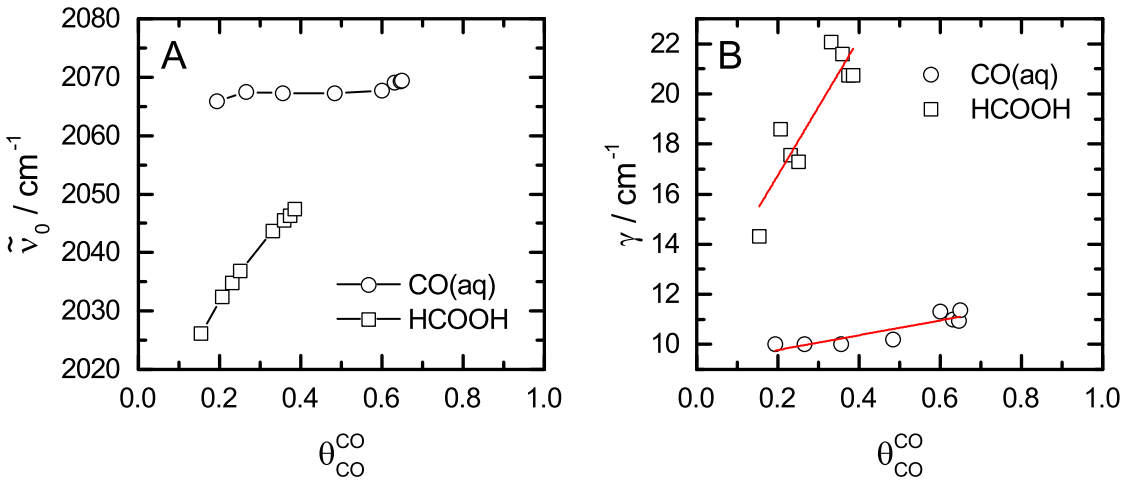

Figure 5.21: Comparison of the fitted CO peak properties formed by HCOOH dehydration and direct adsorption as a function of coverage. A: Fitted CO peak centre $\tilde{\nu}_0$ as a function of coverage determined from the CO stripping charge, θ_{CO}^{CO}. B: Fitted CO peak width γ as a function of coverage. The lines are best fits to the data.

(110)-like edge sites, as suggested from consideration of the stripping voltammograms. This would leave the (111)-like terrace sites unoccupied therefore inhibiting the formation of large islands.

5.3.5 The Rate of CO Formation and Oxidation

To quantify the exact contribution of CO oxidation to the observed current, the rates of CO formation (r_1) and oxidation (r_2) were examined using the procedure developed by Chen *et al.* for Pt thin films, introduced in section 5.2.2.2. [50,52] Although the rates have been measured for Pt thin films, the significant differences in the behaviour of CO on thin films and nanoparticles observed in section 5.3.3.3 suggest that the individual rates of formation/oxidation may also differ. The dynamic nature of CO formation and oxidation in formic acid means that the rate of either reaction can only be measured if it is assumed that the rate of the other reaction is negligible (eq. (5.31)). Such a situation can be found instantaneously after stepping the potential away from the two potential limits, with the rate of CO formation after a period at low potential being negligible due to the existence

of a saturated CO adlayer, and the rate of CO oxidation being negligible after a period at high potential, due to the negligible instantaneous coverage of CO.

$$\frac{d\theta_{CO}}{dt} = r_1 - r_2 = k_1\theta_{\mathrm{HCOOH}} - k_2\theta_{\mathrm{CO}}\theta_{\mathrm{OH}} \tag{5.31}$$

To measure the rate of CO oxidation the catalyst layer was equilibrated at 0.05 V for 30 s to established a saturated CO adlayer, and then stepped to the potential of interest and held for 60 s. This procedure was carried out for potentials of 0.2 V, 0.5 V, 0.7 V and 0.9 V. IR spectra were acquired at a rate of $2\,\mathrm{s}^{-1}$ during the process and were analysed using the one peak model developed in Chapter 4 and applied to HCOOH-derived CO in section 5.3.3.2. The current and fitted, normalised oscillator strength are plotted as a function of time in fig. 5.22 (raw data can be found in fig. C.1). The initial slope of oscillator strength with time at each potential was obtained by a linear least squares regression to the first *circa* 10 s of data and is shown in the figure as solid lines. The rate of CO oxidation was then taken as the product of the initial slope and the calibration slope, $d\theta/d(f/f_0)$ (eq. (5.32), section 5.3.4, where N is the total number of Pt sites. The finite rate of CO oxidation is observed in the current transient, where an initial decrease in current, due to the decaying capacitive current, is followed by an increase as the oxidation of CO releases surface sites on the catalyst for formic acid oxidation.

$$\left[\frac{d\theta_{\mathrm{CO}}}{dt}\right]_{\theta_{\mathrm{CO}}=sat.} = -\left[\frac{r_2}{N}\right]_{\theta_{\mathrm{CO}}=sat.} = \left[\frac{d\theta_{\mathrm{CO}}}{d(f/f_0)}\right]_{\theta_{\mathrm{CO}}>0.45} \times \left[\frac{d(f/f_0)}{dt}\right]_{\theta_{\mathrm{CO}}=sat.} \tag{5.32}$$

A similar procedure was used to obtain the rate of CO formation at different potentials. The potential was held at 1.0 V for 30 s to remove any adsorbed CO before being stepped down to 0.2 V, 0.5 V, 0.7 V and 0.9 V (fig. 5.23, raw data in fig. C.2). Infrared spectra were again fitted using the one peak model and the oscillator strength extracted, allowing calculation of the rate as before, except using the f/θ_{CO} relationship determined at low

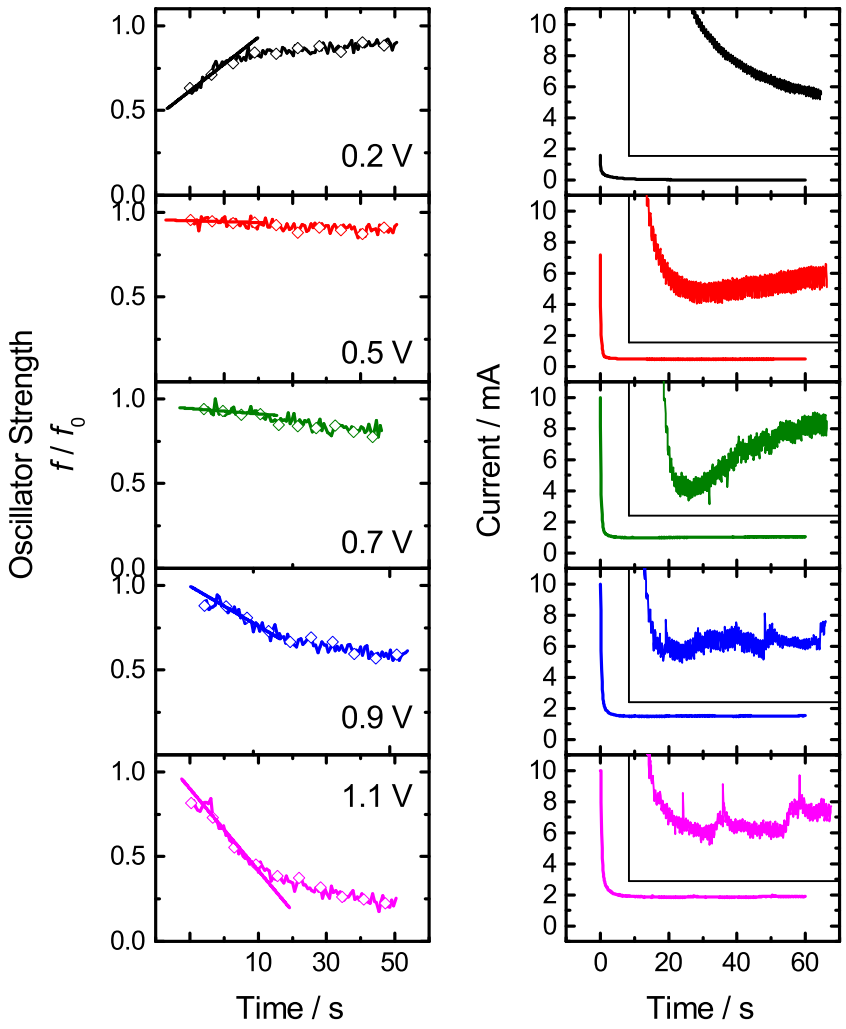

Figure 5.22: Evaluation of the rate of CO oxidation formed from dehydration of formic acid. Solution: 0.1 M HCOOH + 0.5 M $HClO_4$. Flow rate: 3 mL min^{-1}. Left panels: Normalised fitted oscillator strength of the linear CO peak after stepping from 0.05 V to potential indicated. Linear fits shown to first 10 s. Right panels: Current measured after stepping potential from 0.05 V to potential indicated. Inset: Current excluding initial double layer contribution.

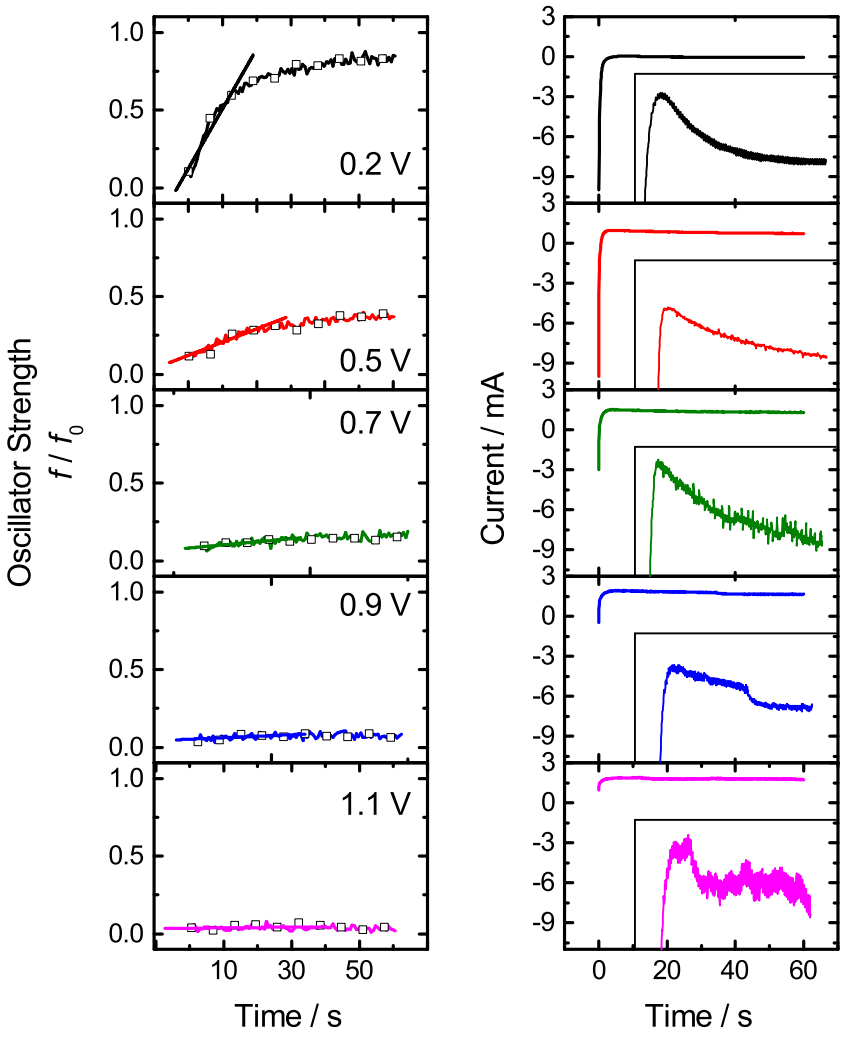

Figure 5.23: Evaluation of the rate of HCOOH dehydration to form adsorbed CO. Solution: 0.1 M HCOOH + 0.5 M $HClO_4$. Flow rate: 3 mL min^{-1}. Left panels: Normalised fitted oscillator strength of the linear CO peak after stepping from 1.2 V to potential indicated. Linear fits shown to first 10 s. Right panels: Current measured after stepping potential from 1.2 V to potential indicated. Inset: Current excluding initial double layer contribution.

Table 5.7: The contribution of the CO pathway to formic acid oxidation current.⋆

Potential	$[d(f/f_0)/dt]_{t=0}$	$[d\theta/dt]^{\dagger}_{t=0}$	Est. Current Density ‡
V vs SHE	s^{-1}	molecule site^{-1} s^{-1}	µA cm^{-2}
HCOOH Dehydration			
0.2	3.85×10^{-2}	2.48×10^{-2}	(1.03×10^{-1})*
0.5	8.52×10^{-3}	5.49×10^{-3}	(2.29)
0.7	1.99×10^{-3}	1.28×10^{-3}	(5.35×10^{-1})
0.9	9.75×10^{-4}	6.29×10^{-4}	(2.62×10^{-1})
1.1	2.46×10^{-4}	1.58×10^{-4}	(6.60×10^{-2})
CO Oxidation			
0.2	1.58×10^{-2}	-1.15×10^{-2}	-4.8
0.5	-5.38×10^{-4}	3.92×10^{-4}	1.63×10^{-1}
0.7	-1.37×10^{-3}	1.00×10^{-3}	4.17×10^{-1}
0.9	-1.17×10^{-2}	8.55×10^{-3}	3.56
1.1	-2.41×10^{-2}	1.76×10^{-2}	7.32

⋆ Evaluated using the method in reference [50].
† Using $\left[\frac{d\theta}{d(f/f_0)}\right]_{\theta<0.3} = 0.730$, $\left[\frac{d\theta}{d(f/f_0)}\right]_{\theta>0.45} = 0.645$, as determined in section 5.3.4.
‡ Conversion from molecule site^{-1} s^{-1} to mol cm^{-2} and was carried out using a surface atom density of 1.3×10^{15} atoms cm^{-2}, after reference [50], and the Faraday constant 96 485 C mol^{-1}, assuming a 2 e$^-$ process.
* Values are in brackets are hypothetical values if HCOOH dehydration involved net electron transfer

(as opposed to high) coverage (eq. (5.33)). The evaluated rates ($d\theta/dt$) for both CO formation and oxidation are collected in table 5.7.

$$\left[\frac{d\theta}{dt}\right]_{\theta_{CO}=0} = \left[\frac{r_1}{N}\right]_{\theta_{CO}=0} = \left[\frac{d\theta_{CO}}{d(f/f_0)}\right]_{\theta_{CO}<0.3} \times \left[\frac{d(f/f_0)}{dt}\right]_{\theta_{CO}=0} \tag{5.33}$$

The process of HCOOH dehydration to form adsorbed CO can be observed both directly, via the increase in CO oscillator strength, and indirectly, via the decrease in

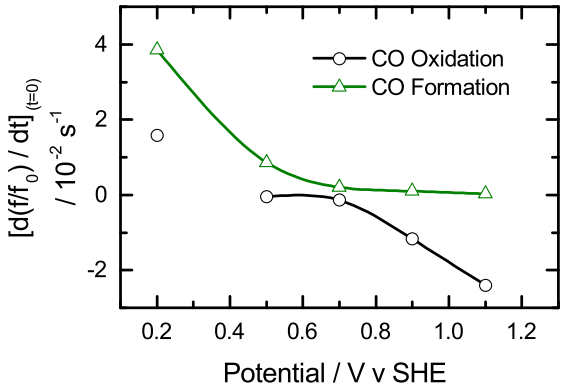

Figure 5.24: The initial slope of the fitted CO peak oscillator strength plotted as a function of applied potential.

formic acid oxidation current over time. Examining a plot of the initial slope of oscillator strength as a function of time (fig. 5.24), it can be seen that the rate of CO formation is much greater at lower potentials. This suggests that dehydration is an electrochemical, rather than purely chemical, step and that the rate determining step involves a reductive electron transfer. This is in line with the mechanism proposed by Cuesta, of subsequent oxidation and reduction steps to form CO (eqs. (5.34) and (5.35), where 'rds' has been added based on the current observations). The rate of CO oxidation can be similarly investigated. One complication, however, is the apparent different saturation coverage of CO at 0.05 V and 0.2 V. This leads to an initial increase in CO coverage during the first step from 0.05 V to 0.2 V and initial slope which does not reflect the rate of CO oxidation. This should not affect the slopes of higher potentials, however.

$$\mathrm{HCOOH} \longrightarrow \mathrm{HCOO(ad)} + \mathrm{H^+} + \mathrm{e^-} \tag{5.34}$$

$$\mathrm{HCOO(ad)} + \mathrm{H^+} + \mathrm{e^-} \xrightarrow{\text{rds}} \mathrm{CO} + \mathrm{H_2O} \tag{5.35}$$

The evaluated turnover frequencies can be compared to those reported previously for HCOOH dehydration and CO oxidation on thin Pt films. [50, 52] The values are plotted alongside the values determined here in fig. 5.25. Note that the values obtained here

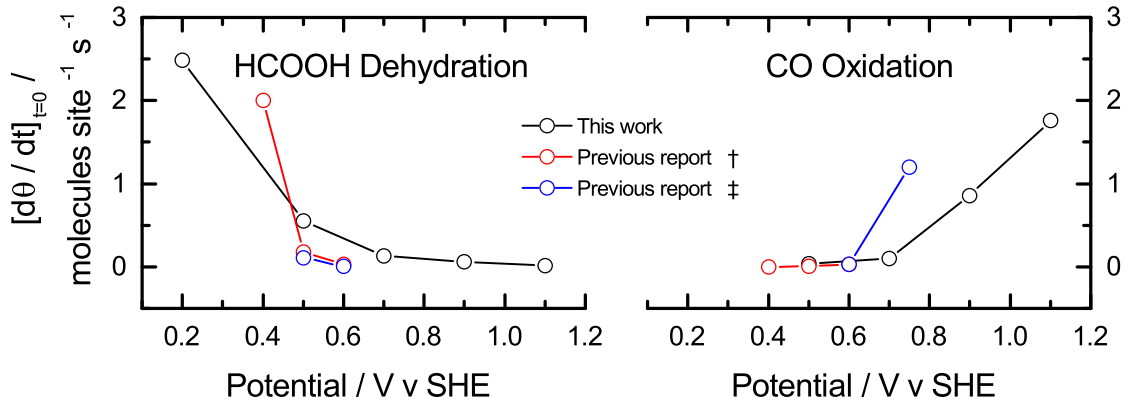

Figure 5.25: Comparison of evaluated turnover frequencies with previous reports. † Data from refenece [52]. ‡ Data from reference [50]. Previously reported data was obtained in 0.1 M HCOOH + 0.5 M H_2SO_4, the data reported here were obtained in $HClO_4$ instead.

were measured in $HClO_4$ rather than the H_2SO_4 solutions used in previous reports. Any reaction involving an adsorption step is therefore likely to be faster here than previously reported. This is seen in the slightly higher rates of HCOOH dehydration. The CO oxidation step only requires adsorption of OH, which is not blocked by SO_4 adsorption, and so therefore should be comparable. [103] This appears to be the case at low potentials, where TOFs are low anyway, however at higher potentials the TOF appears to be slightly lower in the present case than previously reported. It was discussed in Chapter 4 how smaller nanoparticles have higher overpotentials for CO oxidation than bulk surfaces, and this effect could be contributing here.

The observed TOFs can further be converted into current densities, using a surface atom density of 1.3×10^{15} atoms cm^{-2}, and the Faraday constant 96 485 C mol^{-1}. [50] These current densities can then be compared to the measured overall current densities to establish the contribution of the indirect pathway to formic acid oxidation. The overall current densities used were those at quasi-steady state, approximated as the average current density measured 50 s after stepping the potential from the high and potential limits to the potential of interest. [50]

The calculated current densities are shown next to the quasi-steady state current

Table 5.8: Quasi-steady state current densities for formic acid oxidation.†

Potential /	Current Density / µA cm^{-2}			
V vs SHE	Ascending	Descending	Average	CO Oxidation‡
0.2	-2.1	-1.4	-1.7	-
0.5	29.9	18.4	24.1	1.63×10^{-1}
0.7	52.7	41.6	47.2	4.17×10^{-1}
0.9	67.8	61.2	64.5	3.56
1.1	73.5	77.7	75.6	7.32

† Quasi-steady state current density refers to the average current density observed following positive and negative steps to that potential.
‡ Calculated from table 5.7.

densities in table 5.8. To compare the individual current densities with the overall current density, it must be remembered that both HCOOH dehydration and CO oxidation have to occur sequentially to produce any current. Therefore, even though at 1.1 V CO oxidation may be able to contribute to a current density of around 7 µA cm^{-2}, the rate of HCOOH dehydration is two orders of magnitude slower, limiting the actual contribution of CO oxidation to negligible amounts. The rates are closest at 0.7 V, where the calculated current density is 0.42 µA cm^{-2}, or 0.9% of the total current. This suggests that the 'CO pathway' does not represent a major pathway for formic acid oxidation on the present catalyst, consistent with Chen's observations for thin Pt films. [50, 52] It should be noted that this is in contrast to other oxidation reactions, such as that of methanol, where CO oxidation does account for a significant fraction of the current. [104]

5.3.6 The Rate of HCOO(ad) formation

A quantitative analysis of HCOO(ad) formation and oxidation rates is not possible in the same way as it was for CO, since HCOO(ad) does not provide an electrochemical

stripping peak. A peak between 0.38 V and 0.7 V assigned to HCOO(ad) adsorption is available when the scan rate is around 10 V s^{-1}, [70] however such scan rates are likely to produce many errors in potential measurement and control in the spectro-electrochemical cell (fig. 3.20) and so this approach was not pursued in this work. Kinetic information can still be gained, however, based on inspection and comparison with the CO peak. IR spectra were recorded of the catalyst layer in 10 mM HCOOH + 0.5 M $HClO_4$ at a rate of 3 s^{-1} as the potential was stepped from 0.05 V to 0.5 V, 0.7 V, 0.9 V and 1.1 V. The integrated intensity of the peaks assigned to HCOO(ad) and CO_2(aq), the absorbance of the linear CO (CO_L) peak and the current as a function of time are shown in fig. 5.26.

In terms of the HCOO(ad) peak, several features become obvious. First of all it can be seen in the step to 0.7 V that the rate of HCOO(ad) formation is noticeable slower than its loss, the HCOO(ad) peak growing over around 25 s, but being lost in around 1 s. The rates appear to become much closer at higher potentials, however. The second observation is that when HCOO(ad) is observed (at potentials > 0.7 V), the maximum intensity of the peak is the same at all potentials. This suggests that the coverage is independent of potential. When the rates of CO loss and HCOO(ad) formation are compared (fig. 5.26B) it can be seen that they are very well correlated.

5.3.7 The Order of Reaction with Respect to HCOOH

The order of reaction is an easily measurable parameter relating directly to the rate equation and as such can be used to test the validity of a proposed mechanism (section 2.1.3.3). The order of formic acid oxidation with respect to formic acid was examined spectroscopically under both constant potential and potential sweep conditions. The current observed during potential sweeps in 0, 10, 20, 30, 40, 50 and 100 mM formic acid is shown in fig. 5.27A and a log-log plot of the the peak current obtained in the forward and backward scans is plotted as a function of concentration ([HCOOH]) in mM in fig. 5.27B. The

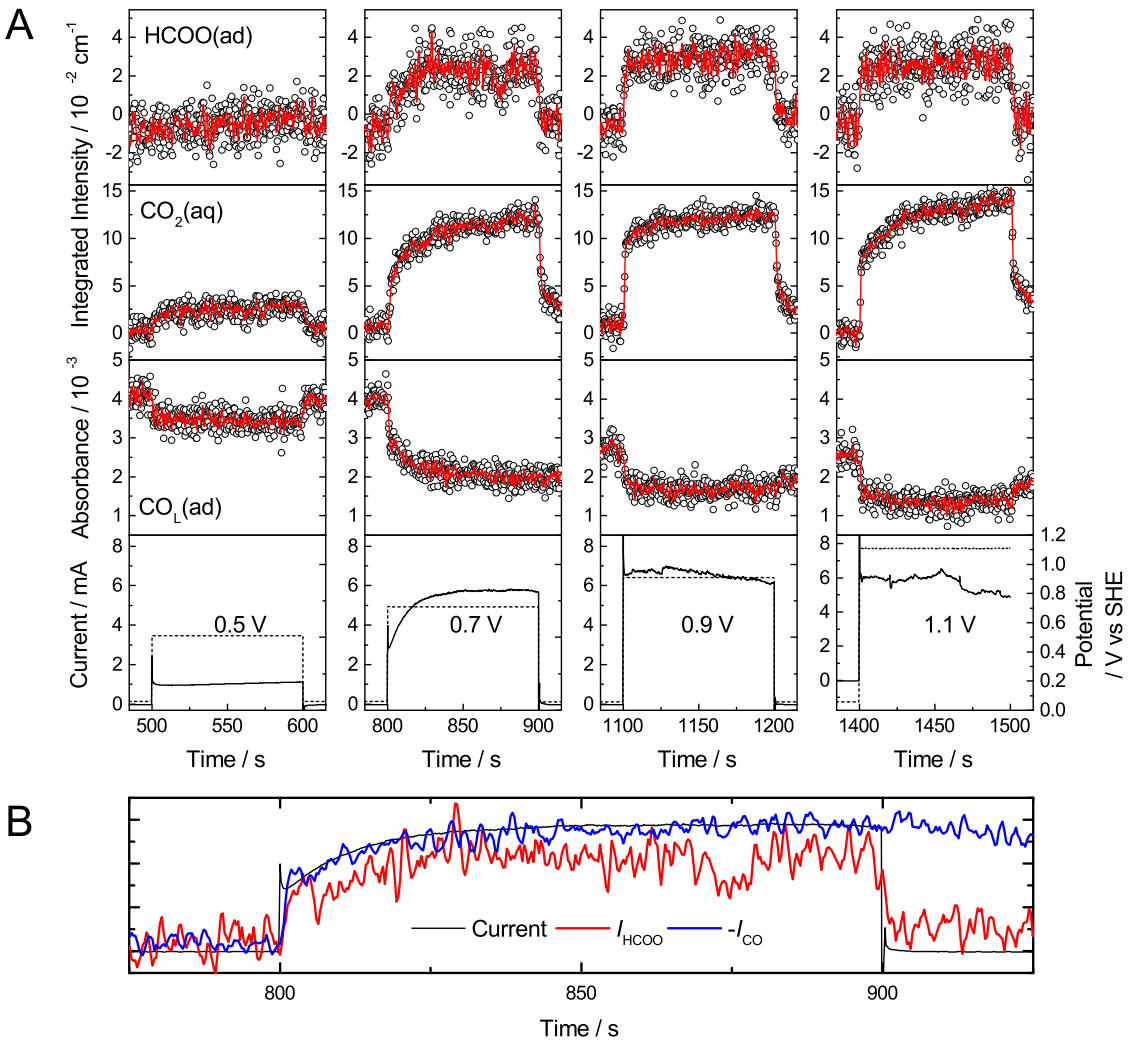

Figure 5.26: Kinetics of formate formation. Solution: 10 mM HCOOH + 0.5 M $HClO_4$. Flow rate: 3 mL min^{-1}. Spectra obtained at a rate of 3 s^{-1}. Background: 0.05 V in $HClO_4$. A: Integrated intensity of HCOO(ad) and CO_2(aq) peaks, absorbance of linear CO (CO_L) peak and current as a function of time following potential step from 0.05 V to 0.5 V, 0.7 V, 0.9 V and 1.1 V (points). Smoothed data using a 6 point adjacent average, corresponding to a 2 s window (red line). The measured potential is also shown (dashed line). (B) Comparison of the rate of CO loss and the rate of HCOO formation at 0.7 V. 2 s average of CO absorbance (sign inverted, blue line), 2 s average of the HCOO integrated intensity (red line) and current (black line).

current peaks in both forward and backward scans increase with concentration in a linear manner at low concentrations, although the increase becomes non-linear as the concentration rises above 40 mM. Linear fits to the log-log plot provide reaction orders of 0.604 for the forward sweep and 0.739 for the reverse sweep. IR spectra were recorded during all of the cycles and representative spectra are shown fig. 5.27C and fig. 5.27D for 10 mM and 50 mM, respectively.

Current transients following potential steps to 0.2 V, 0.4 V, 0.6 V and 0.8 V were recorded at the different concentrations in order to determine the steady state current at each potential. The steady state current was measured 50 s after stepping the potential; although several transients showed signs of current oscillation (a common feature in formic acid oxidation, see section 5.2.2.3) the magnitude of these oscillations was small relative to the absolute value of the current. A log-log plot was again used to determine the order of reaction with respect to HCOOH at different potentials, with the results shown in table 5.9. IR spectra were again obtained throughout the current transients, and are shown co-added over the entire 50 s transient in fig. 5.29. The 1.0 V transient spectra were used as backgrounds for the spectra at each concentration. Note that the none of the IR peaks were observed to vary in intensity with the observed current oscillations, in contrast to the observations of Samjeské *et al.*. [63, 67]

Table 5.9: The order of formic acid oxidation with respect to HCOOH at different potentials.

	Reaction Order			
Measurement	0.2 V	0.4 V	0.6 V	0.8 V
Cyclic voltammetry			0.6	0.739
Chronoamperometry	0.43	0.38	0.80	0.98

The order of reaction is observed to be close to 0.5 at 0.2 V, increasing towards 1

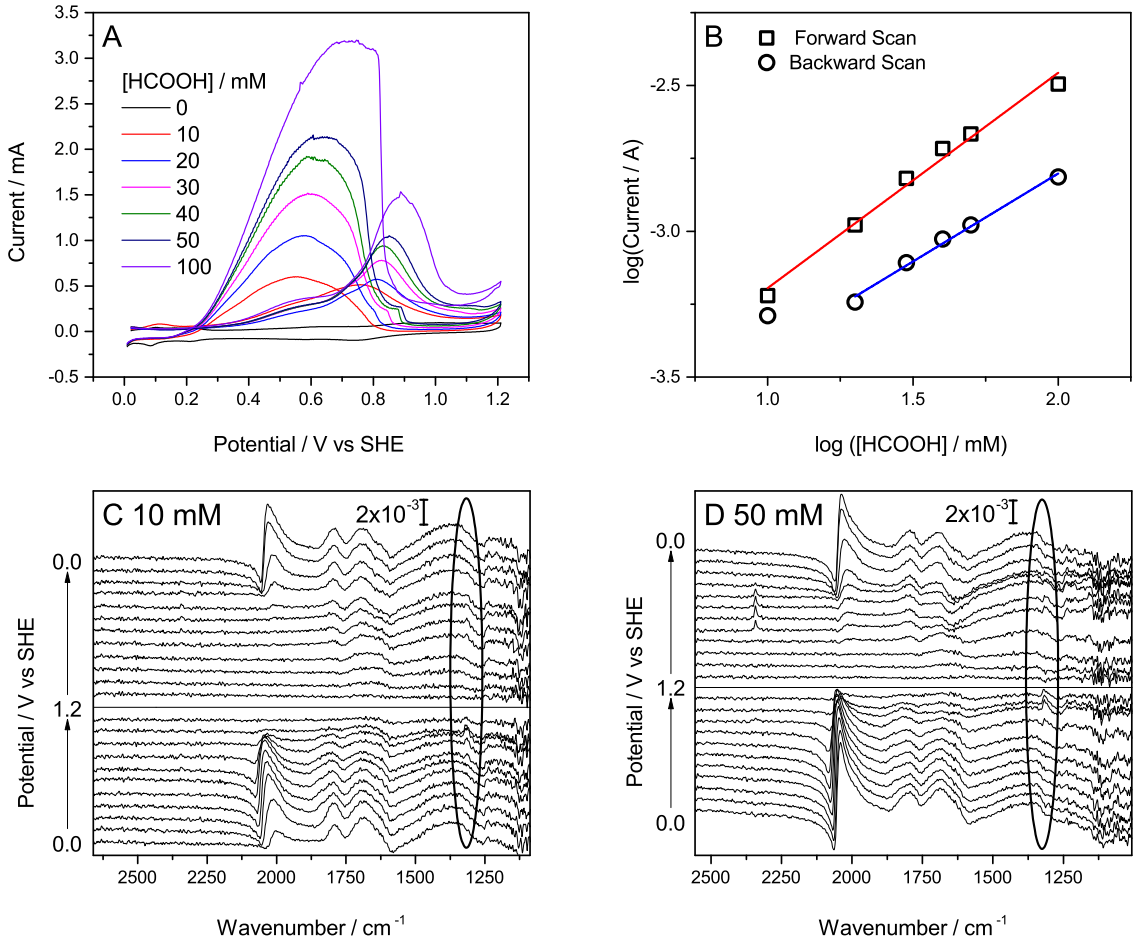

Figure 5.27: Reaction order with respect to formic acid. Solution: HCOOH + 0.5 M H_2SO_4. Flow rate: 3 mL min^{-1}. A: Cyclic voltammograms obtained in different HCOOH concentrations. Scan rate: 10 mV s^{-1}. B: A log-log plot and linear fits of the peak currents obtained during the forward (red fit) and backward (blue fit) sweeps of the cyclic voltammograms in A. C: IR spectra obtained during the voltammogram in 10 mM HCOOH. Background: 1.2 V. D: IR spectra obtained during the cycle in 50 mM HCOOH. Background: 1.2 V. Formate ν_s(OCO) peak is circled.

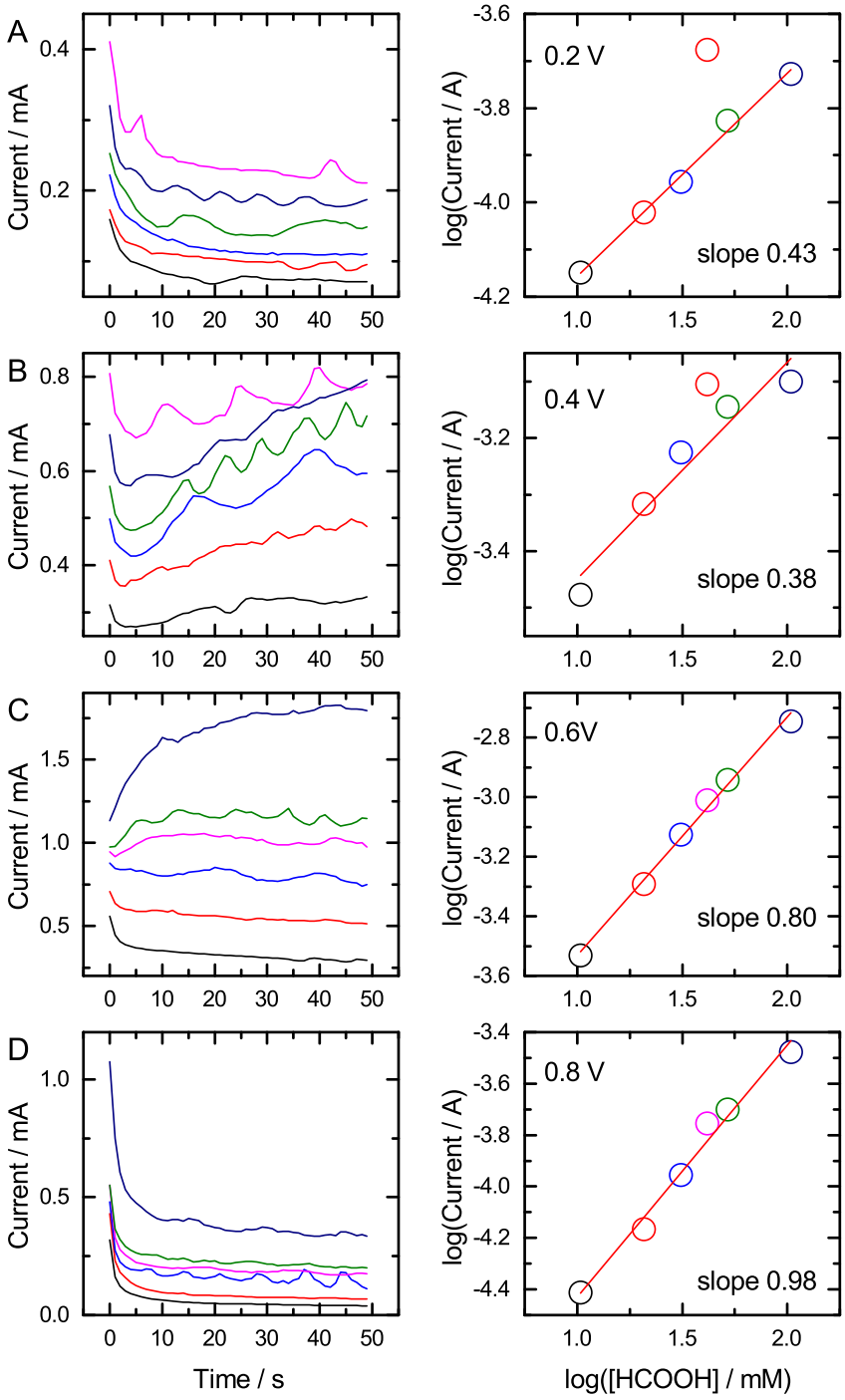

Figure 5.28: Steady state current at different formic acid concentrations. Solution: HCOOH + 0.5 M H_2SO_4. Flow rate: 3 mL min^{-1}. Left: Current transients recorded after stepping from A: 0.0 V to 0.2 V, B: 0.2 V to 0.4 V, C: 0.4 V to 0.6 V, D: 0.6 V to 0.8 V in 10 mM (black), 20 mM (red), 30 mM (blue), 40 mM (pink), 50 mM(green) and 100 mM(blue) formic acid. Right: Plots of log(Current / A) versus log([HCOOH] / mM) (points) and linear fit (red line).

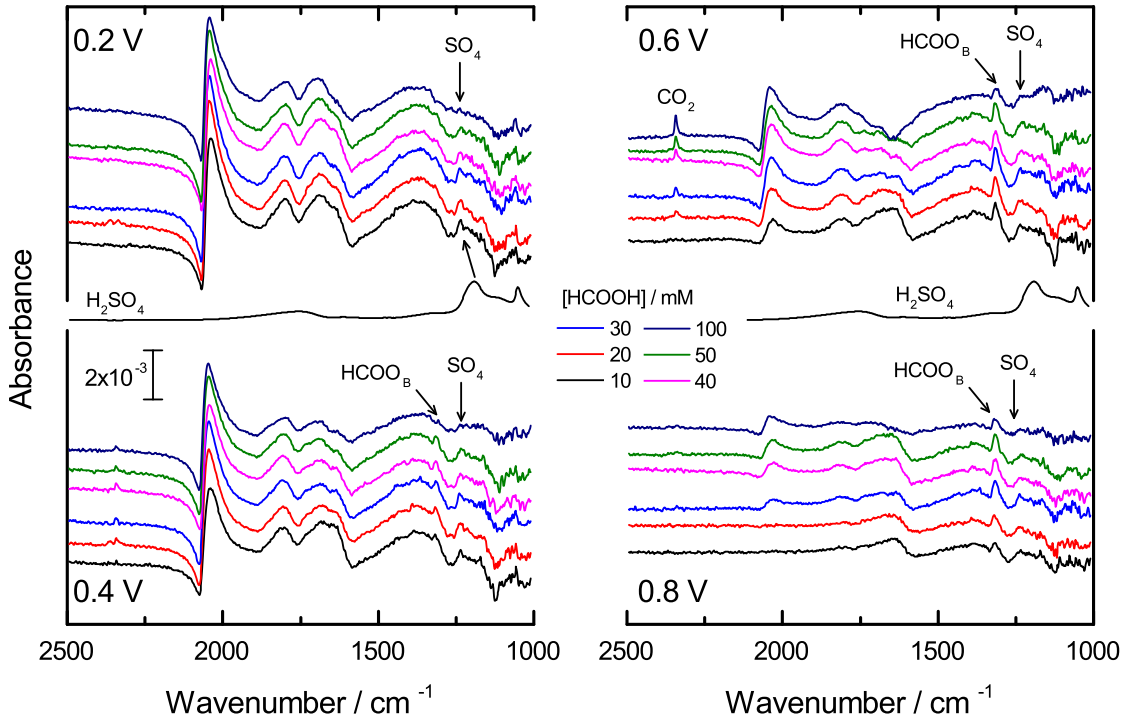

Figure 5.29: *In situ* IR spectra obtained at different formic acid concentrations and potentials, during the current transients shown in fig. 5.28. Solution: HCOOH + 0.5 M H_2SO_4. Flow rate: 3 mL min^{-1}. Background: 1.0 V in respective solution.

as the potential increases. Fractional orders in surface reactions can often be explained on the basis of strong adsorption of intermediates; the accumulation of strongly bound species at the surface leads to an effective decrease in surface area and free sites. If the coverage of species increases with concentration, then the corresponding decrease in surface area will partially counteract the effect of the increasing concentration and give rise to reactions orders less than 1. This interpretation is supported by spectra of the electrode surface, which reveal significant amounts of CO at 0.2 V and both HCOO and CO at higher potentials (fig. 5.29).

At 0.8 V the order is close to 1, yet the coverage of CO as determined from the spectra increases with concentration. If the reaction was occurring at the same sites as CO adsorption, then the order would be expected to be *less* than 1. Consequently, the reaction must be occurring at different sites to those blocked by CO. Since CO was suggested to adsorb on edge sites, based on the smaller coverage and lower wavenumber

of CO from HCOOH as compared to CO adsorbed from CO(aq), the reaction at 0.8 V is suggested to be occurring at terrace sites.

Adsorbed CO is not the only adsorbed species at 0.8 V, however, as HCOO(ad) is also observed in the spectra. In fact, the intensity of HCOO(ad) is observed to increase with concentration, up to 30 mM after which it appears to be saturated. Using the same argument that was applied to CO, the increasing coverage of HCOO(ad) should lead to a fractional order of reaction, if it was blocking the reaction from occurring. Conversely, if the reaction was proceeding through the HCOO(ad) species, then at saturation the order is expected to tend to 0, since an increase in HCOOH concentration cannot increase the coverage of HCOO(ad) beyond saturation. An order of 1 in the presence of saturated HCOO(ad) adlayer therefore suggests that HCOO(ad) neither blocks the reaction, nor itself reacts, but is in fact a promoter of the reaction. This has previously been suggested for HCOO(ad) on Pt(111) based on DFT calculations, where the promotion effect came from the formation of a hydrophobic region around HCOO(ad) which favoured the interaction of HCOOH(aq) in the productive C−H down orientation (section 5.2.2.4). [77] If HCOO(ad) could increase the rate of reaction it could compensate for the surface sites it blocks, resulting in an apparent order of 1.

5.3.8 Kinetic Isotope Effects

Kinetic isotope experiments provide a sensitive way to determine if the bond to a particular atom is involved in the rate determining step (rds). The rate of reaction is compared for two isotopomers, where the particular atom in one isotopomer is substituted for a heavier isotope. If the heavier isotopomer reacts slower then then the bond to the heavier atom is considered to be broken in the rds. This effect was applied to DCOOH to determine the extent of C−D bond breaking in the rds. The current and *in situ* spectra were measured in 10 mM DCOOH under both constant potential and potential sweep conditions and

compared to the current in 10 mM HCOOH (fig. 5.30). In general the current observed in DCOOH is smaller than that measured in HCOOH, clear evidence for a kinetic isotope effect. The KIE arises due to differences in activation energy between isotopes, which is in turn determined by the difference in zero point energies between the ground and transition states (see section 2.1.2.6). The ground state zero point energy of a heavier isotope is smaller than that of the lighter isotope, while the difference in zero point energies in the transition state is determined by the extent of bonding. The weaker the bonding in the transition state the closer the transition state zero point energies of the two isotopes. If the heavier isotope has to start from a lower ground state energy to reach the same transition state energy, it has a larger activation energy. As a result of the higher activation energy the heavier isotope will therefore react slower.

When the KIE is measured a modest value of 1.5 is observed at the start of the voltammogram, increasing to 2.7 at several points as the potential increases. This agrees well with previously reported values of ≈ 1.9 and ≈ 3 for the KIE on thin Pt ATR-SEIRA electrodes, assigned to the CO and direct pathways, respectively. [105] This variation in KIE implies that there is more than one transition state for the reaction and therefore more than one reaction pathway. Considering the possible pathways, it is clear that CO oxidation will not give rise to a KIE since the oxidation of CO is the rds amd does not involve a C−H bond. This is supported by IR spectra obtained during the constant potential measurements between 0.4 V and 0.8 V, which reveal no difference in the CO intensity between HCOOH and DCOOH. In the absence of the CO pathway, at least another 2 pathways must therefore exist to explain the observed variation in KIE.

Evidence for an additional pathway also comes from the IR spectra obtained between 0.4 V and 0.8 V, which reveal much more intense ν_s(OCO) peaks from DCOO(ad) than HCOO(ad), and therefore a higher coverage of DCOO(ad) than HCOO(ad). The adsorption and desorption of HCOO(ad) is not expected to show a KIE, as it is the O−H

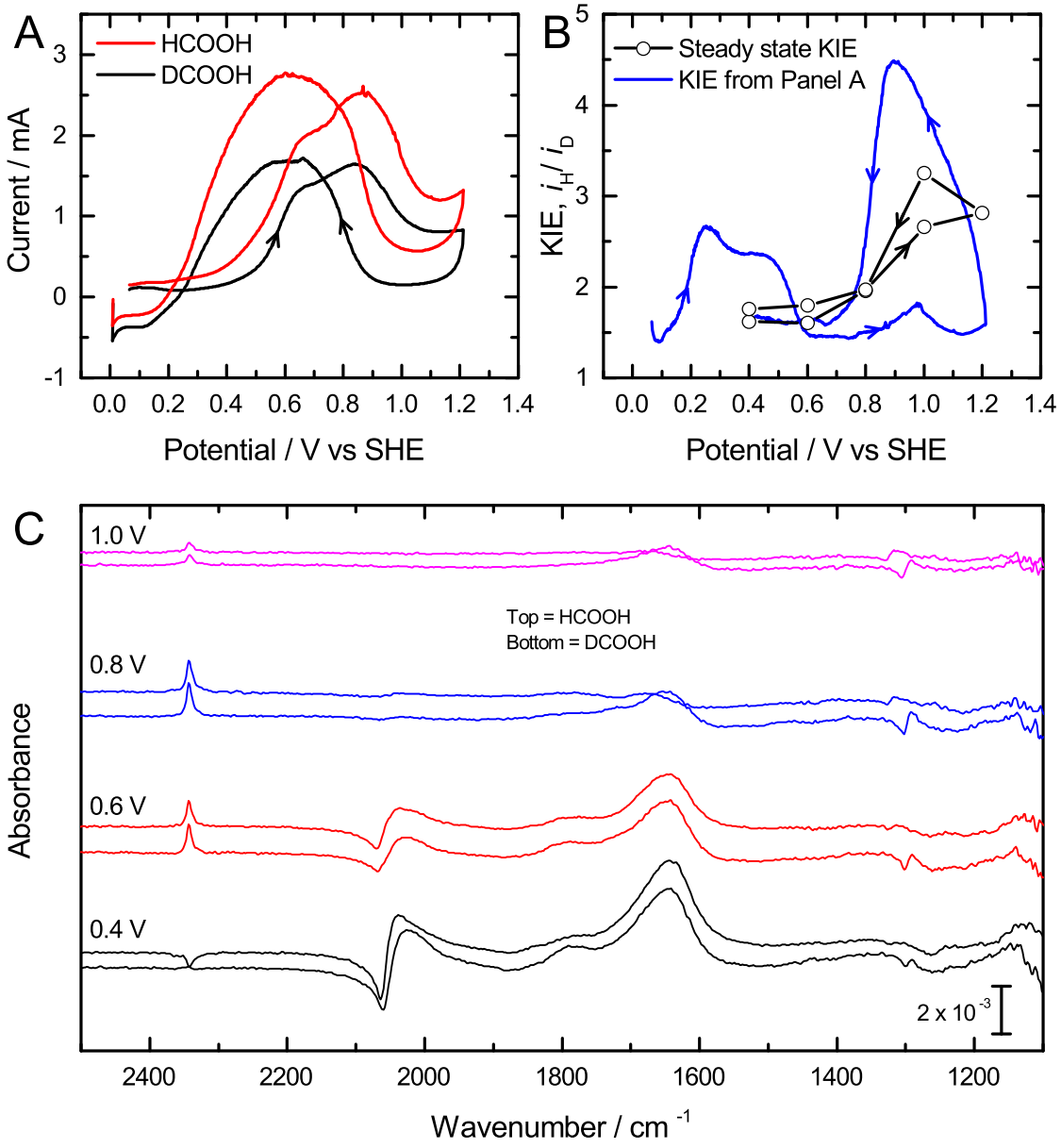

Figure 5.30: The kinetic isotope effect on formic acid oxidation. Solution: 10 mM HCOOH/DCOOH + 0.5 M $HClO_4$. Flow rate: 3 mL min^{-1}. A: Cyclic voltammetry in HCOOH (red) or DCOOH (black). Scan rate: 10 mV s^{-1}. B: Kinetic isotope effect, defined as i_H/i_D, calculated from the cyclic voltammetry in A (line) and separately from the steady state currents 50 s after stepping up then down to 0.4 V, 0.6 V, 0.8 V, 1.0 V and 1.2 V (points). Note KIE from CV not calculated as current approaches zero on the negative going sweep. C: Spectra obtained over the 50 s steady state measurements. Upper spectrum in pair corresponds to HCOOH, lower spectrum to DCOOH. Background: 1.2 V in respective solution.

bond not the C−H bond that is broken on adsorption. However, a subsequent oxidation step would involve breaking the H−COO bond and would therefore give rise to a KIE (eq. (5.36)). The slower oxidation of DCOO(ad) would lead to it accumulating to a greater extent than HCOO(ad) and would explain its increased intensity in the spectra. It is suggested therefore that the HCOO pathway is operational to some degree over the potential range 0.4 V to 0.8 V.

$$\mathrm{HCOOH} \rightleftharpoons \mathrm{HCOO(ad)} + \mathrm{H^+} + \mathrm{e^-} \xrightarrow{KIE} \mathrm{CO_2} + \mathrm{H^+} + \mathrm{e^-} \tag{5.36}$$

At 1.0 V the KIE is at a maximum, both at steady state and on the negative-going sweep of the cyclic voltammogram, yet spectroscopy reveals very little difference between the coverage of HCOO and DCOO. This suggests that the rates of adsorption, desorption and oxidation of HCOO are similar to that for DCOO and therefore cannot explain the large value of the KIE. Furthermore, no CO is observed at this potential, confirming that this pathway is not operational at high potential. A third pathway is therefore required to account for the KIE.

5.3.9 The Effect of Supporting Electrolyte

The use of supporting electrolyte is crucial to ensure the conductivity of an electrolyte solution will not contribute to the potential-dependence of the current. However, the additional ions added to the solution may compete for surface sites, influencing the reaction of interest. For example, in H_2SO_4 solution SO_4^{2-}/HSO_4^- ions have been shown to cover up to 33% of the Pt(111) surface. [103, 106] To understand these effects a reaction is often examined in two or more electrolytes with different adsorption properties. [107] The weakly coordinating anion ClO_4^- used so far will therefore be compared with the more strongly-coordinating ion SO_4^{2-}. Cyclic voltammetry was carried out in 0.5 M H_2SO_4 and

$HClO_4$ supporting electrolyte solutions with 10 mM HCOOH (fig. 5.31A). The difference between the currents in $HClO_4$ and H_2SO_4 is shown as a percentage difference in fig. 5.31B.

Below 0.5 V the current is almost identical in the two solutions. It is tempting to suggest this means SO_4^{2-} is not adsorbed in the potential range, however this is not the case as reported previously for Pt, [103] and as shown by the presence of a peak assigned to SO_4^{2-} in the spectra shown in fig. 5.29. It seems counter-intuitive that a surface which has up to 33% fewer available sites is able to support the same rate of reaction as a surface with (nominally) 100% of its surface available. This suggests that while physically blocking some sites, adsorbed (bi)sulfate is actually able to promote the reaction such that the promoted rate on 66% of the sites can match the un-promoted rate on 100% of the sites. Such an effect has been demonstrated experimentally by Perales-Róndon *et al.*, who measured a decreased activation energy for formic acid oxidation on Pt(111) in the presence of SO_4, especially in the region 0.4 V to 0.65 V. [75]

Above 0.5 V the current becomes up to 80% larger in $HClO_4$ than in H_2SO_4, the increase occuring in two steps: an increase to 15% higher current around 0.65 V, and a further increase to 60% higher currents around 1.0 V. These two increases loosely map onto the two peaks observed in the positive-going scan in the cyclic voltammogram. This emergence of an apparent anion effect after 0.5 V must either correspond to a change in SO_4 adlayer structure, or a change in mechanism, or both.

The SO_4 adlayer is known to undergo a disorder-order transition at 0.45 V. [103] The more ordered adlayer may prove harder to disrupt, leading to a sudden increase in the difference between the anions. Another explanation may be found in the increasing instability of the CO adlayer at above 0.6 V (the peak potential in the CO stripping voltammogram, fig. 5.20). While the oxidation reaction itself is unlikely to be influenced by SO_4, since CO is more strongly adsorbed, the oxidation of CO will lead to the formation of vacant surface sites and a sudden increase in catalytic current. In $HClO_4$ these sites will become

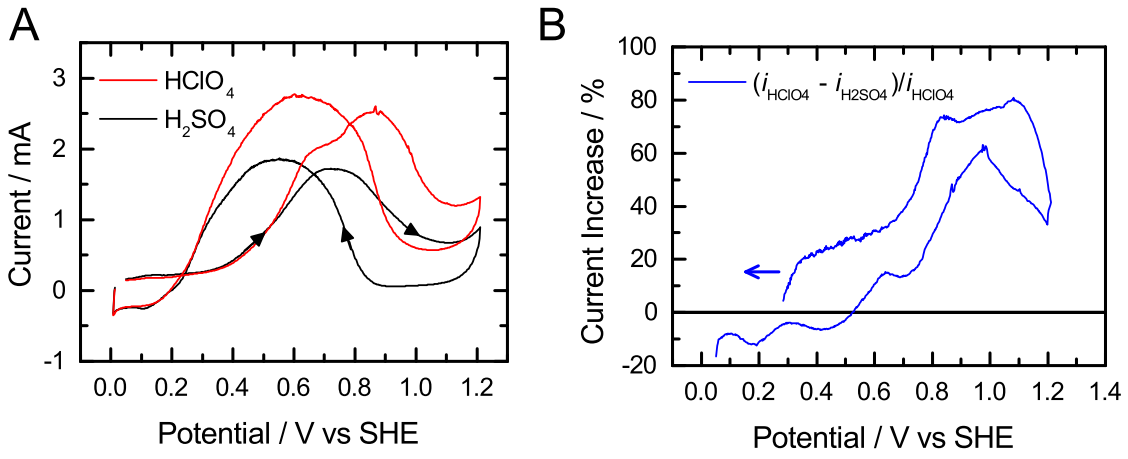

Figure 5.31: The effect of anion on formic acid oxidation current. A: Comparison between oxidation of 10 mM HCOOH in 0.5 M $HClO_4$ and H_2SO_4 electrolytes. Flow rate 3.2 mL min^{-1} B: The difference in current between $HClO_4$ and H_2SO_4.

available for reaction, while in H_2SO_4 HCOOH will have to compete with SO_4^{2-} for these sites, decreasing the effect of this sudden increase in catalytic sites. This latter explanation could be used to describe the difference in currents around the first peak.

5.3.10 The Effect of pH

The effect of pH on the reaction at Pt/C was investigated following the procedure of Joo *et al.* using phosphate-buffered solutions of 10 mM NaOOCH with pH values from 1.5 to 10.5. [71, 72] Cyclic voltammograms were recorded at each pH while simultaneously recording IR spectra (fig. 5.32). Under these conditions the potentiostat struggled to apply the desired potential, with oscillations often observed. It is suggested that the lower ionic strength of the buffer solutions (0.2 M) compared to the acid solutions (0.5 M) led to excessive resistance through the cell, the uncompensated part of which led to the instability of the potentiostat. This is supported by the sharp current spike seen on the return (negative-going) sweep of all of the voltammograms in fig. 5.32, a feature of uncompensated resistance (section 5.2.2.3). Nevertheless, it was possible to record complete voltammograms for each pH and it can be seen that the peak current occurs

between pH 3.5 and pH 4.5 (fig. 5.33), in good agreement with reports by Joo *et al.* [71] and in contrast the pH dependence described by Brimaud *et al.* [56] A discussion of the differences between the two reports was made in the literature review, where it was suggested that the superior buffering ability of the phosphate system used in Joo's work may account for the discrepancies. The significance of the pH optimum is that it lies around the value of the pKa for HCOOH (3.75), suggesting that both HCOOH and $HCOO^-$ species are required for maximum activity.

The presence of peaks due to formate in solution (table 5.4) complicates analysis of spectra obtained at pH values above 1. Comparison of spectra obtained during cyclic voltammograms at pH 2.5, 5.5 and 10.5 (fig. 5.34) suggests that less, if any, formate is adsorbed at higher pH values, although the peak is too small to quantify reliably. The change in HCOO adsorption at different pH values can still be discussed qualitatively, however. The formation of HCOO is likely to be an oxidative process, with deprotonation occurring with loss of an electron (proton-coupled electron transfer). One effect of an increasing pH is to decrease the onset potential for surface oxide formation. This downward shift in the potential of the double layer region, in which HCOO adsorption occurs, leads to a diminished driving force for adsorption and therefore a lower coverage. An alternative explanation for the decrease HCOO coverage at high pH is that HCOO only forms from HCOOH deprotonation, direct adsorption of $HCOO^-$ is not favoured. As the pH increases the concentration of HCOOH decreases and the equilibrium coverage of HCOO also decreases.

In contrast to HCOO, CO was observed in spectra at all pH values. Representative spectra at pH 1.5 and 10.5 are shown in fig. 5.35. The magnitude of the CO peak was sufficient to allow fitting and the resulting fitted CO oscillator strengths are shown for all of the pH values in panels C and D. The behaviour of CO is perhaps most interesting in the positive-going scan (fig. 5.35C). It can be seen that the potential window for CO

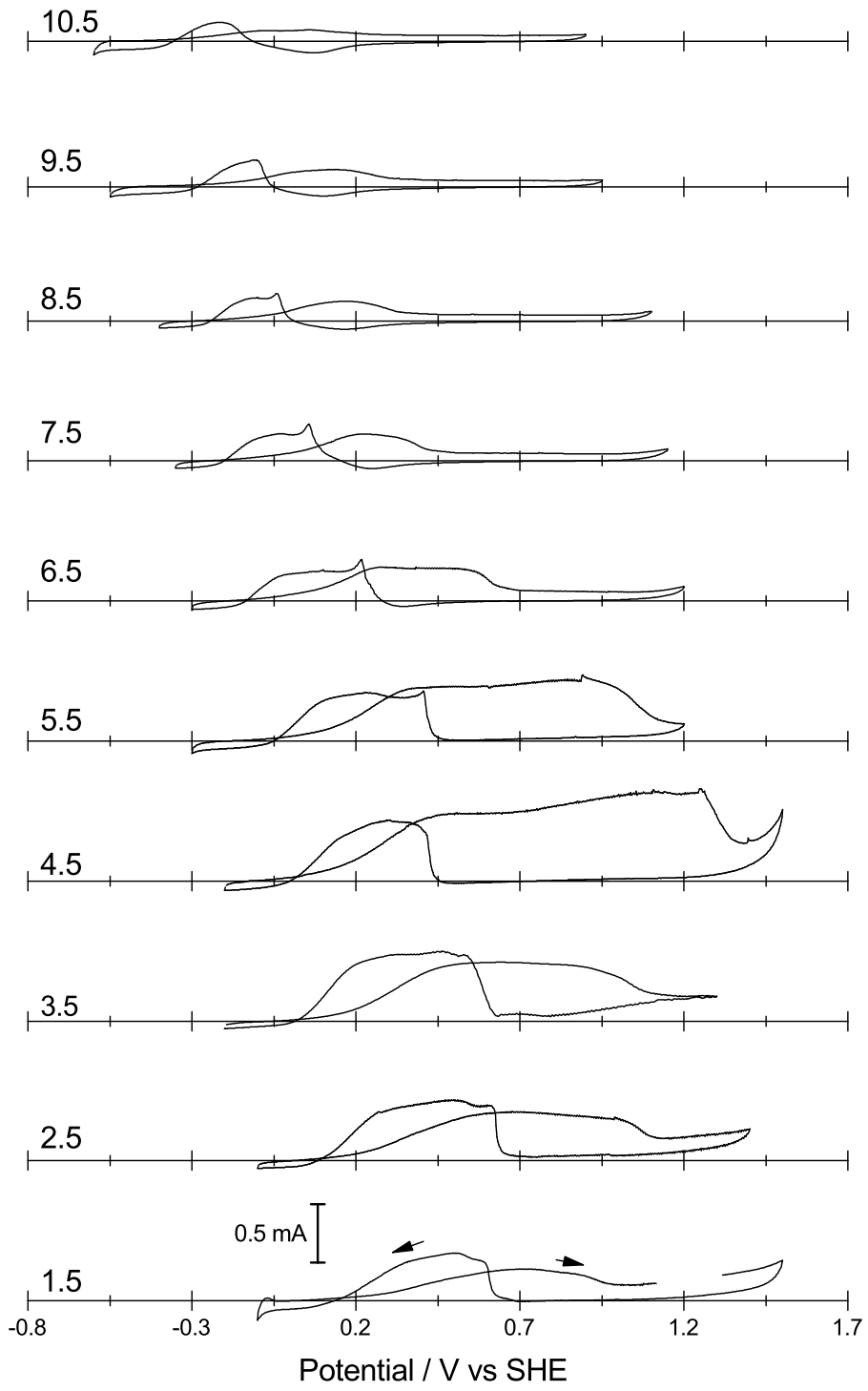

Figure 5.32: Cyclic voltammetry in NaOOCH solutions of different pH. Voltammograms obtained in 10 mM NaOOCH + 0.2 M $H_3PO_4/NaH_2PO_4/Na_2HPO_4$ solutions at pH values from 1.5 to 10.5. Scan rate: 10 mV s^{-1}. The potential window was first determined from the voltammogram in phosphate solution alone (not shown), before NaOOCH solution was added. x-axis represents zero current. Arrows indicate direction of scan.

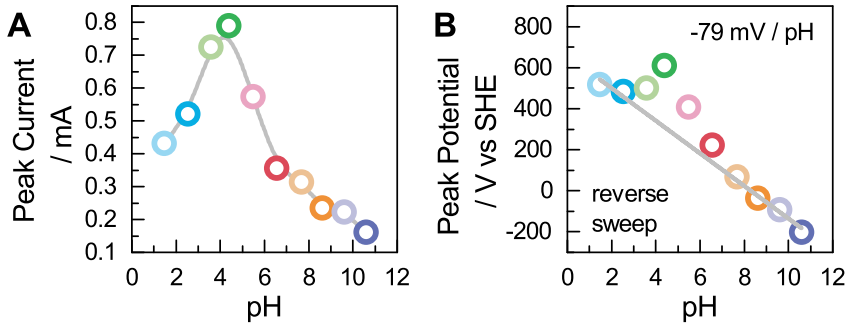

Figure 5.33: Analysis of cyclic voltammetry in NaOOCH solutions of different pH. B: Peak current obtained from voltammograms at each pH. Curve is a guide only. C: Potential of peak current at each pH. Line is a linear fit to data excluding points at pH 3.5, 4.5 and 5.5. The slope is shown on the figure.

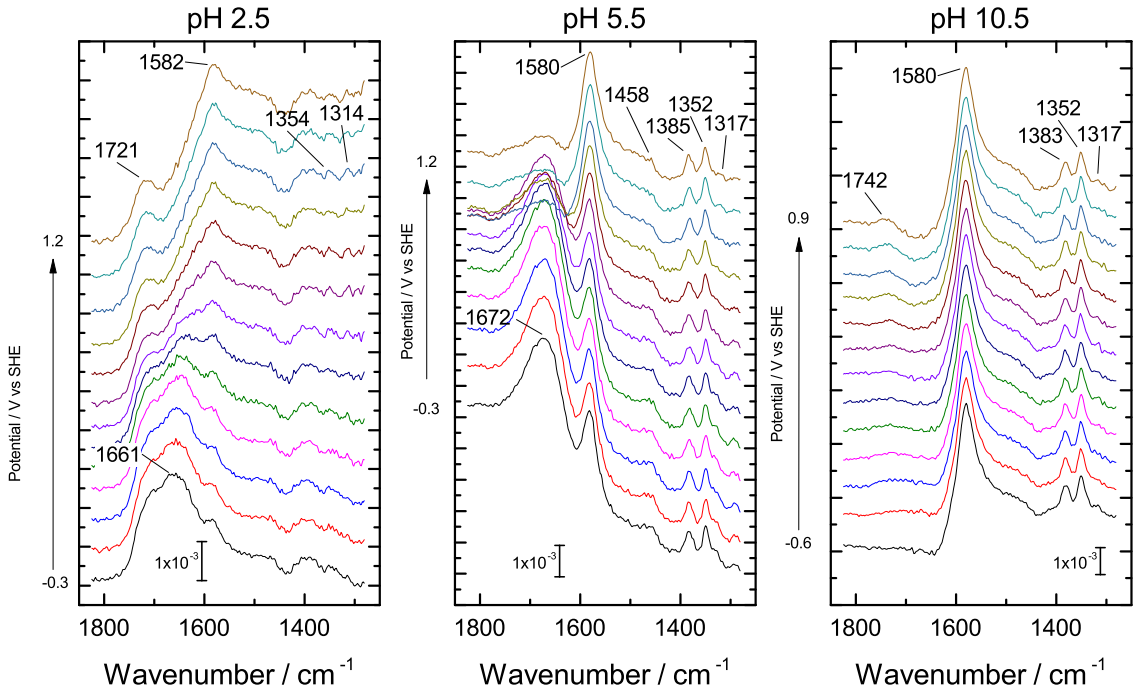

Figure 5.34: Spectra obtained during cyclic voltammograms in NaOOCH at pH 2.5, 5.5 and 10.5. Solution: 10 mM NaOOCH + 0.2 M $H_3PO_4/NaH_2PO_4/Na_2HPO_4$. Background: initial potential in buffer alone.

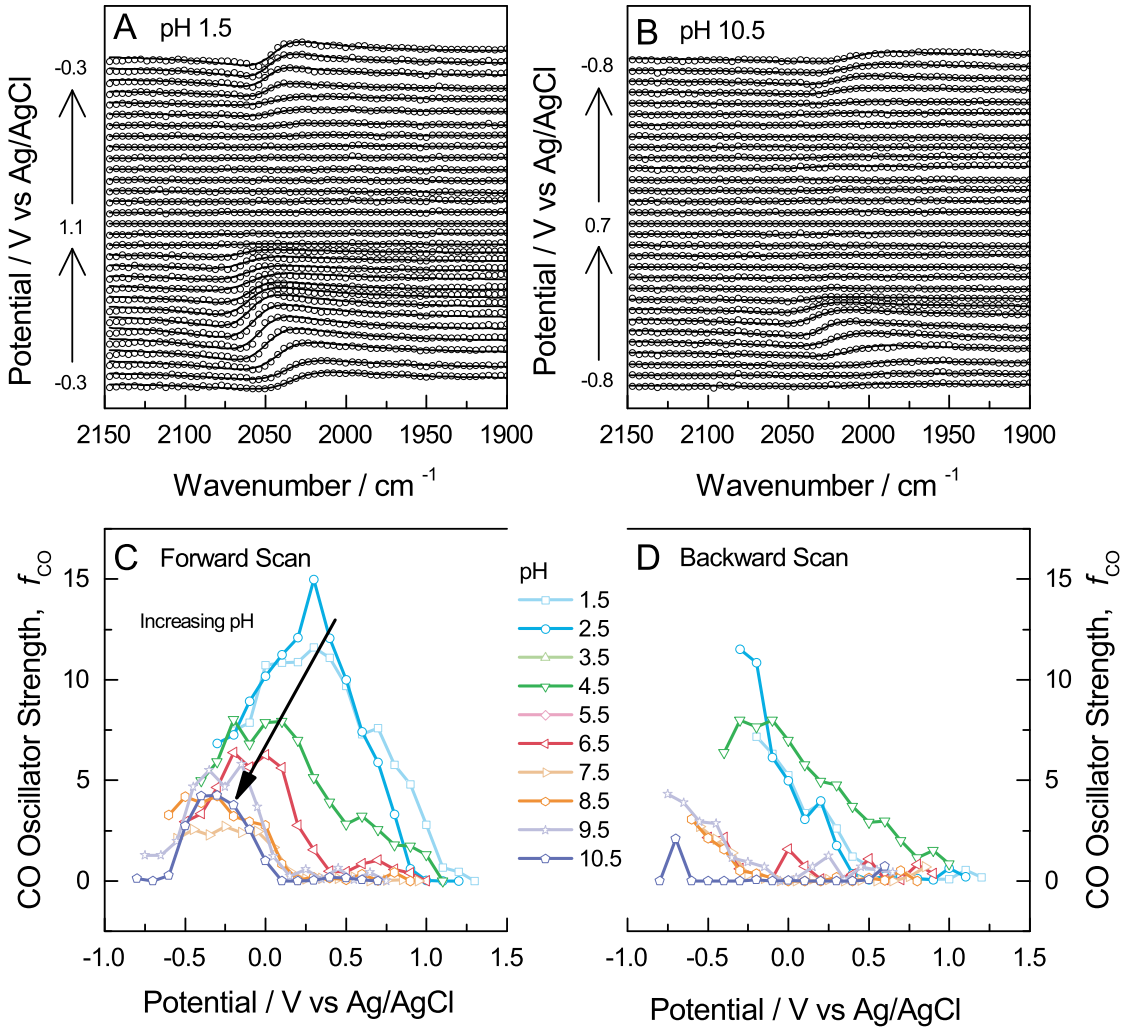

Figure 5.35: Analysis of the CO IR peak observed during the voltammograms shown in fig. 5.32. A, B: Representative spectra obtained at pH 1.5 and pH 10.5, respectively, along with peak fits. C, D The CO oscillator strengths in the postive-(C) and negative-going (D) scans, obtained by fitting the CO peak in spectra at each pH. The pH of each trace is shown in the legend.

existence decreases and shifts to more negative potentials as the pH increases. This can be explained as above, by the fact that the double layer region both decreases in width and shifts to more negative potentials with increasing pH. Since the rate of CO oxidation is determined by the availability of surface OH, [108] as provided by the oxidation of the surface occurring just after the double layer region ends, the double layer window determines the stability window of CO on the surface.

Significantly, the intensity of the CO band also decreases with pH. This can be explained by considering that CO is only formed from either HCOOH or HCOO(ad), the concentration/coverage of both decreasing at high pH. In this theory the presence of detectable amounts of CO despite the very low levels of HCOOH at pH 10.5 is rationalised by considering that CO formation is irreversible - with no pathway for loss at these potentials the CO can just accumulate, as shown from CO dose-strip experiments using µM CO concentrations. [109]

5.3.11 The Mechanism of Oxidation on Supported Pt Nanoparticles

The reactions likely to be occurring at different potentials during formic acid oxidation on Pt nanoparticles can be discussed by comparison of the observations made above with those reported in the literature. Three potential regions are discussed: 0.0 V to 0.4 V, 0.4 V to 0.7 V and 0.7 V to 1.2 V. The various pathways are shown in fig. 5.36, adapted from reference [71].

5.3.11.1 0.0 V to 0.4 V

It is inferred from the selective inhibition of H adsorption on edge sites and the low wavenumber of CO(ad), that CO formed via HCOOH dehydration at low potential only occupies edge sites. It is also observed that CO oxidation proceeds at negligible rates at low potentials, as measured directly in potential step experiments and further corroborated

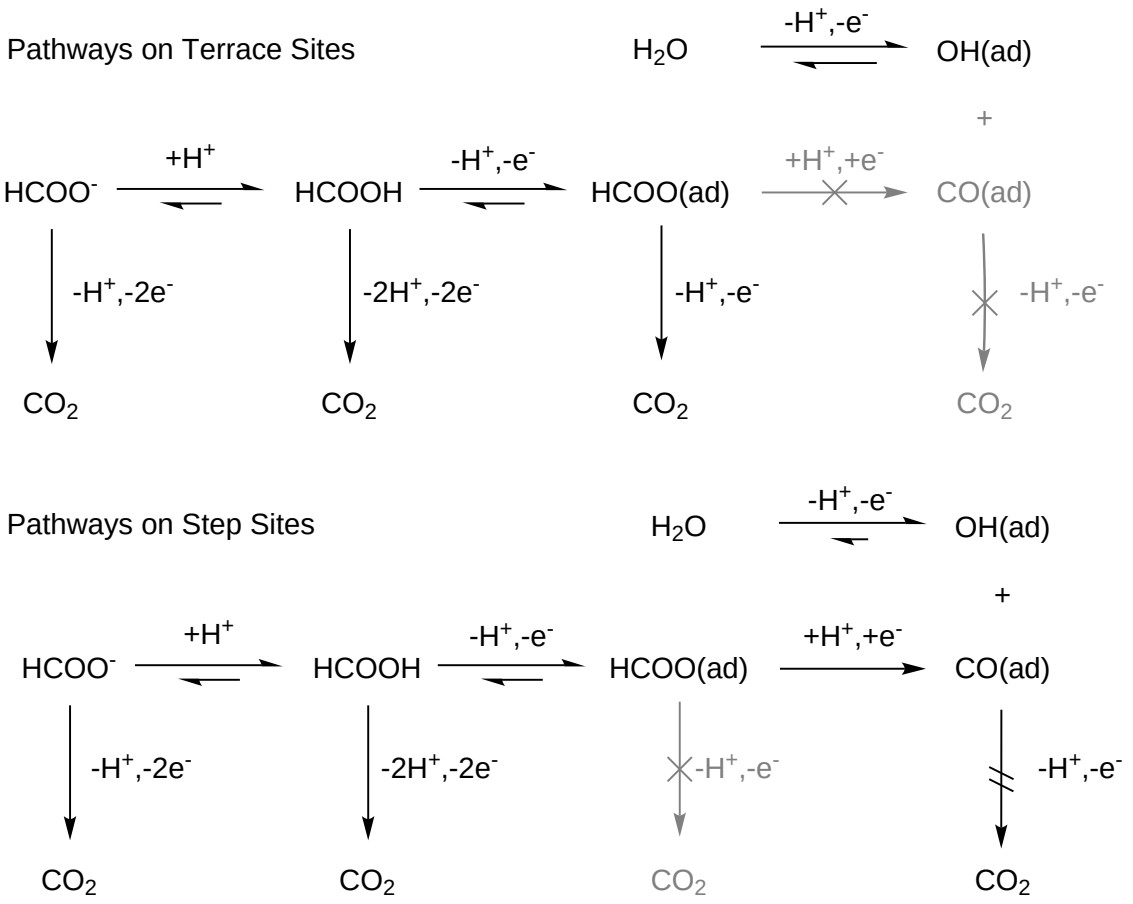

Figure 5.36: Mechanisms postulated to occur during formic acid oxidation at terrace and step sites. Pathways in light grey with a cross through them are not thought to operate. Pathways with a double bar are too slow to be catalytic. Modified from the table of contents figure in reference [71].

by the stability of the CO adlayer in stripping experiments. As a result, throughout this region very little CO oxidation occurs and step sites remain blocked, implying that any observed current must arise from a non-CO pathway occurring predominantly on terrace sites.

At these potentials neither HCOO(ad) nor DCOO(ad) is observed, suggesting that this species cannot be responsible for any significant current. This means a third pathway must be in operation to provide the observed current, and since no further intermediates are observed, it is likely to arise from direct reaction of a solution species with the surface. The increasing current with pH from 1.5 to 4.5 in this region suggests that it is $HCOO^{-}$(aq)

as opposed to HCOOH(aq) that is reacting.

The observation that there is no difference in current between H_2SO_4 and $HClO_4$ in this potential region, despite the presence of adsorbed (bi)sulfate which will decrease the number of surface sites, suggests that adsorbed (bi)sulfate acts to promote the reaction, the promoted rate compensating for the decrease in free surface sites, as suggested by Perales-Rondón *et al.* [75]

In the range 0.0 V to 0.4 V the electrooxidation of formic acid on Pt/C is therefore considered to proceed via direct oxidation of $HCOO^-$(aq) at terrace sites, promoted by the presence of adsorbed (bi)sulfate.

5.3.11.2 0.4 V to 0.7 V

At higher potentials, between 0.4 V and 0.7 V, the increase in DCOO(ad) coverage over HCOO(ad) coverage suggests a kinetic isotope effect is present, and therefore that HCOO(ad) oxidation is occurring. The difference in coverage is greatest at 0.6 V, after which it decreases, suggesting this pathway increases and then decreases in importance, possibly poisoning itself as suggested by Samjeské *et al.* [63] This is supported by the change in proportionality between the rate of HCOO(ad) formation and the current; at low coverages the current is proportional to the rate of change of HCOO(ad) with time, as the coverage increases the relationship reverses, and the current continues to increase as the rate of change of HCOO(ad) decreases.

The hypothesis that the HCOO(ad) pathway is in operation is supported by the increase in the current-dependence on the anion, with the current in H_2SO_4 being significantly lower. While adsorbed (bi)sulfate was suggested to promote the direct reaction, it is still likely to inhibit the HCOO(ad) reaction, by decreasing the number of adjacent vacant sites for C−H bond activation.

In experiments where the formic acid concentration is increased, the HCOO(ad) inten-

sity reaches saturation at around 30 mM HCOOH while the current continues to increase. This suggests that a second pathway is also operational in this region, in addition to the formate pathway. The CO peak is observed to decrease in this region, suggesting this reaction could be contributing somewhat to the current, although measurement of the CO oxidation rate put an upper limit of 1% on this contribution. It is therefore the direct reaction which is likely to be contributing the remaining current in this region. While the number of vacant terrace sites at which the direct pathway can proceed are decreased by the coverage of HCOO(ad), there is an increasing number of edge sites available due to the oxidation of CO, providing an explanation for the increasing current at higher potential.

In the region 0.4 V to 0.7 V the current is therefore be ascribed to a combination of the HCOO(ad) pathway, which increases in importance with potential before poisoning itself after around 0.6 V, and the direct pathway, facilitated by the increasing number of vacant edge sites left by CO oxidation.

5.3.11.3 0.7 V to 1.2 V

The region 0.7 V to 1.0 V sees the formation of 2 peaks in the 10 mV s^{-1} voltammogram and an increase in the steady state KIE from 1.2 to 2.8. The increase in KIE suggests a change in the mechanism, or at least in the relative contributions of the contributory pathways, towards one with a more product-like transition state. If the transition state is considered to involve some degree of Pt−H bond formation, at the expense of the H−COOH bond, then it could be suggested that the transition state at edge sites would possess stronger Pt−H bonds than the same transition state at a terrace site, due to the higher energy of the local *d*-band, and therefore give rise to a larger KIE.

It is therefore suggested that the second peak in the voltammogram, and the large peak in the reverse scan, arise from direct reaction at step sites. On account of their higher *d*-band, the step sites are also the first sites to be oxidised to PtO. As a result,

the second rise in current in the voltammogram is short lived as the contribution of steps is diminished by surface oxidation, once again leaving the direct pathway at terraces to provide all of the current. This idea is supported by the overlap between the first oxide formation peak in the blank voltammogram with the second formic acid oxidation peak, and the fact that HCOO(ad) is observed on the (terrace) surface well after the current has started to decrease. In addition, the fact that the order of reaction with respect to HCOOH concentration remains very close to 1 at 1.0 V, not becoming fractional despite the slight increase in (step) CO with concentration suggests that the reaction is not affected by the number of vacant step sites, implying the reaction is not proceeding at them.

5.4 Conclusions

The presence of HCOO(ad) during formic acid oxidation at a commercial fuel cell catalyst has been confirmed for the first time. Along with adsorbed CO, these species represent the only intermediates detected under both potential sweep and steady state conditions.

Furthermore, in addition to the previously reported symmetric OCO vibration of HCOO(ad), a second vibration assigned to HCOO(ad) is observed. Consideration of its wavenumber led to its tentative assignment to the C−H wagging mode. The C−H bond is the final bond broken before CO_2 formation from HCOO(ad), making such a spectroscopic probe particularly relevant. The observation that the wavenumber of this mode is identical to that in $HCOO^-$(aq) suggest that there is no activation of the C−H bond on adsorption, and therefore that oxidation via this pathway is not particularly favourable.

Consideration of the wavenumber of the HCOO(ad) and CO(ad) species has enabled tentative assignment to specific adsorption sites, that is terrace or edge sites. A combination of potential sweep, potential step, kinetic isotope, pH, supporting electrolyte and reaction order experiments were carried out with simultaneous electrochemical and IR spectroscopic measurement. The data support the idea of a third 'direct' pathway oper-

ating via the $HCOO^-$ anion, on which both HCOO(ad) and adsorbed (bi)sulfate have a promotional effect. While this pathway may be responsible for the majority of the current, the contribution of the other two pathways, proceeding via CO(ad) and HCOO(ad) species, respectively, cannot be dismissed entirely.

These conclusions are based on observation of supported Pt nanoparticles only; where comparisons to other Pt electrodes have been made in the discussion it has become clear that both similarities and differences exist between the surfaces. In particular it was observed that the potential dependence of HCOO(ad) on Pt/C tracked almost exactly the dependence at a thin ATR-SEIRA electrode, while the dependence of CO(ad) varied dramatically. This difference in behaviour highlights the need to characterise real catalysts, as well as model systems, in order to understand the reactions occurring at the surface.

Outside the context of formic acid oxidation, the observation of an IR peak tentatively assigned to the C−H wagging mode of HCOO(ad) represents the first such report on any metal surface under any conditions. The explanation for its absence in all previously reported spectra is that its dipole moment is perfectly parallel to the surface, such that its excitation is forbidden by the surface selection rule. It is suggested that in the present case, the small size of the nanoparticles used in this work leads to a weakening of the selection rule, as predicted by Greenler. [93] While further work is suggested to confirm this assignment, if true it could be highly significant, not just in terms of studies of formic acid oxidation, but for many other studies in which intermediates are postulated but not observed, based on the surface selection rule.

The ability to replicate many of the experiments devised for model electrocatalysts on real, supported nanoparticle catalysts should advance the understanding of reactions at such catalysts, in particular the effects of nanoparticle shape, size and composition, which in turn should feed back into the rational design of novel catalysts.

References

[1] C. Rice, S. Ha, R. I. Masel, P. Waszczuk, A. Wieckowski, and T. Barnard, "Direct formic acid fuel cells," *Journal of Power Sources*, vol. 111, no. 1, pp. 83–89, 2002.

[2] C. Rice, S. Ha, R. I. Masel, and A. Wieckowski, "Catalysts for direct formic acid fuel cells," *Journal of Power Sources*, vol. 115, no. 2, pp. 229–235, 2003.

[3] X. Yu and P. G. Pickup, "Recent advances in direct formic acid fuel cells (DFAFC)," *Journal of Power Sources*, vol. 182, no. 1, pp. 124–132, 2008.

[4] C. A. Rice and A. Wieckowski, "Electrocatalysis of Formic Acid Oxidation," in *Electrocatalysis in Fuel Cells* (M. Shao, ed.), no. 9 in Lecture Notes in Energy, pp. 43–67, Springer London, 2013.

[5] C. A. Rice, A. Bauskar, and P. G. Pickup, "Recent Advances in Electrocatalysis of Formic Acid Oxidation," in *Electrocatalysis in Fuel Cells* (M. Shao, ed.), no. 9 in Lecture Notes in Energy, pp. 69–87, Springer London, 2013.

[6] N. V. Rees and R. G. Compton, "Sustainable energy: a review of formic acid electrochemical fuel cells," *Journal of Solid State Electrochemistry*, vol. 15, no. 10, pp. 2095–2100, 2011.

[7] H. Jeon, B. Jeong, J. Joo, and J. Lee, "Electrocatalytic Oxidation of Formic Acid: Closing the Gap Between Fundamental Study and Technical Applications," *Electrocatalysis*, vol. 6, no. 1, pp. 20–32, 2014.

[8] I. M. Al-Akraa, A. M. Mohammad, S. Mohamed, and E. Bahgat, "Advances in Direct Formic Acid Fuel Cells: Fabrication of Efficient Ir/Pd Nanocatalysts for Formic Acid Electro-Oxidation," *Int. J. Electrochem. Sci*, vol. 10, pp. 3282–3290, 2015.

[9] A. Capon and R. Parson, "The oxidation of formic acid at noble metal electrodes: I. Review of previous work," *Journal of Electroanalytical Chemistry and Interfacial Electrochemistry*, vol. 44, no. 1, pp. 1–7, 1973.

[10] A. Capon and R. Parsons, "The oxidation of formic acid on noble metal electrodes: II. A comparison of the behaviour of pure electrodes," *Journal of Electroanalytical Chemistry and Interfacial Electrochemistry*, vol. 44, no. 2, pp. 239–254, 1973.

[11] A. Capon and R. Parsons, "The oxidation of formic acid at noble metal electrodes Part III. Intermediates and mechanism on platinum electrodes," *Journal of Electroanalytical Chemistry and Interfacial Electrochemistry*, vol. 45, no. 2, pp. 205–231, 1973.

[12] A. Capon and R. Parsons, "The oxidation of formic acid at noble metal electrodes: IV Platinum + palladium alloys," *Journal of Electroanalytical Chemistry and Interfacial Electrochemistry*, vol. 65, no. 1, pp. 285–305, 1975.

[13] R. Parsons and T. VanderNoot, "The oxidation of small organic molecules: A survey of recent fuel cell related research," *Journal of Electroanalytical Chemistry*, vol. 257, no. 1-2, pp. 9–45, 1988.

[14] K. Jiang, H.-X. Zhang, S. Zou, and W.-B. Cai, "Electrocatalysis of formic acid on palladium and platinum surfaces: from fundamental mechanisms to fuel cell applications," *Physical Chemistry Chemical Physics*, vol. 16, no. 38, pp. 20360–20376, 2014.

[15] J. K. Sass, D. Lackey, and J. Schott, "Electrochemical hydration and reaction processes on metal surfaces studied by gas phase adsorption," *Electrochimica Acta*, vol. 36, no. 11–12, pp. 1883–1887, 1991.

[16] E. M. Stuve and N. Kizhakevariam, "Chemistry and physics of the "liquid"/solid interface: A surface science perspective," *Journal of Vacuum Science & Technology A*, vol. 11, no. 4, pp. 2217–2224, 1993.

[17] T. D. Jarvi and E. M. Stuve, "Fundamental aspects of vacuum and electrocatalytic reactions of methanol and formic acid on platinum surfaces," in *Electrocatalysis*, vol. Lipkowski, Jacek; Ross Philip N. (eds.) of *Frontiers of electrochemistry*, pp. 75–153, New York ; Chichester: Wiley-VCH, 1998.

[18] P. Hofmann, S. R. Bare, N. V. Richardson, and D. A. King, "Orientation of chemisorbed species from electron impact and dipole selection rules: The formate ion on Pt{110}," *Surface Science*, vol. 133, no. 1, pp. L459–L464, 1983.

[19] M. R. Columbia and P. A. Thiel, "The interaction of formic acid with transition metal surfaces, studied in ultrahigh vacuum," *Journal of Electroanalytical Chemistry*, vol. 369, no. 1–2, pp. 1–14, 1994.

[20] N. R. Avery, "Reaction of HCOOH with a Pt(111)-O surface; identification of adsorbed monodentate formate," *Applications of Surface Science*, vol. 14, no. 2, pp. 149–156, 1983.

[21] N. R. Avery, "Adsorption of formic acid on clean and oxygen covered Pt(111)," *Applications of Surface Science*, vol. 11–12, pp. 774–783, 1982.

[22] J. L. Falconer and R. J. Madix, "The desorption kinetics of water and formic acid from Ni(110) following low-temperature adsorption," *Journal of Catalysis*, vol. 51, no. 1, pp. 47–63, 1978.

[23] Y.-K. Sun and W. H. Weinberg, "Catalytic decomposition of formic acid on Ru(001): Transient measurements," *The Journal of Chemical Physics*, vol. 94, no. 6, pp. 4587–4599, 1991.

[24] J. McCarty, J. Falconer, and R. J. Madix, "Decomposition of formic acid on Ni(110): I. Flash decomposition from the clean surface and flash desorption of reaction products," *Journal of Catalysis*, vol. 30, no. 2, pp. 235–249, 1973.

[25] E. Müller, "Die elektrolytische Oxydation der Ameisensäure," *Zeitschrift für Elektrochemie und angewandte physikalische Chemie*, vol. 29, no. 11-12, pp. 264–274, 1923.

[26] S. B. Brummer and A. C. Makrides, "Adsorption and Oxidation of Formic Acid on Smooth Platinum Electrodes in Perchloric Acid Solutions," *The Journal of Physical Chemistry*, vol. 68, no. 6, pp. 1448–1459, 1964.

[27] S. G. Sun, J. Clavilier, and A. Bewick, "The mechanism of electrocatalytic oxidation of formic acid on Pt (100) and Pt (111) in sulphuric acid solution: an emirs study," *Journal of electroanalytical chemistry and interfacial electrochemistry*, vol. 240, no. 1, pp. 147–159, 1988.

[28] J. Clavilier, R. Parsons, R. Durand, C. Lamy, and J. M. Leger, "Formic acid oxidation on single crystal platinum electrodes. Comparison with polycrystalline platinum," *Journal of Electroanalytical Chemistry and Interfacial Electrochemistry*, vol. 124, no. 1–2, pp. 321–326, 1981.

[29] A. Bewick and S. Pons, "Advances in infrared and raman spectroscopy.," vol. 12 of *Advances in infrared and Raman spectroscopy.*, pp. 1–63, London: Wiley and Heyden, 1985.

[30] V. Climent and J. M. Feliu, "Thirty years of platinum single crystal electrochemistry," *Journal of Solid State Electrochemistry*, vol. 15, no. 7-8, pp. 1297–1315, 2011.

[31] R. R. Adžić, A. V. Tripković, and W. E. O'Grady, "Structural effects in electrocatalysis," *Nature*, vol. 296, no. 5853, pp. 137–138, 1982.

[32] S. Motoo and N. Furuya, "Electrochemistry of platinum single crystal surfaces: Part II. Structural effect on formic acid oxidation and poison formation on Pt (111), (100) and (110)," *Journal of Electroanalytical Chemistry and Interfacial Electrochemistry*, vol. 184, no. 2, pp. 303–316, 1985.

[33] V. Grozovski, V. Climent, E. Herrero, and J. M. Feliu, "Intrinsic activity and poisoning rate for HCOOH oxidation on platinum stepped surfaces," *Physical Chemistry Chemical Physics*, vol. 12, no. 31, pp. 8822–8831, 2010.

[34] V. Grozovski, F. J. Vidal-Iglesias, E. Herrero, and J. M. Feliu, "Adsorption of Formate and Its Role as Intermediate in Formic Acid Oxidation on Platinum Electrodes," *ChemPhysChem*, vol. 12, no. 9, pp. 1641–1644, 2011.

[35] W. Gao, J. A. Keith, J. Anton, and T. Jacob, "Theoretical Elucidation of the Competitive Electro-oxidation Mechanisms of Formic Acid on Pt(111)," *Journal of the American Chemical Society*, vol. 132, no. 51, pp. 18377–18385, 2010.

[36] A. Cuesta, M. Escudero, B. Lanova, and H. Baltruschat, "Cyclic Voltammetry, FTIRS, and DEMS Study of the Electrooxidation of Carbon Monoxide, Formic Acid, and Methanol on Cyanide-Modified Pt(111) Electrodes," *Langmuir*, vol. 25, no. 11, pp. 6500–6507, 2009.

[37] J. Solla-Gullón, F. J. Vidal-Iglesias, A. López-Cudero, E. Garnier, J. M. Feliu, and A. Aldaz, "Shape-dependent electrocatalysis: methanol and formic acid electrooxidation on preferentially oriented Pt nanoparticles," *Physical Chemistry Chemical Physics*, vol. 10, no. 25, pp. 3689–3698, 2008.

[38] V. Grozovski, J. Solla-Gulloń, V. Climent, E. Herrero, and J. M. Feliu, "Formic Acid Oxidation on Shape-Controlled Pt Nanoparticles Studied by Pulsed Voltammetry," *The Journal of Physical Chemistry C*, vol. 114, no. 32, pp. 13802–13812, 2010.

[39] V. Grozovski, V. Climent, E. Herrero, and J. M. Feliu, "Intrinsic Activity and Poisoning Rate for HCOOH Oxidation at Pt(100) and Vicinal Surfaces Containing Monoatomic (111) Steps," *ChemPhysChem*, vol. 10, no. 11, pp. 1922–1926, 2009.

[40] Q.-S. Chen, J. Solla-Gullón, S.-G. Sun, and J. M. Feliu, "The potential of zero total charge of Pt nanoparticles and polycrystalline electrodes with different surface structure: The role of anion adsorption in fundamental electrocatalysis," *Electrochimica Acta*, vol. 55, no. 27, pp. 7982–7994, 2010.

[41] K. J. J. Mayrhofer, B. B. Blizanac, M. Arenz, V. R. Stamenković, P. N. Ross, and N. M. Marković, "The Impact of Geometric and Surface Electronic Properties of Pt-Catalysts on the Particle Size Effect in Electrocatalysis," *The Journal of Physical Chemistry B*, vol. 109, no. 30, pp. 14433–14440, 2005.

[42] B. Beden, A. Bewick, and C. Lamy, "A study by electrochemically modulated infrared reflectance spectroscopy of the electrosorption of formic acid at a platinum electrode," *Journal of Electroanalytical Chemistry and Interfacial Electrochemistry*, vol. 148, no. 1, pp. 147–160, 1983.

[43] B. Beden, A. Bewick, and C. Lamy, "A comparative study of formic acid adsorption on a platinum electrode by both electrochemical and emirs techniques," *Journal of Electroanalytical Chemistry and Interfacial Electrochemistry*, vol. 150, no. 1, pp. 505–511, 1983.

[44] S. C. Chang, L. W. H. Leung, and M. J. Weaver, "Metal crystallinity effects in electrocatalysis as probed by real-time FTIR spectroscopy: electrooxidation of formic acid, methanol, and ethanol on ordered low-index platinum surfaces," *The Journal of Physical Chemistry*, vol. 94, no. 15, pp. 6013–6021, 1990.

[45] S.-C. Chang, Y. Ho, and M. J. Weaver, "Applications of real-time infrared spectroscopy to electrocatalysis at bimetallic surfaces: I. Electrooxidation of formic acid and methanol on bismuth-modified Pt(111) and Pt(100)," *Surface Science*, vol. 265, no. 1–3, pp. 81–94, 1992.

[46] M. Arenz, V. Stamenković, T. J. Schmidt, K. Wandelt, P. N. Ross, and N. M. Marković, "The electro-oxidation of formic acid on Pt–Pd single crystal bimetallic surfaces," *Physical Chemistry Chemical Physics*, vol. 5, no. 19, pp. 4242–4251, 2003.

[47] S. Brimaud, Z. Jusys, and R. J. Behm, "Shape-selected nanocrystals for in situ spectro-electrochemistry studies on structurally well defined surfaces under controlled electrolyte transport: A combined in situ ATR-FTIR/online DEMS investigation of CO electrooxidation on Pt," *Beilstein Journal of Nanotechnology*, vol. 5, pp. 735–746, 2014.

[48] O. Wolter, J. Willsau, and J. Heitbaum, "Reaction Pathways of the Anodic Oxidation of Formic Acid on Pt Evidenced by 18O Labeling—A DEMS Study," *Journal of The Electrochemical Society*, vol. 132, no. 7, pp. 1635–1638, 1985.

[49] J. Willsau and J. Heitbaum, "Analysis of adsorbed intermediates and determination of surface potential shifts by dems," *Electrochimica Acta*, vol. 31, no. 8, pp. 943–948, 1986.

[50] Y. X. Chen, S. Ye, M. Heinen, Z. Jusys, M. Osawa, and R. J. Behm, "Application of In-situ Attenuated Total Reflection-Fourier Transform Infrared Spectroscopy for

the Understanding of Complex Reaction Mechanism and Kinetics: Formic Acid Oxidation on a Pt Film Electrode at Elevated Temperatures," *The Journal of Physical Chemistry B*, vol. 110, no. 19, pp. 9534–9544, 2006.

[51] A. Cuesta, G. Cabello, C. Gutiérrez, and M. Osawa, "Adsorbed formate: the key intermediate in the oxidation of formic acid on platinum electrodes," *Physical Chemistry Chemical Physics*, vol. 13, no. 45, p. 20091, 2011.

[52] Y. X. Chen, M. Heinen, Z. Jusys, and R. J. Behm, "Kinetics and Mechanism of the Electrooxidation of Formic Acid—Spectroelectrochemical Studies in a Flow Cell," *Angewandte Chemie International Edition*, vol. 45, no. 6, pp. 981–985, 2006.

[53] A. Miki, S. Ye, and M. Osawa, "Surface-enhanced IR absorption on platinum nanoparticles: an application to real-time monitoring of electrocatalytic reactions," *Chemical Communications*, no. 14, pp. 1500–1501, 2002.

[54] F. Hahn, B. Beden, and C. Lamy, "In situ infrared reflectance spectroscopic study of the adsorption of formic acid at a rhodium electrode," *Journal of Electroanalytical Chemistry and Interfacial Electrochemistry*, vol. 204, no. 1–2, pp. 315–327, 1986.

[55] R. Gómez and M. J. Weaver, "Electrochemical infrared studies of monocrystalline iridium surfaces Part I: Electrooxidation of formic acid and methanol," *Journal of Electroanalytical Chemistry*, vol. 435, no. 1–2, pp. 205–215, 1997.

[56] S. Brimaud, J. Solla-Gullón, I. Weber, J. M. Feliu, and R. J. Behm, "Formic Acid Electrooxidation on Noble-Metal Electrodes: Role and Mechanistic Implications of pH, Surface Structure, and Anion Adsorption," *ChemElectroChem*, vol. 1, no. 6, pp. 1075–1083, 2014.

[57] H. Okamoto, Y. Numata, T. Gojuki, and Y. Mukouyama, "Different behavior of adsorbed bridge-bonded formate from that of current in the oxidation of formic acid on platinum," *Electrochimica Acta*, vol. 116, pp. 263–270, 2014.

[58] G. L. Beltramo, T. E. Shubina, and M. T. M. Koper, "Oxidation of Formic Acid and Carbon Monoxide on Gold Electrodes Studied by Surface-Enhanced Raman Spectroscopy and DFT," *ChemPhysChem*, vol. 6, no. 12, pp. 2597–2606, 2005.

[59] B. Braunschweig and A. Wieckowski, "Surface spectroscopy of Pt(1 1 1) single-crystal electrolyte interfaces with broadband sum-frequency generation," *Journal of Electroanalytical Chemistry*, vol. 716, pp. 136–144, 2014.

[60] X. Xia, T. Iwasita, and W. Vielstich, "Study of the Nature of Formic Acid Adsorbates on Rough Pt and its Interaction with CO," *Dianhuaxue (Electrochemistry)*, vol. 3, no. 1, pp. 26–39, 1997.

[61] J. A. Herron, J. Scaranto, P. Ferrin, S. Li, and M. Mavrikakis, "Trends in Formic Acid Decomposition on Model Transition Metal Surfaces: A Density Functional Theory study," *ACS Catalysis*, vol. 4, no. 12, pp. 4434–4445, 2014.

[62] Y.-X. Chen, M. Heinen, Z. Jusys, and R. J. Behm, "Bridge-Bonded Formate: Active Intermediate or Spectator Species in Formic Acid Oxidation on a Pt Film Electrode?†," *Langmuir*, vol. 22, no. 25, pp. 10399–10408, 2006.

[63] G. Samjeské, A. Miki, S. Ye, A. Yamakata, Y. Mukouyama, H. Okamoto, and M. Osawa, "Potential Oscillations in Galvanostatic Electrooxidation of Formic Acid on Platinum: A Time-Resolved Surface-Enhanced Infrared Study," *The Journal of Physical Chemistry B*, vol. 109, no. 49, pp. 23509–23516, 2005.

[64] P. Strasser, J. Christoph, W.-F. Lin, M. Eiswirth, and J. L. Hudson, "Standing Wave Oscillations in an Electrocatalytic Reaction," *The Journal of Physical Chemistry A*, vol. 104, no. 9, pp. 1854–1860, 2000.

[65] M. T. M. Koper, T. J. Schmidt, N. M. Marković, and P. N. Ross, "Potential Oscillations and S-Shaped Polarization Curve in the Continuous Electro-oxidation of CO on Platinum Single-crystal Electrodes," *The Journal of Physical Chemistry B*, vol. 105, no. 35, pp. 8381–8386, 2001.

[66] T. J. Schmidt, B. N. Grgur, N. M. Marković, and P. N. Ross Jr, "Oscillatory behavior in the electrochemical oxidation of formic acid on Pt (100): rotation and temperature effects," *Journal of Electroanalytical Chemistry*, vol. 500, no. 1, pp. 36–43, 2001.

[67] G. Samjeské and M. Osawa, "Current Oscillations during Formic Acid Oxidation on a Pt Electrode: Insight into the Mechanism by Time-Resolved IR Spectroscopy," *Angewandte Chemie*, vol. 117, no. 35, pp. 5840–5844, 2005.

[68] Y. Mukouyama, M. Kikuchi, G. Samjeské, M. Osawa, and H. Okamoto, "Potential Oscillations in Galvanostatic Electrooxidation of Formic Acid on Platinum: A Mathematical Modeling and Simulation," *The Journal of Physical Chemistry B*, vol. 110, no. 24, pp. 11912–11917, 2006.

[69] D. Mei, Z.-D. He, D. C. Jiang, J. Cai, and Y.-X. Chen, "Modeling of Potential Oscillation during Galvanostatic Electrooxidation of Formic Acid at Platinum Electrode," *The Journal of Physical Chemistry C*, vol. 118, no. 12, pp. 6335–6343, 2014.

[70] J. Xu, D. Yuan, F. Yang, D. Mei, Z. Zhang, and Y.-X. Chen, "On the mechanism of the direct pathway for formic acid oxidation at a Pt(111) electrode," *Physical Chemistry Chemical Physics*, vol. 15, no. 12, pp. 4367–4376, 2013.

[71] J. Joo, T. Uchida, A. Cuesta, M. T. M. Koper, and M. Osawa, "Importance of Acid–Base Equilibrium in Electrocatalytic Oxidation of Formic Acid on Platinum," *Journal of the American Chemical Society*, vol. 135, no. 27, pp. 9991–9994, 2013.

[72] J. Joo, T. Uchida, A. Cuesta, M. T. M. Koper, and M. Osawa, "The effect of pH on the electrocatalytic oxidation of formic acid/formate on platinum: A mechanistic study by surface-enhanced infrared spectroscopy coupled with cyclic voltammetry," *Electrochimica Acta*, vol. 129, pp. 127–136, 2014.

[73] A. Cuesta, G. Cabello, F. W. Hartl, M. Escudero-Escribano, C. Vaz-Domínguez, L. A. Kibler, M. Osawa, and C. Gutiérrez, "Electrooxidation of formic acid on gold: An ATR-SEIRAS study of the role of adsorbed formate," *Catalysis Today*, vol. 202, pp. 79–86, 2013.

[74] W. Gao, E. H. Song, Q. Jiang, and T. Jacob, "Revealing the Active Intermediates in the Oxidation of Formic Acid on Au and Pt(111)," *Chemistry – A European Journal*, vol. 20, no. 35, pp. 11005–11012, 2014.

[75] J. V. Perales-Rondón, E. Herrero, and J. M. Feliu, "Effects of the anion adsorption and pH on the formic acid oxidation reaction on Pt(111) electrodes," *Electrochimica Acta*, vol. 140, pp. 511–517, 2014.

[76] M. Neurock, M. Janik, and A. Wieckowski, "A first principles comparison of the mechanism and site requirements for the electrocatalytic oxidation of methanol and formic acid over Pt," *Faraday Discussions*, vol. 140, no. 0, pp. 363–378, 2008.

[77] H.-F. Wang and Z.-P. Liu, "Formic Acid Oxidation at Pt/H2O Interface from Periodic DFT Calculations Integrated with a Continuum Solvation Model," *The Journal of Physical Chemistry C*, vol. 113, no. 40, pp. 17502–17508, 2009.

[78] W. Gao, J. E. Mueller, Q. Jiang, and T. Jacob, "The Role of Co-Adsorbed CO and OH in the Electrooxidation of Formic Acid on Pt(111)," *Angewandte Chemie International Edition*, vol. 51, no. 37, pp. 9448–9452, 2012.

[79] A. Cuesta, G. Cabello, M. Osawa, and C. Gutiérrez, "Mechanism of the Electrocatalytic Oxidation of Formic Acid on Metals," *ACS Catalysis*, vol. 2, no. 5, pp. 728–738, 2012.

[80] F. Rositani, P. L. Antonucci, M. Minutoli, N. Giordano, and A. Villari, "Infrared analysis of carbon blacks," *Carbon*, vol. 25, no. 3, pp. 325–332, 1987.

[81] H. P. Boehm, "Some aspects of the surface chemistry of carbon blacks and other carbons," *Carbon*, vol. 32, no. 5, pp. 759–769, 1994.

[82] R. L. Redington, "Vibrational spectra and normal coordinate analysis of isotopically labeled formic acid monomers," *Journal of Molecular Spectroscopy*, vol. 65, no. 2, pp. 171–189, 1977.

[83] K. G. Kidd and H. H. Mantsch, "Formate anion: The physical force field," *Journal of Molecular Spectroscopy*, vol. 85, no. 2, pp. 375–389, 1981.

[84] G. Jacobs, P. M. Patterson, L. Williams, E. Chenu, D. Sparks, G. Thomas, and B. H. Davis, "Water-gas shift: in situ spectroscopic studies of noble metal promoted ceria catalysts for CO removal in fuel cell reformers and mechanistic implications," *Applied Catalysis A: General*, vol. 262, no. 2, pp. 177–187, 2004.

[85] G. Jacobs, P. M. Patterson, U. M. Graham, A. C. Crawford, and B. H. Davis, "Low temperature water gas shift: the link between the catalysis of WGS and formic acid decomposition over Pt/ceria," *International Journal of Hydrogen Energy*, vol. 30, no. 11, pp. 1265–1276, 2005.

[86] A. M. Levendorf, D.-J. Chen, C. L. Rom, Y. Liu, and Y. J. Tong, "Electrochemical and in situ ATR-SEIRAS investigations of methanol and CO electro-oxidation on PVP-free cubic and octahedral/tetrahedral Pt nanoparticles," *RSC Advances*, vol. 4, no. 41, pp. 21284–21293, 2014.

[87] R. Kodiyath, G. V. Ramesh, E. Koudelkova, T. Tanabe, M. Ito, M. Manikandan, S. Ueda, T. Fujita, N. Umezawa, H. Noguchi, K. Ariga, and H. Abe, "Promoted C–C bond cleavage over intermetallic TaPt3 catalyst toward low-temperature energy extraction from ethanol," *Energy & Environmental Science*, vol. 8, no. 6, pp. 1685–1689, 2015.

[88] H. Okamoto, W. Kon, and Y. Mukouyama, "Five Current Peaks in Voltammograms for Oxidations of Formic Acid, Formaldehyde, and Methanol on Platinum," *The Journal of Physical Chemistry B*, vol. 109, no. 32, pp. 15659–15666, 2005.

[89] C. da Fonseca, F. Ozanam, and J. N. Chazalviel, "In situ infrared characterisation of the interfacial oxide during the anodic dissolution of a silicon electrode in fluoride electrolytes," *Surface Science*, vol. 365, no. 1, pp. 1–14, 1996.

[90] G. Samjeské, A. Miki, S. Ye, and M. Osawa, "Mechanistic Study of Electrocatalytic Oxidation of Formic Acid at Platinum in Acidic Solution by Time-Resolved Surface-Enhanced Infrared Absorption Spectroscopy," *The Journal of Physical Chemistry B*, vol. 110, no. 33, pp. 16559–16566, 2006.

[91] M. S. Akhter, J. R. Keifer, A. R. Chughtai, and D. M. Smith, "The absorption band at 1590 cm-1 in the infrared spectrum of carbons," *Carbon*, vol. 23, no. 5, pp. 589–591, 1985.

[92] T. Ohtani, J. Kubota, A. Wada, J. N. Kondo, K. Domen, and C. Hirose, "IRAS and TPD study of adsorbed formic acid on Pt(110)-(1 × 2) surface," *Surface Science*, vol. 368, no. 1–3, pp. 270–274, 1996.

[93] R. G. Greenler, D. R. Snider, D. Witt, and R. S. Sorbello, "The metal-surface selection rule for infrared spectra of molecules adsorbed on small metal particles," *Surface Science*, vol. 118, no. 3, pp. 415–428, 1982.

[94] J. V. Perales-Rondón, A. Ferre-Vilaplana, J. M. Feliu, and E. Herrero, "Oxidation Mechanism of Formic Acid on the Bismuth Adatom-Modified Pt(111) Surface," *Journal of the American Chemical Society*, vol. 136, no. 38, pp. 13110–13113, 2014.

[95] K. A. Friedrich, F. Henglein, U. Stimming, and W. Unkauf, "Size dependence of the CO monolayer oxidation on nanosized Pt particles supported on gold," *Electrochimica Acta*, vol. 45, no. 20, pp. 3283–3293, 2000.

[96] O. V. Cherstiouk, P. A. Simonov, V. I. Zaikovskii, and E. R. Savinova, "CO monolayer oxidation at Pt nanoparticles supported on glassy carbon electrodes," *Journal of Electroanalytical Chemistry*, vol. 554–555, pp. 241–251, 2003.

[97] T. Sato, K. Kunimatsu, H. Uchida, and M. Watanabe, "Adsorption/oxidation of CO on highly dispersed Pt catalyst studied by combined electrochemical and ATR-FTIRAS methods: Part 1. ATR-FTIRAS spectra of CO adsorbed on highly dispersed Pt catalyst on carbon black and carbon un-supported Pt black," *Electrochimica Acta*, vol. 53, no. 3, pp. 1265–1278, 2007.

[98] S. Park, Tong, A. Wieckowski, and M. J. Weaver, "Infrared Spectral Comparison of Electrochemical Carbon Monoxide Adlayers Formed by Direct Chemisorption and Methanol Dissociation on Carbon-Supported Platinum Nanoparticles," *Langmuir*, vol. 18, no. 8, pp. 3233–3240, 2002.

[99] S. Chumillas, C. Busó-Rogero, J. Solla-Gullón, F. J. Vidal-Iglesias, E. Herrero, and J. M. Feliu, "Size and diffusion effects on the oxidation of formic acid and ethanol on platinum nanoparticles," *Electrochemistry Communications*, vol. 13, no. 11, pp. 1194–1197, 2011.

[100] M. Arenz, K. J. J. Mayrhofer, V. Stamenković, B. B. Blizanac, T. Tomoyuki, P. N. Ross, and N. M. Marković, "The Effect of the Particle Size on the Kinetics of CO Electrooxidation on High Surface Area Pt Catalysts," *Journal of the American Chemical Society*, vol. 127, no. 18, pp. 6819–6829, 2005.

[101] F. Maillard, E. R. Savinova, P. A. Simonov, V. I. Zaikovskii, and U. Stimming, "Infrared Spectroscopic Study of CO Adsorption and Electro-oxidation on Carbon-Supported Pt Nanoparticles: Interparticle versus Intraparticle Heterogeneity," *The Journal of Physical Chemistry B*, vol. 108, no. 46, pp. 17893–17904, 2004.

[102] J. Solla-Gullón, P. Rodríguez, E. Herrero, A. Aldaz, and J. M. Feliu, "Surface characterization of platinum electrodes," *Phys. Chem. Chem. Phys.*, vol. 10, no. 10, pp. 1359–1373, 2008.

[103] B. Braunschweig and W. Daum, "Superstructures and Order-Disorder Transition of Sulfate Adlayers on Pt(111) in Sulfuric Acid Solution," *Langmuir*, vol. 25, no. 18, pp. 11112–11120, 2009.

[104] L. W. Liao, S. X. Liu, Q. Tao, B. Geng, P. Zhang, C. M. Wang, Y. X. Chen, and S. Ye, "A method for kinetic study of methanol oxidation at Pt electrodes by electrochemical in situ infrared spectroscopy," *Journal of Electroanalytical Chemistry*, vol. 650, no. 2, pp. 233–240, 2011.

[105] Y.-X. Chen, M. Heinen, Z. Jusys, and R. J. Behm, "Kinetic Isotope Effects in Complex Reaction Networks: Formic Acid Electro-Oxidation," *ChemPhysChem*, vol. 8, no. 3, pp. 380–385, 2007.

[106] A. M. Funtikov, U. Linke, U. Stimming, and R. Vogel, "An in-situ STM study of anion adsorption on Pt(111) from sulfuric acid solutions," *Surface Science*, vol. 324, no. 1, pp. L343–L348, 1995.

[107] N. Marković and P. N. Ross, "The effect of specific adsorption of ions and underpotential deposition of copper on the electro-oxidation of methanol on platinum single-crystal surfaces," *Journal of Electroanalytical Chemistry*, vol. 330, no. 1–2, pp. 499–520, 1992.

[108] S. Gilman, "The Mechanism of Electrochemical Oxidation of Carbon Monoxide and Methanol on Platinum. II. The "Reactant-Pair" Mechanism for Electrochemical Oxidation of Carbon Monoxide and Methanol1," *The Journal of Physical Chemistry*, vol. 68, no. 1, pp. 70–80, 1964.

[109] S.-C. Chang and M. J. Weaver, "Coverage-dependent dipole coupling for carbon monoxide adsorbed at ordered platinum(111)-aqueous interfaces: Structural and electrochemical implications," *The Journal of Chemical Physics*, vol. 92, no. 7, pp. 4582–4594, 1990.

Chapter 6

Conclusions

A new approach to *in situ* IR spectroscopy of supported nanoparticle electrocatalysts has been developed and successfully applied to the study of two reactions of relevance to fuel cells: carbon monoxide stripping and formic acid oxidation.

The spectroelectrochemical cell designed in this work offers solution flow over the catalyst layer to remove mass transport limitations, provides accurate potential control over the catalyst at scan rates up to $1\,\mathrm{V\,s^{-1}}$ and allows sensitive IR sampling of the catalyst with spectral acquisition times as low as 0.5 s. Electronic synchronisation of IR and electrochemical measurements with solution flow enables accurate timing and reproducibility of complex experiments.

The utility of the setup is demonstrated by studying carbon monoxide stripping on a commercial carbon-supported Pt catalyst. Spectra collected during CO stripping exhibit a variety of features but are dominated by the bipolar shape of the CO peaks. It is shown that these anomalous peak shapes can be satisfactorily modelled using a Lorentzian peak shape and consideration of the reflectivity of the catalyst layer. The model enables fitting of the anomalous peaks and, in connection with electrochemical measurements, allows quantification of the coverage of adsorbed CO. The fitted oscillator strength, peak position and width are all found to be a function of coverage, suggesting that CO on

the surface of the catalyst is strongly coupled and forms islands. Further peak fitting carried out on spectra obtained during the stripping voltammogram appears to show a correlation between specific CO species in the spectra and the multiple current peaks seen in the voltammogram. Two IR peaks in the linear CO region in particular correlated with the main stripping current peak and were assigned to CO on step and terrace sites of the polycrystalline catalyst particles. Quantitative analysis suggests that CO on terraces starts to be oxidised first, followed by CO at edge sites, consistent with the 'active site' model for CO oxidation.

The cell and peak fitting methodology were extended to a study of formic acid oxidation at the same catalyst. *In situ* characterisation of the catalyst during oxidation revealed two potential-dependent adsorbed species: adsorbed CO, CO(ad), and for the first time on a supported nanoparticle during electrocatalysis, adsorbed formate, HCOO(ad). Furthermore, the surface selection rule-prohibited C−H wagging mode of HCOO(ad) was observed for the first time on any metal surface under any conditions. This suggests that the surface selection rule is weakened for species on small nanoparticles as previously predicted.

The rates of both CO formation and oxidation in formic acid were found to be significantly slower on the supported catalyst used here than on the thin deposited Pt layers used in previous (ATR-SEIRA) *in situ* mechanistic studies. In contrast, the rate of formate adsorption/desorption were found to be identical. The slow rate of CO formation and oxidation was confirmed in independent rate measurements. These results suggest that any differences in formic acid oxidation reactivity between model catalyst layers used in ATR-SEIRA experiments and nanoparticles are likely to arise from the reaction of CO. This analysis provides a clear illustration of the need for *in situ* studies on nanoparticles.

Further measurements of the reaction order, along with supporting electrolyte, pH and kinetic isotope effects, provide evidence for the existence of multiple pathways in addition

to the CO pathway, as proposed for macroscopic electrodes. In particular it is suggested that the majority of formic acid oxidation current from the catalyst comes from direct reaction of the aqueous formate anion, rather than from the decomposition of adsorbed formate.

6.1 Further Work

The spectroelectrochemical approach developed in this thesis has been able to provide insight into two electrocatalytic reactions occurring on a commercial fuel cell catalyst. In future the technique can be extended to the examination of novel electrocatalysts, such as those with compositions or structures tailored for particular reactions. It should enable the electrochemical data obtained from routine testing of such catalysts to be augmented with information on the identity and state of adsorbed species, allowing the effect of various modifications to the catalyst to be understood in detail. Furthermore, developments in the time resolution of the electrochemical and spectroscopic measurements should also be possible, following refinements to the design, and would enable aspects such as adsorption to be studied in similar detail.

Finally, this work also poses some fundamental questions which require further experimental work before they can be answered. For example, the weakening of the surface selection rule at small nanoparticles has long been predicted, and preliminary work in this thesis appears to provide some evidence for it, however further work is needed to confirm this. The ability to overcome the surface selection rule would be a significant development, as it would enable many mechanisms to be tested for which intermediates have been postulated but never detected. The approach presented in this work should therefore be of use in both fundamental and applied studies of supported nanoparticle electrocatalysts.

Appendix A

Fabrication Methods

Many different approaches to the fabrication of inert, sealed spectroelectrochemical cells were trialled during the research presented in this thesis and are described here in detail.

A.1 Electrochemically Inert Methods for Sealing Optics

A.1.0.4 Araldite Resin

A shallow circular recess was machined into the baseplate to enable the resin (CY1300 GB, Hunstsman) to surround the edges of the IRE. The resin was prepared at 80 °C by mixing base resin with hardener before pouring into the recess and curing at this temperature for 2 hours. Once cured the whole top face of the mounting plate, including the IRE, was

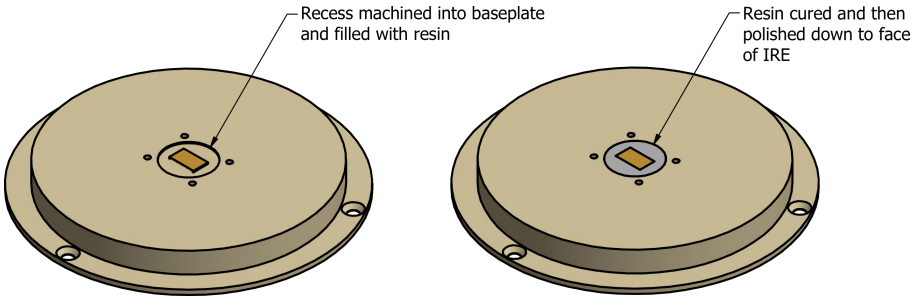

Figure A.1: Using resin to seal the ATR crystal into the baseplate. A shallow recess is made in the baseplate and resin is poured into the recess and over the IRE. After curing the resin is lapped and polished down to the crystal.

lapped and polished to a mirror finish. This produced a highly flat surface on which to seal, however the resin flowed too easily and contaminated the bottom face of the IRE. In addition, small bubbles formed in the mixing process remained in the resin on curing and left weak points around the IRE which ruptured during use and caused the cell to leak. This approach was not pursued due to the high failure rate and difficulty in extracting the crystal from the resin.

A.1.0.5 Vacuum Sealing Wax

A similar approach to that used for the resin was trialled with sealing wax (Wax W, Apiezon). The wax is marketed for several applications including sealing components into vacuum systems and acting as an acid resist in etching processes, both of which make it a good candidate for use in the present situation. To make the seal the wax was either positioned around the IRE in the circular recess and heated with a heat gun until it flowed, or was dissolved in toluene, painted onto the mating surfaces and again heated until it melted. Unfortunately the wax strongly absorbs in the IR region of interest and contributed unwanted peaks to the spectra unless meticulously removed from the reflecting faces of the IRE. As with the resin above, this cleaning process was time consuming and another alternative was sought.

A.1.0.6 Direct Si bonding

Rather than seal the ATR crystal into the baseplate to form a larger surface on which to seal, an alternative approach is to make a new, larger optic which can be directly sealed on to. In theory, such an optic can be created from two individual optics bonded together just using van der Waals forces, with the internal reflection of the original ATR crystal unaffected by the addition of additional surrounding material. Such a direct bonding approach has been investigated in the field of integrated circuit manufacturing and was

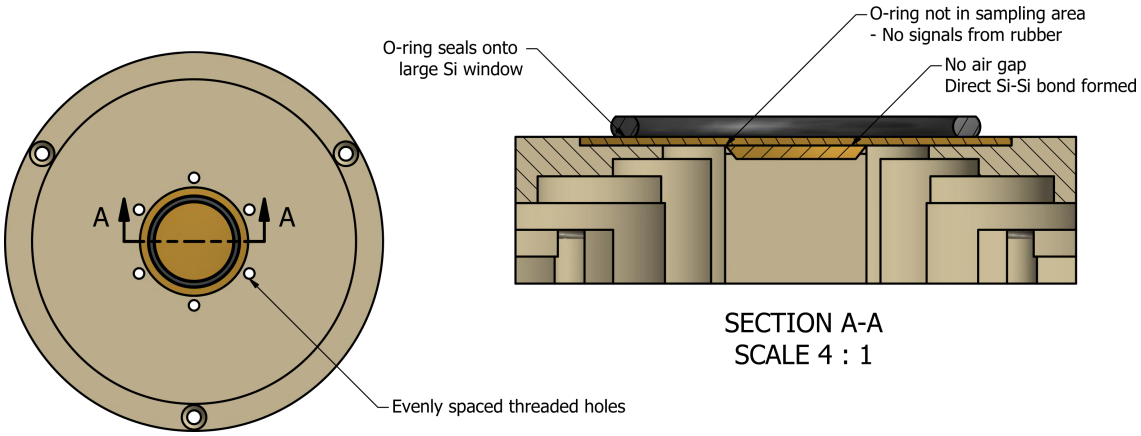

Figure A.2: The ATR crystal-window concept.

therefore attempted. [1] A Si IRE and a 1 inch Si window (CrysTran) were obtained with a high quality surface finish. In a clean room the two pieces were cleaned by ultrasonication in isopropanol for 8 minutes followed by 10 minutes of O_2 plasma treatment. The pieces were then manually aligned inside a multifunction anodic bonder which was then evacuated to 1×10^{-5} mbar. A force of 200 N was then applied for 5 minutes. On removal the pieces remained joined until a small amount of force was applied using tweezers and the pieces moved. The two pieces were realigned and later heated to 1000 °C for 2 hours to try and fully form the bond. However this step was carried out in air and both surfaces were substantially oxidised - no bond was formed. This method was not pursued due to time constraints although it remains an attractive long term solution, perhaps where conditions cause other methods to become inappropriate.

A.2 Inert electrical connections

The importance of making low resistance connections can be seen in table A.1, where the potential drop due to the passage of current through materials of different resistivity found in the spectroelectrochemical cell is calculated. Silver epoxy is often used to make low resistance electrical connections to components that are not suitable for soldering. However, if the connection is not sufficiently well isolated from the electrolyte solution the

Table A.1: The resistivity of materials used in the electrochemical cell.

Material	Resistivity / $\Omega\,$cm	(ℓ/A) / cm^{-1}	Resistance / Ω	iR(1 mA) / V	Ref.
PG[a]	5×10^{-4}	6×10^{-1}	3×10^{-4}	3×10^{-7}	b
PG[c]	5×10^{-1}	3×10^{-1}	1.5×10^{-1}	1.5×10^{-4}	b
Ag	1.63×10^{-6}	1×10^{2}	1.63×10^{-4}	1.63×10^{-7}	b
Ag epoxy	$< 1 \times 10^{-3}$	$\sim 1 \times 10^{-1}$	num1e-4	1×10^{-7}	b
Pt/C	8.49×10^{-2}	2.50×10^{-6}	2.12×10^{-7}	2.12×10^{-10}	d

[a] In plane
[b] Provided by the manufacturer
[c] Normal to plane
[d] Approximate value based on conductivity measurements of 5 catalyst films.

Ag can leach out and give rise to unwanted signals. To avoid Ag leaching an alternative solution would be to use a non-metallic conductive paste. A carbon-based paste was made by mixing 10% by weight Vulcan XC72R carbon black with Araldite resin at 80°. The resulting connections showed a resistance of around 30 Ω. Despite this the cyclic voltammetry seemed relatively undistorted when low concentrations of HCOOH were used. To further minimise the effects of the high resistance connection, the working and sense electrodes of the potentiostat were decoupled to allow individual connection to the flow field. Since the potential measurement circuit is now fully isolated from the current carrying circuit the Ohmic losses should be negligible. This is seen in fig. 3.13, where the peaks in the voltammogram have shifted down to lower overpotential, indicating that the real potential drop between the working electrode and solution is greater for the same applied potential. This approach was not continued however as the connections were brittle and broke when the cell was disassembled.

References

[1] A. Plößl and G. Kräuter, "Wafer direct bonding: tailoring adhesion between brittle materials," *Materials Science and Engineering: R: Reports*, vol. 25, pp. 1–88, Mar. 1999.

Appendix B

MATLAB Code

B.1 importsec

```
%% IMPORTSEC
% Imports and co-adds infrared kinetic data in *.spc files
   from Resolutions Pro and
% correlates it with electrochemical data exported as *.csv
   from NOVA.
%
%% Exporting data for use with the script
% To export an *.spc file from a kinetics data file, click
   the 'Export
% Regions' tab in the kinetics window. Use the time selection
    tool to select
% all of the data in the bar at the bottom of the lower
   chromatogram window.
%
% To export a *.csv file from Nova, open the data in the
   database window,
% make sure you are on the spreadsheet setting and right
   click on the top,
% left corner of the spreadsheet and select 'Export to ASCII
   '. Remember to
% add the '.csv' suffix to the filename.
%
%% What the script does
% The script imports both sets of data and co-adds the
   spectra to achieve
% the desired potential resolution, ie. if you enter 25 mV,
   it will co-add
% all the spectra in each 25 mV window. It then uses the time
    data in each
% set to correlate the spectra to a particular potential. It
   assumes that
% both sets of data start at the same point in time i.e. you
   haven't run a
```

```
% previous electrochemical step whilst the kinetics spectra
   were being
% collected.
%
% The script outputs the parameters it used for the
   correlation and asks for
% a filename to output the results. The file it saves has the
    ending
% '.sec'. It can be opended in Origin if the appropriate
   filter is in the
% user scripts folder.
%
%% Import the data
% Clear the workspace of all previous variables except the
   filepath
clear answer Eapp Emid j results spectra tapp timefactor tmid
    x y y1
% Define the filenames of the infrared and electrochemical
   data to be
% imported by user interface, store filename and filepath
   separately

if exist('datapath','var')
    [IRfilename_temp, IRpathname_temp] =uigetfile('*.spc', '
       Select a Resolutions .SPC file',datapath);
else [IRfilename_temp, IRpathname_temp] =uigetfile('*.spc', '
   Select a Resolutions .SPC file');
end

[ECfilename_temp, ECpathname_temp] =uigetfile('*.csv', '
   Select a NOVA .CSV file',IRpathname_temp);
datapath=num2str(IRpathname_temp);
% Output the filepath as a text strong for the results log
line1_temp = ['IR filename is ',IRpathname_temp,
   IRfilename_temp,''];
line2_temp = ['EC filename is ',ECpathname_temp,
   ECfilename_temp,''];
% Create the full filepath by joining directory and filename
   together into new
% variable
IRfile_temp = strcat(IRpathname_temp,IRfilename_temp);
ECfile_temp = strcat(ECpathname_temp,ECfilename_temp);
% Create a dialog box to prompt the user for the wait time,
   potential
% resolution and baseline point. The wait time is necessary
   as Nova starts
% counting time once the procedure is started, even if the
   procedure
% involves waiting for a trigger from the spectrometer. In
   addition, there
```

```
% is often a time period where spectra are being collected
   but Nova is not
% collecting data points, eg the wait time before cyclic
   voltammetry. To
% enable the Nova time and Spectrometer time to correlate,
   the delay
% between starting the Nova procedure and the spectrometer
   trigger must be
% subtracted. This is doen by setting the first Nova point to
    0. Then the
% time between the spectrometer trigger and the onset of Nova
    data
% collection must also be accounted for, and this is what is
   input by the
% user. The potential resolution parameter defines how many
   spectra are
% averaged together to produce to the final data. The script
   calculates
% this by calculating the scan rate and how many spectra are
   collected per
% second. The baseline point is set to 0 by translating the
   spectrum up or
% down. This enables the spectra to be presented as a stack
   with an even
% gap between each one.
prompt_temp = {'Enter wait time in seconds:','Enter potential
    resolution in mV:', 'Enter baseline point in cm-1:'};
dlg_title_temp = 'Processing Parameters';
num_lines_temp = 1;
def_temp = {'100','100','2500'};
answer_temp = inputdlg(prompt_temp,dlg_title_temp,
   num_lines_temp,def_temp);
% Stores the potential resolution as potres_temp.
potres_temp = str2double(answer_temp(2));
% Import the electrochemical data into structure 'ECdata'
ECdata_temp=importdata(ECfile_temp);
Eapp=ECdata_temp.data(:,1);
j=ECdata_temp.data(:,3);
tapp=ECdata_temp.data(:,2);
% Correct the timebase for the EC data. Nova starts counting
   once it starts
% waiting for the DIO trigger, so this waiting period must be
    subtracted.
waittime_temp = str2double(answer_temp(1));
timefactor=ECdata_temp.data(1,2)-waittime_temp;
corrtime_temp=ECdata_temp.data(:,2)-timefactor;
% Use the spc import function to read the SPC file into the
   structure
% spc_data
spc_data_temp=tgspcread(IRfile_temp);
% Extract the X values to variable 'x'.
```

```
x=spc_data_temp.X;
%% Calculate some parameters from the data
% Define the potential resolution and the scan rate of the CV
    to calculate the number of spectra to be averaged/co-
   added. The number must be
% stored as an integer, not as a floating point double.
pot_resolution_temp = int32(potres_temp);
% Calculate the ec scan rate by looking at the magnitude of
   delta E/delta t
scan_rate_temp = abs(1e3*(ECdata_temp.data(2,1)-ECdata_temp.
   data(1,1))/(corrtime_temp(2)-corrtime_temp(1)));
% Calculate the CV step potential (for reference only)
step_potential_temp = 1e3*(ECdata_temp.data(2,1)-ECdata_temp.
   data(1,1));
% Calculate how many spectra were recorded per second
spectra_collection_frequency_temp=1/(spc_data_temp.Z(3)-
   spc_data_temp.Z(2));
% Calculate what time range to average over to get specified
   potential
%resolution
averaging_time_temp=double(pot_resolution_temp/scan_rate_temp
   );
% Calculate how many spectra to co-add to get the specified
   potential
% resolution, given the calculated CV scan rate and spectra
   collection rate
timeres_temp= int32(spectra_collection_frequency_temp*
   averaging_time_temp);
% Get the number of spectra in the file
points_temp=size(spc_data_temp.Y,2);
% Calculate the final number of spectra. This must be a
   multiple of the time
% resolution. The 'idivide' function divides the number of
   spectra by the
% time resolution, and 'floor' rounds down to the nearest
   whole number.
spectra=idivide(points_temp,timeres_temp,'floor');
%% Process the data
% Create a new variable with the correct number of spectra to
    use for the
% averaging i.e. the remainder when the number of spectra is
   divided by the
% time resolution, taken from the last spectrum.
data_temp=spc_data_temp.Y(1:end,1:spectra*timeres_temp);
% This function stacks up every nth spectrum (where n is the
   time
% resolution) so that the rows can be averaged.
data_3D_temp=reshape(data_temp,int32(size(spc_data_temp.X,1))
   ,timeres_temp,spectra);
% This averages the data along the rows.
avg_data_temp=mean(data_3D_temp,2);
```

```
% This reshapes the matrix to be 2 dimensional again and
   names the data
% 'y'.
y=double(reshape(avg_data_temp,int32(size(spc_data_temp.X,1))
   ,spectra));
% Now calculate the average time point for each averaged
   spectrum.
% First create a new time variable with the correct number of
    time points.
time_temp=spc_data_temp.Z(1:spectra*timeres_temp);
% Then treat this matrix in the same way as the spectra
   matrix to get
% average the same way.
time_2D_temp=reshape(time_temp,1,timeres_temp,spectra);
%Average along dimension 2, the 'timeres'.
avg_time_temp=mean(time_2D_temp,2);
%Return the matrix to a 1xN matrix.
tmid = reshape(avg_time_temp,1,spectra);
%Lookup the potentials using the calculated time
Emid = interp1(corrtime_temp,ECdata_temp.data(:,1),tmid);
%% The results log
% Display all data used for processing
line3_temp = ['Potential resolution is ', num2str(
   pot_resolution_temp), ' mV'];
line4_temp = ['Calculated scan rate is ', num2str(
   scan_rate_temp), ' mV/s'];
line5_temp = ['Calculated step potential is ',num2str(
   step_potential_temp), ' mV'];
line6_temp = ['CV starts at ', num2str(waittime_temp), ' s'];
line7_temp = ['Spectra were collected every ', num2str((
   spc_data_temp.Z(3)-spc_data_temp.Z(2))), ' s'];
line8_temp = ['Calculated number of spectra to co-add is ',
   num2str(timeres_temp),''];
line9_temp = ['Final number of spectra is ', num2str(spectra)
   ,''];
results_array = char(line1_temp,line2_temp,line3_temp,
   line4_temp,line5_temp,line6_temp,line7_temp,line8_temp,
   line9_temp);
results_str={line1_temp,line2_temp,line3_temp,line4_temp,
   line5_temp,line6_temp,line7_temp,line8_temp,line9_temp};
disp(results_array)
h = msgbox(results_str,'Results');
%% Optional Ratio Step
% Ratio the data to a spectrum within its own set. This
   eliminates run to
% run differences such as water vapour, detector ice bands
   after filling
% etc. The second part of the RHS ratios each spectrum to the
    37th
% spectrum, in this case the 3rd spectrum of the second cycle
   . The final
```

```
% part of the expression normalises the spectra to a flat
   region (here 2500
% cm-1)
%for i=1:spectra
%y1(:,i)=y(:,i)-y(:,37)-y(850,i);
%end
%clear i
%% Export the data
% Join the calculated data together into one matrix for
   export
columns_temp=horzcat(x,y);
header1_temp=vertcat(horzcat(0, tmid),columns_temp);
results_array=vertcat(horzcat(0, Emid),header1_temp);
%name the file and give it the extension *.sec
prompt_temp = {'Enter output filename:'};
dlg_title_temp = 'Output Parameters';
num_lines_temp = 1;
def_temp = {IRfilename_temp};
outputdata_temp = inputdlg(prompt_temp,dlg_title_temp,
   num_lines_temp,def_temp);
filename_temp=outputdata_temp{1};
suffix_temp='.sec';
% Output the delimited file into the original directory
outputpath_temp=strcat(datapath,filename_temp,suffix_temp);
dlmwrite(outputpath_temp,results_array);
% Remove all the temporary variables used in the averaging
   process from the workspace.
clearvars *_temp
clear i
```

B.2 fitPeak

```
% fitPeak Select, ratio, baseline correct, fit and export
   infrared spectra.
%
% Ian McPherson 2015

clear nPeaks useKK A B xx yy X LB UB options X1 b@x...
    resnorm residual exitflag output lambda yfit bl m

nPeaks = 1; % Number of peaks to fit, currently between 1-3
   are allowed

%linearandbridge_co_parameters
linear_co_parameters
%bridge_co_parameters
%hcooh_parameters
% Options
useKK = 1; % Kramers-Kronig transform
useBaseline = 1; % Linear baseline
fitAll = 1; % Fit >1 spectra
```

```
showFit = 1; % Plot fits during fitting
fitPointbyPoint = 1; % Previous fit is subsequent starting
   point
saveData = 1; % Save the input data, fitted curves and fitted
    parameters

% Open data
if exist('x','var') == 0
    run SECimport
end

% Interesting wavenumber ranges
v1 = [1600:1750];
v2 = [1950:2150];
v3 = [1775:1950];
...
% Wavenumber range to use
V = v2; % wavenumber range
A = [round((V(1)-x(1))/(x(2)-x(1))):...
    round((V(size(V,2))-x(1))/(x(2)-x(1)))]; % Calculated x
       point range
% A = [575:724]; % alternatively specify x point range
   directly
xx=x(A);

% Column numbers of interesting spectra
B1 = 1;
B2 = 210;
B3 = 178;

% Ranges
R1 = [B1:B2];


% Matrices of interesting spectra
yy1 = y(A,R1);
yy2 = y(A,B2);

% Background spectrum
bb1 = y(A,B3); % Background to subtract (single spectrum)
BB1 = bb1*ones(1,size(yy1,2)); % Matrix of backgrounds

% Matrix of background subtracted spectra
yy = yy1-BB1;

% Fitting Parameters



% Function handle
if nPeaks == 1
```

```
    if useKK == 1
        fun=@peak1KK;
    else
        fun=@peak1LL;
    end
elseif nPeaks == 2
    if useKK == 1
        fun=@peak2KK;
    else
        fun=@peak2LL;
    end
elseif nPeaks ==3
    if useKK == 1
        fun=@peak3KK;
    else
        fun=@peak3LL;
    end
end

%fun = @peak2Gaussian;

% Baseline
if useBaseline == 1
    i = 1;
%     f0=fit(xx,yy(:,i),'poly1','Exclude',10:size(yy,1)-10);
%     m(i,:)=coeffvalues(f0);
%     bl(:,i)=m(i,1).*xx+m(i,2);
%     yy(:,i)=yy(:,i)-bl(:,i);%+yy(1,i);
    f0=fit(xx,yy(:,i),'poly1','Exclude',10:size(yy,1)-10);
    m(i,:)=coeffvalues(f0);
    bl(:,i)=m(i,1).*xx+m(i,2);
    yy(:,i)=yy(:,i)-bl(:,i);%+yy(1,i);

    if fitAll ==1
        for i=1:size(yy,2)
            f0=fit(xx,yy(:,i),'poly1','Exclude',10:size(yy,1)
               -10);
            m(i,:)=coeffvalues(f0);
            bl(:,i)=m(i,1).*xx+m(i,2);
            yy(:,i)=yy(:,i)-bl(:,i);%+yy(1,i);

        end
    end
end

% Fitting options
options=optimoptions(@lsqcurvefit,...
    'ToLFun',1e-15,...
    'TolX',1e-15,...
    'MaxFunEvals',1e3,...
    'MaxIter',1e3,...
```

```
    'display','off');

% Typical options
% options=optimoptions(@lsqcurvefit,...
%     'ToLFun',1e-15,...
%     'TolX',1e-15,...
%     'MaxFunEvals',12e4,...
%     'MaxIter',1e4,...
%     'display','off');

% Fit the first spectrum
i = 1;
[X1(:,i), resnorm(:,i), residual(:,i), exitflag, output,
   lambda] ...
    = lsqcurvefit(fun,X,xx,yy(:,i),LB,UB,options);
yfit(:,i)=fun(X1(:,i),xx);

% Plot the results
plot(xx,yy,xx,yfit);
set(gca,'XDir','Reverse');
xlabel 'wavenumber / cm^{-1}';
ylabel '\Delta A';

% Fit any remaining spectra
tic
if fitAll == 1
    if fitPointbyPoint ==0
        for i = 2:size(yy,2)
        [X1(:,i), resnorm(:,i), residual(:,i), exitflag,
           output, lambda] ...
            = lsqcurvefit(fun,X,xx,yy(:,i),LB,UB,options);
        yfit(:,i)=fun(X1(:,i),xx);
            if showFit == 1
                plot(xx,yy(:,i),xx,yfit(:,i));
                set(gca,'XDir','Reverse');
                xlabel 'wavenumber / cm^{-1}';
                ylabel '\Delta A';
                pause (0.5)
            end
        end
    else
        for i = 2:size(yy,2)
            [X1(:,i), resnorm(:,i), residual(:,i), exitflag,
               output, lambda] ...
                = lsqcurvefit(fun,X1(:,i-1),xx,yy(:,i),LB,UB,
                   options);
            yfit(:,i)=fun(X1(:,i),xx);
                if showFit == 1
                    plot(xx,yy(:,i),xx,yfit(:,i));
                    set(gca,'XDir','Reverse');
                    xlabel 'wavenumber / cm^{-1}';
```

```
                    ylabel '\Delta A';
                    pause (0.5)
                end
                i
        end
    end
end
toc
 % Save the data as a csv file?

if saveData == 1

    fileprompt_temp='Choose a filename for the output file ';
    filename=input(fileprompt_temp);

    if exist('Emid','var')==1
        H = Emid(R1);
    elseif exist('t','var')==1
        H = t(R1);
    else
        H = ones(size(R1,2))';
    end

    M1 = [H;X1;resnorm]';
    strA=[filename '-params.csv'];
    dlmwrite(strA,M1)
    M2 = [xx yy];
    strB=[filename '-data.csv'];
    dlmwrite(strB,M2)
    M3 = [xx yfit];
    strC=[filename '-fit.csv'];
    dlmwrite(strC,M3)
end
```

B.2.1 linear_co_parameters.m

```
% linear_co_parameters

% Fitting Parameters
% X is the initial value, UB/LB are the upper/lower bounds
% Baseline refractive index noo
X(1) = 1;     LB(1) = 0;       UB(1) = 3;

% Peak 1
X(2) = 156;      LB(2) = 0;       UB(2) = 500;
X(3) = 2070;     LB(3) = 1950;    UB(3) = 2100;
X(4) = 15;       LB(4) = 10;      UB(4) = 50;
% Peak 2
    if nPeaks > 1
X(5) = 0;        LB(5) = 0;       UB(5) = 500;
X(6) = 2050;     LB(6) = 2040;    UB(6) = 2060;
X(7) = 15;       LB(7) = 10;      UB(7) = 50;
```

```
% Peak 3
    if nPeaks > 2
X(8) = 500;        LB(8) = 100;       UB(8) = 1500;
X(9) = 2075;     LB(9) = 2000;    UB(9) = 2100;
X(10) = 15;      LB(10) = 10;     UB(10) = 50;
% Peak 4
    if nPeaks > 3
X(11) = 5;       LB(11) = 0;      UB(11) = 1500;
X(12) = 2083;    LB(12) = 2080;   UB(12) = 2095;
X(13) = 15;      LB(13) = 5;      UB(13) = 20;
    end
    end
    end
```

B.3 peak1KK

```
function f=peak1KK(X,x)
% Extract variables from the fitting parameters
noo = X(1);
f1 = X(2);
x01 = X(3);

g1 = X(4);


dw = x(2)-x(1);
w = [-x(size(x,1)):dw:x(size(x,1))]; % Create negative
   wavenumbers
maxf = size(w,2);
minf = size(w,2) - (size(x,1)-1);

i = sqrt(-1);

% Specify the known parameters
theta=39;
n1=3.43;

% Calculate the refraction and absorption indices and combine
    into a
% complex refractive index
kw = imag(-f1./(x01.^2-w.^2+i.*g1.*w)); % Negative sign
   ensure peak is pointing up, must have missed a negative
   somewhere when adding in the negative wavenumbers

nw = KK(kw,dw) + noo; % KK transform of kw plus noo (indep of
    x)
n2 = complex(nw,kw); % Complex index of refraction

% Calculate the reflection coefficent for s-polarised light
   and the
% reflectivity
```

```
r = rS(theta,n1,n2);
R = real(r.*conj(r));
R0=0.68; % R=0.68

% Convert the reflectivity into absorption
f=-log10(R(minf:maxf)./R0)';

    function n=KK(kw,dw)
        nir = kw; % imaginary part refractive index
        [dt,nit,t] = icft(dw,nir); % inverse FT
        nit = 2*imag(nit); % take only imaginary part
        nrt = nit .* sign(t); % make symmetric as opposed to
           antisymmetric
        [~,nrw] = cft(dt,nrt); % FT
        n = real(nrw); % take only real part

                function [dt,ft,t] = icft(dw,Fw)
                    N = length(Fw); % number of points
                    dt = 2*pi/(N*dw); % time spacing
                    ft = ifft(Fw) / dt; % inverse Fourier
                       transform
                    if nargout > 2
                    t = [0:ceil(N/2)-1, -floor(N/2):-1].*dt;
                end
                end
                function [dw,Fw,w] = cft(dt,ft)
                    N = length(ft); % number of points
                    Fw = fft(ft) * dt; % inverse Fourier
                       transform
                    dw = 2*pi/(N*dt); % time spacing
                    if nargout > 2
                    w = [0:ceil(N/2), -floor(N/2):-1].*dw; %
                       floor/ceiling rounding used to ensure
                       frequency vector is same length as
                       time vector (otherwise odd numbers end
                        up losing a point due to rounding)
                end
end


    end
    function r=rS(theta,n1,n2)
        n=n2./n1;
        r=(cosd(theta)-(n.^2-sind(theta).^2).^0.5)./(cosd(
           theta)+(n.^2-sind(theta).^2).^0.5);
    end
end
```

Appendix C

Raw Data

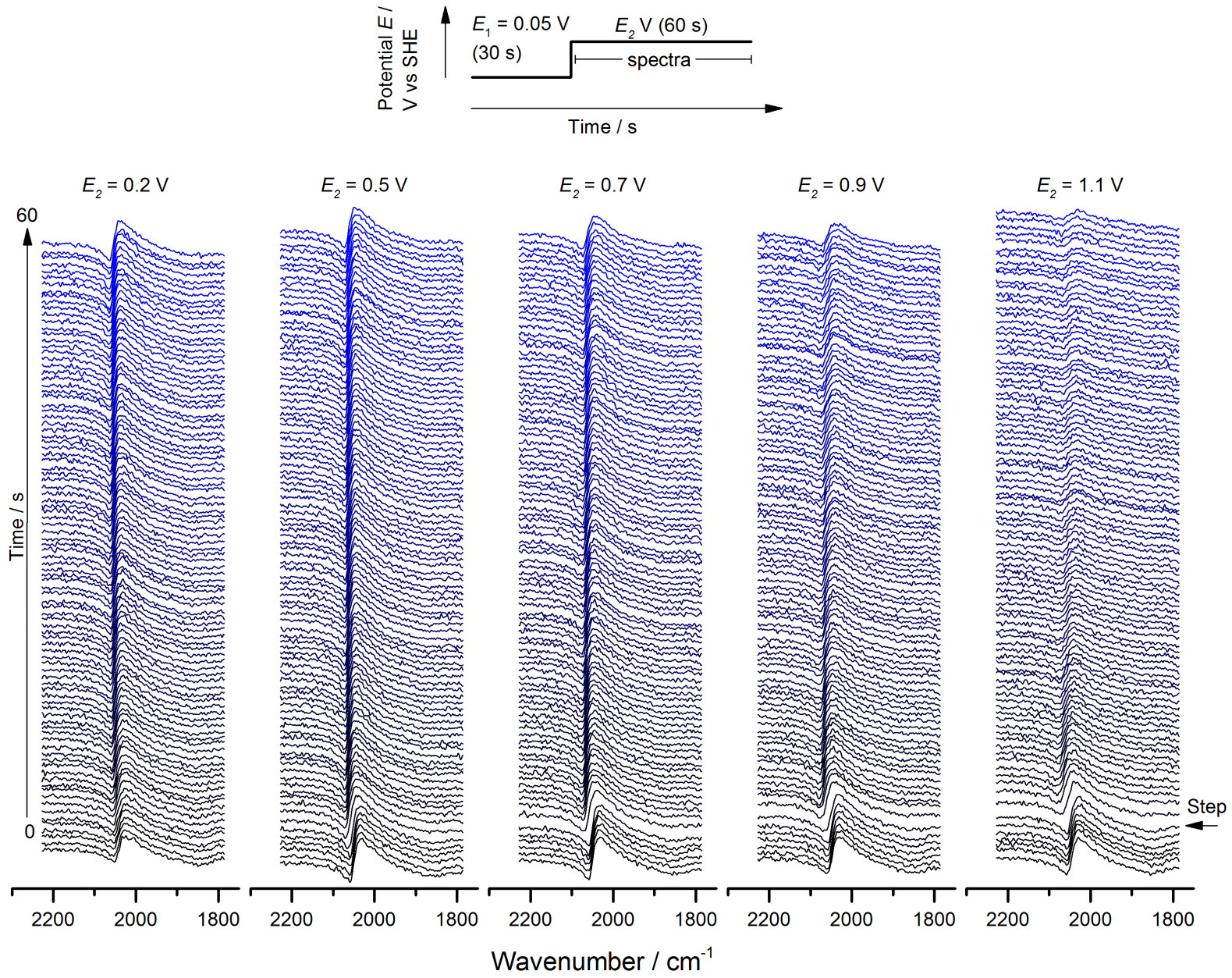

Figure C.1: Spectra acquired to determine the rate of CO oxidation in HCOOH. Solution: 0.1 M HCOOH + 0.5 M $HClO_4$. Flow rate: 3 mL min^{-1}.

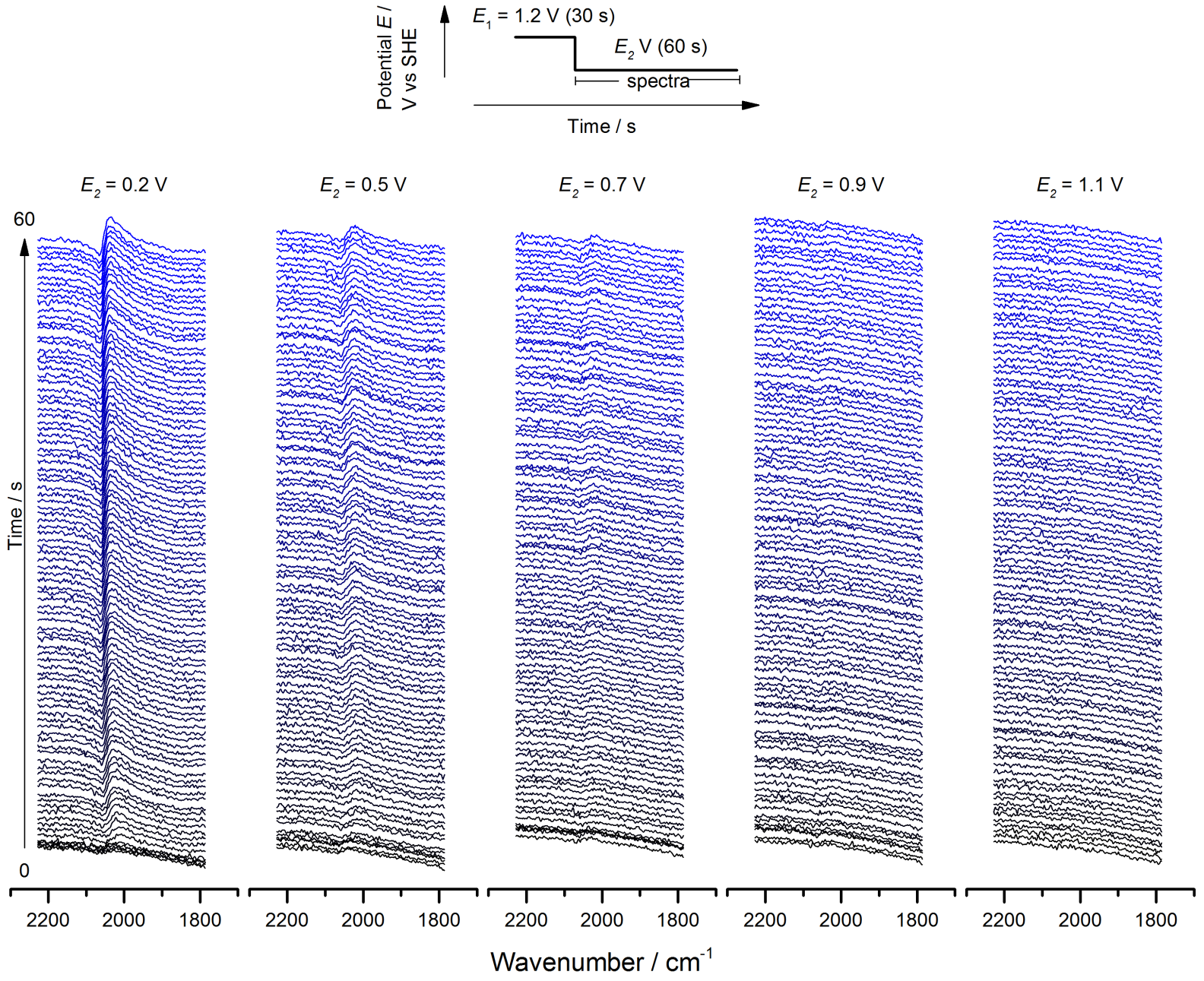

Figure C.2: Spectra acquired to determine the rate of CO formation form HCOOH. Solution: 0.1 M HCOOH + 0.5 M $HClO_4$. Flow rate: 3 mL min^{-1}.